AN ELECTROCHEMICAL STUDY OF WELL-DEFINED NAFION COATED PLATINUM AND PLATINUM-BIMETALLIC ELECTRODES

A thesis submitted to

Cardiff University

For the degree of

Philosophiae Doctor

By

Mujib Ahmed B.Sc.

Department of Chemistry

Cardiff University

Dedication

With all of my love to my beautiful wife Sharifa. As one wonderful chapter in my life has ended, an exciting new chapter, to be filled with so much love, joy and happiness begins with you.

Abstract

In this investigation, cyclic voltammetry (CV), X-ray photoelectron spectroscopy (XPS) and rotating disc electrode (RDE) measurements of the oxygen reduction reaction (ORR) have been used to explore the complex three-phase Nafion-platinum-electrolyte interface. This interface is at the heart of the functioning membrane electrode assembly (MEA) of a fuel cell.

CV was primarily used to analyse ultra-thin Nafion films, deposited (without contamination) onto various flat and stepped platinum and platinum bimetallic single crystal electrodes. For Pt{111}, XPS measurements were also used to determine Nafion surface layer thickness and to obtain surface chemical composition. CV results have shown that Nafion is a probe of adsorbed OH on platinum electrodes and for stepped surfaces, unusual structural sensitivity of Nafion-induced voltammetric peaks, ascribable to Nafion interactions with step sites, is observed as a function of average terrace width.

Voltammetric results for palladium adlayers (up to two monolayers) adsorbed on Nafion coated Pt{111} and {100} in aqueous 0.1M $HClO_4$, show the first layer palladium hydrogen underpotential deposition (H_{UPD}) peak being much sharper and intense as compared to Nafion free surfaces. A similar phenomenon was found for platinum-palladium surface alloys in that Nafion adsorption would produce sharper, palladium H_{UPD} peaks. This behaviour is ascribed to stronger specific adsorption of the Nafion sulphonate groups with palladium compared to platinum. It was interesting to note that for bismuth adlayers adsorbed onto Nafion coated Pt{111} and {100}, attenuation of H_{UPD} features was identical whether or not Nafion was adsorbed but the Bi-OH redox features for Nafion coated surfaces exhibited marked differences, again ascribable to competitive adsorption of sulphonate and OH.

Using RDE, it was found that the ORR for various Nafion coated Pt{hkl} electrodes was inhibited compared to Nafion free electrodes. The electrooxidation of formic acid on palladium modified, Nafion coated Pt{111}, in aqueous 0.1M $HClO_4$, was found not to be affected by the presence of Nafion. However methanol electrooxidation was inhibited on palladium modified, Nafion coated Pt{111}. Finally a number of actual fuel cell electrocatalysts, provided by Johnson Matthey were characterised using CV. The {111} and {100} surface site densities were quantified using bismuth and germanium as surface probes. Comparisons between Nafion coated electrocatalysts and Nafion free electrocatalysts are also reported. It was found that only very marginal differences between the CV responses of both types of catalyst are recorded (in contrast to the single crystal data).

Acknowledgements

I would like to thank first and foremost Professor Gary A. Attard for all his help, support and guidance over the past four years. His passion for science has been an incredible source of encouragement and motivation, indeed it has been an honour to have been his student.

At Johnson Matthey, I would like to extend my gratitude to Dr Jonathon Sharman, Dr Dave Thomspsett and Dr Ed Wright. I would like to thank you all for the extensive knowledge and guidance provided over the last four years, which were key to the research and my development.

I would also like to thank Johnson Matthey and the EPSRC for funding this study.

At Cardiff, I would like to thank Dr Dave Morgan for undertaking the XPS experiments for this study, and also to thank all technical members of staff at Cardiff University for the excellent services provided.

I would like to this opportunity to thank all members of the Electrochemical Surface Science research group at Cardiff University. In particular I would like to thank Sharon Huxter and Dr Robert Taylor for providing the initial training and support when I started my research in 2008. I would like to thank also all BSc and MChem project students that I have had the pleasure of working with. I would also like to thank Mahmud Aban and Dr Txell Casadesus, Dr Peter Jenkins, Shaoliang Guan, Ashley Brew and Jinyu Ye. I have had a great pleasure in working with you all and forging lifelong friendships. Good luck with the rest of your research, I hope to see you all soon.

Most importantly, I would like to thank all of my family for their love and support. To my mum, dad, brothers and whole family, thank you all for just being there over the last four years.

Finally, this study would not have been completed without the help of Allah.

Publications

1) **Mujib Ahmed, David Morgan, Gary Anthony Attard, Edward Wright, David Thompsett, and Jonathan Sharman** *"Unprecedented Structural Sensitivity toward Average Terrace Width: Nafion Adsorption at Pt{hkl} Electrodes"*, J. Phys. Chem. C, 115, (2011), 17020.

2) **Mujib Ahmed, Gary A. Attard, Edward Wright, Jonathan Sharman** *"Methanol and formic acid electrooxidation on nafion modified Pd/Pt{1 1 1}: The role of anion specific adsorption in electrocatalytic activity"* (Article in press in Catalysis Today)

Contents

Chapter 2 Theoretical Background

Chapter 3 Experimental

Chapter 4 Unprecedented Structural Sensitivity toward Average Terrace Width and ORR activity: Nafion Adsorption at Pt*{hkl}* Electrodes

Chapter 6 Methanol and Formic acid Electrooxidation on Nafion Modified Pd/Pt{111}: the role of Anion Specific Adsorption in Electrocatalytic Activity

Chapter 7 Surface Structural Characterisation of Platinum High Surface Area (HSA) electrocatalysts

Chapter 8 Conclusion

List of Symbols

English

Symbol	Description	Units
A	Electrode area	cm^2
B	Frequency factor	s^{-1}
C	Capacitance	F
C_B	Bulk concentration of oxygen in solution	$1.1\ x10^{-3}$ mol dm^{-3}
C_o	Concentration gradient	mol cm^{-3}
D_o	Diffusion co-efficient	$cm^2\ s^{-1}$
D_e	Dissociation energy	kJ mol^{-1}
e^-	Charge on one electron	-1.602×10^{-19} C
E	Applied potential	V
E'	Working potential	V
E_e	Equilibrium potential	V
E	Energy	eV, J, J mol^{-1}
E_{kin}	Kinetic energy	eV, J, J mol^{-1}
E_B	Binding energy	eV, J, J mol^{-1}
E_F	Fermi energy	eV
E_{vac}	Vacuum energy	eV
F	Faraday constant	9.649×10^4 C mol^{-1}

h	Planck's constant	6.626×10^{-34} J s
J_O	Flux	mol m^{-2} s^{-1}
j_a	Anodic current	A
j_c	Cathodic current	A
j_L	Limiting current	A cm^{-2}
j_k	Kinetic current density	A cm^{-2}
j_0	Exchange current density	A cm^{-2}
K	Boltzmann constant	1.381×10^{-23} J K^{-1}
k_{ox}	Rate constant of oxidation reaction	
k_{red}	Rate constant of reduction reaction	
L	Bond length	Å, nm
n	Number of electrons	-
N_A	Avogadro's constant	6.022×10^{-23} mol^{-1}
Q	Charge	C
R	Gas constant	8.314 J K^{-1} mol^{-1}
t	Time	s
T	Temperature	K
ν	Frequency	s^{-1}
ν	kinematic viscosity of solution	ca 0.01 cm^2 s^{-1}
ν	Scan rate	V s^{-1}
V	Potential	V

Greek

Symbol	Description	Units
α	Transfer co-efficient	Dimensionless
η	Overpotential	V
ω	Angular rotation rate	radians per second
Φ	Work function	eV

Abbreviations

AFC	Alkaline fuel cells
CV	Cyclic Voltammetry/cyclic voltammogram
DAFC	Direct alcohol fuel cell
DFT	Density Functional Theory
E_{PZC}	Potential of zero charge
HER	Hydrogen evolution reaction
HOR	hydrogen oxidation reaction
H UPD	Hydrogen underpotential deposition
MCFC	molten carbonate fuel cells
MEA	membrane electrode assembly
NMR	Nuclear Magnetic Resonance
ORR	oxygen reduction reaction
Ox	Oxidised species

PAFC	phosphoric acid fuel cell
PEMFC	Proton exchange membrane fuel cell
PEM	Proton exchange membrane
PZTC	Potential of zero total charge
PTFE	Polytetrafluoroethylene (Teflon®)
RDE	Rotating disc electrode
Red	Reduced species
SAXS	small angle X-ray scattering
SOFC	solid oxide fuel cell
UHV	Ultra High Vacuum
WAXS	Wide angle X-ray scattering
XPS	X-Ray photoelectron spectroscopy

Chapter One

Introduction

1.1 An overview of proton exchange membrane fuel cells (PEMFC)

Rising global energy demand and the environmental impact of energy use from traditional sources pose serious challenges to human health, energy security, environmental protection and the sustainability of natural resources. Over the last century the burning of fossil fuels for day to day production of electricity and for the use in automobiles for example has had an adverse effect on the environment. The combustion of fossil fuels leads to the production of greenhouse gases such as CO_2, NO_x and SO_x which have a detrimental effect on the environment. Thus there is a need for alternative, clean and more energy efficient devices that can be used to produce electricity for day to day use as well as for automotive transportation. Fuel cells are energy conversion devices that convert chemical energy to electrical energy via a direct electrochemical reaction. Fuel cells are by no means "new" technologies, they are one of the oldest electrical energy conversion devices known to man, first invented by a Welshman, Sir William Grove in the middle of the 19th century. Grove would develop a stack of 50 cells, which he would call a "gaseous voltaic battery". However it was over a century later in 1937 when Francis T Bacon would work on fuel cells for practical uses and in 1950 develop a 40 cell fuel cell stack capable of producing 5kW of electricity[1]. Fuel cell systems would successfully be used by NASA for their space programmes. Gemini V would utilise a polymer electrolyte membrane fuel cell (PEMFC) and the Apollo moonshot missions would utilise an alkaline fuel cell (AFC). However, because of their high cost, fuel cell systems were limited to mainly space missions such as those highlighted above where cost was not an issue. It wasn't until the late 1980s and early 1990s, when research by Ballard Power Systems in particular resulted in a growth in demand for fuel cell technologies, that wider applications, not just niche areas such as space missions, could lead to economically viable installations. Today, rivalry between battery and fuel cell technological solutions to the problem of replacing the internal combustion engine motor vehicle with the “all electric car” are driving innovation and progress ever faster.

Fuel cells differ from batteries in that the fuel and oxidant required are supplied from external sources, therefore fuel cells are capable of providing a continuous source of electricity until

the fuel source is exhausted[2]. The five most common fuel cell technologies are proton exchange membrane (also known as polymer electrolyte membrane) fuel cells (PEMFCs), alkaline fuel cells (AFCs), phosphoric acid fuel cells (PAFCs), molten carbonate fuel cells (MCFCs) and solid oxide fuel cells (SOFCs). The acronyms of each fuel cell is dependent on the type of fuel that is used. Alkaline fuel cells typically use potassium hydroxide as the electrolyte and these possess the highest electrical efficiency of any fuel cell. However AFCs suffer economically not only because of the need for ultra-pure gases for its fuel but also from reaction with carbon dioxide to form carbonates. The operating temperatures are below 100 ^{O}C, higher temperatures are required for improved hydrogen oxidation reaction (HOR) kinetics. The expected power output of an AFC can be in the range of tens of MW[3]. Phosphoric acid fuel cells are commercially the most advanced system due to simple construction and the thermal and chemical stability of the phosphoric acid electrolyte at an operating temperature in the range of 150 - 200 ^{O}C. PAFC are mainly used for stationary power ranging from dispersed power to on-site generation plants. Power outputs values for PAFCs of 0.2 - 20 MW are able to supply shopping malls and hospitals with electricity, heat, hot water and are commonly used as primary or backup power for these sites[3]. Molten carbonate and solid oxide fuel cells operate at very high temperatures, 600 - 800 ^{O}C and 800 - 1000 ^{O}C respectively. These fuel cells are again useful mainly for stationary applications. MCFCs use liquid lithium carbonate or lithium sodium carbonate stabilised in a matrix as the electrolyte for the system, while SOFCs utilise ceramics as the solid electrolyte. This is the main advantage of SOFCs over MCFCs as the solid electrolyte eliminates the need for a liquid electrolyte[3].

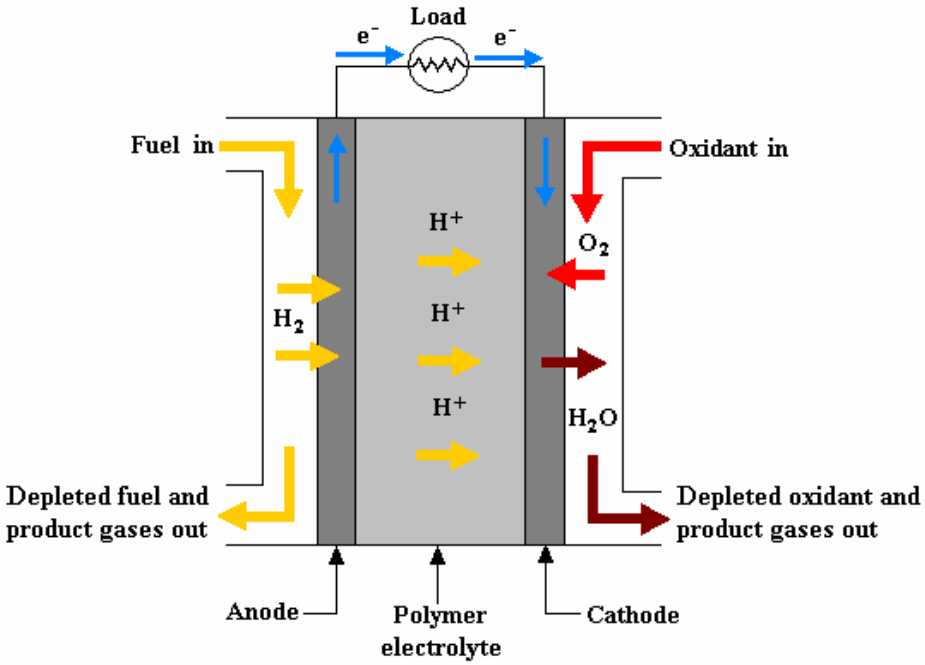

Fig 1.1 Schematic of a PEMFC. Reprinted from ref[4].

A typical schematic diagram of a PEM fuel cell is provided in figure 1.1. The key component of a PEM fuel cell, known as the membrane electrode assembly (MEA), consists of the polymer electrolyte membrane sandwiched in between the anode and cathode electrodes on either side. The electrodes are usually made of platinum or a platinum bimetallic electrocatalyst on a carbon support whilst Nafion is typically used as the polymer electrolyte membrane. From fig 1.1 it is seen that at the anode electrode, hydrogen is introduced and dissociates into protons and electrons. This is known as the hydrogen oxidation reaction (HOR). The protons are conducted through the polymer electrolyte membrane to the cathode whilst the electrons travel along an external circuit to the cathode, creating an electrical current. The polymer electrolyte membrane ensures that only protons are conducted through the membrane and prevents unwanted molecular transport. The PEM usually consists of strongly acidic groups which aid proton transport. At the cathode electrode, oxygen is fed into the system and reacts with the protons and electrons to form water, the only reaction by-product of a fuel cell system based on hydrogen/oxygen, which flows out of the cell. This is known as the oxygen reduction reaction (ORR). The two electrode reactions are as follows:

Anode reaction:

$$H_2 \rightarrow 2H^+ + 2e^- \qquad \text{(eq 1.1)}$$

corresponding to an anode potential, $E_a^0 = 0.00\ V$ *vs* standard hydrogen electrode (SHE).

Cathode Reaction:

$$1/2O_2 + 2H^+ + 2e^- \rightarrow H_2O \qquad \text{(eq 1.2)}$$

corresponding to a cathode potential, $E_c^0 = 1.23\ V$ *vs* SHE. The overall reaction is therefore:

$$H_2 + 1/2O_2 \rightarrow H_2O \qquad \text{(eq 1.3)}$$

The splitting of hydrogen is relatively easy on a platinum electrocatalyst[5]. The exchange current density for HOR on platinum has been calculated to be 0.1 A cm^{-2} which is very high compared to ORR where the exchange current density is 6 μA cm^{-2} [5], The exchange current density values are much lower for ORR because of the sluggish ORR kinetics due to the difficulty in splitting the oxygen molecule on a platinum surface. This in turn induces a significant activation loss for the fuel cell.

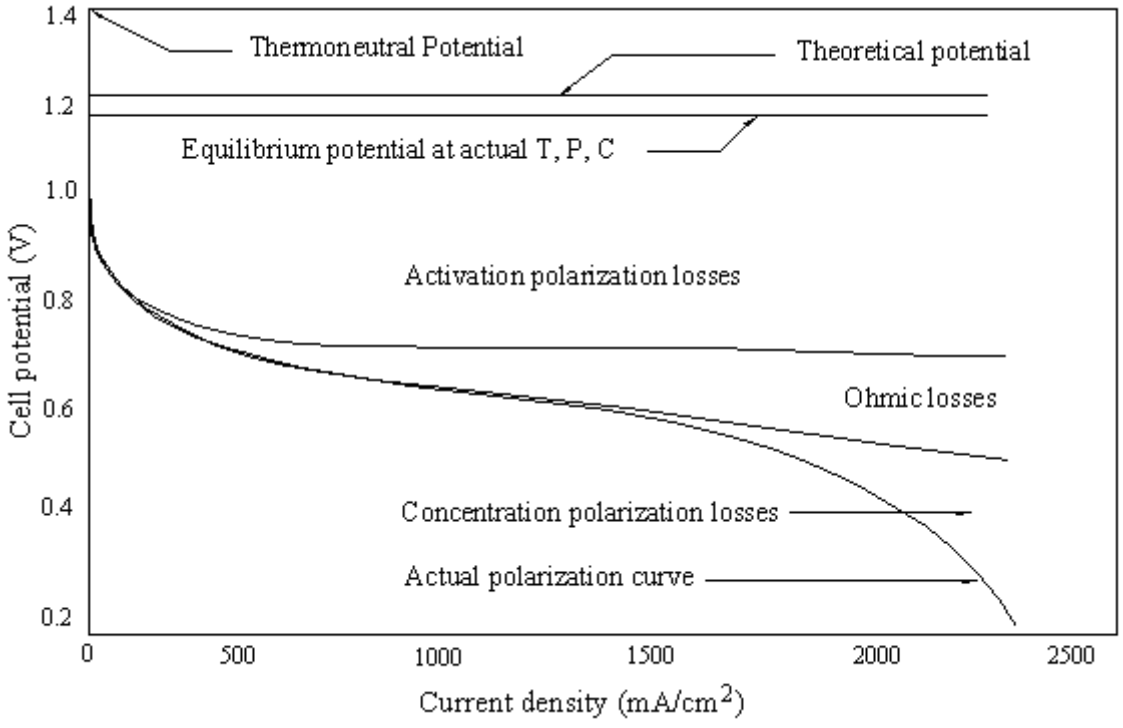

Fig 1.2 Voltage losses for a PEM fuel cell. Reprinted from ref[4].

In theory, during fuel cell operation, the fuel cell should maintain a voltage of 1.2 V *vs* SHE as current density is increased. However significant voltage losses occur during operation which are shown in figure 1.2. Fuel cell voltage losses can be summarised into three categories:

- activation polarisation
- Ohmic polarisation
- concentration polarisation

At low current density values, activation polarisation occurs due to a sharp drop in the fuel cell potential due to the sluggish oxygen reduction reaction (ORR) kinetics[1]. As the current density increases, voltage loss caused by Ohmic polarisation becomes significant and results mainly from flow of ions in the polymer electrolyte and resistance to the flow of electrons through the electrode[1]. At high current density values, cell potential drops drastically due to concentration polarisation. This is because mass transport effects of the reactant fuel is limiting through the electrocatalyst layers[1].

The reaction sites at the MEA of a PEMFC are composed of the Nafion polymer electrolyte membrane sandwiched in between the anode and cathode electrodes on either side. The electrodes are usually made of platinum or a platinum bimetallic electrocatalyst on a carbon support. At the heart of the MEA, the electrocatalytic HOR and ORR reactions occur on the electrode surface. These reactions are crucial to the fuel cell, but so is the nature of the reaction site that they are occurring on. From fundamental single crystal studies, activity *vs* structure relationships of electrocatalytic reactions have shown that the nature of the reaction site can either enhance or inhibit electrocatalytic reactions. These relationships have been used in order to tailor make real electrocatalysts for various processes. To understand this problem, it is important to have an understanding of catalysis/electrocatalysis, why the nature of the reaction site is crucial to an electrocatalytic reaction and the reported structures that Nafion forms at the “three-phase interphase” between ionomer, support and metal catalyst particle on the surface.

1.2 What is catalysis/electrocatalysis

Catalysis is an extremely important phenomenon for our modern industrial economy and a vital technology in today's world. Approximately 90% of all our chemicals and materials are produced using catalysis at one stage or another. In turn, many developed countries are net exporters of such chemicals and thus rely on catalysis for the health of their economies. The earliest systematic studies of catalysis began in the early 19th century when Davy began experiments on catalytic combustion with Pt gauzes. Later, Berzelius coined the term 'catalysis' in the following direct quotation:

> "*Many bodies have the property of exerting in other bodies an action which is very different from chemical affinity. By means of this action they produce decomposition in bodies, and form new compounds into the composition of which they do not enter. This new power, hitherto unknown, I shall call it catalytic power. I shall also call catalysis the decomposition of bodies by this force.*"
>
> J. Berzelius, Edinburgh New Philosophical Journal, 21 (1836), 223.

This may now be an outdated definition of catalysis and a more specific definition may be attained in the light of new chemical knowledge.

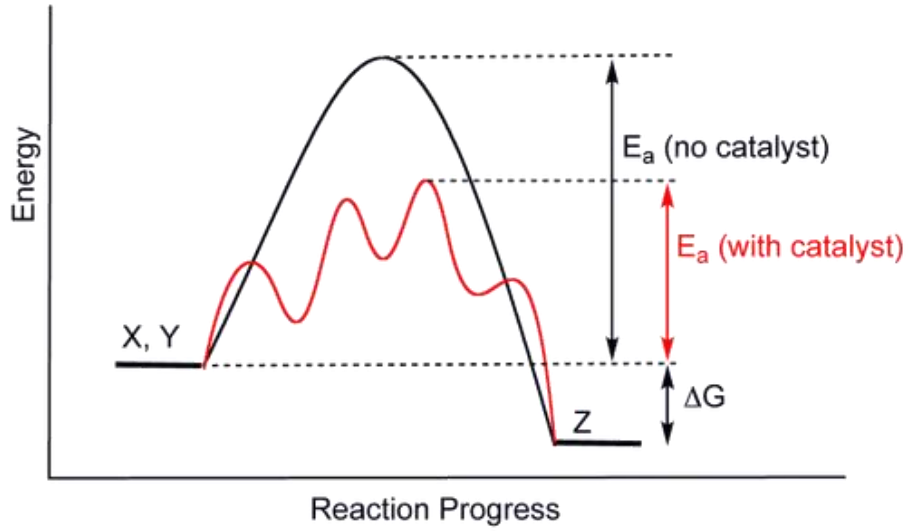

Figure 1.3 Energetics of a catalysed and non-catalysed reaction [6].

Consideration of the reaction energy profiles for catalysed and non-catalysed reactions depicted in Figure 1.3 leads to the following points concerning catalysis [7-11]:

1. The effect of the presence of a catalyst is that it causes an increase in the rate at which the given products are formed.
2. Catalysts increase the reaction rate by lowering the activation barrier between reactants and products.
3. A catalyst does not influence the position of equilibrium. The reverse reaction is therefore just as catalysed as the forward reaction. For example, a good hydrogenation catalyst will under the appropriate conditions, also be a good dehydrogenation catalyst.
4. The catalyst itself is not consumed during the reaction i.e. it is used and then regenerated.

From the above four observations, a catalyst/electrocatalyst can therefore be termed as "a substance that increases the rate at which a reaction reaches equilibrium without itself being consumed in the process". Just as in heterogeneous catalysis, electrocatalysis involves converting reactants into products without loss of the catalyst. But in electrocatalysis it is possible to drive a reaction out of equilibrium by means of the addition or subtraction of charge. In the next section, this will be explained with the use of basic electrode kinetics.

1.2.1 Basic electrode kinetics

Let us consider a simple one electron redox reaction

$$Ox + e \leftrightarrow Red \qquad \text{(eq 1.4)}$$

where Ox represents the oxidised species and Red represents the reduced species. At the anode the oxidation reaction occurs and the cathode is where the reduction reaction occurs. The rate of the reduction reaction is:

$$r = k_{red}[Ox] \qquad \text{(eq 1.5)}$$

and the rate of the oxidation reaction is:

$$r = k_{ox}[Red] \quad \text{(eq 1.6)}$$

where k_{red} and k_{ox} are the rate constants for the reduction and oxidation reactions. The current flowing in either the reductive or oxidative reaction is given by the following expressions. For the reductive reaction the *current density* j_c (current/electrode area A) is related to Faraday's constant, F, the rate constant k_c and the surface concentration of the reactant. The flow of current through an electrode of unit area is therefore given by[12,13]:

$$j_c = Fk_{red}[Ox] \quad \text{(eq 1.7)}$$

A similar expression is obtained for oxidative current density, now labelled j_a and is dependent on the surface concentration of species [Red] and rate constant k_a:

$$j_a = Fk_{ox}[Red] \quad \text{(eq 1.8)}$$

The total net flow of current is given as

$$j_{net} = j_a - j_c \quad \text{(eq 1.9)}$$

$$j_{net} = Fk_{ox}[Red] - Fk_{red}[Ox] \quad \text{(eq 1.10)}$$

It is reasonable to assume that electron transfer reactions behave in an analogous manner to chemical rate processes, and therefore may be described using the transition state model. This model views the reaction as occurring via a path that involves the reactants overcoming an energy barrier, the summit of which is known as the transition state, en route to becoming the product. Using transition state theory it is possible to relate the free energies of activation to the rate constant, this is given by[12,13]

$$k_{ox} = B_a e^{\frac{-\Delta G_{ox}}{RT}} \quad \text{(eq 1.11)}$$

$$k_{red} = B_c e^{\frac{-\Delta G_{red}}{RT}} \quad \text{(eq 1.12)}$$

therefore j_{net} becomes

$$j_{net} = B_a Fk_{ox}[Red]e^{\frac{-\Delta G_{ox}}{RT}} - B_c Fk_{red}[Ox]e^{\frac{-\Delta G_{red}}{RT}} \quad \text{(eq 1.13)}$$

where B is the frequency factor, the rate of collisions of the electrochemically active species with the electrode. Transition state theory is effected by the applied potential, the term α is now introduced. The value of α simply reflects the sensitivity of the transition state to the drop in applied potential between the electrode and electrolyte solution. If α is close to zero then the transition state resembles the reactants in its potential dependence whereas when it approaches unity, α resembles the products. In fact, α is found to be close to 0.5 for most reactions suggesting that the transition state has an intermediate stage for most reactions[12,13]. Therefore changes to the applied potential not only alter the absolute values of the free energies of reactants, products and the transition state but also their relative values as well. The consequence of this is that the free energy barriers to the oxidation and reduction reactions are altered and this can be seen to be the origin of the potential dependence of the kinetics of the electrode reactions. In order to drive an electrochemical reaction, a potential different to that of the equilibrium potential is required since at equilibrium, no net current flows. The deviation from the equilibrium potential is now known as the overpotential, η[12,13]

$$\eta = E' - E_e \qquad \text{(eq 1.14)}$$

where E' is the working potential and E_e is the equilibrium potential. Applying potential to the electrode reactions mean that equations 1.11 and 1.12 pertaining to the rate constants change to

$$k_{red} = Be^{\left(\frac{\Delta G_0^{\#}}{RT}\right)}e^{\left(\frac{-\alpha F\eta}{RT}\right)} \qquad \text{(eq 1.15)}$$

$$k_{ox} = Be^{\left(\frac{\Delta G_0^{\#}}{RT}\right)}e^{\left(\frac{(1-\alpha)F\eta}{RT}\right)} \qquad \text{(eq 1.16)}$$

where the free energies of activation for the oxidation and reduction reactions are[12,13]

$$\Delta G_{ox} = \Delta G_0^{\#} - (1-\alpha)F\eta \qquad \text{(eq 1.17)}$$

$$\Delta G_{red} = \Delta G_0^{\#} + \alpha F\eta \qquad \text{(eq 1.18)}$$

The relationships for the rate constants can be simplified by introducing new rate constants, k_{red}^0 and k_{ox}^0, that are independent of overpotential, the expressions for the rate constant become

$$k_{red} = k_{red}^{0} e^{\left(\frac{-\alpha F\eta}{RT}\right)} \qquad \text{(eq 1.19)}$$

$$k_{ox} = k_{ox}^{0} e^{\left(\frac{(1-\alpha)F\eta}{RT}\right)} \qquad \text{(eq 1.20)}$$

Finally, all that remains is to insert equations 1.19 and 1.20 into the equation for J_{net} when potential is applied. After simplification, the all important Butler Volmer equation is obtained[12,13]

$$j_{net} = j_0 \left\{ \left(e^{\frac{(1-\alpha)F\eta}{RT}} \right) - \left(e^{\frac{-\alpha F\eta}{RT}} \right) \right\} \qquad \text{(eq 1.21)}$$

where j_0 is called the *exchange current density*. j_0 is of crucial importance in electrocatalysis because it is a quantitative measure of how good a particular substance is for a given electrocatalytic reaction, the larger the value of the exchange current density, the better the material for electrocatalysing the process. The Butler-Volmer equation is fundamental to electrode kinetics. The variation of current as a function of overpotential is shown in figure 1.4.

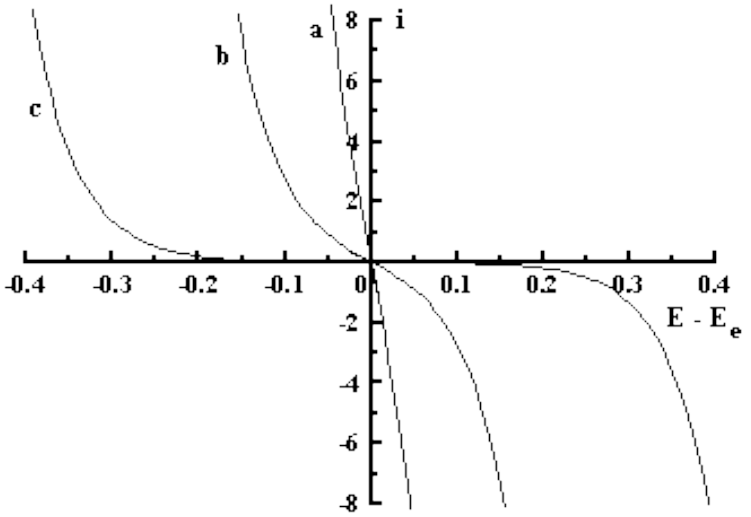

Fig 1.4 Change in current as a function of overpotential for an electrocatalytic reaction with increasing values of exchange current density and constant α = 0.5, j_o (a) > j_o (b) > j_o (c).[14]

It is seen from fig 1.4 that there are two limiting cases, at high and low values of exchange current density. When j_0 is 'large' (curve a) then a small change in overpotential results in a large current change. Essentially there is little or no activation barrier to the electrochemical reactions. For this case the electrode reaction is said to be reversible since both k_{red} and k_{ox} are large. At the other extreme when j_0 is very 'small' (curve c) then a large overpotential is needed to alter the current. This reflects the fact that there is now a high barrier to activation and so the rates of the reduction and oxidation processes become slow. Electrode reactions of this type are termed irreversible. Intermediate behaviour is generally referred to as quasi-reversible (curve b). Not surprisingly the different rates of electrode kinetics give rise to substantially different behaviour in voltammetric and impedance analysis.

1.2.2 Overpotential and energy levels

Metals contain a lattice of closely packed atoms. The overlap of atomic orbitals in the lattice ensures that electrons are able to move freely. The electrons occupy an effective continuum of energy states in the metal up to the maximum energy level, termed the Fermi energy. An applied potential to metals acts to increase or decrease the energy of the Fermi level (fig 1.5).

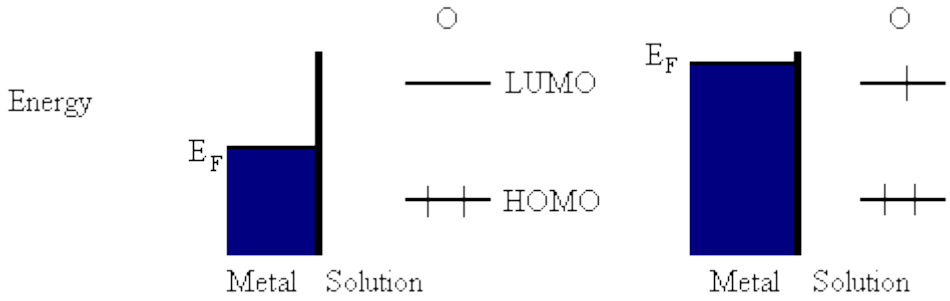

Fig 1.5 Effect of overpotential on the Fermi level relative to HOMO and LUMO levels on redox species[14].

In fig 1.5, a reactant molecule O, capable of undergoing a charge transfer reaction is introduced. Some of the energy states of O are depicted and in particular in the figure on the left hand side, the energy of the LUMO is higher than the Fermi energy of the metal. However if the Fermi energy of the metal is raised above the LUMO of O thanks to an overpotential, electron transfer is then thermodynamically favourably as seen in the figure on the right. The majority of electrocatalytic processes are dependent on the j_0 of the electrocatalyst and Fermi level of the electrocatalyst that is used and this can essentially be

altered with overpotential since the energy of electrons at the Fermi energy is being perturbed by the electrode potential. Different electrocatalysts will have different values of j_0 and subsequently will need different values of overpotential to drive a reaction. Therefore a new definition of electrocatalysis can be termed:

"when rate of electrochemical reaction is dependent on the nature of the electrode material used".

1.3 The effect of surface structure on electrocatalysis

1.3.1 The structure of bulk metal surfaces

The surface structure of a metal catalyst is of prime importance in any heterogeneous catalytic reaction[15]. The surface structure may contain, step, terrace and kink sites, all of which have different surface properties which in turn lead to different catalytic properties. Therefore it is desirable to understand the chemical and physical properties of metal surfaces.

When metals solidify from the molten state, the atoms arrange themselves into the simplest three dimensional repeating pattern (the unit cell), as a result forming a crystal. The crystal will contain many small crystalline domains that are randomly distributed throughout the metal and the metal is classed as "polycrystalline". The surface arrangement of atoms must reflect the underlying bulk structure of the metal. Macroscopic measurements on polycrystalline surfaces cannot therefore take into account reactions occurring at individual sites such as grain boundaries, steps, terraces, kinks or vacancies[16,17]. The results of any such measurement performed on polycrystalline surfaces are therefore an average of all surface sites present and often ignore the microscopic detail[18].

The use of well defined electrodes has yielded results on surface properties and composition with regards to catalytic activity and to the chemisorption and physisorption of species. Variation of the adsorption site is under the control of the experimentalist. Therefore, single crystal facets are employed since they exhibit the simplest adsorption behaviour of all surfaces, because the variation in adsorption site is limited by the geometry of the unit cell generating the crystal. Greater complexity can be introduced to the surface structure by cutting a crystal surface at a particular angle, creating step and kinks sites on the surface[19].

1.3.2 The surface structure of metals - the Miller index system

The Miller index is a system that is used to describe a particular crystallographic plane. Cutting through a metal surface at a particular angle will produce a surface that will have a specific surface structure[20]. The periodicity of the plane can be defined by its Miller index. The Miller indices for platinum *{hkl}* are defined by the vectors $\vec{a}$, $\vec{b}$ and $\vec{c}$, these represent the three axes of the unit cell. The distance from the origin to the intercept points in the crystal plane with vectors $\vec{a}$, $\vec{b}$ and $\vec{c}$ are defined as a, b and c respectively. The Miller indicies *h*, *k* and *l* of a particular crystal plane are defined as:

$$h = {|\vec{a}|}/{a} \qquad \text{(eq 1.22)}$$

$$k = {|\vec{b}|}/{b} \qquad \text{(eq 1.23)}$$

$$l = {|\vec{c}|}/{c} \qquad \text{(eq 1.24)}$$

If *h*, *k* or *l* take fractional values, the three Miller indices are converted to the smallest integers having the same ratio as *h*, *k* and *l* by multiplying by a common factor. For example {1/4, 2/4, 1} becomes {1, 2, 4}. Where a negative intercept happens to result, this is indicated by placing a bar above the appropriate value of the index[20]. The three most common low Miller index planes of fcc metals are the *{111}*, *{100}* and the *{110}*. These surfaces are called the basal planes and are commonly used for measurements due to their low surface free energies, high symmetries and relative stabilities[17]. The structural arrangement of atoms of all three planes is depicted in figure 1.6 in relation to the fcc unit cell.

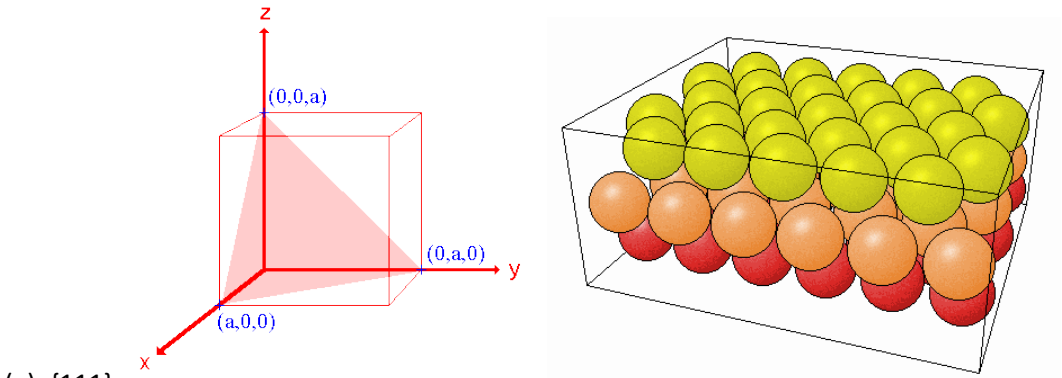

(a). {111}

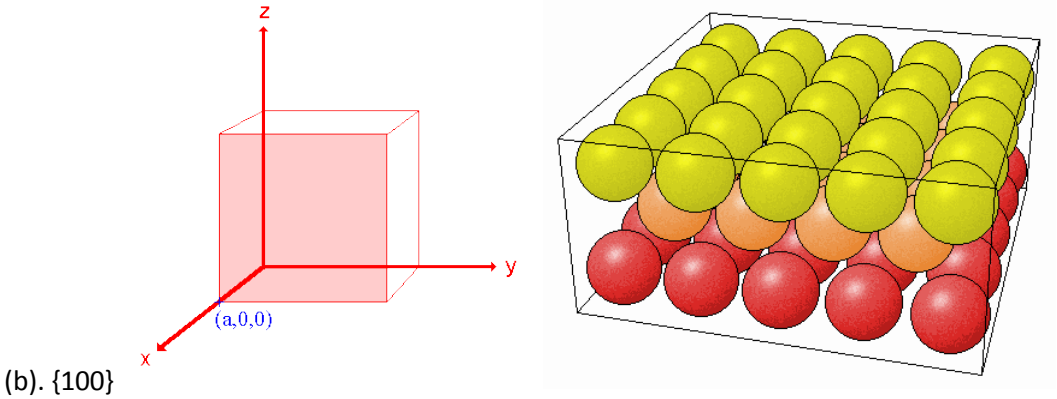

(b). {100}

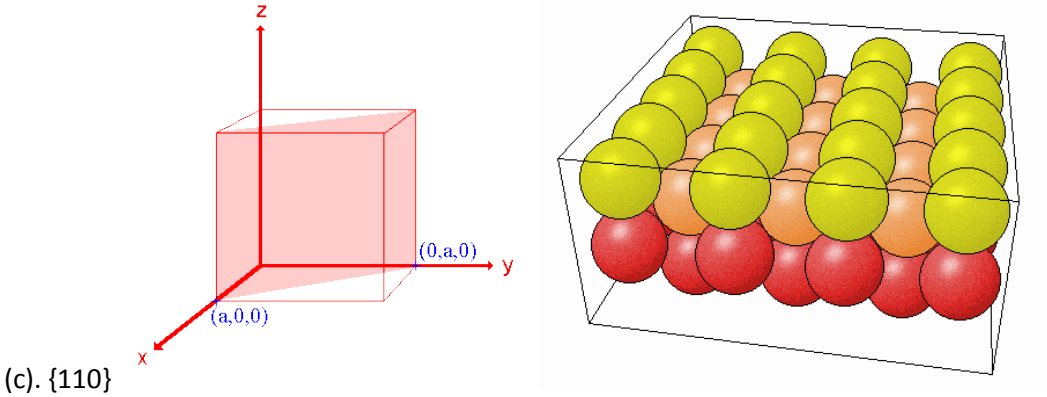

(c). {110}

Figure 1.6 The fcc basal planes and corresponding unit cells reprinted from[21,22].

If the plane of the fcc single crystal intersects any of the three axes at a fractional value of the lattice constant, then one of the *{hkl}* values will be greater than 1. These surfaces are known as high Miller index planes. High Miller index planes are produced by cutting a metal crystal in such a way that the resulting surface is rough on an atomic scale. This will result in surface containing either:

- Terraces of one of the three low Miller index planes that are separated by a monoatomic step. The terrace width is dependent on the cutting angle with respect to the low Miller index planes and are known as stepped surfaces[23].
- A combination of terraces, steps and kinks. These surfaces are known as kinked surfaces[24].

In each case, different stepped surfaces and kinked surfaces will exhibit a specific geometric arrangement of atoms. The adsorption properties and therefore, the chemical reactivity of each surface will therefore be different.

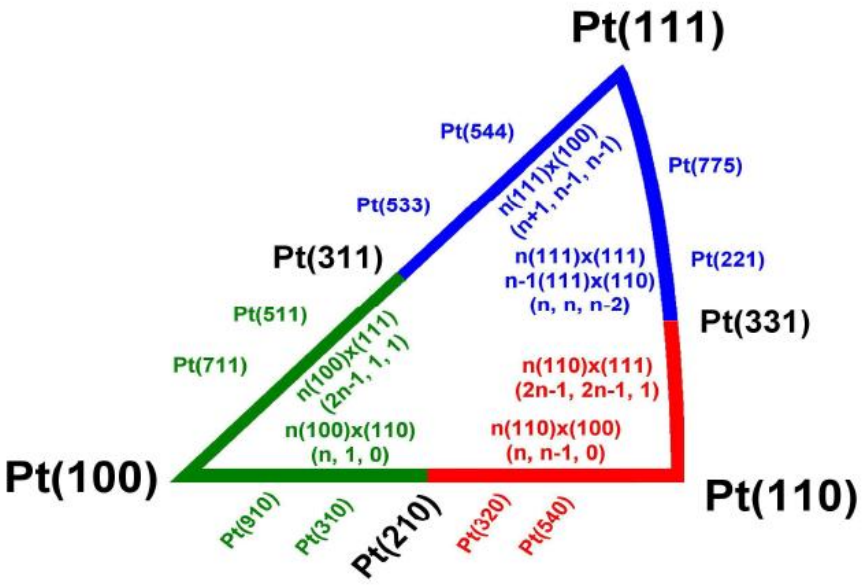

Fig 1.7 The stereographic triangle showing the relative positions and microfacet notations for a range of fcc single crystal surfaces (platinum in this case), reprinted from[25].

Fig 1.7 shows the three basal planes at the corners (poles) of the stereographic triangle. Each side (zone) represents the range of stepped surfaces associated with sites containing each pole. The equations to convert the microfacet notation to Miller index notation are given within the triangle. Taking the zone between fcc *{111}* and fcc *{100}* as an example, a surface which exhibits *{111}* terraces, n atoms long separated by a monatomic *{100}* step may be denoted (n+1,n-1,n-1). For example, a surface with a *4{111}×{100}* label in microfacet notation will have a Miller index of *{533}*[20]. Note that each zone of the stereographic triangle has a point where *n* in the microfacet notation is 2, i.e. when there is a step for every two atoms of terrace in length. The contributions therefore from each basal plane is effectively equivalent, this point is called the *turning point* of the zone.

1.4 Cyclic voltammetry of well defined platinum single crystal electrode surfaces

Cyclic voltammetry (CV) and variations of CV such as the rotating disc electrode (RDE) are used as the main electrochemical techniques used to characterise metal surfaces and monitor electrocatalytic reactions. A detailed analysis is provided of cyclic voltammetry in chapter 2 but in brief the experiment is a structure sensitive electrochemical technique that locks into the local charge of an electroactive material that changes as a function of potential, which in turn leads to the adsorption and desorption of ions which is read as electric current as potential changes.

Will[26] was the first investigator to measure CV from single crystal platinum electrodes. In the 1960s Will electrochemically "activated" single crystal platinum electrodes by repeated potential cycling between the so-called hydrogen and oxide potentials. He was also one of the first to interpret the two reversible 'hydrogen peaks' on platinum observed by CV in aqueous acidic media, which were termed 'weakly' and 'strongly' bonded states. Will showed that the peak at more negative potentials ≈ 0.125 V, the 'weakly' bonded state, corresponded to hydrogen on the {110} surface sites (by using electrochemically activated Pt{110} single crystal electrodes). The peaks at more positive potentials ≈ 0.275 V, the 'strongly' bonded state, corresponded to hydrogen on the Pt{100} surface sites using a similarly prepared Pt{100} single crystal electrode. The voltammetry of a platinum surface is well understood and is often used in studies of adsorption. Fig 1.8 shows a typical cyclic voltammogram of a polycrystalline platinum electrode. The voltammogram was obtained using 0.1M H_2SO_4 as the electrolyte, a scan rate of 0.05 V s^{-1} and all potentials quoted with respect to the Pd/H electrode. All details for the preparation of the electrochemical cell are provided in chapter 3 section 3.2.1. The different regions highlighted represent the different adsorption processes occurring on a Pt electrode as a function of potential in aqueous electrolyte.

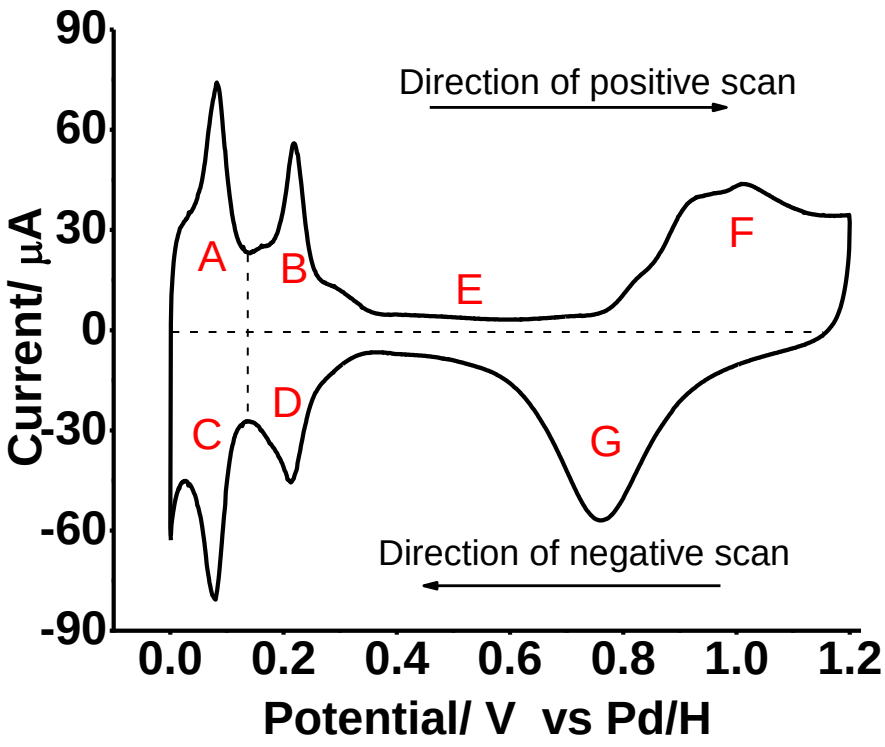

Fig 1.8 CV of a polycrystalline platinum electrode in 0.1M H_2SO_4.

Regions A, B, C and D highlighted in Fig 1.8 represent the region known as the H_{UPD} region, that is the underpotential deposition of hydrogen onto the surface of the platinum electrode. Regions A and B constitute the oxidation of underpotentially deposited $H^+_{(aq)}$ ions[27]. Electrons from the adsorbed hydrogen on the surface transfer to the bulk electrode, producing an anodic current. The adsorbed hydrogen desorbs from the surface and into the electrolyte:

$$H_{(ads)} \rightarrow H^+_{(aq)} + e^- \qquad \text{(eq 1.25)}$$

From the CV in fig 1.8 it can be seen that peak A represents hydrogen desorption from the {110} surface sites and region B hydrogen desorption from the {100} surface sites. At the {110} surface sites, the hydrogen is much more weakly bound compared to the {100} surface sites[27]. It should be noted that for the measurement of single crystal electrodes, the complete desorption of the hydrogen layer can provide the real surface area of the electrode. This is because it is known that:

1. one electron is transferred per one platinum site,
2. the number of platinum atoms per cm^{-2} can be calculated for the different surface crystal from the bulk density.

For example, for Pt{111}, Pt{100} and Pt{110} electrodes, a H_{UPD} charge of 241, 209 and 175 μC cm^{-2} respectively is estimated[28] assuming a (1x1) surface[28]. For polycrystalline platinum electrodes, a charge of 210 μC cm^{-2} (the average of the three low Miller index planes) is often used. It should be noted however that for Pt{111}, only 160 μC cm^{-2} of the total charge is attributable to the H_{UPD}, the rest being ascribed to anion adsorption (see later). Similarly, for Pt{110} a somewhat greater charge is observed due to partial reconstruction to the (1x2) phase. Nonetheless, good agreement with experiment is found.

Since regions A and B are where adsorbed hydrogen is oxidised and removed from the surface, regions C and D are the reverse of these processes. In regions C and D, the current that is generated at the {110} and {100} surface sites is from the reduction of $H^{+}_{(aq)}$ in the electrolyte to form adsorbed hydrogen adatoms, $H_{(ads)}$ (the reverse of eq 1.25).

Region E is the double layer region. Here, the only current that is flowing is because of the capacitative charge of the electrochemical double layer[13]. In this region, non-Faradaic processes are occurring where ions of the opposite charge are migrating to the surface which is becoming positively charged. The width of the double layer is important because it is proportional to the capacitance of the electrode (current density /sweep rate). The capacitance of the electrode is not only dependent on the electrode material but the surface area of the electrode itself. There are a wide variety of models proposed for the distribution of ions at the electrode/electrolyte interface that lead to capacitative processes which will not be discussed further. For further information on the double layer the reader is referred to Bard and Faulkner, Electrochemical Methods[13].

Regions F - G are the oxide regions of the platinum surface. The onset of platinum surface oxide formation is under way at 0.8 V in region D. Oxide formation is caused by the adsorption and splitting of water from the electrolyte with subsequent adsorption of OH species onto the platinum surface[29]. The splitting of water at 0.8 V results in the formation of adsorbed hydroxide and solution phase hydrogen cations:

$$Pt + H_2O \rightarrow PtOH_{(ads)} + H^{+}_{(aq)} + e^{-} \qquad \text{(eq 1.26)}$$

As the potential is increased further a second water molecule can be split resulting in the formation of a second adsorbed hydroxide species.

$$PtOH_{(ads)} + H_2O \rightarrow Pt(OH)_{2(ads)} + H^{+}_{(aq)} + e^{-} \qquad \text{(eq 1.27)}$$

The adsorbed hydroxide is strongly chemisorbed onto the electrode and will eventually undergo place exchange[30], where the adsorbed hydroxide enters the bulk electrode structure.

$$Pt(OH)_{2(ads)} \rightarrow PtO_{(ads)} + H_2O \qquad \text{(eq 1.28)}$$

Once the final potential limit is reached on the positive scan of the CV (1.2V in Fig 1.8) the potential is reversed. Eventually region G is reached where the place exchanged oxide that was formed in region F is reduced and desorbed from the surface via the reverse processes of eq 1.26 - eq 1.28. This gives rise to significant hysteresis in the CV due to the slow rate of the process[29,30]:

$$PtO_{(ads)} + 2H^+_{(aq)} + 2e^- \longrightarrow Pt + H_2O \qquad \text{(eq 1.29)}$$

Region G is known as the 'oxide stripping region' because of the removal of the oxide. The regenerated platinum sites left behind will not be geometrically the same as before the oxidation process. Instead the surface will have formed clusters and will have a rough topography[29,30]. Therefore for single crystal measurements, the upper potential limit is capped to 0.85V *vs* Pd/H (0.95V when measuring for example Nafion coated Pt{111}), in order to maintain surface integrity order during measurements.

In the 1970s, the correlation of the adsorption of hydrogen onto specific crystallographic planes was undertaken by combining CV with UHV techniques[31-34] to confirm Will's earlier findings. Many research groups agreed with the findings of Will, particularly Hubbard and Ross in terms of the presence of 'weakly' bound hydrogen on the {110} plane and 'strongly' bound hydrogen on the {100} plane. However, results obtained for the {111} plane had proved inconclusive due to irreproducibility's in the data[33,34]. It wasn't until the 1980s when Clavilier revolutionised the preparation of single crystal electrodes[35]. Clavilier produced polyorientated platinum single crystal bead electrodes, which were orientated with respect to the {111} facet edges using a laser, cut at certain angles to produce single crystal surfaces. A detailed method used at Cardiff to produce platinum single crystal electrodes is provided in the PhD thesis of Dr Omar Hazzazi[19]. For experimental use, Clavilier would flame anneal the platinum single electrodes in a hydrogen-oxygen flame to remove impurities and then quench with ultra-pure water while still at a few hundred degrees Kelvin. The CVs of the {100} and {110} surfaces produced from the Clavilier method were very similar to those produced from the UHV studies[35]. The results however for the {111} plane showed results never before

observed. That is, what is now known as bi-sulphate adsorption onto {111} terraces between 0.3 V - 0.5 V, was originally thought of as a pseudocapacitative peak from electrosorbed hydrogen[35]. Cahan *et al*[36] would later perform low energy electron diffraction (LEED) studies of flame annealed Pt{hkl} produced from the Clavilier bead method. These experiments confirmed long range order of Clavilier flame annealed surfaces with highly ordered, sharp diffraction spots. Finally, figure 1.9 contains the typical cyclic voltammograms of flame annealed, cooled in a steady hydrogen stream, low Miller index Pt*{hkl}* electrodes in 0.1M H_2SO_4 at a sweep rate of 50 mVs^{-1}. The main features in the CV of Pt{111} are between 0 V - 0.3 V for hydrogen adsorption/desorption and 0.35 V - 0.55 V for bisulphate adsorption desorption, including a sharp characteristic peak at 0.44 V, which reflectsthe extent of long range order. For Pt{100}, the two electrosorption peaks at 0.225 V and 0.325 V represent the {100} x {111} step sites and (1 x 1) long range order of Pt{100} terrace sites respectively[37]. Finally the sharp electrosorption peaks at 0.086 V represents the adsorption/desorption of hydrogen on {110} surface sites.

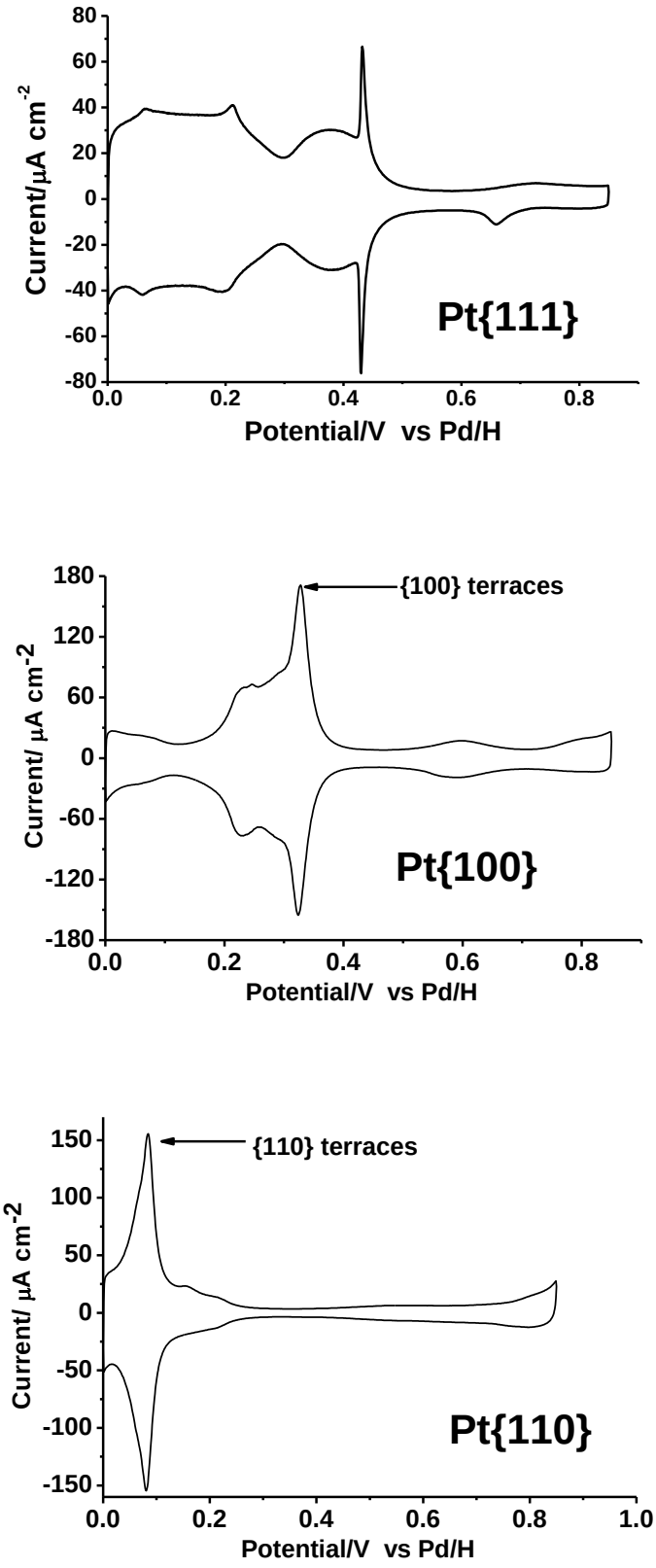

Fig 1.9 CVs of Pt {hkl} single crystal electrodes in 0.1M H_2SO_4 at 50 mVs^{-1}.

1.5 Well defined shape controlled nanoparticles

Catalytic reactions at surfaces are known to be very sensitive to the nanoscale and atomic level structure of the heterogeneous interface at which they take place[38]. In fact, insight obtained from studies with well defined, single crystals have allowed for the production of well defined, shaped nanoparticles for use in various catalytic/electrocatalytic reactions. Shapes of the synthesised nanoparticles can be determined using imaging methods such as transmission electron microscopy (TEM) and the surface can be characterised using cyclic voltammetry. Various research groups have synthesised well defined shaped Pt nanoparticles. A landmark paper in this respect was published by El-Sayed *et al*[39] in 1996, in which they demonstrated the possibility of tuning the particle shape of platinum nanoparticles by changes in the ratio of the platinum cation concentration to the concentration of the capping polymer material (a polyacrylate) during synthesis. The dominant structures found were cubes and tetrahedrons (triangular particles), as well as cubo-octahedrons.

Variants of this synthesis method now exist, giving rise to different Pt nanostructures, and their properties and applications have been reviewed. To controllably obtain a high density of steps on such nanoparticles is not straightforward. Sun and co-workers have recently analysed/established the correlations between surface structure and nanoparticle shape using the stereographic triangle of a fcc metal[40,41]. High-energy nanoparticles with high-index facets such as tetrahexahedral Pt nanocrystals have been synthesized by Tian *et al*[42] by starting from conventional Pt nanocrystals, and subjecting them to a square-wave potential electrochemical treatment. Juan Feliu's research group in Alicante have reproducibly synthesised colloidal Pt nanoparticles of different shapes, as well as providing a quantitative estimate of the {111} and {100} surface sites using bismuth and germanium as surface probes respectively[43].

1.6 Bimetallic surface chemistry

Ultra thin layers of metals supported on metal substrates have played a fundamental role in electrocatalysis. The formation of low dimensional metallic overlayers impart new physical and chemical properties to the surface as well exhibiting superior electronic/catalytic properties compared to the bulk material [44,45]. Thus interest in ultra-thin metallic layers from a commercial aspect has focused on electrocatalysis where the presence of submonolayer to monolayer quantities of a foreign metal adatom can change drastically the reactivity of the

surface, it selectivity and also its resistance to poisoning in both liquid and gas phase environments.

1.6.1 Thin film growth at single crystal electrode surfaces

The three basic growth modes are named after their original investigators:

a) Frank-Van der Merwe (FM) growth refers to when the deposited metal grows in a layer-by-layer fashion, with the formation of the second layer only commencing after the completion of the first.

b) Stranski-Krastanov (SK) growth describes when a film grows one or two monolayers followed by three-dimensional islands forming on top of the first or completed layer.

c) Volmer-Webber (VW) growth occurs when three dimensional islands are formed at all stages of metal deposition.

These growth mechanisms along with that of simultaneous multilayer formation are depicted schematically in Fig 1.12

The thermodynamically stable growth of one material on the surface of another is governed by two thermodynamic properties: (i) the instability free energy of the film, which is the sum of the surface free energy of the growing film on the substrate ($\gamma_{F/S}$) and the interfacial energy between the film and the substrate (y_I); (ii) the surface free energy of the substrate (γ_S). Comparison of the instability free energy ($\gamma_{F/S} + y_I$) and the surface free energy (γ_S) yields the three stable modes of film growth. Pseudomorphic (FM) growth takes place when ($\gamma_{F/S} + \gamma_I$) $< \gamma_S$ at all stages of metal deposition. Three dimensional (VW) growth occurs when ($\gamma_{F/S} + \gamma_I$) $> \gamma_S$ at all stages of metal deposition. The third (SK) growth is a combination of the two in that the condition ($\gamma_{F/S} + \gamma_I$) $< y_S$ must hold for at least one monolayer (FM growth) followed subsequently by VW growth (($\gamma_{F/S} + \gamma_I$) $> \gamma_S$)).

The validity of these models in predicting the growth mode depends on the local surface equilibrium and kinetic factors, including surface diffusion, which has to be rapid in

comparison with the rate of vapour impinging on the time scale of the deposition. Since overlayer growth is a dynamic process, the growth mode can change with substrate temperature and with crystallographic orientation of the substrate, indicating that kinetic factors can often be more dominant than thermodynamic considerations. Indeed, if kinetic limitations prevent the attainment of equilibrium, the whole energetic description is inappropriate[46,47].

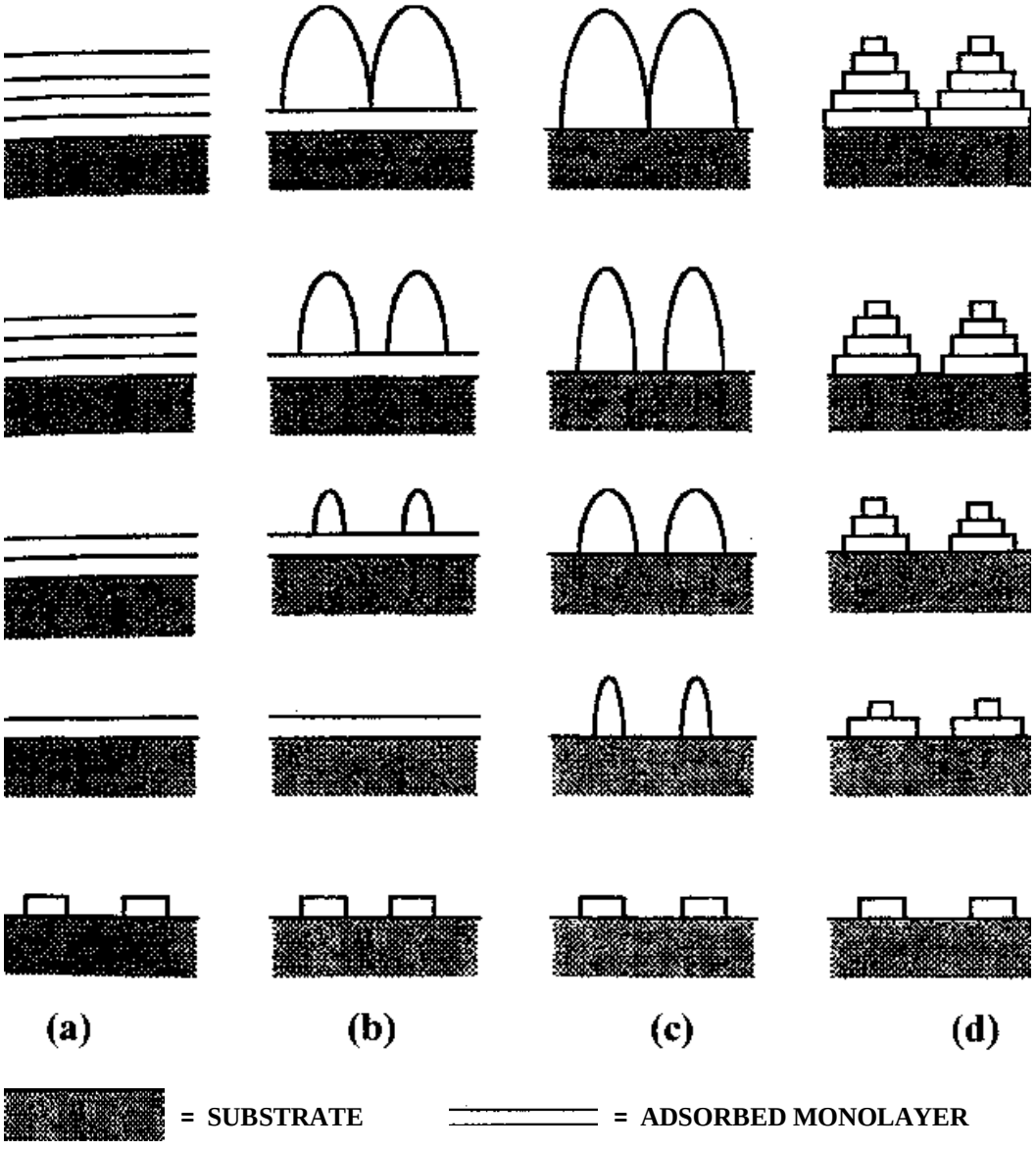

Figure 1.12. Schematic diagram of different growth modes. (a) Frank-Van der Merwe growth, (b) Stranski-Krastanov growth, (c) Volmer-Weber growth and (d) simultaneous multilayer formation. Reprinted from [18].

1.6.2 Methods of preparing bimetallic surfaces

Usually, well-defined bimetallic surfaces are prepared by one of the following methods:

a) Cutting and polishing a bulk single crystal alloy[48].

b) Condensing the vapour of one metal onto a clean, well defined single crystal surface of another pure metal in UHV [48].

c) Electrodeposition of one metal onto a clean, well-defined single crystal surface of another pure metal in UHV[49].

1.6.2.1 Bulk single crystal alloys

The manufacture of bulk single crystal alloy electrodes using a modification of the Clavilier bead method was reported in Cardiff by Dr Dave Watson[18]. However, this procedure is only suitable for metals that do not interact strongly with oxygen whilst being flame annealed. Thus, the method is satisfactory for palladium and platinum, but not for nickel or copper, which upon heating in air form an inert oxide that distorts the lattice of the crystal and does not allow for the formation of a single crystal electrode. Furthermore bulk alloy formation is only favoured by this method if the two metals participating in the alloy exhibit similar atomic radii. This is because large differences in atomic radii tend to disrupt the crystal lattice and a single crystal bead is not formed.

Many well-defined platinum-metal alloy systems have been reported in the literature. In addition to the face specific systems of $Pt_{(25)}Rh_{(75)}$ {100} and {111}[50], $Pt_{(25)}Rh_{(75)}$ {110}[51], $Pt_{(50)}Ni_{(50)}$ {100}[52], and $Pd_xPt_{(1-x)}${111} (where x = 0.1, 0.5, 0.9)[53], polycrystalline palladium/platinum alloys of various compositions were studied by Kuijers *et al.*[54] as far back as 1976. For platinum/rhodium alloy crystals, strong surface segregation of platinum was reported (up to 80% for all samples). This was also observed in the platinum/nickel system where the segregation was found to be 80 to 95% in platinum relative to nickel for the 50:50 alloy. However, in the case of the single crystal and polycrystalline platinum/palladium alloys, it was the palladium that was found to surface segregate. One might therefore also expect all single crystal surfaces of palladium/platinum to exhibit enrichment of palladium since a polycrystalline sample must still contain a random distribution of fundamental {111},

{100} and {110} planes. However, the role of surface structure in controlling the extent of surface segregation in platinum/palladium alloys remains obscure.

1.6.2.2 Vapour deposition

The study of metal on metal vapour deposition is one of the most widely and intensively studied areas of surface science[48]. A number of distinct kinetic surface processes must be taken into account when discussing the growth of metals from the gaseous phase. These include scattering (either elastic or inelastic), adsorption (chemisorption or physisorption), random movement or migration on the surface, chemical reaction, and place exchange with the surface by metallic adatoms to form a surface alloy[55]. All of these possible processes are shown schematically in Figure 1.13. In the case of metal adsorption onto a metal substrate, scattering of the adatom is actually negligible due to the high sticking probability (usually equal to unity), and the predominant processes that occur are migration, reaction (including nucleation of islands) and inter-penetration to form surface alloys.

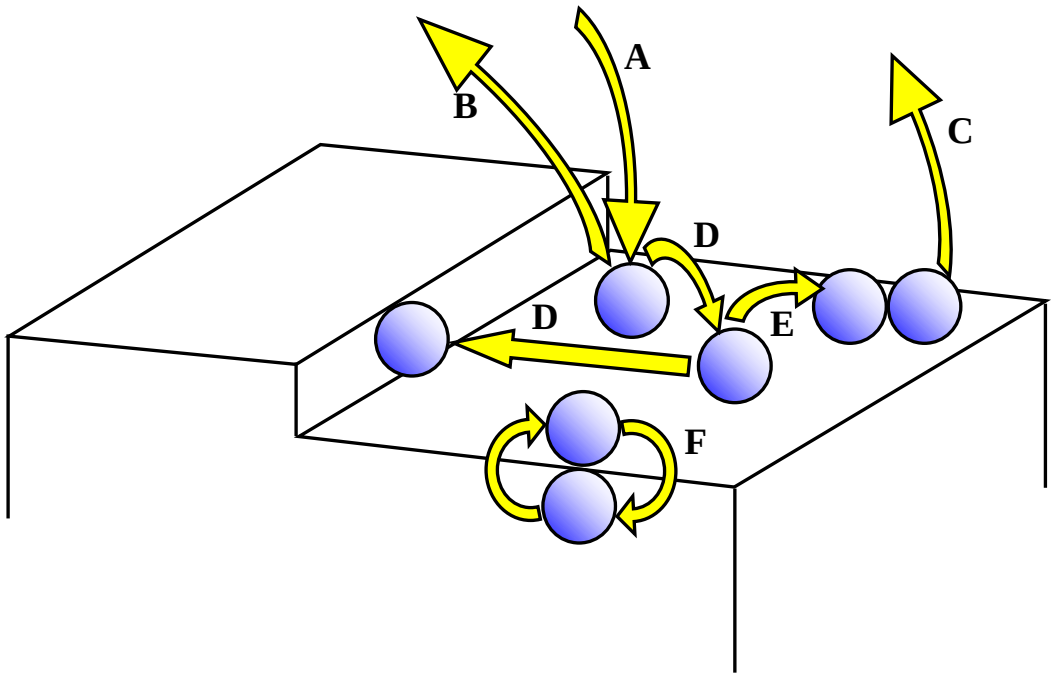

Figure 1.13 Diagram showing processes that may occur when metal adatoms collide with a clean metal surface in vacuum: (A) deposition, (B) scattering (C) desorption of adsorbed atom, (D) surface migration of adsorbed atom, (E) nucleation and (F) place exchange to form alloy surface. Reprinted from[18]

1.6.2.3 Electrochemical deposition

In 1834 Faraday developed the fundamental theoretical principles for the electrodeposition of thin metal films onto a metal substrate from solution. The overall deposition reaction may be expressed as:

$$[M^{Z+}(H_2O)_n]_{(aq)} + ze^- \rightarrow M_{lattice} + nH_2O$$

The electrodeposition method has found widespread application in a number of investigations concerning the process of crystal growth and its classification[56]. The method of electrodepositon includes the following stages[57]:

1. Metallic ions in solution acquire a complete hydration shell.
2. Transport of such ions to the cathode surface occurs under an applied electric field yielding an adsorbed ion.
3. Charge transfer occurs between the electrode and the adsorbed ion (reduction of ion).
4. Gradual loss of the hydration shell occurs as the metal atom becomes adsorbed.
5. The adsorbed adatom diffuse over the surface to preferred adsorption sites such as kinks, steps or vacancies which act as nucleation sites for further growth.

The morphology of an electrodeposited film depends on factors such as, the current density, the nature of the anions and cations in the solution, the presence of additional agents or impurities, whether the current is continuous or pulsed, the morphology of the substrate surface, metal ion concentration, and temperature[56]. Nucleation and growth of metal electrodeposits follow similar constraints to those outlined in Section 1.5.1[56,58], but the most important difference is the environment that surrounds the crystal surface. Although in both cases the condition of a "clean" surface is assumed, the metal-electrolyte interface consists of a condensed phase of molecules in the so-called double layer region, which means that the adsorption is achieved via a replacement process. Therefore, the mobility of ions or atoms is expected to be modified. The charge transfer reaction will occur only under the effect of the high electric fields which are present at the electrode surface and this highlights another difference in adsorption from the gas phase. Whereas, in gas phase deposition, metal atoms

arrive at the substrate with large thermal energies, in electrochemical deposition the process takes place at ambient temperatures, and hence differences in rates of surface diffusion and therefore surface morphology are to be expected.

1.7 Adsorption on well defined single crystal electrodes

The preferential concentration of ions, atoms and molecules at the surface of a solid is referred to as adsorption. Adsorption/desorption processes are central to a large number of phenomena at the solid/gas or solid/liquid interfaces[59]. There are two important differences between metal-gas and metal-solution interfaces. The first is that a dilute phase (gas) is replaced by a condensed phase (solution); hence, for electrolytic systems, adsorption always corresponds to a replacement process. The second is the greater ease by which the local field may be varied at the electrochemical interface than at the gas-solid interface.

The fractional coverage of adsorbate, θ, is defined as:

$$\theta = \frac{\text{Number of adsorption sites occupied by adsorbate}}{\text{Total number of adsorption sites on the surface of the substrate}}$$

When $\theta = 1$, the adsorbate ensemble is called a monolayer[20].

There are two broad classifications of adsorption that can be distinguished depending on the magnitude of the enthalpies of adsorption: physisorption and chemisorption.

1.7.1 Physisorption

In physisorption, the bonding interaction between adsorbate and adsorbent (substrate surface) is weak (when compared to normal covalent or ionic bonds) and is associated with long range van der Waals-type interactions such as exist between molecules in the liquid state. Hence, bonding is characterised by a redistribution (a rearrangement) of electron charge density within the adsorbate and the adsorbent separately. Interaction may include electrostatic attraction in the case of molecules with permanent dipole moments or induced dipole moments for readily polarisable molecules; dispersion forces such as those caused by a slight fluctuation in electron density are the only forces of attraction between non-polar atoms or

molecules and the surface[60]. The energy released when a particle is physisorbed is of the same order of magnitude as its enthalpy of condensation; this is a small energy and can be dissipated as lattice vibrations and thermal motion. A molecule diffusing rapidly across the surface will gradually lose its energy and finally adsorb on to it in the process of accommodation[17]. Enthalpies of physisorption exhibit a somewhat small range of between 2-30 kJ mol^{-1} as found for heats of liquefaction, or vaporisation. However, some higher values have been reported, especially for highly polar molecules such as water adsorbing on ionic solids[60]. That ΔH°_{ads} is invariably somewhat greater than $\Delta H^{\circ}_{condensation}$ is attributed to the fact that there is always a surface potential at the interface between two different phases, and more especially at solid-gas interfaces, whereby an 'overspill' of electron charge from the solid into the gas phase results in an imbalance of electron density on either side of the interface. The resulting surface potential generates an additional bonding interaction which becomes more significant as the polarisability of the adsorbate increases[20].

Multilayers by adsorbed molecules can form on a surface. Because the bonding in physisorbed systems is weak, it also tends to be reversible, in the sense that the adsorbate layer is always in equilibrium with the molecules of the gas phase. As such, physisorbed gas molecules, such as argon and krypton, are ideal probe molecules for the determination of surface areas via measurements of their Langmuir or BET isotherms[20].

1.7.2 Chemisorption

Chemisorption is usually distinguished from physisorption on the basis of the magnitude of $\Delta H^{\circ}_{ads.}$ The enthalpy of chemisorption is very much greater than that for physisorption, ranging from 40 to 250 kJ mol^{-1} ($-\Delta H^{\circ}_{chemisorption} > 35$ kJ mol^{-1}). In this type of adsorption, the molecules form one or more chemical bonds to the surface and tend to find sites that maximise their co-ordination number with respect to the substrate[60]. Because chemisorption is characterised by an exchange of electrons between the adsorbate and the adsorbent (and hence can be discussed in terms of traditional notions of covalent, ionic, and metallic bonding), spectroscopic methods can be used to confirm the nature of the surface bonding involved. The adsorbate may be associatively adsorbed or dissociatively chemisorbed. Associative adsorption is said to occur when a molecule adsorbs on to the surface from the gas phase without fragmentation (the adsorbate forms a bond with the surface but does not break apart on doing so). If the adsorbate is dissociatively chemisorbed the adsorbate is

fragmented to a greater or lesser degree, and the fragments are chemically bonded to the substrate. Dissociative chemisorption is quite common[20].

The enthalpy of chemisorption depends strongly on the surface coverage of adsorbate, largely as a result of adsorbate-adsorbate lateral interactions. For example, ΔH°_{ads} for CO on Pd{111} decreases with increased surface coverage of adsorbate[20]. Chemisorption provides for the activation and transformation of adsorbates, and leads to a rich variety of surface chemistry which is often unique in the sense of having no analogue in organometallic chemistry at the molecular level. A chemisorbed molecule may be torn apart in response to the demand of the unsatisfied valencies of the surface atoms, and the existence of molecular fragments on the surface as a result of dissociative chemisorption is one reason why solid surfaces catalyse reactions[60].

1.8 Fuel cell electrode reactions

Established in section 1.1 the two reactions that happen at the PEMFC electrodes are the hydrogen oxidation reaction (HOR) and oxygen reduction reaction (ORR). Fuel cell electrodes are usually composed of a platinum based alloy, platinum being the best surface for both reactions. The HOR reaction occurs readily on platinum, however problems arise if impure hydrogen is used, therefore it is desirable to use pure hydrogen for best performance. However pure hydrogen can be very expensive to obtain and is difficult to store[5]. Therefore an alternative fuel source is required, this comes in the form of alcohols such as methanol and ethanol and also formic acid which are regularly used as fuels in alcohol fuel cells. The oxidation of alcohols produces CO as an intermediate on the surface which acts a poison. The CO must be oxidised at a very low potential. For ORR, the reaction occurs very slowly on a platinum surface because it is difficult to dissociate the oxygen molecule on the platinum electrode close to the thermodynamic equilibrium potential of 1.23 V. This is because platinum forms a surface oxide at potentials greater than 0.7 V which inhibit the ORR reaction (only metallic sites dissociate the oxygen molecule) thus providing sluggish kinetics. Therefore for ORR, electrocatalysts must be designed to shift the formation of electrosorbed oxide to more positive potentials whilst still affording the key oxygen molecular dissociation step. For methanol and formic acid electrooxidation, a different set of criteria obtain. The electrocatalyst must be able to tolerate the surface-poisoning side product of such electrooxidation reactions, namely chemisorbed carbon monoxide. Surfaces that destabilise

adsorbed CO and facilitate electrooxidation of adsorbed CO to gaseous carbon dioxide at potentials < 0.5 V would be deemed good electrocatalysts for this process. New electrocatalysts may first be designed by performing fundamental studies with well defined surfaces, which can be altered by having step sites introduced thus altering the terrace width of the surface or by doping the surface with controlled amounts of foreign metal adatoms which can alter the electrocatalytic properties of the surface.

1.8.1 Oxygen reduction reaction (ORR)

The reaction scheme, proposed by Wrablowa *et al*[61] is given below.

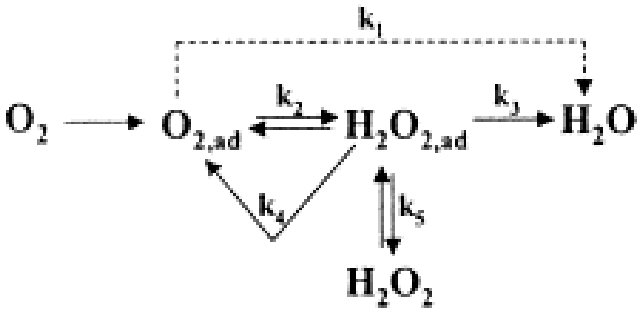

Fig 1.14 The mechanism of the oxygen reduction reaction. Reprinted from[38].

There are four possible pathways for ORR:

1. The "direct" 4 electron reduction, with O_2 reacting with four protons and four electrons to form water.
2. A two electron reduction pathway where oxygen is reduced to hydrogen peroxide.
3. A "series" pathway where oxygen undergoes a two electron reduction to hydrogen peroxide followed by a two electron reduction of the peroxide to water.
4. A parallel pathway where a combination of steps 1, 2 and 3 occur.

The ORR mechanism on platinum has been investigated using theoretical calculations based on the electronic structure using density functional theory[62-64]. The dissociative mechanism and associative mechanism have been proposed for low current density range and high current density range respectively[62,63].

Dissociative mechanism:

$$1/2O_2 + * \rightarrow O*$$

$$O^* + H^+ + e \rightarrow OH^*$$

$$OH^* + H^+ + e \quad H_2O$$

where * denotes a site on the Pt surface. In this mechanism, no H_2O_2 is produced. On a Pt surface, the O = O bond breaks and forms adsorbed atomic O, which further gains two electrons in the two consecutive steps, forming water. Since there is no O_2 on the Pt surface, H_2O_2 cannot be produced. This mechanism can be considered a detailed form of the direct four electron pathway.

Associative mechanism:

$$O_2 + * \rightarrow O_2$$

$$O_2^* + H^+ + e \rightarrow HO_2^*$$

$$HO_2^* + H^+ + e \rightarrow H_2O + O^*$$

$$O^* + H^+ + e \rightarrow OH^*$$

$$OH^* + H^+ + e \rightarrow H_2O + *$$

Since adsorbed O_2 is present, the O = O bond may not be broken initially. This results in the formation of H_2O_2. The H_2O_2 can further be reduced to water or it may be itself a final product.

As mentioned earlier, the equilibrium potential for ORR is 1.23 V *vs* RHE. Platinum is the best electrode to use to perform ORR because it has the best activity[5], however at potentials greater than 0.8 V *vs* RHE, platinum forms a surface oxide. The kinetics for ORR are therefore not expected to be the same at different potential ranges. In fact depending on the observed potential range, Tafel slopes with gradients of 60 mV/dec and 120 mV/dec are obtained for low and high overpotential ranges respectively[5]. The difference in the Tafel slopes indicates that the mechanism on a Pt/PtO surface is different to a pure Pt surface. On a Pt/PtO surface the rate determining step is a pseudo 2 electron pathway, which gives a Tafel slope of 60 mV/dec[5]. On an oxide free Pt surface, the first electron transfer is the rate determining step resulting in a Tafel slope of 120 mV/dec[5]. Norskov and co-workers, using a DFT model, calculated the dissociative mechanism gave a Tafel slope of 60 mV/dec[63],

unfortunately not enough literature is available to devote enough attention to the associative mechanism.

ORR has been studied on various well defined Pt electrodes and has found to be structure sensitive to the nature of the surface in acidic media[65]. The studies performed by Markovic and co-workers in 1994 of ORR on low Miller index Pt{hkl} in perchloric and sulphuric acid found that in both electrolyte solutions, the {110} surface was the most active[65]. In sulphuric acid, the {100} surface is more active compared to the {111} surface whereas the reverse is true in perchloric acid. The difference in the activity of Pt{111} and {100} in different electrolyte solutions was attributed to the strong adsorption of bisulphate anions on the {111} surface[65]. In contrast, Feliu *et al* found that the {111} surface had the lowest electrocatalytic activity of the three low Miller index planes in both electrolyte solutions[66]. Studies by Feliu and co workers later found that by introducing step sites to the surface, ORR was sensitive to the terrace width of the surface[66]. The authors demonstrated that the low catalytic activity of the Pt{111} electrode with respect to the stepped surface electrodes in sulphuric acid is related to the specific adsorption and the bi-dimensionally ordered adlayer of bisulphate anions on Pt{111}. As the bisulphate/platinum interaction decreased for surfaces with a narrow terrace width, differences were observed in the electrocatalytic activity of the surface to ORR[66].

Recently, activity *vs* surface structure relationships developed on well defined Pt{hkl} electrodes have been extended to studies to develop well defined shaped nanoparticles. For example, using scanning electron microscopy (SEM), Herrero *et al* showed improved electrocatalytic activity for ORR on hexagonal Pt nanoparticles in perchloric and sulphuric acid[67]. In addition, the study also outlined that preferentially orientated platinum nanoparticles significantly change their electrocatalytic activity because of the specific adsorption of bisulphate anions, confirming the earlier results on well defined single crystal electrodes[66].

Depositing foreign metal adatoms on a well defined Pt{hkl} surface has been known to alter the electrocatalytic activity of the surface. The electrocatalytic activity of platinum towards ORR strongly depends on its O_2 adsorption energy, the dissociation energy of the O = O bond and the binding energy of OH on a platinum surface. These parameters are strongly affected by the Pt-Pt interatomic distance and Pt *d*-band vacancy[5]. Alloying causes a lattice contraction, leading to a more favourable Pt-Pt distance for the dissociation of O_2 and can also increase the *d*-band vacancy, producing a strong metal-O_2 interaction then weakening the

O = O bond. One of the most important discoveries of ORR on a Pt bimetallic surface was that by Stamenkovic *et al*[68]. The authors found that on a Pt_3Ni{hkl} surfaces, ORR was enhanced (90 times faster) compared to pure platinum[68].

1.8.2 Electrooxidation of formic acid

The electrooxidation of formic acid on platinum occurs via the accepted dual pathway mechanism postulated by Capon and Parsons[69,70]. The reaction scheme is expressed as:

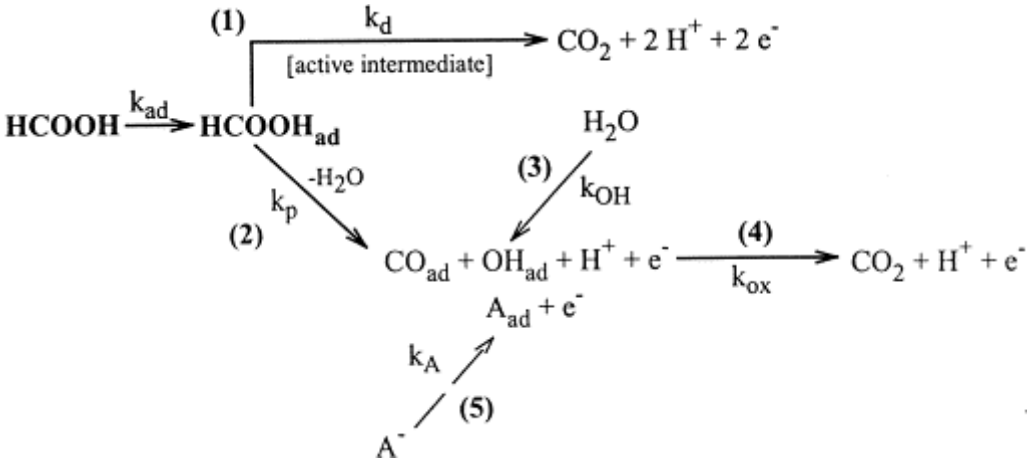

Fig 1.15 Dual reaction pathway for formic acid electrooxidation. Reprinted from[38].

The direct pathway, where adsorbed formic acid undergoes dehydrogenation to form carbon dioxide, is preferred. The indirect pathway, where adsorbed formic acid undergoes dehydration to produce carbon monoxide is considered an important side reaction. Carbon monoxide acts as a catalyst poison and needs to be further oxidised to form carbon dioxide. Studies on well defined Pt{hkl} electrodes by various authors such as Weaver[71] and Kita[72] have shown that the reaction is structure sensitive. The studies exemplified the effectiveness of the {111} plane being resistive to poisoning compared to the {100} and {110} planes. Behm and co-workers performed studies of formic acid electrooxidation on thin Pt films as a function of temperature combining electrochemical and IR spectroscopic techniques together[73]. Two adsorbed intermediates were detected, CO_{ad} and $HCOO_{ad}$. Temperature had a significant impact on the surface coverage of the intermediates: an increase in temperature resulted in an increase in the coverage of CO_{ad} and a decrease in the coverage of $HCOO_{ad}$[73]. Previous studies have demonstrated the use of foreign metal adatoms as surface modifiers to enhance the electrocatalytic properties of the surface. Clavilier found in particular for

Pt{100} modified with submonolayer amounts of palladium, an enhancement was found in the electrocatalytic activity[74], a much greater current and a reduction in the onset potential was observed. For Pt{111}, the maximum activity and onset potential are not greatly enhanced, relative to palladium free Pt{111}, when the surface was doped with palladium. However it should be noted that the electrolyte used by Clavilier was sulphuric acid, the electrolyte used plays a significant role in the electrooxidation of formic acid. Markovic[75] and Weickowski[76] have both found that formic acid is enhanced greatly for palladium modified platinum single crystal electrodes in perchloric acid.

1.8.3 Electrooxidation of methanol

Parsons[77] and Jarvi and Stuve[78] have all postulated the dual pathway mechanism for the electrooxidation of methanol:

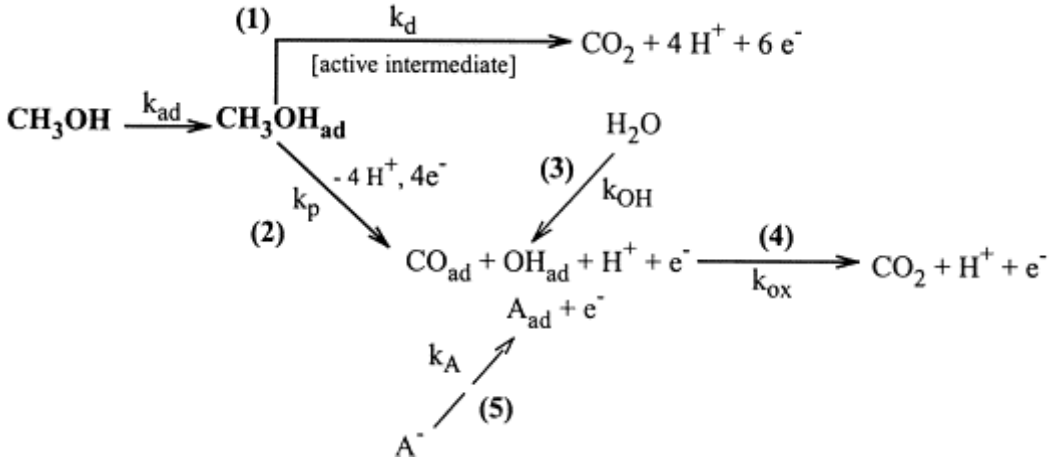

Fig 1.16 Dual pathway for methanol electrooxidation. Reprinted from[38].

Here the decomposition of methanol is analogous to the dual pathway of formic acid, that is to form CO_{ad} is referred to as the indirect pathway and the formation of soluble intermediates is referred to as the direct pathway[38]. The electrocatalyst of choice for methanol oxidation should break the C-H bond and then allow the resulting residue to react with oxygen containing species to form CO_2.

Weaver and co-workers[71] have compared the structural sensitivity of methanol electrooxdiation on well defined low miller index platinum single crystal electrodes using *in situ* FTIR coupled with cyclic voltammetry. This study underlined the effectiveness of Pt{111} for methanol electrooxidation, which was characterised by voltammograms where

the onset of electrooxidation of methanol would occur at the lowest potential of the three surfaces studied. Xia *et al* would also study the structure sensitivity of methanol electrooxidation on well defined Pt{hkl} and would also find that Pt{111} was the best surface[79].

Perchloric and sulphuric acid are commonly used as supporting electrolytes for studies of methanol electrooxidation. It should be noted that methanol electrooxidation is affected by the anion of the supporting electrolyte used. This is clearly the case for Pt{111} and Pt{100} electrodes, where CVs of methanol electrooxidation exhibit much larger currents in perchloric acid than in sulphuric acid[80,81]. The difference was explained by the specific adsorption of sulphate anions at platinum electrodes which hinder methanol electrooxidation. Kita *et al*[81] observed for Pt{111} a factor of ten higher current observed in perchloric acid than in sulphuric acid, while for Pt{100} the enhancement was a factor of two.
Chrzanowski and Wieckowski[82] and Chrzanowski *et al*[82] demonstrated that electrocatalysis of either polycrystalline Pt or Pt single crystal electrodes towards methanol electrooxidation was enhanced by irreversibly adsorbed Ru. The most active surface was Pt{111} covered by ca. 0.2 mL of Ru. However Iwasita[83] compared the electrocatalytic activities of methanol electrooxidation on UHV-cleaned PtRu bulk alloys, UHV-evaporated Ru onto Pt{111} and irreversibly adsorbed Ru onto Pt{111}. It was found that the electrocatalytic activity of the PtRu bulk alloys between 10 and 40 % Ru is up by a factor of 10 higher than the activity of the Ru modified Pt{111} surface.

1.9 Nafion - the context of the present study, a literature review

The main function of the membrane in the PEM fuel cell is to transport the protons from the anode electrode to the cathode electrode. The other functions include keeping the fuel and oxidant separated, thus preventing the mixing of the two and to withstand harsh conditions such as high temperatures or temperature fluctuations. Therefore, the ideal membrane should have excellent proton conductivity, chemical and thermal stability low cost and good availability amongst other properties[84]. Nafion is the most common polymer that is used as the polymer electrolyte in a membrane electrode assembly. It is a copolymer of tetrafluoroethylene and sulphonyl fluoride vinyl ether and has a semi-crystalline structure [84,85]. This structure, which resembles Teflon, gives Nafion long term stability in oxidative and reductive conditions [84]. The polymer was first developed by the DuPont company and the chemical structure is that of an aliphatic perfluorinated backbone (hydrophobic in nature)

with ether linked side chains ending in sulphonate cation exchange sites (hydrophillic in nature) (figure 1.17) [84].

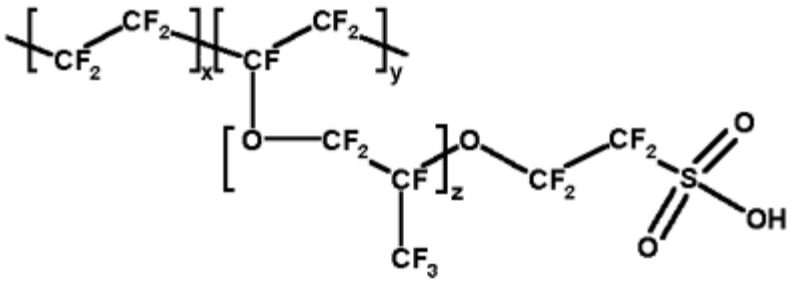

Fig 1.17 Structure of Nafion. Reprinted from [84].

When wet, protons on the sulphonate group can jump from one neighbouring moiety to another. In this manner protons pass along the length of the polymer chain, through the pores of the membrane, creating a net flow of current[84]. Nafion exhibits good thermal and mechanical stability within the operating range of H_2 PEMFCs[86] but can be problematic in Direct alcohol fuel cells (DAFCs). If the membrane dries out it will not conduct protons. This limits the temperature at which the fuel cell can operate. Even though improved kinetics would be achieved and heat management would be simplified above 80ºC (preferably above 100º), the need to keep the Nafion supplied with a significant amount of water requires the effective operating range be maintained below this[84,86]. If however the electrode surface becomes too wet, access of O_2 to the active metal sites becomes restricted.

1.9.1 Neutron and X-ray scattering methods

At the core of the PEMFC, the MEA, reaction sites are composed of an ion conducting solid polymer electrolyte (ionomer) typically Nafion, next to the electrocatalytic surface such as platinum or its alloy nanoparticles embedded in an interpenetrating network of electronic and ionic conductors. The reactants, typically hydrogen at the anode and oxygen at the cathode react at these interfaces generating energy and producing water as the only by product. Such a local reaction site is often referred to as the three phase interface where the ion conducting polymer electrolyte phase (which also affects the transport of species in and out of the interface), is in contact with an electronic phase, an electrocatalyst surface, and the reactant phase components, which are usually comprised of adsorbing anions (supporting electrolyte) and/or reactants and reaction intermediates, from the “solution” environment. Despite many

years of studies, very little is known regarding the true nature of such interfaces; a longstanding difficulty has been the lack of experimental methods for preparing and characterizing well-defined three phase interfaces for electrochemical studies. As expected many studies have been performed in order to better understand the complex interface and various models have been proposed in the literature to describing the structure of the ionomer component.

Yeager and Steck[87] proposed that the ionomer is a three phased material comprised of a polymer matrix, an ionic cluster and an interfacial zone. Later Hsu and Gierke further improved on this study[88,89], using small angle x-ray scattering (SAXS) and wide angle x-ray diffraction (WAXD) to determine Nafion has a semi-crystalline structure in which ionic clusters are interconnected by small narrow ionic channels, are dispersed in a continuous tetrafluoroethylene phase. Assuming the ionic clusters are spherical, are fully hydrated and that they are spatially arranged on a cubic array, Hsu and Gierke[88] were able to estimate their size. typically 3-5 nm and interconnected by narrow water channels of 1 nm width. They found that the cluster size was smaller than the inter cluster distance deduced from the ionomer peak position in the SAXS data (in the framework of their model). Since Nafion membranes present excellent ionic conductivity, they deduced that a percolation should occur in the swollen membranes and they assumed the presence of small connecting ionic channels. An inverted micelle structure was proposed for one of the clusters (fig 18).

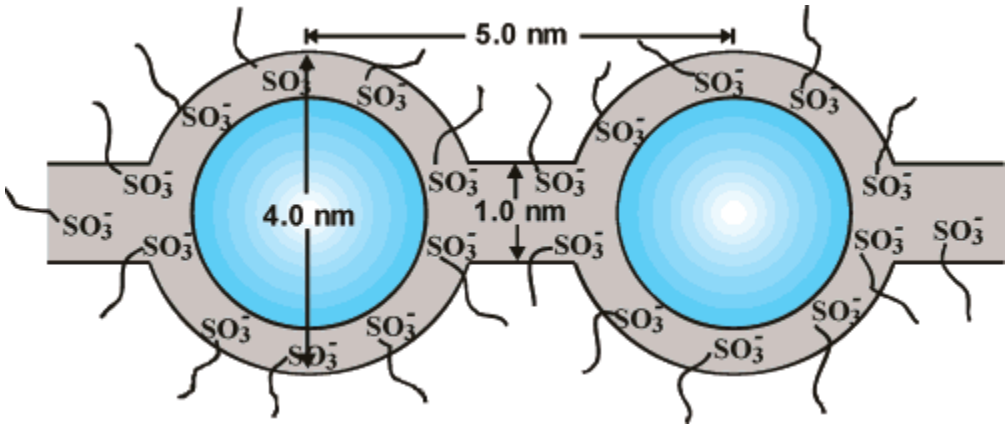

Figure 1.18 Inverted micelle structure of Nafion. Reprinted from [84].

The ionomer components within each cluster are expected to be in equilibrium with various interaction forces such as the electrostatic interaction with the solvated proton, the dipole interaction with neighbouring clusters, a van der Waals type interaction with the other polymer segments, a covalent interaction with the matrix, and the solvation energy arising

from the waters of hydration. When the membrane absorbs water, the ionic domains swell up and form proton conducting channels above a critical water content. The proton conductivity increases with water content up to a point, as the water content increases further past this point, the concentration of protons is diminished and conductivity is decreased. The model was termed the Cluster Network Model by Gierke. Although this model gives a phenomenological rationalization for the selective ionic conductivity of Nafion and provides a qualitative explanation of the ‘‘ionomer’’ peak in small angle X-ray scattering (SAXS) data, it has since been shown to be quantitatively inconsistent with data over a wider range of scattering angles[90,91] and from membranes oriented by tensile draw[92]. Furthermore, it takes no account of crystallinity in the fluorocarbon phase[93] and is not compatible with the inverse micelle structure of Nafion aggregates dissolved in solution[94,95]. The Nafion membrane has been extensively studied using X-ray and neutron scattering techniques, various models of the structure that Nafion forms on a surface, as well as transport properties have been proposed. In section 1.7.2, a selection of these models are highlighted.

Litt[96] proposed a simple lamellar model of Nafion with water absorbing between hydrophilic micelles separated by hydrophobic lamellae after re-examining Gierke's original SAXS data. It was found that a plot of ionomer peak shift *vs* increasing water content was linear in agreement with the dilution of a lamellar structure. However the SAXS data were not fitted and the extension of both the lamellae and the domains that they are orientated on are not discussed.

A related model is the rectangular parallel piped sandwich model[97] proposed by Haubold *et al* with a core region sandwiched between shells made of hydrophilic groups and polymer side-chains. The lateral dimensions are 1.5 – 4.5 nm and the total thickness of the sandwich is about 6 nm. The core region is empty in the dry membrane and filled with water in hydrated Nafion. The anisotropic distribution of this basic structural unit gives rise to water channels. The model mainly presents information about the basic structural unit without dealing explicitly with the mesoscale

Gebel et *al*[90,94,98] have analyzed SANS and ultra SAXS to probe Nafion structure in the length scale from 1 nm to 1 mm. Their structural model is based on elongated (cylindrical or ribbon like) polymer aggregates with a diameter of about 4 nm and length larger than 100 nm. These aggregates are surrounded by ionic groups and packed in bundles with ordered orientation. On addition of water, swelling occurs between aggregates, as opposed to the cluster-network model in which there is swelling of the aggregates themselves. Gebel an co-

workers have shown the fibrillar model can also be applied to Nafion in solution (a polyelectrolyte as opposed to a polymer electrolyte), since it was developed with the whole solvent concentration range in mind[99-101] however, it may understate the degree of structural reorganization that can take place during swelling. The ionomer peak in SAXS represents the average distance between the aggregates in a typical bundle. The bundles are randomly arranged at the mesoscale.

Kim et al[102] have recently proposed a model based on SANS results in which ionic clusters can form a network with cylindrical water channels. Schmidt-Rohr and Chen[91] have used neutron scattering among other techniques to establish that self-assembly of Nafion leads to the formation of both hydrophobic and hydrophilic polymeric regions. The hydrophilic regions are reported to consist of hydrophilic channels (containing exclusively sulphonate substituents of the polymer) which can vary from 2 to 10 nm in diameter and are thought to facilitate proton transfer perpendicular to the electrode surface from one electrode of the fuel cell to the other. The channel properties are strongly dependent on the overall water content of the Nafion polymeric film.

Ladwig *et al*[103] performed SANS, SAXS and WAXS on Nafion and Nafion nanocomposite membranes. The nanocomposite membranes were prepared from Nafion 117 and a systematic range of organically functionalised silicon alkoxide using an *in situ* sol gel synthesis technique. WAXS data shows that there is a loss in crystallinity of the composite membranes compared to Nafion. SAXS data revealed significant differences in the scattering behaviour of the Nafion composite membranes compared to Nafion and SANS data was able to resolve the Nafion ionomer peak in the composite membranes. A model was produced showing greater selectivity of proton transport for the nanocomposite membranes over Nafion.

Kreuer explained the transport and swelling properties of Nafion and sulphonated polyetherketones (SPEEK) in terms of distinct differences of the microstructure and the pKa[104]. Using SAXS and NMR techniques, Kreuer found the less pronounced separation of hydrophobic/hydrophillic components in sulphonated polyetherketones compared to Nafion corresponds to narrower, less connected hydrophilic channels and to larger separation between less acidic sulphonate groups[104].

Yang and Manthiram[105] would show using SAXS that at sulphonation levels less than 50%, SPEEK membranes have narrower pathways for methanol/water transport compared to Nafion. Therefore this would lead to a greater methanol crossover in the fuel cell if Nafion

was used. This suggests that SPEEK membranes may evolve to be promising alternatives to Nafion for direct methanol fuel cells (DMFC)[105].

Quasi-elastic neutron scattering (QENS) studies have been performed to examine the dynamics of water molecules in PFSA membranes. Pivovar and Pivovar[106] examined water dynamics in Nafion 117 using QENS at 295 K for λ varying from 1 (nearly dry) to 16 (well hydrated). Note that λ represents the number of water molecules attached to the sulphonate goup. The authors fitted their data using a simple model based on continuous diffusion within a sphere. All the extracted parameters were found to change rapidly in the low λ range and to tend toward asymptotic values in the high λ range. This is consistent with the observation that the increase of water uptake by Nafion with increasing relative humidity[107] has a gradual slope for $\lambda < 6$ and a steep slope for higher λ, which indicates that water molecules are more likely to be bound to sulphonate groups at low λ.

A recent QENS study by Perrin et al.[108] has examined molecular motion in Nafion 112 (51 μm thick) at 298 K for λ ranging from 3 to 17.5. The authors used a single theoretical model based on Gaussian statistics valid over the whole entire range of q studied to interpret their data. At all hydration levels examined, two distinct populations of protons were observed. Both have characteristic length scales of 0.2-0.4 nm, but the characteristic time scales differ by a factor of about 50 at all hydration levels (2–8 ps vs. 160–500 ps). The authors [108] have identified the slow proton dynamics with hydronium ion (H_3O^+) dynamics and estimated the H_3O^+ lifetime in Nafion to be of the order of 1 ns in contrast to the H_3O^+ lifetime of 10^{-4} ns in bulk water[109]. The fast proton dynamics have been associated with local diffusion of water molecules. It has been proposed that the proton exists as H_3O^+ ion at low λ and as H_3O^+ ion surrounded by H_2O molecules in the fully hydrated membrane. The difference in the time scale of the two populations is explained by the stronger binding of the H_3O^+ to the SO_3^- group. The conclusion of Perrin et al.[108] that proton transport in Nafion occurs by the vehicular mechanism only involving a well defined H_3O^+ ion at all hydration levels

Paddison *et al* reported high frequency dielectric measurements of hydrated Nafion at different states of hydration[110]. The results showed a strong dependence of the dielectric constant with water content, as water content increased so did the dielectric constant. Much like the behaviour of water, the dielectric constant decreases with increasing frequency.

1.9.2 Transport and hydration properties of Nafion using other spectroscopic techniques

Vibrational spectroscopy techniques provide insights into the environments surrounding chemical functional groups. Various studies have provided detailed information about structural properties of the Nafion side chain, PTFE backbone and information about the transport properties of Nafion as well. Buzzoni *et al*[111] monitored the transport properties of Nafion using IR and Raman spectroscopy. Using IR and Raman spectroscopy, proton transfer of Nafion was inferred due to modifications in the SO_3H substituent to SO_3^-. The authors also noticed changes in the O-H stretching and H-O-H bending modes ascribed to different water molecules present in different environments such as nanometer scale clusters[111].

Ludvigsson *et al* performed an FTIR study on a thin film Nafion membrane at different values of relative humidity[112]. Ludvigsson *et al* also calculated the number of water molecules per sulphonate group at different values of relative humidity. The FTIR study showed the transfer of protons from the SO_3H group to H_2O resulting in the formation of the hydronium ion H_3O^+. Byun *et al*[113] compared the hydration and dehydration properties of proton exchanged bis imide (PFSI) materials to Nafion using transmission IR. Both Nafion and PFSI contain a strong adsorption band in the IR spectra at 1060 cm^{-1}, attributed to the symmetric stretching of the sulphonate anion, SO_3^-, in Nafion and asymmetric S-N-S stretching within the sulphonyl imide endgroup, $SO(N^-)SO_2CF_3$. For Nafion, the position and width of the band is found to very sensitive to the level of hydration of the Nafion membrane whereas it is not so for PFSI materials. Byun *et al* suggested that greater charge delocalisation of the sulphonyl imide moiety and shielding of hydrophillic species by the terminal CF_3 group accounted for the differences.

However Webber *et al*[114] explain why the assignment of bands to a single functional group as has been done for several decades precludes proper analysis of analysis of spectra. Using a combination of IR and density functional theory (DFT), it is suggested that the consideration of mechanically coupled internal coordinates of the SO_3^- and COC groups is essential for the analysis of IR spectra of Nafion[114]. It is also essential for the correlation of said spectra with the state of hydration and the effects of ion exchange.

Warren *et al*[115] used a combination of ATR-IR and DFT to study the model compound perfluoro(2-ethoxyethane) sulphonic acid (PES) and the spectral changes induced by humidity variations to improve understanding of the IR spectrum of Nafion. This work was

supported by density functional theory (DFT) calculations of the PES molecule and ion complexes to confirm assignments and determine local modes that contributed to specific absorptions in the IR spectrum. However, the loss of degeneracy in the SO_3^- asymmetric stretching mode is clearly observed in difference spectra, and the use of DFT calculations provides an insight into changes induced by the variation in humidity.

Laporta *et al*[116] reported using FTIR that small water clusters form in Nafion 117 for hydration levels $\lambda < 3$, aggregate to large clusters for $\lambda = 3$ to 5 and start coalescing to form a water network for $\lambda > 6$. Later Moilanen *et al*[117,118] used IR spectroscopy to analyse water in Nafion over a range of λ from 1 - 9. Their findings indicate that an abrupt structural change occurs for $\lambda = 5$, which drastically reduces the number of bound water molecules. Moilanen *et al*[117,118] state that some water molecules are in close proximity to the fluorocarbon backbone. However Basnayake *et al* performed transmission IR spectroscopy to probe water inside the pores and channels of the Nafion membrane exchanged with either protons of sodium ions. Spectra of the H^+ exchanged Nafion membrane is dominated by $(H_2O)_nH^+$ clusters. Banayake *et al* found no evidence of water incorparation near the fluorocarbon[119].

Gruger *et al* performed an IR and Raman study on acidic Nafion[120] to explore the conformational changes in the PTFE backbone with water content. The results showed that whatever the water uptake of the membrane, the ionomer retained the helical "zigzag" conformation of PTFE and the $-(CF_2CF_2)-$ links prevail on the fluorocarbon part of the pendant side chain.

Liang *et al* used FTIR to study the microstructural differences between surface and bulk Nafion membrane[121]. It was found that thermal treatment results in the membrane changing in structural and physical properties. As temperature is increased, movement of the side chain brings the sulphonate group out of the bulk and to the surface.

Osawa et al suggested that the electrochemical microenvironment within Nafion can be investigated by in situ infrared reflection absorption spectroscopy (IRRAS)[122]. Malevich et al studied a cast Nafion film on Pt polycrystalline by normalized interfacial Fourier transform infrared reflection spectroscopy (SNIFTIRS) in the IRRAS configuration, and it was demonstrated that sulphonic acid groups were coordinated to or displaced from the Pt surface depending on the applied potential[123]. Later, Malevich et al. investigated the effect of Nafion on CO adsorption and electrooxidation at Pt nanoparticles and observed that a film of Nafion slows the CO oxidation reaction[124].

The interface has been characterized in $HClO_4$ aqueous solutions using surface enhanced infrared absorption spectroscopy (SEIRAS) by Ayato et al. A potential-dependent band was found around 1100 cm^{-1} and assigned to the symmetric vibration of the SO_3^- groups of the ionomer membrane, and the OH stretching band of non hydrogen bonded water molecules associated with the Nafion structure was observed for the first time at 3680 cm^{-1} [125].

Zeng *et al*[126] have performed SERS measurements on Nafion adsorbed onto SiO_2@Au nanoparticles and Pt coated SiO_2@Au nanoparticles. It was found from the spectra that Nafion adsorbs onto Pt and Au via the sulphonate group, yielding a significantly red shifted sulphonate peak.

1.9.3 NMR reports on Nafion

Several reports have been published on ^1H NMR and ^2H NMR investigations of Nafion. Fyfe *et al*[127,128], Pak *et al*[129] and Chen *et al*[130] have all shown that the chemical shift and the line width of proton and deuteron peaks depend on the water content of Nafion, therefore any of these parameters may be used as an indirect measure of the water content. Nosaka *et al*[131,132] and Chen *et al*[130] have shown for instance, by increasing the temperature the line width of the proton and deuteron peaks decrease which shows that the mobility of water molecules becomes higher and the chemical environments become more homogeneous. Ye *et al*[133] confirmed proton exchange between water and sulphonic acid groups by high-resolution ^1H solid state NMR for Nafion and SPEEK membranes. The proton mobility was found to depend not only on the water content but also on the temperature. Boyle *et al*[134,135] have shown ^1H NMR relaxation time measurements on Nafion with different water contents over a wide range of temperature indicated that there is a distribution of heterogeneous water sites in the membranes. In general it is found by Fontanella *et al* that by increasing the water content, the T_1 (spin-lattice relaxation time) values increase[136]. The general trends for the deuteron relaxation data is similar to those in ^1H NMR, but Rankothge *et al* have shown that the deuteron relaxation times in the membrane is 5-6 times shorter than in aqueous solution [137]. The dependence of the relaxation data on the degree of hydration is reported also for deuteron relaxation times by Pak *et al*[130].

^{19}F NMR studies of Nafion in different solvents by Schlick *et al* showed that separate signals from nuclei in the backbone and in the pendant chain can be detected[95]. The first ^{19}F magic angle NMR spectra with different spinning speed from 5-35 kHz was reported by Dec et al[138].

It was shown that in general going to the higher spinning speed as well as increasing the water content can decrease the line width of the spectra and increase the resolution. The original assignment of ^{19}F and ^{13}C NMR resonances of Nafion, given by Dec et. al[138], was corrected later by Chen and Schmidt-Rohr using two-dimensional (2D) ^{13}C - ^{19}F heteronuclear correlation and ^{19}F 2D-exchange NMR experiments under 30 kHz magic angle spinning[139]. This later assignment was then confirmed in a solution NMR study of Takasaki *et al* where the ^{19}F and ^{13}C assignments of Nafion was determined on the basis of the assignments of the model compounds in solution, and the analysis of spin couplings between ^{19}F and ^{13}C [(140)].

The molecular motions of the fluorocarbon backbone in Nafion membranes were studied through ^{19}F NMR relaxation in different water content[135,141]. It was mentioned that because of the effect of water as a plasticizer as well as possible cross-relaxation effects between the ^{19}F and ^{1}H spin systems, interpretation of the ^{19}F relaxation data for the hydrated acid is complicated. In contrast to ^{1}H and ^{2}H relaxation data, it is reported that the fluorine T_1 and T_2 values are almost independent of the level of hydration, and unaffected by the presence or absence of a hydrating medium[135,141]. Also, no distinction between H_2O and D_2O hydration was reported[141]. On the other hand, the observation of non exponential T_1 and $T_1\rho$ decay is indicative of a heterogeneous system. Broad minima as well as very short relaxation times, and little changes with temperature were mentioned to be a characteristic of large solid polymers[141].

The motions of the perfluoroether side chains and the effect of the pendant chain on the ionomer mobility in Nafion were also evaluated by the sideband analysis in variable temperature solid-state ^{19}F NMR[142]. A sideband analysis indicated that the side chain is more mobile than the main chain. This effect was also confirmed by comparing the line-widths for Teflon and Nafion[95]. Molecular level information from these analyses in combination with SAXS and DMA data support the assignment of the β relaxation process to the genuine T_g of Nafion, and the α relaxation process to the onset of long range mobility of chains/side chains via a thermally activated destabilization of the electrostatic network[142]. A similarity in the relaxation behaviour of the side and main chains was derived from ^{19}F NMR relaxation data which can be explained with the dynamically coupled motions of the side chains and main chains[142]. The initial increase in $T_1\rho$ as a function of increasing temperature has been attributed to backbone rotations that increase with increasing temperature[142]. The maxima

observed in the $T_1\rho$ plots was attributed a change in the dominant relaxation mechanism at that temperature[142].

1.9.4 Theoretical studies on Nafion

Experimental studies of Nafion leave many unanswered questions about the hierarchical structure of the membrane and the dynamics of protons and small molecules. This is because proton transfer from the acidic group to the proton solvent, proton transport, rearrangement of the proton solvent network, and polymer dynamics take place on different time and length scales, the key processes are often transient, and there is overlap of transport mechanisms (e.g., Grotthuss hopping and vehicular transport). Due to the inability of experimental studies to directly probe the nanoscale morphological changes and transport phenomena, there is a need for multi scale modelling studies to be performed in conjunction with experiments in this field. This section will shed light on structural changes and transport processes that occur at the nanoscale.

Paddison et al[143] used density functional theory (DFT) to show that the ether oxygens in the Nafion side-chain are not hydrophilic, because of the strong electron withdrawing effect of the two CF_2 groups. Systematic addition of H_2O molecules to triflic acid[144] taken as a Nafion sidechain analogue) showed that at least three H_2O molecules are needed to dissociate the proton from CF_3SO_3H. When 6 H_2O molecules were added, the hydrated proton moved further away from the SO_3^- group suggesting that with increasing hydration the H_2O molecules shield the proton from interaction with the SO_3^- group. Paddison and Elliott [145-147] augmented this study of isolated fragments with subsequent work on the effect of side chain length and flexibility, backbone conformation and energetics of local hydration on proton transfer. They observed that the number of water molecules required to dissociate the proton from the SO_3H group was reduced when these groups were brought closer together due to partial folding of the backbone [145-147].

Urata et al[148] and Cui et al[149] have used classical MD simulations to model hydrated Nafion. Urata et al[148] observed the aggregation of SO_3^- groups and binding of H_2O molecules to sulphonate groups at low hydration levels ($\lambda = 2.8$). At high hydration levels ($\lambda = 35.4$), frequent exchange occurred between bound and free H_2O molecules. The side-chain was found to preferentially orient perpendicular to the hydrophilic/hydrophobic interface. The residence time of H_2O molecules near SO_3^- groups was found to be ~1 ps. Cui et al[149] used

simulated a shorter Nafion chain with 3 monomers instead of the 10-monomer chain simulated by Urata et al[148] Their simulations revealed that clustering of H_2O molecules was strongly dependent on the hydration level. Small isolated H_2O clusters formed at low λ and became connected into a single cluster as λ increased. Cui et al[149] attributed the poor proton conductivity at low λ to the poor hydration of the H_3O^+ ion and the lack of connectivity between water clusters. Blake et al[150] have also concluded that the large concentration of ions and small channel size serve to reduce the diffusion of H_2O molecules based on their MD simulation of hydrated Nafion with Na^+ counterions.

While the diffusion coefficient typically reported by MD simulations is due to contributions from molecules in different local environments, Blake et al have shown that H_2O diffusion is mainly due to the free H_2O molecules in the middle of the channel. This conclusion is consistent with the most recent findings of Paul and Paddison[151], based on a statistical mechanical model of proton transport in PFSA membranes[152] that proton transport occurs mainly in the centre of the Nafion pore, well separated from the sulphonate groups.

MD simulations are also well suited to examine the role of molecular architecture in determining membrane nanostructure. For example Jang et al[153] have used classical molecular dynamics to examine two extreme monomeric sequences of Nafion. In the dispersed sequence, the polar groups are uniformly distributed along the chain with a separation of 2.2 nm between adjacent sulphonic acid groups in a fully extended chain. In the blocky sequence, the polar groups are clustered together and the distance between adjacent sulphonic acid groups is 0.6 nm when the chain is fully extended. In reality, Nafion membrane is expected to have sequences that are distributed between these two extremes. For $\lambda = 16$, Jang et al[153] found that SO_3^- groups are more uniformly distributed in the equilibrated MD simulation cell, there is less phase segregation, the hydrophilic domains (H_2O clusters and channel) are smaller, the SO_3^- groups are solvated by more H_2O molecules, and the H_2O diffusion coefficient is smaller for the dispersed sequence compared to the blocky sequence. This work shows the potential for improving membrane properties by changing the molecular architecture.

Malek *et al*[154,155] performed coarse-grained molecular dynamics (CG - MD) simulation to study the microscopic structures and the effect of water on the phase-segregated morphology of the Nafion ionomer. It was found that the ionomer clusters do not penetrate into the carbon agglomerates. Side chains are buried inside hydrophilic domains with a weak contact to carbon domains. Ionomer domains are attached with their backbones to the surface of carbon

agglomerates and the mesoscopic structures exhibit "sponge like" morphologies. Hydrophilic domains of water, protons, and anionic side chains form a random three-dimensional network, which is embedded in a matrix of hydrophobic backbone aggregates. Sizes of hydrophilic domains increase from 1 to 3 nm upon water uptake. At low water content, hydrophilic domains are roughly spherical and poorly connected. At higher water content, they convert into elongated cylindrical shapes with high connectivity.

Kendrick *et al*[156] performed DFT calculations in combination with IR spectroscopy. The DFT and IR results reported suggests that Nafion forms an ordered structure on the surface due to the side chain sulphonate and CF_3 group coadsorbing onto the Pt surface. These "anchoring" functional groups reduce the degrees of freedom available for backbone and side chain CF_2 dynamics.

Various authors have performed course grained mesoscale simulations of hydrated Nafion. Wu *et al*[157-159] and Yamamoto and Hyodo[160] have used a dissipative particle dynamics (DPD), where as Wescott *et al*[161] and Galperin *et al*[162] have used dynamic mean field theory (DMFT), to show that no direct evidence of either parallel channels or discrete spherical clusters in phase segregated morphologies. Instead, they tend to favour disordered structures in which continuous networks of ionic aggregates form as the water content is increased.

Other models that make use of energies developed based on London forces or lattice-gas models incorporating the impact of electrostatic interaction between the ionomer and the electrode surfaces also have been reported[163-165]. Zhdanov[163] considered the generic reaction:

$$A + B \rightarrow AB$$

in a three phase system consisting of metal, electrolyte and gas, in the context of electrochemical applications. Species A represents the ion, whereas B is the gas, migration of A to the gas–metal boundary and reaction with B results in the formation of AB in the gas phase. According to the Tafel law for this system, the reaction rate should increase exponentially with the electrode potential however, the kinetic Monte Carlo (KMC) simulations revealed lower reaction rates as a result of diffusion limitations.

Zhdanov would later scrutinise the electrochemical processes occurring at fuel cell electrodes at the atomic and mesoscopic scale. In particular CG-MD simulations was applied to the

phase separation on the nanometer scale to wetted Nafion or Nafion type polymer electrolytes and in the double layer formed by Nafion near the charged metal surface[165].

Zhdanov[164] would propose a Mote Carlo lattice-gas model to mimic the separation on the nanometer scale in polymer electrolytes. The main underlying idea behind the calculation was the behaviour of the system under consideration is governed by the hydrophillic and hydrophobic interactions of its components. The model was used to generate the likely distribution of water in Nafion under various situations[164] and to evaluate spatial fluctuations of the potential in the double layer near the metal surface[164].

1.9.5 Microscopic reports on Nafion

Crucial information on the Nafion membranes structure and transport properties are gained from experimental scattering methods, computational methods and spectroscopic techniques mentioned above. However there is still a pressing need for experimental methods to provide detailed information at the nanometre scale, with the aim of understanding the morphology of the nanophase segregation in this area and the complex relationship between chemical structure, physiochemical properties and electrochemical kinetics. Microscopic studies have the advantage of providing a direct visualisation of the size, shape and geometrical distribution of the ionic clusters, crystalites and the continuous perfluoronated matrix.

Fan and Bard[166] first studied a spin coated Nafion film on mica using scanning electrochemical microscopy (SECM). The authors found a domain like structure, consisting of circular structures 1-2 nm in diameter made up from a conductive central zone surrounded by a less conductive region.

One of the earliest studies of Nafion using atomic force microscopy (AFM) was by Lehmani *et al*[167]. The authors used tapping mode AFM (TM-AFM) to report the presence of globular/cluster like structures with an average size of 45 nm. Later James *et al* [168,169] using SAXS and TM-AFM reported the imaging of hydrophobic and hydrophillic regions of Nafion. James *et al* reported the hydrophillic region was in a cluster like arrangement.

Affoune *et al*[170,171] observed a wet Nafion film that was stored in water and in methanol prior to AFM imaging; however, the imaging itself was carried out in air. They found that a Nafion surface exhibits considerably rough structures when it is stored in water and not in methanol. Kanamura *et al*[172] used *in situ* FTIR and AFM to demonstrate that AFM allowed the imaging

of ion channels, betwenn 40 - 100 nm. FTIR measurements show that the chemical compositon of the Pt Nafion interface is changed as humidity is increased, leading to an increase in H_2O and decrease in hydrophobic regions.

Umemura *et al*[173] reported the AFM characterization and nanolithography of a Nafion film in liquids and air. It was found that a Nafion film was much softer in water than in 5% methanol. This was the first report where the mechanical properties of a Nafion film in liquids were studied on the nanoscale. It is known that Nafion polymers expand in water because of hydration[174-176]. It can be speculated that Nafion polymers soften as a result of hydration. In the AFM nanolithography, Umemura *et al*[173] successfully fabricated nanopatterns on a Nafion surface in liquids and not in air. Further, Umemura suggested that the hydration of a Nafion film might be a key point for the AFM lithography in liquids[173].

Aleksandrova *et al*[177] performed EC-AFM measurements on a Nafion membrane. Simultaneously measured was the surface topography and the lateral ionic conductivity. The hydrophobic and hydrophillic regions could not be distinguished from surface topography. However, an electrochemical signal was obtained from the hydrophillic regions when in contact with the conductive AFM tip.

Mclean *et al*[178] developed a new AFM method where low oscillation amplitudes were used to resolve ionic clusters on the surface. Tapping mode AFM was used to the fluropolymer backbone. Recently, Koestner *et al*[179] used *in situ* AFM to image Nafion being adsorbed onto a HOPG surface. At low concentrations it was found that preferential adsorption occurs along the step edge at low polymer coverage[179].

Scanning tunneling microscopy has been established as a method for characterizing surface structures down to the nanometer scale in real space. It has the advantage that it can work under vacuum conditions as well as in ambient air, and in an electrochemical cell under potentiostatic control between the tip and sample. In addition to the surface information, a variety of different properties have been measured, including electronic[180] as well as electrochemical properties[181]. Therefore, a measuring technique based on an STM has the potential to give an insight into the structure of even complex composite materials, like the electrodes used in fuel cells, and to provide details of the structure-reactivity correlation on the nanometer scale. Hiesgen *et al*[182] performed *in situ* EC-STM measurements on a Nafion coated a platinum electrocatalyst. Unlike the study by Aleksandrova[177], the hydrophillic regions of Nafion were observed, zooming into the hydrophillic regions an image consisting

of circular globules was produced. Very few studies are available where STM has been used to characterise the metal/ionomer fuel cell interface.

1.9.6 Electrochemical measurements of electrode/ionomer interface

Even with the use of scattering methods, computational studies, spectroscopic and imaging techniques, very little is still known about the interfacial structure of the Pt electrocatalyst and polymer electrolyte membrane. The electrochemical profile of platinum is well understood using cyclic voltammetry (CV). CV provides detailed information of the electrochemical processes occurring on platinum, from the charge transfer processes occurring due anion adsorption and monitoring the change in substrate profile due to the adsorption of foreign metal adatoms. CV allows for the monitoring of various fuel cell electrocatalytic reactions such as alcohol oxidation, HOR and ORR as well. Various electrochemical studies have been performed on Nafion coated platinum electrodes, although the modification of platinum electrochemistry caused by the presence of the Nafion interface is obvious in the voltammetry shown in a number of papers, this aspect has not received significant attention. For example Jiang & Kucernak[183,184] reported the effect of Nafion deposition onto a nanostructured Pt film, electrodeposited onto a gold disc electrode, on the hydrogen oxidation and methanol electrooxidation reactions. The voltammograms produced of the Nafion free platinum film shows the presence of a typical polycrystalline platinum CV, with sharp H_{UPD} peaks and broad oxide region. As Nafion is coated or impregnated onto the Pt film, the voltammograms clearly show that the charge under the H_{UPD} and oxide regions is reduced, suggesting that Nafion or other organic compounds in the Nafion mixture are adsorbed onto the surface. It was also found that both electrooxidation reactions studied were dependent on many factors such as temperature and water content of Nafion. Tu *et al* reported voltammagrams of Pt/black powder electrocatalyst pressed against a Nafion membrane[185]. As expected, the moment the electrocatalyst came in contact with the membrane, the Pt features were inhibited.

There are many reports on the study of Nafion coated platinum electrodes and the effect on many fuel cell processes such as the methanol electroxidation reaction, hydrogen oxidation reaction and oxygen reduction reaction. Chu *et al* studied the effect of Nafion on the activity of PtRu electrocatalysts for methanol electrooxidation[186]. No voltammograms were provided in order to characterise the Nafion free and coated PtRu electrocatalyst, however

voltammograms of methanol electrooxidation were provided. Chu reported that an enhancement in the electrooxidation of methanol for PtRu:Nafion electrocatalyst in the ratio of 63.6:36.4 *wt%*. Maruyama *et al* explored the influence of a Nafion film on the hydrogen oxidation reaction[187]. Nafion was coated onto a bare polycrystalline platinum electrode, the voltammogram of the Nafion coated electrode produced a sharp spike in the H_{UPD} region with a minimal inhibition of the oxide region[187]. The HOR kinetics were found to be enhanced on the Nafion coated electrode[187].

Miyatake *et al* explored ORR on a Pt-black electrocatalyst coated with a sulphonated polyimide sulphonated ionomer[188]. The CVs of the ionomer coated electrocatalyst showed no difference to the ionomer free electrocatalyst. ORR was found to be kinetically controlled for a thin ionomer coating but for thicker ionomer films, oxygen diffusion through the film was found to be negligible[188].

Lawson *et al* [189], Gottesfeld *et al* [190] and Floriano *et al* [191] have shown in the cases of HOR and ORR, an increase in electrocatalytic activity. This has been attributed to higher O_2 and H_2 solubilities in recast Nafion than those in aqueous solutions, which is mainly due to the presence of the hydrophobic fluorocarbon phase. However, the detailed mechanism of these modifications is still under discussion, and another possible explanation could be a change of the catalyst properties by the membrane-electrode interaction.

On the other hand, other studies by Ayad *et al* and Zecevic *et al*, have concluded that the presence of Nafion does not modify the kinetic parameters of ORR[192,193], the reaction is identical on Nafion free and Nafion coated electrodes. In contrast Yano *et al* and Ohma *et al* have both shown that Nafion-coated Pt systems showed lower apparent ORR activity and more H_2O_2 production than the bare Pt electrode system, indicating that sulphonate groups in Nafion strongly adsorb on Pt sites and modify the surface properties[194,195].

Parthasarathy *et al*[196] have reported the behaviour of ORR on a Nafion coated Pt microelectrode compared to Nafion free Pt microelectrode. The authors would find that the ORR was inhibited for a Nafion coated microelectrode compared to a bare Pt microelectrode. Later Electrochemical Impedence Spectroscopic (EIS) analysis of ORR on a Nafion coated Pt microelectrode found that the ionic conductivity of Nafion was potential dependent due to the production of water from ORR[197].

Chu *et al*[198] reported the behaviour of the redox couple Fe^{2+}/Fe^{3+} at a Pt/Nafion interface and Au/Nafion inteface. It was found that there is an enhancement in the electrosorption peaks of

the redox couple at the Pt interface, however the redox couple is inhibited at the Au/Nafion interface.

The studies performed in the previous references have been on platinum electrocatalysts and none were on single crystal electrodes. At a fundamental level, single crystal electrodes are often used to characterise electrochemical processes and electrocatalytic reactions. Very recently in two articles, the pioneering studies of Markovic *et al*[199,200] reported the first time the adsorption of Nafion onto low Miller index platinum single crystal electrodes. The authors reported the "Spring Model" deducing that sulphonate adsorption onto Pt was dependent on the electrode potential [199]. Later ORR studies by the authors on the Nafion coated electrodes, found that the ORR reaction was in fact inhibited on the Nafion coated electrodes compared to the clean electrodes [200]. Later, studies by Feliu *et al*[201] would use *in situ* FTIR and electrochemical approaches on the Nafion-electrode-electrolyte interface at the Pt{111} electrode. Here the changes induced onto the local envioronment by the potential at sulphonate groups and water in the proton channels as a function of potential were emphasised.

1.10 Aims of research

The aim of this study is to elucidate in detail how Nafion interacts with well defined electrode surfaces. The following experiments will be performed to further expand our knowledge of this area of electrochemical science:

- to investigate, Nafion adsorption onto low Miller index platinum single crystal electrodes using cyclic voltammetry (CV) .
- using CV, the above study will be extended to Nafion adsorbed onto a series of stepped surfaces where the terrace width is modified to observe any structural changes that may occur.
- to measure the elemental composition and film thickness of Nafion films adsorbed onto the electrodes using X-ray photoelectron spectroscopy .
- the kinetics of the ORR of selected Nafion coated platinum single crystal electrodes will be investigated and compared to the Nafion free platinum single crystal electrodes using the rotating disc electrode (RDE), .

- to adsorb foreign metal adatoms such as palladium and bismuth onto Nafion coated and Nafion free platinum single crystal electrodes.
- use CV to investigate the electrooxidation of methanol and formic acid on Nafion coated and Nafion free Pt{111}.
- to investigate the electrooxidation of methanol and formic acid on nafion coated and Nafion free bimetallic surfaces of PdPt{111}.
- to investigate the adsorption of Nafion onto "real" fuel cell electrocatalyst as received from Johnson Matthey.

1.11 References

(1) Barbir; Frano. PEM fuel cells: theory and practice; Elsevier Academic Press: New York, 2005.

(2) Wagner, F. T.; Lakshmanan, B.; Mathias, M. F. *Journal of Physical Chemistry Letters* **2010**, *1*.

(3) Carrette, L.; Friedrich, K. A.; Stimming, U. *Chemphyschem* **2000**, *1*, 162.

(4) http://electrochem.cwru.edu/encycl/art-f04-fuel-cells-pem.htm.

(5) Zhang; Jiujun. PEM Fuel Cell Electrocatalysts and Catalyst Layers

Fundamentals and Applications; Springer, 2008.

(6) http://chemistry.about.com/od/imagesclipartstructures/ig/Science-Clipart/Catalysis-Energy-Diagram.htm.

(7) Bowker; M *The Basis and Applications of Heterogeneous Catalysis*; Oxford University Press, 1988.

(8) *Catalyst Handbook*, Second Edition ed.; Manson Publishing Ltd, 1996.

(9) Santen, v.; A., R. *Chemical Kinetics and Catalysis*; Plenum Press, 1995.

(10) Sildberg; S., M. *Chemistry The Molecular Nature Of Matter And Change*; McGraw-Hill, 2000.

(11) Gasser; H., R. P. *An Introduction to Chemisorption and Catalysis by Metals*; Oxford Scientific Publications, 1985.

(12) Fischer, A. C. Electrode Dynamics; Oxford University Press, 1996.

(13) Bard, A. J. F., L.R. Electrochemical Methods, Fundamentals and Applications; Wiley, 1980.

(14) http://www.cartage.org.lb/en/themes/Sciences/Chemistry/Electrochemis/Electrochemical/ElectrodeKinetics/ElectrodeKinetics.htm.

(15) Kolasinski, K. W. Surface Science; Wiley, 2002.

(16) Kolb, D. M. *Surface Science* **2002**, *500*, 722.

(17) Somorjai, G. A. Introduction to Surface Chemistry and Catalysis; John Wiley and Sons, Inc.: New York, 1994.

(18) Watson, D. J. PhD Thesis, Cardiff University, 2002.

(19) Abdullah, H. O. PhD Thesis, Cardiff University, 2002.

(20) Attard, G. Surfaces; Barnes, C., Ed.; Oxford University Press: New York, 1998.

(21) http://www.chem.qmul.ac.uk/surfaces/scc/scat1.htm.

(22) http://www.fhi-berlin.mpg.de/~hermann/Balsac/SSDpictures.html.

(23) Clavilier, J.; Armand, D.; Sun, S. G.; Petit, M. *Journal of Electroanalytical Chemistry* **1986**, *205*, 267.

(24) Lang, B.; Somorjai, G. A.; Joyner, R. W. *Surface Science* **1972**, *30*, 440.

(25) Smale, S. P. PhD Thesis, Cardiff University, 2008.

(26) Will, F. G.; Knorr, C. A. *Zeitschrift Fur Elektrochemie* **1960**, *64*.

(27) Will, F. G. *Journal of the Electrochemical Society* **1965**, *112*, 451.

(28) Clavilier, J.; Elachi, K.; Rodes, A. *Chemical Physics* **1990**, *141*, 1.

(29) Wieckowski, A. Interfacial Electrochemistry: Theory, Experiment and Applications; CRC Press, **1999**.

(30) Conway, B. E.; Barnett, B.; Angersteinkozlowska, H.; Tilak, B. V. *Journal of Chemical Physics* **1990**, *93*, 8361.

(31) Ishikawa, R. M.; Hubbard, A. T. *Journal of Electroanalytical Chemistry* **1976**, *69*.

(32) Yamamoto, K.; Kolb, D. M.; Kotz, R.; Lehmpfuhl, G. *Journal of Electroanalytical Chemistry* **1979**, *96*.

(33) Ross, P. N. *Journal of the Electrochemical Society* **1979**, *126*.

(34) Yeager, E.; Ogrady, W. E.; Woo, M. Y. C.; Hagans, P. *Journal of the Electrochemical Society* **1978**, *125*.

(35) Clavilier, J.; Faure, R.; Guinet, G.; Durand, R. *Journal of Electroanalytical Chemistry* **1980**, *107*, 205.

(36) Feddrix, F. H.; Yeager, E. B.; Cahan, B. D. *Journal of Electroanalytical Chemistry* **1992**, *330*.

(37) Hazzazi, O. A.; Attard, G. A.; Wells, P. B.; Vidal-Iglesias, F. J.; Casadesus, M. *Journal of Electroanalytical Chemistry* **2009**, *625*.

(38) Markovic, N. M.; Ross, P. N. *Surface Science Reports* **2002**, *45*.

(39) Ahmadi, T. S.; Wang, Z. L.; Green, T. C.; Henglein, A.; ElSayed, M. A. *Science* **1996**, *272*.

(40) Zhou, Z.-Y.; Tian, N.; Huang, Z.-Z.; Chen, D.-J.; Sun, S.-G. *Faraday Discussions* **2008**, *140*.

(41) Tian, N.; Zhou, Z.-Y.; Sun, S.-G. *Journal of Physical Chemistry C* **2008**, *112*.

(42) Tian, N.; Zhou, Z.-Y.; Sun, S.-G.; Ding, Y.; Wang, Z. L. *Science* **2007**, *316*.

(43) Rodriguez, P.; Herrero, E.; Solla-Gullon, J.; Vidal-Iglesias, F. J.; Aldaz, A.; Feliu, J. M. *Electrochimica Acta* **2005**, *50*, 4308.

(44) Clavilier, J.; Fernandezvega, A.; Feliu, J. M.; Aldaz, A. *Journal of Electroanalytical Chemistry* **1989**, *258*.

(45) Ruckman, M. W.; Strongin, M. *Accounts of Chemical Research* **1994**, *27*.

(46) Kunkel, R.; Poelsema, B.; Verheij, L. K.; Comsa, G. *Physical Review Letters* **1990**, *65*.

(47) Stumpf, R.; Scheffler, M. *Physical Review Letters* **1994**, *72*.

(48) Campbell, C. T. *Annual Review of Physical Chemistry* **1990**, *41*.

(49) Kolb; M., D. *Advances in Electrochemistry and Electrochemical Engineering*; John Wiley & Sons: New York, 1978; Vol. 11.

(50) Platzgummer, E.; Sporn, M.; Koller, R.; Forsthuber, S.; Schmid, M.; Hofer, W.; Varga, P. *Surface Science* **1999**, *419*.

(51) Platzgummer, E.; Sporn, M.; Koller, R.; Schmid, M.; Hofer, W.; Varga, P. *Surface Science* **1999**, *423*.

(52) Gauthier, Y.; Baudoingsavois, R.; Rundgren, J.; Hammar, M.; Gothelid, M. *Surface Science* **1995**, *327*.

(53) Radosavkic, D.; Barrett, N.; Belkhou, R.; Marsot, N.; Guillot, C. *Surface Science* **2002**, *516*.

(54) Kuijers, F. J.; Tieman, B. M.; Ponec, V. *Surface Science* **1978**, *75*.

(55) Venables, J. A. *Surface Science* **1994**, *299*.

(56) R, L. K. *Physics of Thin Films*; Academic: New York, 1967; Vol. 4.

(57) Vielstich, W.; Hamann, K. H.; Heitbaum, J.; Schmickler, W.; Schmidt, H.; Schwarzer, E.; J, H. *Treatise on Solid State Chemistry*; Plenum Press: New York, 1976; Vol. 6B.

(58) Parsons, R. *Surface Science* **1980**, *101*.

(59) Brivio, G. P.; Grimley, T. B. *Surface Science Reports* **1993**, *17*.

(60) Atkins, P. P., J. de. Atkins' Physical Chemistry; 9th ed.; Oxford University Press, 2010.

(61) Wroblowa, H. S.; Pan, Y. C.; Razumney, G. *Journal of Electroanalytical Chemistry* **1976**, *69*.

(62) Zhdanov, V. P.; Kasemo, B. *Electrochemistry Communications* **2006**, *8*.

(63) Norskov, J. K.; Rossmeisl, J.; Logadottir, A.; Lindqvist, L.; Kitchin, J. R.; Bligaard, T.; Jonsson, H. *Journal of Physical Chemistry B* **2004**, *108*.

(64) Shi, Z.; Zhang, J. J.; Liu, Z. S.; Wang, H. J.; Wilkinson, D. P. *Electrochimica Acta* **2006**, *51*.

(65) Markovic, N. M.; Adzic, R. R.; Cahan, B. D.; Yeager, E. B. *Journal of Electroanalytical Chemistry* **1994**, *377*.

(66) Kuzume, A.; Herrero, E.; Feliu, J. M. *Journal of Electroanalytical Chemistry* **2007**, *599*, 333.

(67) Sanchez-Sanchez, C. M.; Solla-Gullon, J.; Vidal-Iglesias, F. J.; Aldaz, A.; Montiel, V.; Herrero, E. *Journal of the American Chemical Society* **2010**, *132*.

(68) Stamenkovic, V. R.; Fowler, B.; Mun, B. S.; Wang, G. F.; Ross, P. N.; Lucas, C. A.; Markovic, N. M. *Science* **2007**, *315*, 493.

(69) Capon, A.; Parsons, R. *Journal of Electroanalytical Chemistry* **1973**, *44*.

(70) Capon, A.; Parsons, R. *Journal of Electroanalytical Chemistry* **1973**, *45*.

(71) Chang, S. C.; Leung, L. W. H.; Weaver, M. J. *Journal of Physical Chemistry* **1990**, *94*.

(72) Kita, H.; Lei, H. W. *Journal of Electroanalytical Chemistry* **1995**, *388*.

(73) Chen, Y. X.; Ye, S.; Heinen, M.; Jusys, Z.; Osawa, M.; Behm, R. J. *Journal of Physical Chemistry B* **2006**, *110*.

(74) Llorca, M. J.; Feliu, J. M.; Aldaz, A.; Clavilier, J. *Journal of Electroanalytical Chemistry* **1994**, *376*.

(75) Arenz, M.; Stamenkovic, V.; Schmidt, T. J.; Wandelt, K.; Ross, P. N.; Markovic, N. M. *Physical Chemistry Chemical Physics* **2003**, *5*, 4242.

(76) Lu, G. Q.; Crown, A.; Wieckowski, A. *Journal of Physical Chemistry B* **1999**, *103*.

(77) Parsons, R.; Vandernoot, T. *Journal of Electroanalytical Chemistry* **1988**, *257*.

(78) Jarvi, T. D.; Sriramulu, S.; Stuve, E. M. *Colloids and Surfaces a-Physicochemical and Engineering Aspects* **1998**, *134*.

(79) Xia, X. H.; Iwasita, T.; Ge, F.; Vielstich, W. *Electrochimica Acta* **1996**, *41*.

(80) Markovic, N.; Ross, P. N. *Journal of Electroanalytical Chemistry* **1992**, *330*.

(81) Kita, H.; Gao, Y. Z.; Nakato, T.; Hattori, H. *Journal of Electroanalytical Chemistry* **1994**, *373*.

(82) Chrzanowski, W.; Wieckowski, A. *Langmuir* **1998**, *14*.

(83) Iwasita, T.; Hoster, H.; John-Anacker, A.; Lin, W. F.; Vielstich, W. *Langmuir* **2000**, *16*.

(84) Mauritz, K. A.; Moore, R. B. *Chemical Reviews* **2004**, *104*, 4535.

(85) Huang, C. D.; Tan, K. S.; Lin, H. Y.; Tan, K. L. *Chemical Physics Letters* **2003**, *371*.

(86) Mallant, R. K. A. M. *Journal of Power Sources* **2003**, *118*, 424.

(87) Yeager, H. L.; Kipling, B.; Steck, A. *Journal of the Electrochemical Society* **1980**, *127*, C404.

(88) Hsu, W. Y.; Gierke, T. D. *Journal of the Electrochemical Society* **1982**, *129*, C121.

(89) Hsu, W. Y.; Gierke, T. D. *Journal of Membrane Science* **1983**, *13*.

(90) Rubatat, L.; Rollet, A. L.; Gebel, G.; Diat, O. *Macromolecules* **2002**, *35*.

(91) Schmidt-Rohr, K.; Chen, Q. *Nature Materials* **2008**, *7*, 75.

(92) Rollet, A. L.; Diat, O.; Gebel, G. *Journal of Physical Chemistry B* **2004**, *108*.

(93) Rollet, A. L.; Diat, O.; Gebel, G. *Journal of Physical Chemistry B* **2002**, *106*.

(94) Rubatat, L.; Gebel, G.; Diat, O. *Macromolecules* **2004**, *37*.

(95) Schlick, S.; Gebel, G.; Pineri, M.; Volino, F. *Macromolecules* **1991**, *24*.

(96) H., L. M. *Polym Prepr* **1997**, *38*, 80.

(97) Haubold, H. G.; Vad, T.; Jungbluth, H.; Hiller, P. *Electrochimica Acta* **2001**, *46*.

(98) Gebel, G.; Diat, O. *Fuel Cells* **2005**, *5*.

(99) Gebel, G.; Loppinet, B. *Journal of Molecular Structure* **1996**, *383*.

(100) Loppinet, B.; Gebel, G. *Langmuir* **1998**, *14*.

(101) Gebel, G. *Polymer* **2000**, *41*.

(102) Kim, M.-H.; Glinka, C. J.; Grot, S. A.; Grot, W. G. *Macromolecules* **2006**, *39*.

(103) Ladewig, B. P.; Knott, R. B.; Hill, A. J.; Riches, J. D.; White, J. W.; Martin, D. J.; da Costa, J. C. D.; Lu, G. Q. *Chemistry of Materials* **2007**, *19*.

(104) Kreuer, K. D. *Journal of Membrane Science* **2001**, *185*, 29.

(105) Yang, B.; Manthiram, A. *Journal of Power Sources* **2006**, *153*.

(106) Pivovar, A. A.; Pivovar, B. S. *Journal of Physical Chemistry B* **2005**, *109*.

(107) Zawodzinski, T. A.; Neeman, M.; Sillerud, L. O.; Gottesfeld, S. *Journal of Physical Chemistry* **1991**, *95*.

(108) Perrin, J.-C.; Lyonnard, S.; Volino, F. *Journal of Physical Chemistry C* **2007**, *111*.

(109) Geissler, P. L.; Dellago, C.; Chandler, D.; Hutter, J.; Parrinello, M. *Science* **2001**, *291*.

(110) Paddison, S. J.; Reagor, D. W.; Zawodzinski, T. A. *Journal of Electroanalytical Chemistry* **1998**, *459*, 91.

(111) Buzzoni, R.; Bordiga, S.; Ricchiardi, G.; Spoto, G.; Zecchina, A. *Journal of Physical Chemistry* **1995**, *99*, 11937.

(112) Ludvigsson, M.; Lindgren, J.; Tegenfeldt, J. *Electrochimica Acta* **2000**, *45*, 2267.

(113) Byun, C. K.; Sharif, I.; DesMarteau, D. D.; Creager, S. E.; Korzeniewski, C. *Journal of Physical Chemistry B* **2009**, *113*, 6299.

(114) Webber, M.; Dimakis, N.; Kumari, D.; Fuccillo, M.; Smotkin, E. S. *Macromolecules* **2010**, *43*, 5500.

(115) Warren, D. S.; McQuillan, A. J. *Journal of Physical Chemistry B* **2008**, *112*, 10535.

(116) Laporta, M.; Pegoraro, M.; Zanderighi, L. *Physical Chemistry Chemical Physics* **1999**, *1*.

(117) Moilanen, D. E.; Piletic, I. R.; Fayer, M. D. *Journal of Physical Chemistry A* **2006**, *110*.

(118) Moilanen, D. E.; Piletic, I. R.; Fayer, M. D. *Journal of Physical Chemistry C* **2007**, *111*.

(119) Basnayake, R.; Peterson, G. R.; Casadonte, D. J., Jr.; Korzeniewski, C. *Journal of Physical Chemistry B* **2006**, *110*, 23938.

(120) Gruger, A.; Regis, A.; Schmatko, T.; Colomban, P. *Vibrational Spectroscopy* **2001**, *26*, 215.

(121) Liang, Z. X.; Chen, W. M.; Liu, J. G.; Wang, S. L.; Zhou, Z. H.; Li, W. Z.; Sun, G. Q.; Xin, Q. *Journal of Membrane Science* **2004**, *233*.

(122) Osawa, M.; Nakane, T.; Ito, K.; Suetaka, W. *Journal of Electroanalytical Chemistry* **1989**, *270*.

(123) Malevich, D.; Zamlynny, V.; Sun, S. G.; Lipkowski, J. *Zeitschrift Fur Physikalische Chemie-International Journal of Research in Physical Chemistry & Chemical Physics* **2003**, *217*.

(124) Malevich, D.; Li, J.; Chung, M. K.; McLaughlin, C.; Schlaf, M.; Lipkowski, J. *Journal of Solid State Electrochemistry* **2005**, *9*.

(125) Ayato, Y.; Kunimatsu, K.; Osawa, M.; Okada, T. *Journal of the Electrochemical Society* **2006**, *153*.

(126) Zeng, J.; Jean, D.-i.; Ji, C.; Zou, S. *Langmuir* **2012**, *28*.

(127) Sondheimer, S. J.; Bunce, N. J.; Lemke, M. E.; Fyfe, C. A. *Macromolecules* **1986**, *19*.

(128) Bunce, N. J.; Sondheimer, S. J.; Fyfe, C. A. *Macromolecules* **1986**, *19*.

(129) Pak, Y. S.; Xu, G. *Journal of the Electrochemical Society* **1993**, *140*.

(130) Chen, R. S.; Jayakody, J. P.; Greenbaum, S. G.; Pak, Y. S.; Xu, G.; McLin, M. G.; Fontanella, J. J. *Journal of the Electrochemical Society* **1993**, *140*.

(131) Nosaka, A. Y.; Watanabe, S.; Toyoda, I.; Nosaka, Y. *Macromolecules* **2006**, *39*.

(132) Nosaka, A. Y.; Nosaka, Y. *Journal of Power Sources* **2008**, *180*.

(133) Ye, G.; Janzen, N.; Goward, G. R. *Macromolecules* **2006**, *39*.

(134) Boyle, N. G.; Coey, J. M. D.; McBrierty, V. J. *Chemical Physics Letters* **1982**, *86*.

(135) Boyle, N. G.; McBrierty, V. J.; Eisenberg, A. *Macromolecules* **1983**, *16*.

(136) Fontanella, J. J.; Edmondson, C. A.; Wintersgill, M. C.; Wu, Y.; Greenbaum, S. G. *Macromolecules* **1996**, *29*.

(137) Rankothge, M.; Haryadi; Moran, G.; Hook, J.; Vangorkom, L. *Solid State Ionics* **1994**, *67*.

(138) Dec, S. F.; Wind, R. A.; Maciel, G. E. *Macromolecules* **1987**, *20*.

(139) Chen, Q.; Schmidt-Rohr, K. *Macromolecules* **2004**, *37*.

(140) Takasaki, M.; Kimura, K.; Kawaguchi, K.; Abe, A.; Katagiri, G. *Macromolecules* **2005**, *38*.

(141) MacMillan, B.; Sharp, A. R.; Armstrong, R. L. *Polymer* **1999**, *40*.

(142) Page, K. A.; Jarrett, W.; Moore, R. B. *Journal of Polymer Science Part B-Polymer Physics* **2007**, *45*.

(143) Paddison, S. J. *Annual Review of Materials Research* **2003**, *33*.

(144) Paddison, S. J. *Journal of New Materials for Electrochemical Systems* **2001**, *4*.

(145) Elliott, J. A.; Paddison, S. J. *Physical Chemistry Chemical Physics* **2007**, *9*.

(146) Paddison, S. J.; Elliott, J. A. *Journal of Physical Chemistry A* **2005**, *109*.

(147) Paddison, S. J.; Elliott, J. A. *Physical Chemistry Chemical Physics* **2006**, *8*.

(148) Urata, S.; Irisawa, J.; Takada, A.; Shinoda, W.; Tsuzuki, S.; Mikami, M. *Journal of Physical Chemistry B* **2005**, *109*.

(149) Cui, S.; Liu, J.; Selvan, M. E.; Keffer, D. J.; Edwards, B. J.; Steele, W. V. *Journal of Physical Chemistry B* **2007**, *111*.

(150) Blake, N. P.; Mills, G.; Metiu, H. *Journal of Physical Chemistry B* **2007**, *111*.

(151) Paul, R.; Paddison, S. J. *Journal of Chemical Physics* **2005**, *123*.

(152) Paddison, S. J.; Paul, R.; Zawodzinski, T. A. *Journal of the Electrochemical Society* **2000**, *147*.

(153) Jang, S. S.; Molinero, V.; Cagin, T.; Goddard, W. A. *Journal of Physical Chemistry B* **2004**, *108*.

(154) Malek, K.; Eikerling, M.; Wang, Q.; Navessin, T.; Liu, Z. *Journal of Physical Chemistry C* **2007**, *111*, 13627.

(155) Malek, K.; Eikerling, M.; Wang, Q.; Liu, Z.; Otsuka, S.; Akizuki, K.; Abe, M. *Journal of Chemical Physics* **2008**, *129*.

(156) Kendrick, I.; Kumari, D.; Yakaboski, A.; Dimakis, N.; Smotkin, E. S. *Journal of the American Chemical Society* **2010**, *132*.

(157) Wu, D.; Paddison, S. J.; Elliott, J. A. *Energy & Environmental Science* **2008**, *1*.

(158) Wu, D.; Paddison, S. J.; Elliott, J. A. *Macromolecules* **2009**, *42*.

(159) Wu, D.; Paddison, S. J.; Elliott, J. A.; Hamrock, S. J. *Langmuir* **2010**, *26*.

(160) Yamamoto, S.; Hyodo, S. A. *Polymer Journal* **2003**, *35*.

(161) Wescott, J. T.; Qi, Y.; Subramanian, L.; Capehart, T. W. *Journal of Chemical Physics* **2006**, *124*.

(162) Galperin, D. Y.; Khokhlov, A. R. *Macromolecular Theory and Simulations* **2006**, *15*.

(163) Zhdanov, V. P. *Physical Review E* **2003**, *67*.

(164) Zhdanov, V. P.; Kasemo, B. *Electrochemistry Communications* **2006**, *8*, 561.

(165) Zhdanov, V. P.; Kasemo, B. *Surface Science* **2004**, *554*, 103.

(166) Fan, F. R. F.; Bard, A. J. *Science* **1995**, *270*.

(167) Lehmani, A.; Durand-Vidal, S.; Turq, P. *Journal of Applied Polymer Science* **1998**, *68*.

(168) James, P. J.; Elliott, J. A.; McMaster, T. J.; Newton, J. M.; Elliott, A. M. S.; Hanna, S.; Miles, M. J. *Journal of Materials Science* **2000**, *35*.

(169) James, P. J.; McMaster, T. J.; Newton, J. M.; Miles, M. J. *Polymer* **2000**, *41*.

(170) Affoune, A. M.; Yamada, A.; Umeda, M. *Langmuir* **2004**, *20*.

(171) Affoune, A. M.; Yamada, A.; Umeda, M. *Journal of Power Sources* **2005**, *148*.

(172) Kanamura, K.; Morikawa, H.; Umegaki, T. *Journal of the Electrochemical Society* **2003**, *150*.

(173) Umemura, K.; Wang, T.; Hara, M.; Kuroda, R.; Uchida, O.; Nagai, M. "Nano-characterization of a nafion thin film in air and in water by atomic force microscopy"; International Conference on Nanoscience and Technology, 2007, Basel, SWITZERLAND.

(174) Gebel, G.; Aldebert, P.; Pineri, M. *Polymer* **1993**, *34*.

(175) Elliott, J. A.; Hanna, S.; Elliott, A. M. S.; Cooley, G. E. *Polymer* **2001**, *42*.

(176) Domke, J.; Radmacher, M. *Langmuir* **1998**, *14*.

(177) Aleksandrova, E.; Hiesgen, R.; Eberhard, D.; Friedrich, K. A.; Kaz, T.; Roduner, E. *Chemphyschem* **2007**, *8*.

(178) McLean, R. S.; Doyle, M.; Sauer, B. B. *Macromolecules* **2000**, *33*.

(179) Koestner, R.; Roiter, Y.; Kozhinova, I.; Minko, S. *Langmuir* **2011**, *27*.

(180) Hiesgen, R.; Meissner, D. *Electrochimica Acta* **1997**, *42*.

(181) Hiesgen, R.; Eberhardt, D.; Meissner, D. *Surface Science* **2005**, *597*.

(182) Hiesgen, R.; Eberhardt, D.; Aleksandrova, E.; Friedrich, K. A. *Fuel Cells* **2006**, *6*.

(183) Jiang, J. H.; Kucernak, A. *Journal of Electroanalytical Chemistry* **2004**, *567*.

(184) Jiang, J. H.; Kucernak, A. *Journal of Electroanalytical Chemistry* **2005**, *576*.

(185) Tu, W. Y.; Liu, W. J.; Cha, C. S.; Wu, B. L. *Electrochimica Acta* **1998**, *43*.

(186) Chu, Y. H.; Shul, Y. G.; Choi, W. C.; Woo, S. I.; Han, H. S. *Journal of Power Sources* **2003**, *118*.

(187) Maruyama, J.; Inaba, M.; Katakura, K.; Ogumi, Z.; Takehara, Z. *Journal of Electroanalytical Chemistry* **1998**, *447*.

(188) Miyatake, K.; Omata, T.; Tryk, D. A.; Uchida, H.; Watanabe, M. *Journal of Physical Chemistry C* **2009**, *113*.

(189) Lawson, D. R.; Whiteley, L. D.; Martin, C. R.; Szentirmay, M. N.; Song, J. I. *Journal of the Electrochemical Society* **1988**, *135*.

(190) Gottesfeld, S.; Raistrick, I. D.; Srinivasan, S. *Journal of the Electrochemical Society* **1987**, *134*.

(191) Floriano, J. B.; Ticianelli, E. A.; Gonzalez, E. R. *Journal of Electroanalytical Chemistry* **1994**, *367*.

(192) Ayad, A.; Naimi, Y.; Bouet, J.; Fauvarque, J. F. *Journal of Power Sources* **2004**, *130*.

(193) Zecevic, S. K.; Wainright, J. S.; Litt, M. H.; Gojkovic, S. L.; Savinell, R. F. *Journal of the Electrochemical Society* **1997**, *144*.

(194) Yano, H.; Higuchi, E.; Uchida, H.; Watanabe, M. *Journal of Physical Chemistry B* **2006**, *110*.

(195) Ohma, A.; Fushinobu, K.; Okazaki, K. *Electrochimica Acta* **2010**, *55*.

(196) Parthasarathy, A.; Srinivasan, S.; Appleby, A. J.; Martin, C. R. *Journal of the Electrochemical Society* **1992**, *139*.

(197) Parthasarathy, A.; Dave, B.; Srinivasan, S.; Appleby, A. J.; Martin, C. R. *Journal of the Electrochemical Society* **1992**, *139*.

(198) Chu, D.; Tryk, D.; Gervasio, D.; Yeager, E. B. *Journal of Electroanalytical Chemistry* **1989**, *272*.

(199) Subbaraman, R.; Strmcnik, D.; Stamenkovic, V.; Markovic, N. M. *Journal of Physical Chemistry C* **2010**, *114*, 8414.

(200) Subbaraman, R.; Strmcnik, D.; Paulikas, A. P.; Stamenkovic, V. R.; Markovic, N. M. *Chemphyschem* **2010**, *11*, 2825.

(201) Ma Gomez-Marin, A.; Berna, A.; Feliu, J. M. *Journal of Physical Chemistry C* **2010**, *114*, 20130.

Chapter Two

Theoretical Background

2.1 The electrode/electrolyte interface - The electrical double layer

The electrical double layer is an array of charged particles and/or orientated dipoles that exist in every material interface. For the electrode/electrolyte interface, such a layer reflects the different ionic zones that are formed in solution to compensate for the excess charge at the electrode surface. A positively charged electrode will therefore attract a layer of negatively charged ions of the electrolyte and *vice versa*.

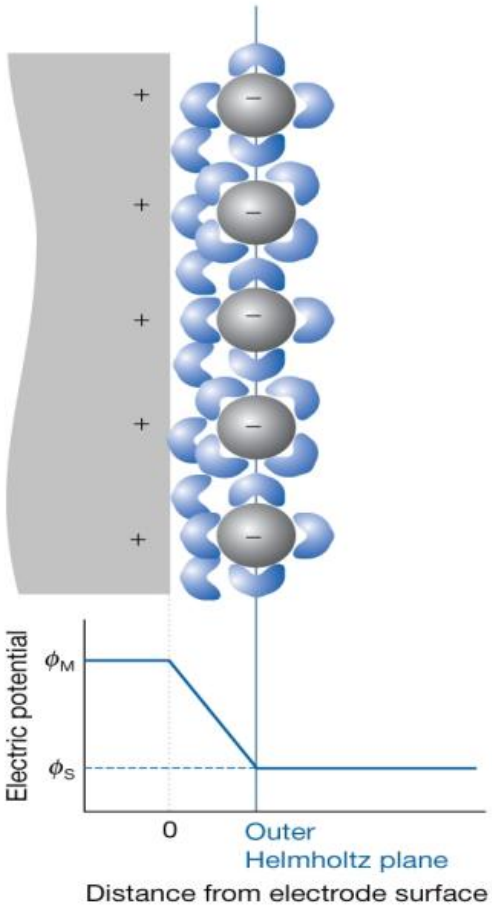

Fig 2.1 The Helmholtz model of the electrical double layer.

The first model for the double layer was proposed by Helmholtz in the 1850s (fig 2.1). Helmholtz proposed that the ions (with the opposite charge to the charged electrode), in the

electrolyte will form a layer balancing the electrode charge. This layer is known as the Outer Helmholtz Plane (OHP)[1,2] . The distance of approach of the OHP is assumed to be limited to the radius of the ion and a single sphere of solvation round each ion. The OHP is rigidly bound due to strong electrostatic bonds. In essence, ions from the electrolyte form a parallel "plate capacitor" to the electrode.

Gouy and Chapman later proposed the diffuse double layer model (fig 2.2)[1,2]. Figure 2.2 shows how the local concentrations of the cations and anions differ in the Gouy - Chapman model from their bulk concentrations. Ions of opposite charge to the electrode cluster close to the electrode surface and ions of the same charge are repelled into the bulk solution. The concentration of the ionic species at a given distance from the surface decays exponentially (fig 2.2).

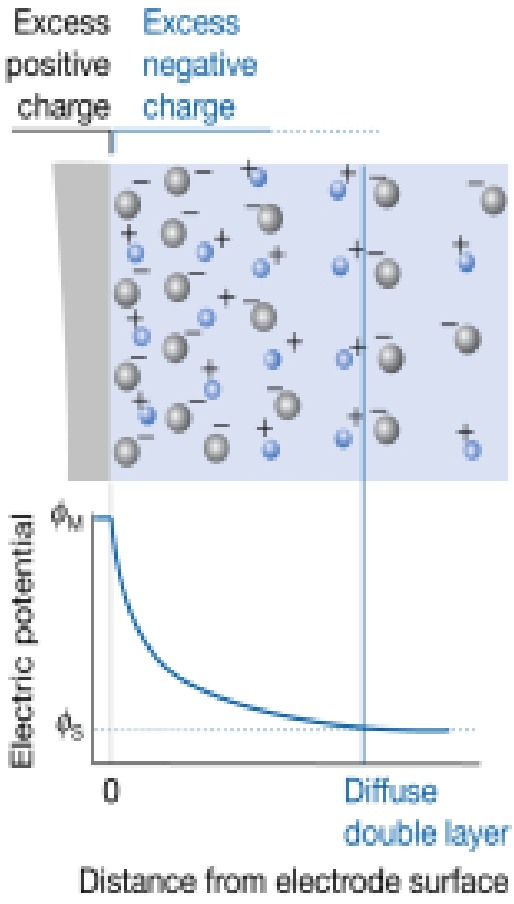

Fig 2.2 The Gouy Chapman model of the double layer.

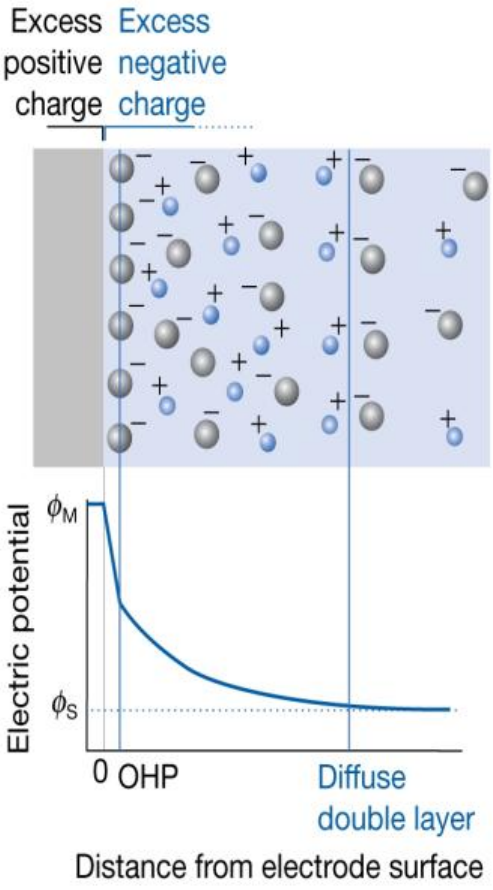

Fig 2.3 Stern-Grahame model of the double layer.

The Gouy - Chapman model underemphasises the rigidity of the double layer whilst the Helmholtz model overemphasises the rigidity of the double layer. Neither is a good representation of the structure of the double layer. The Stern - Grahame model of the double layer (fig 2.3)[1,2], was proposed where both the Helmholtz and Gouy - Chapman models were combined. Here it was proposed that ions closest to the electrode surface are constrained into a rigid Helmholtz plane, whilst the ions outside this plane are diffuse as in the Gouy Chapman model. A further level of sophistication was added to the double layer model by Stern and Grahame when Grahame added the Inner Helmholtz Plane (IHP) to the structure of the double layer. The IHP is the inner most layer and contains solvent molecules and ions that have specifically adsorbed onto the electrode surface. The IHP is defined by the locus for the centres of the specifically adsorbed ions.

The electrical double layer resembles an ordinary (parallel plate) capacitor. For an ideal capacitor, the charge (Q) is proportional to the potential difference:

$$Q = CE \qquad \text{(eq 2.1)}$$

where C is capacitance (in farads, F), the ratio of charge stored with respect to the applied potential E (V). The charge-potential relationship for the electrical double layer is given by equation 2.2:

$$Q = C_{DL}A(E - E_{PZC}) \quad \text{(eq 2.2)}$$

where C_{DL} is the capacitance of the double layer (F), A is the electrode area (cm^{-2}) and E_{PZC} is the potential of zero charge, where no net charge exists on the electrode. The capacitance of the double layer consists of a combination of the Helmholtz and the Gouy-Chapman layers. For two capacitors in series, the total capacitance is given by:

$$\frac{1}{C} = \frac{1}{C_H} + \frac{1}{C_{GC}} \quad \text{(eq 2.3)}$$

where C_H and C_{GC} represent the capacitance of the Helmholtz and Gouy-Chapman layers. The smaller of these capacitances determines the observed behaviour. By analogy, with a parallel plate capacitor, C_H is given by:

$$C_H = -\frac{\varepsilon}{4\pi d} \quad \text{(eq 2.4)}$$

where d is the distance between the surface and the counterionic layer, and ε is the dielectric constant. C_H increases with the separation of the surface and counter ionic layer as well as the dielectric constant. The value of C_{GC} is affected by the concentration of electrolyte whereas C_H is largely independent. For example, if a strong concentration of electrolyte is used, most of the charge is stored in the Helmholtz layer and little in the diffuse layer. Therefore capacitance is proportional to the capacitance of the Helmholtz layer:

$$C = C_H \quad \text{(eq 2.5)}$$

In contrast for dilute solutions, C_{GC} is larger than C_H and capacitance is proportional to the capacitance of the Gouy-Chapman layer:

$$C = C_{GC} \quad \text{(eq 2.6)}$$

Figure 2.6 displays the change in double layer capacitance with the change in electrolyte concentration and applied potential. It can be seen that at strong concentrations of electrolyte, the capacitance of the double layer resembles that of a parallel plate capacitor. The

capacitance is independent of the applied potential and concentration. However, at low concentrations of electrolyte, a sharp dip in the capacitance curve is observed at the PZC of the surface, reflecting the contribution of the Gouy-Chapman layer. Comparison of the double layer with a parallel plate capacitor is more appropriate when using strong concentrations of electrolyte.

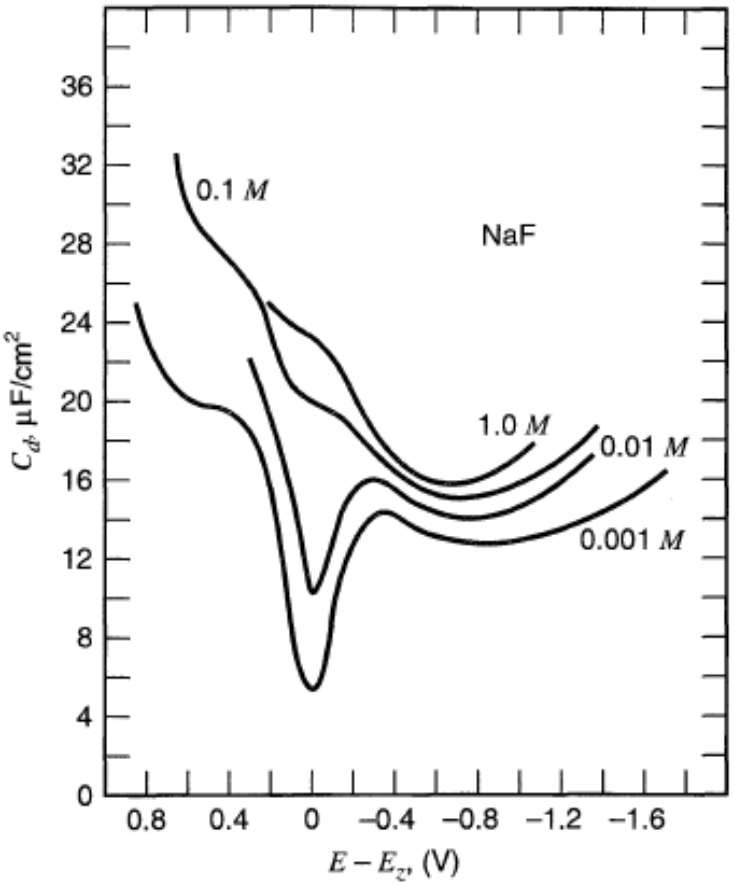

Fig 2.4 Effect of concentration and potential on double layer capacitance, reprinted from[3,4].

2.2 Cyclic voltammetry (CV)

Cyclic voltammetry (CV) is a powerful electrochemical technique that is used for the study of electroactive species. For the electrochemical characterisation of electrode surfaces and the electrochemical study of biological materials or compounds, CV is often the first experiment performed. The technique is easy to perform (see chapter 3 section 3.2) with the resulting voltammograms providing concise results which can be analogous to a conventional spectrum in that information is conveyed as a function of an energy scan.

A typical CV experiment involves the measurement of current density with respect to an applied voltage. A voltage, applied to the working electrode (W.E.) with respect to the reference electrode (R.E.). This potential is swept between two potential limits ($E_{initial}$ - E_{final}), to the working electrode (W.E.) versus the reference electrode (R.E)[5,6] at a constant scan rate, *v* (V s^{-1}). The potentiostat used for the experiments ensures that the current that is generated at the W.E. as a result of the voltage sweep is passed through a third electrode known as the counter electrode (C.E.). The 'cyclic' term is introduced when the applied voltage reaches the E_{final} potential limit and is then swept back to the $E_{initial}$ potential limit. The current that is generated as a result of the potential sweep is often normalised to the electrode surface area and referred to as current density. Hence a cyclic voltammogram (CV), a plot of current density (j = current/electrode area) versus potential (E), is presented[6 5]. Fig 2.5 represents the saw-tooth waveform that is applied during cyclic voltammetry. In this example the potential is swept between 0 - 0.85 V at a scan rate of 0.05 Vs^{-1}.

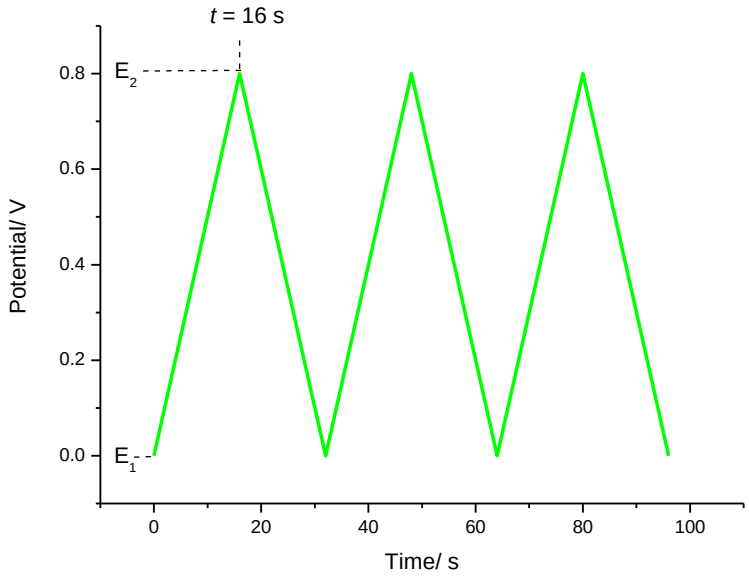

Fig 2.5 Sawtooth potential waveform applied to working electrode during a voltammogram.

2.2.1 Cyclic voltammetry of Faradaic processes

A Faradaic process is a non-adsorptive process that take place due to electron transfer across the electrode/electrolyte interface. The transfer of electrons across the electrode/electrolyte interface will result in redox reactions occurring. The subsequent electrical current generated

as a result of the redox reactions is known as a faradaic current because it obeys Faraday's Law[7]:

$$I_F = \frac{dQ}{dt} = n_e F \frac{dN}{dt} = n_e FAv \qquad \text{(eq 2.7)}$$

In other words, the charge *Q* related to a Faradaic process which passes through the working electrode equals the amount of reactant (*N*) converted multiplied by the number of electrons exchanged (*ne*) in the process and the Faraday constant (*F*). As a result, the current I_F can be directly related to the reaction rate *v* (in mol s^{-1} m^{-2}) for a given surface area *A*. The redox reaction occurring at the electrode surface can be represented in the form of eq 2.8:

$$Ox + ne^- \leftrightarrow Red \qquad \text{(eq 2.8)}$$

The reaction is reversible where Ox represents the oxidised species, n is the number of electrons and Red is for the reduced species. A voltammogram is shown in Fig 2.6 of the reversible redox process in reaction 2.8.

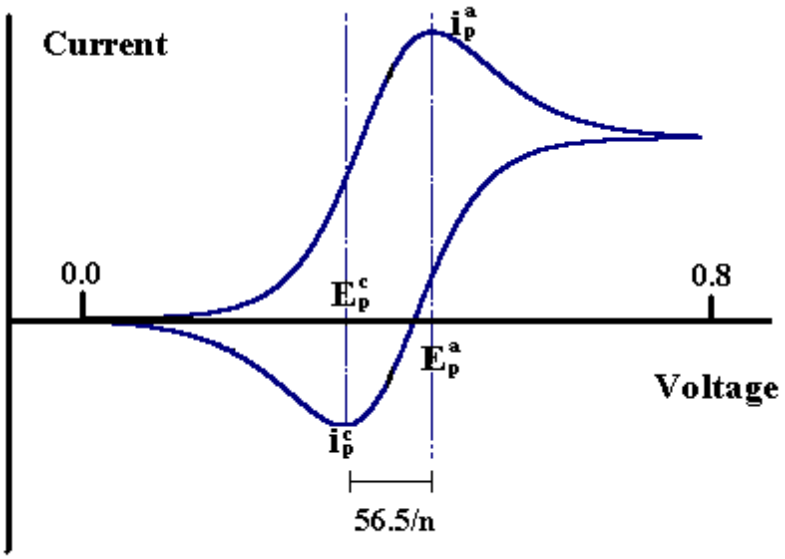

Fig 2.6 CV of a reversible redox process.

Provided that the reaction is reversible, where:

- rate of electron transfer at the surface electrode is fast,
- the peak potential is independent of sweep rate and concentration (see later),

the concentration ratio of the oxidised and reduced species at the surface electrode will be controlled by the Nernst equation, eq 2.9.

$$E = E^0 + \frac{RT}{nF} \ln \frac{[Ox]}{[Red]} \qquad \text{(eq 2.9)}$$

Here E is the applied potential in V, E^0 is the standard equilibrium potential in V, R is the universal gas constant (8.314 J K^{-1} mol^{-1}), T is the temperature in K, n is the number of electrons, F is Faraday's constant (96487 C mol^{-1}) and [Ox] and [Red] are the concentrations of the oxidised and reduced species at the electrode surface. At 25°C, the peak current i_p measured in amps (A), for the forward and reverse reactions in Fig 2.6 should be the same and can be calculated from the *Randles-Sevcik* equation:[4,7,8]

$$i_p = (2.69 \times 10^5) n^{3/2} \cdot A \cdot D_o^{1/2} \cdot \nu^{1/2} \cdot C_o \qquad \text{(eq 2.10)}$$

where A is the electrode area in cm^{-2}, D_o is the diffusion coefficient in cm^2 s^{-1}, ν is the scan rate in V s^{-1} and C_o is concentration of the electroactive species in bulk solution in mol cm^{-3}. From equation 2.10, it can be seen that peak current is proportional to concentration and the square root of the scan rate. Therefore the magnitude of the peak height in a CV should increase as scan rate in increased (fig 2.7)

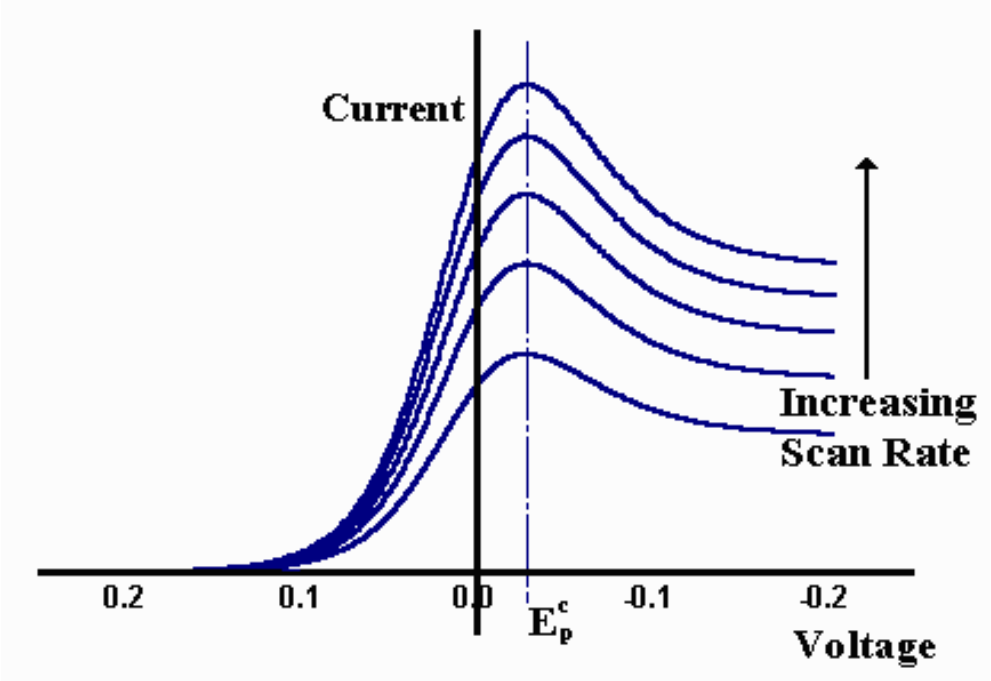

Fig 2.7 Effect of increasing scan rate on peak height.

The cathodic and anodic peaks are separated by a potential of 56.5/n mV in fig 2.6 where n is the number of electrons transferred. The peak separation of a reversible reaction can be defined by equation 2.11[4,7,8]:

$$\left|E_p^{Ox} - E_P^{Red}\right| = 2.2\frac{RT}{nF} = \frac{56.5}{n}\ mV \qquad \text{(eq 2.11)}$$

Here E_p^{Ox} and E_p^{Red} are the peak potentials of the oxidation and reduction processes, R is the universal gas constant (8.314 J K^{-1} mol^{-1}), T is the temperature in Kelvin K, n is the number of electrons transferred and F is Faraday's constant (96487 C mol^{-1}). Provided that the system can reach equilibrium during the time to complete an electron transfer, the system will approach thermodynamic equilibrium where upon the small change in the direction of the applied voltage, a reversal in the process in equation 2.8 will occur. This will give the resulting voltammogram in Fig 2.6.

An irreversible reaction can be described by the reaction:

$$Ox + ne^- \rightarrow Red \qquad \text{(eq 2.12)}$$

Where the sluggish kinetics of the reverse reaction means that the rate of the reverse reaction is negligible. The concentration ratio of the oxidised and reduced species is not controlled by the Nernst equation. This is because of the sluggish kinetics of reaction 2.12 and therefore the electrode potential is not independent of scan rate (see later). For an irreversible process, the electrode potential (E_p) is not independent of scan rate since the system is not at equilibrium whilst the peak current (i_p) remains proportional to the square root of the scan rate[4,7,8]. The following equations now hold true for i_p and E_p:

$$\left|I_p\right| = 3.01x10^5 n\sqrt{\left\{\frac{2.3RT}{bF}\right\}}D^{1/2}C_0 v^{1/2} \qquad \text{(eq 2.13)}$$

$$E_p = E_{1/2} - b\left[0.52 - \frac{1}{2}\log\left(\frac{b}{D}\right) - \log k_s + \frac{1}{2}\log v\right] \qquad \text{(eq 2.14)}$$

Where b is the gradient from a Tafel slope (a plot of $\log_e I$ *vs* E) measured in V^{-1}, k_s is the specific rate constant at the standard potential found from a plot of E_p against log v. F, R, T D, C_O, v and n have the same meanings as above.

2.2.2 Cyclic voltammetry of non-Faradaic processes

A second type of current arises due to the presence of the electrochemical double layer. Non-Faradaic process occur due to adsorption and desorption of ions from the electrode surface, however no chemical reaction will occur and electrons are not transferred across the electrode/electrolyte interface. The adsorption and desorption of ions from the surface results in an electric current due to the charging of the double layer given by the following equation:

$$I_{DL} = AC_{DL}v \qquad \text{(eq 2.15)}$$

Where the double layer current (I_{DL} measured in ampere, A) is proportional to the surface electrode area (A measured in cm^{-2}), the capacitance of the double layer (C_{DL} measured in farad, F) and the scan rate (v measured in V s^{-1}). The current that is generated from the charging of the double layer is classed as a non-faradaic current and both faradaic and non-faradaic processes occur when electrode reactions occur. Therefore, in the CV in fig 2.6, the total current that flow is the sum of the faradaic and non-faradaic contributions to the current. Most often, it is the faradaic current that is of interest and the associated 'extra' charge from non-faradaic pseudo capacitative charging of the double layer must be subtracted from the total current in order to measure charge transfer reactions. The reader is directed to ref[4] for a more detailed view of non-Faradaic processes.

2.3 The rotating disc electrode (RDE)

The RDE is a specialised hydrodynamic method used in the study of kinetics and the mechanism of electrode reactions. Cyclic voltammetry employs the use of stationary electrodes, where the mode of mass transport of the reactive species to the electrode is solely by diffusion. It is disadvantageous to use CV for kinetic and mechanistic measurements, this is because when analysing the oxygen reduction (ORR) for example, it is found that CV is mass transport limited due to a growth in diffusion layers (see later)[4,8]. It is preferable to use RDE for ORR measurements because it will overcome the mass transport limitations of CV. The mode of mass transport for the RDE is forced convection. Electrodes in the RDE are connected to a motor and are rotated (see chapter three section 3.4 for experimental details). This results in the controlled flow of electroactive species perpendicular to the surface and subsequently being “flung out” parallel to the surface and all mass transport issues

overcome[4,8]. Therefore, there is an important need in distinguishing and understanding better the different modes of mass transport.

2.3.1 Mass transport by diffusion processes for stationary electrodes

Diffusion occurs in all solutions and arises from uneven local concentration distributions. Diffusion acts to maximise entropy by "evening out" the concentration distribution within any system. For an electroactive species, its conversion to the product form will only take place at the electrode surface. Consequently, a concentration gradient will exist where there is a lower concentration of the electroactive species at the electrode surface compared to the bulk electrolyte. Similarly, a higher concentration of the product will exist near the electrode compared to the bulk electrolyte. The rate of diffusion is therefore dependent on the concentration gradient and it is possible to mathematically model the rate of diffusion. In the 1850s, Fick described diffusion mathematically by considering the simple case of linear diffusion to a planar surface[2,4,8].

Ficks' first law of diffusion states :

$$J_0 = -D_0 \left\{ \frac{\partial C_0}{\partial x} \right\} \qquad \text{(eq 2.21)}$$

where J_o is flux (rate of diffusion of electroactive species), D_o is the diffusion coefficient and C_o is the concentration gradient. Ficks first law of diffusion relates the diffusional flux to the concentration gradient. The negative sign of the diffusion coefficient implies that diffusion occurs down the concentration gradient, (from high concentration to low concentration). In practice, for electrochemists it is more important to know how concentration of the electroactive species changes at a specific point (such as adjacent to the electrode surface), as a function of time. This gives Fick's second law of diffusion (eq 2.22)[2,4]:

$$\frac{\partial C_0}{\partial t} = D_0 \left\{ \frac{\partial^2 C_0}{\partial x^2} \right\} \qquad \text{(eq 2.22)}$$

The differential equation (eq 2.22) is an important relationship. It enables the electrochemist to predict any change in the concentration of electroactive material close to the electrode surface. Let us explore a simple electrooxidation reaction of electroactive species A to A^+:

$$A_{(aq)} \longrightarrow A^{+}_{(aq)} + e^{-} \qquad \text{(eq 2.23)}$$

During a CV experiment, if no potential is applied to the working electrode where reaction 2.23 will occur, a uniform bulk concentration of A will remain in solution. Once potential is applied to the working electrode, electroactive species A at the electrode surface will convert to the oxidised form A^{+}. As a result, a concentration gradient is created between the electrode and the bulk solution, the concentration gradient will act to force a flux of electroactive species A, from the bulk solution to the electrode surface as described in Ficks first law of diffusion (eq 2.21). Gradually a "diffusion layer" is created close to the electrode surface where the concentration of electroactive species A. At the electrode surface will differ from the bulk solution[2,4,8]. This is shown in fig 2.8 where the growth of the diffusion layer is shown to increase as a function of time. The scale of the diffusion layer grows steadily as reaction 2.23 occurs, in principle the diffusion layer growth can grow without limit until it has exhausted all of electroactive species A. However, as the "diffusion layer" increases with time, the rate of diffusion will decrease. This is because it will take longer for the electroactive material to reach the surface electrode.

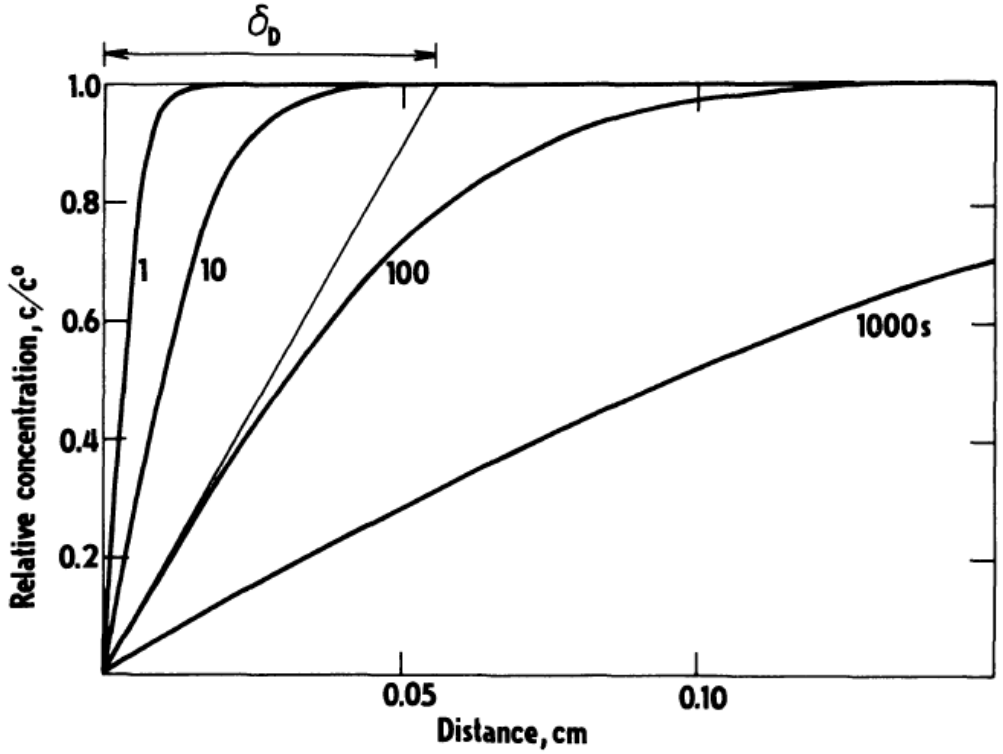

Fig 2.8 The growth of diffusion layer thickness as a function of time[1].

2.3.2 Mass transport by convection for hydronamic electrodes

A hydrodynamic electrode is one where forced convection is deliberately induced to dominate the transport of the electrode. Convection within an electrochemical cell is induced in several ways. The electrode can either be in a fixed position and electrolyte is allowed to flow across the surface, or the electrode may move (by rotation) inducing convection in the solution[2,4,8].

For this study, platinum single crystal and bimetallic electrodes will be act as rotating disc electrodes, (RDE), connected to the shaft of the RDE apparatus. The electrode face was centred with respect to the rotating shaft, meniscus contact with the electrolyte was made and was then rotated at different rotation rates. The RDE is a commonly used hydrodynamic electrode and its role is to overcome the mass transport limitations of steady state experiments. As the electrode is rotated at constant speed, electrolyte is drawn into the surface at constant rotation rate and then "spun out" away from the surface in a radial direction. This movement in turn will sustain a "fresh" supply of electroactive material to the surface at a constant rate[2,4]. RDE experiments are designed so that electroactive material from bulk electrolyte is drawn to the surface in laminar flow. In laminar flow, the solution moves smoothly in layers along constant directions (fig 2.9). This is in contrast with the chaotic motion that characterises turbulent flow (fig 2.9). Therefore rotation rates must be used where turbulent flow is at a minimum.

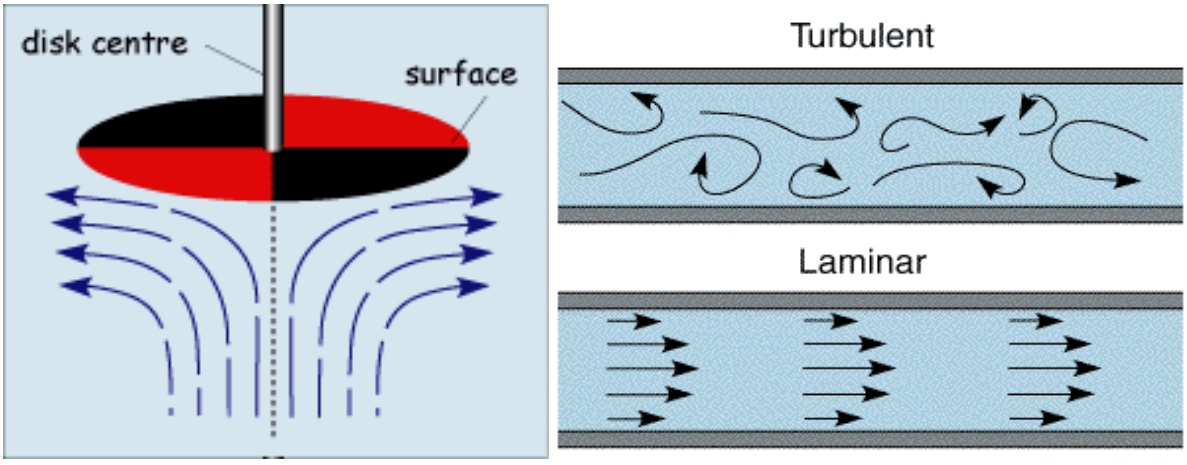

Fig 2.9 Effect of rotation on flux of electroactive material and Fig 2.9a Difference between laminar and turbulent flow.

The transition from laminar flow to turbulent flow can be calculated by the Reynolds number[2,8], (eq 2.24), a dimensionless parameter:

$$Re = \frac{\omega r_c^2}{v} \qquad \text{(eq 2.24)}$$

where Re is the Reynolds number (dimensionless), ω is the rotation speed in rad s^{-1}, r_c is the radius of the cylinder (cm^{-2}) and *v* is the viscosity of solution. Provided that the Reynolds number does not exceed $1x10^5$, the flow induced in the solution will be laminar and has the pattern shown in fig 2.9. If laminar flow of the electrolyte is achieved, to predict the flux of the electroactive species both diffusion and convection must be considered. Under steady-state mass transport is therefore defined as:

$$\frac{\partial[C]}{\partial t} = D_C \frac{\partial^2[C]}{\partial z^2} - v_z \frac{\partial[C]}{\partial z} \qquad \text{(eq 2.25)}$$

where C is the concentration mol dm^{-3} of the electroactive species and v_z is the velocity of the flow of electroactive species close to the electrode surface. The velocity in direction *z* is:

$$v_z = -Cz^2 \qquad \text{(eq 2.26)}$$

where C has been shown to be:

$$C = 0.5.10\omega^{3/2}v^{1/2}D^{-1/3} \qquad \text{(eq 2.27)}$$

and ω is the angular rotation rate in radians per second ($2\pi f$ where *f* is the rotation rate in rpm), *v* is the kinematic viscosity of the solution (ca 0.01 cm^2 s^{-1}) and D is the diffusion coefficient of oxygen ($1.93\ x10^{-5}$ cm^2 s^{-1}).

For RDE experiments, the limiting current for ORR can be found from the Levich equation where:

$$j_L = nFAC_b D_0^{2/3} v^{-1/6} \omega^{1/2} \qquad \text{(eq 2.28)}$$

where j_L is the limiting current (A cm^{-2}), n is the number of electrons, F is Faradays constant (96484 C mol^{-1}), A is the electrode area (cm^{-2}), C_b is the bulk concentration of oxygen in solution ($1.1\ x10^{-3}$ mol dm^{-3}), D_O is the diffusion coefficient of oxygen ($1.93\ x10^{-5}$ cm^2 s^{-1}), *v* is the kinematic viscosity of the solution (ca 0.01 cm^2 s^{-1}) and ω is the angular rotation rate in

radians per second ($2\pi f$ / 60 where f is the rotation speed in rpm). A plot of i_L against $\omega^{1/2}$ will show a linear dependence of i_L against $\omega^{1/2}$ where the slope is proportional to the number of electrons and zero intercept. For ORR experiments, the slope of the line should be equal to four (since O_2 reduction to H_2O is a 4 electron process), however if the reaction is inhibited and hydrogen peroxide is produced, then the slope should equal two (since O_2 reduction to H_2O_2 is a two 2 electron process).

The kinetic current density (j_k) for the ORR reaction can be found from the Koutecky-Levich equation where:

$$\frac{1}{j} = \frac{1}{j_k} + \frac{1}{B\omega} \qquad \text{(eq 2.29)}$$

where j_k^{-1} is the kinetic current density (A cm^{-1}) B is equal to $nFAC_bD_0^{2/3}v^{-1/6}$ where all symbols have their previous meanings. A plot of j^{-1} versus ω^{-1} yields a straight line where the slope is equal to B and the intercept is equal to j_k^{-1}. The value of B allows one to assess the number of electrons involved in the ORR and the intercept to evaluate the rate constant.

Tafel plots allow one to determine the reaction mechanism that is occurring. The Tafel equation for a cathodic reaction can be expressed as:

$$j_c = j_0\left\{e^{\frac{n\alpha F\eta}{RT}} - e^{\frac{n(1-\alpha)F\eta}{RT}}\right\} \qquad \text{(eq 2.30)}$$

where j_c is the cathodic current (A cm^{-2}), η is the applied overpotential (V), j_0 is the exchange current density and all other symbols have their previous meanings. If the overpotential is large then the reverse reaction can be ignored and the equation becomes:

$$j_c = j_0\left\{e^{\frac{n\alpha F\eta}{RT}}\right\} \qquad \text{(eq 2.31)}$$

Re-arrangement of the Tafel gives the forward reaction as:

$$\eta = \frac{2.303RT}{\alpha nF}\log j_0 - \frac{2.303RT}{\alpha nF}\log j \qquad \text{(eq 2.32)}$$

A plot of η versus log j should yield a straight line with the slope equal to 2.3RT/nαF and intercept equal to j_0. The Tafel equation shows that at certain current density range

overpotential is linearly dependent on the logarithm of current density. The higher the Tafel slope, the faster the overpotential increases with current density, therefore for an electrochemical reaction to obtain a high current at low overpotential values, the reaction should exhibit a low Tafel slope. For ORR measurements, two Tafel slopes are obtained, at 60 mV/dec and 120 mV/dec depending on the potential range studied and the electrode material.

As mentioned earlier, for this study platinum single crystal electrodes were used. The single crystal bead electrodes were orientated so that the crystal face was centred with respect to the rotation shaft. A meniscus contact was made between the crystal face and electrolyte ensuring that a "hanging meniscus-RDE" was formed. The meniscus contact ensures that in theory the resulting polarisation curve is produced from the flat crystal face. However, it has been shown by Villullas and Teijelo[9,10] that the height of the meniscus can greatly affect the limiting current of the polarisation curve. If the height of the meniscus is too low, lateral wetting of the sides of the bead will occur. The wetting of sides will contribute to the polarisation curve and a larger limiting current than normal will be obtained. If the height of the meniscus is too high, the meniscus becomes constricted in the centre and a limiting current that is smaller than normal is obtained. The correct meniscus height is obtained when the meniscus is hanging perpendicular to the electrolyte. After consulting the works of Feliu[11] and Markovic[12] it was found that to obtain the correct meniscus height for ORR experiments, the limiting current of the polarisation curve should read between 5.8 $x10^{-3}$ - 6 $x10^{-3}$ A cm^{-2} at a rotation speed of 1600 rpm. These values of limiting current give n = 4 for the Levich and Koutecky Levich plots.

2.4 X-ray photoelectron spectroscopy (XPS)

XPS is one of the most versatile methods for analysing electrode surfaces. In this study it will be used to gain the surface composition and film thickness of Nafion adsorbed onto a Pt{111} single crystal electrode. The basis of the technique lies in Einstein's explanation of the photoelectric effect, whereby photons can induce electron emission from a solid provided the photon energy ($h\nu$) is greater than the work function, Φ. The work function of a solid is defined as the minimum energy required to remove an electron from the Fermi level, (highest occupied energy level in the solid)[13,14], to the vacuum level. The vacuum level is the energy

of an electron at rest (zero kinetic energy) in a vacuum far removed from neighbouring particles such that no interactions take place between them.

In XPS, a monochromatic beam of X-rays is incident upon the electrode surface, causing photoemission from both core and valence levels of surface atoms into the vacuum[13,14]. Core levels are defined as the inner quantum shells, which do not participate in chemical bonding, whereas valence levels are electrons in the more weakly bound, partially filled outer quantum shells. Figure 2.10 illustrates schematically the excitation of core level electrons.

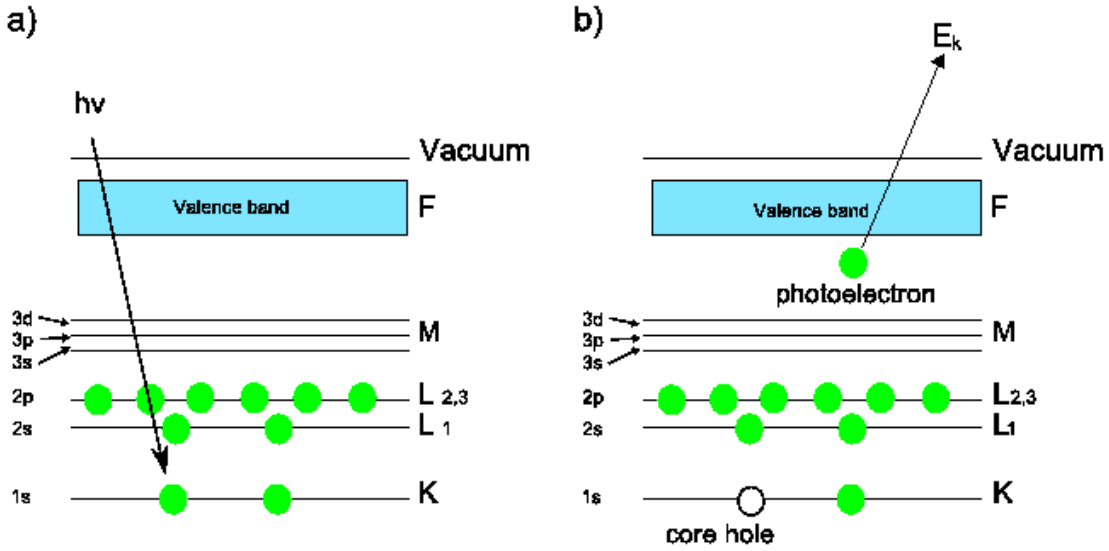

Fig 2.10 XPS excitation of core level electrons. Reprinted from ref[15]

The key chemical identification is that the core electrons deep inside atoms are largely insensitive to their surroundings when condensed into the solid phase and retain binding energies E_B that are signatures of the atom type, i.e. the number of protons in the nucleus. The outermost electrons, which participate in chemical bonding in a solid, are broadened into a 'valence band'. Emission from the valence band is most effectively probed by ultra-violet photoemission spectroscopy. This method will not be described further, the reader is forwarded to reference[13].

Applying the principle of energy conservation, the kinetic energy of emitted photoelectrons can be estimated:

$$E_{kin} = hv - E_B + \Phi \qquad \text{(eq 2.33)}$$

By convention the binding energy of a core level is measured with respect to the Fermi level. The total energy available to excite a core electron is clearly equal to the photon energy (*hv*).However some of the photon energy must be consumed in overcoming the potential energy barrier, associated with the attraction of the electron for the nucleus, $E_B + \Phi$. The remaining energy is transformed into the kinetic energy of the photoemitted electrons. Hence it is clear that for a fixed photon energy, photoemission from an atom with well-defined core levels (of a particular binding energy) will produce photoelectrons with well defined kinetic energies varying systematically from element from element. The higher the nuclear charge of an adatom, the higher the binding energy of a given core level. The electron energy distribution (the number of electrons detected, N(E), as a function of their kinetic energy) can be measured using an electrostatic energy analyser consisting of two electrically isolated concentric hemispheres with a potential with a potential difference between them as shown in figure 2.11.

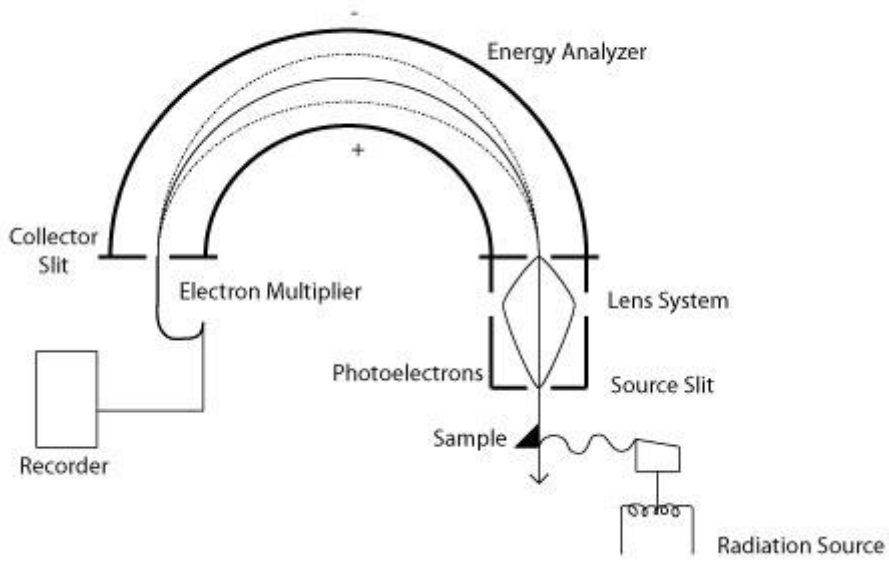

Fig 2.11 Electrostatic energy analyser used in electron/ion spectroscopic analysis of surfaces. Reprinted from ref[16]

Fig 2.11 shows that the electrostatic field separates electrons by allowing electrons of a specific kinetic energy (the "pass energy") through to the detector (the continuous line). Electrons of kinetic energy less than the "pass energy" are attracted by the inner positive hemisphere and neutralised. The higher energy electrons hit the outer hemisphere and are lost. The scanning of electron kinetic energies to produce a photoelectron spectrum is

achieved by "retarding" (slowing down) the electrons to the pass energy using a negative electrode (the "retard" plate). By changing the negative voltage of the "retard" plate, electrons with differing kinetic energies are allowed through the analyser to the detector. While it is usually the kinetic energy of the outgoing electrons that is measured, spectra are usually displayed on a binding energy scale to allow ease for elemental identification. This is achieved by rearranging equation 2.33 to give

$$E_B = hv - E_{kin} - \Phi \qquad \text{(eq 2.34)}$$

Siegbahn and co-workers have shown[17] that XPS is a probe of the chemical environment or "oxidation state" of surface species to which it is bonded. Charge transfer may leave atoms with a partial positive or negative charges, leading to a shift in core levels to higher or lower binding energies associated with increased or decreased Coulombic attraction between core electrons and the nucleus. Therefore, atoms in a formal higher oxidation state will yield XPS at high binding energy relative to the same atom in a low oxidation state. The magnitude of the chemical shift is dependent on the local environment surrounding the atom in question.

In principle, separate XPS peaks should be observed for every chemically distinct atom. However this is often not the case in practice because the 'energy spread' of the incident radiation is considerably larger than the chemical shift. Hence, peaks separated by small chemical shifts (of the order of tenths of an electron volt) remain unresolved. The relative intensity of different XPS peaks will depend on a number of factors, including the concentration of the atoms of the element in the selvedge, the probability of photoemission occurring for a particular core level, the IMFP (inelastic mean free path) of the of the electron itself and the efficiency of the spectrometer for detection of electrons as a function of kinetic energy. For XPS peaks of similar binding energy, both the IMFP and instrumental factors may be ignored. If two elements, say A and B for example are distributed homogeneously throughout the sample depth, then the relative concentrations may be obtained using the following expression

$$\frac{C_A}{C_B} = \frac{I_A}{I_B} \times \frac{\sigma_B}{\sigma_A} \qquad \text{(eq 2.36)}$$

where C_A = atomic concnetration of A , C_B = stomic concentration of B, I_A = XPS peak area of the core level of atom A, I_B = XPS peak area of the core level of atom B, σ_A = photoemission cross-section of core level of atom A and σ_B = photoemission cross-section of core level of atom B.

2.5 References

(1) Koryta, J. Principles of Electrochemistry; 2nd ed.; John Wiley & Sons: New York, 1993.

(2) Fischer, A. C. Electrode Dynamics; Oxford University Press, 1996.

(3) Grahame, D. C. *Chemical Reviews* **1947**, *41*, 441.

(4) Bard, A. J. F., L.R. Electrochemical Methods, Fundamentals and Applications; Wiley, 1980.

(5) Mabbott, G. A. *Journal of Chemical Education* **1983**, *60*, 697.

(6) Kissinger, P. T.; Heineman, W. R. *Journal of Chemical Education* **1983**, *60*, 702.

(7) Wang, J. Analytical Electrochemistry; John Wiley & Sons: New York, 2001.

(8) Brett, C. M. A. B., A. M. O. Electrochemistry Principles, Methods, and Applications; Oxford University Press, 1993.

(9) Villullas, H. M.; Teijelo, M. L. *Journal of Electroanalytical Chemistry* **1995**, *385*, 39.

(10) Villullas, H. M.; Teijelo, M. L. *Journal of Electroanalytical Chemistry* **1995**, *384*, 25.

(11) Kuzume, A.; Herrero, E.; Feliu, J. M. *Journal of Electroanalytical Chemistry* **2007**, *599*, 333.

(12) Stamenkovic, V. R.; Fowler, B.; Mun, B. S.; Wang, G. F.; Ross, P. N.; Lucas, C. A.; Markovic, N. M. *Science* **2007**, *315*, 493.

(13) Attard, G. Surfaces; Barnes, C., Ed.; Oxford University Press: New York, 1998.

(14) Atkins, P. P., J. de. Atkins' Physical Chemistry; 9th ed.; Oxford University Press, 2010.

(15) http://www2.warwick.ac.uk/fac/sci/physics/current/postgraduate/regs/mpags/ex5/techniques/electronic/xps/.

(16) http://chemwiki.ucdavis.edu/Physical_Chemistry/Spectroscopy/Photoelectron_Spectroscopy/Photo-Electron_Spectroscopy%3A_Application.

(17) Siegbahn, K. *Philosophical Transactions of the Royal Society of London Series a-Mathematical Physical and Engineering Sciences* **1986**, *318*.

Chapter Three

Experimental

3.1 Introduction

Cyclic Voltammetry (CV) was the principle experimental method used in the present study. It was used to investigate the adsorption of Nafion® onto platinum and platinum bimetallic single crystal electrodes. In addition, the electroxidation of formic acid and methanol on Nafion® - coated and Nafion® - free Pt{111} and Pt/Pd{111} together with High Surface Area (HSA) supported platinum electrocatalysts supplied by Johnson Matthey were examined. Rotating Disc Electrode (RDE) was used to study the effects of Nafion® adsorption on the kinetics of the Oxygen Reduction Reaction (ORR) of Pt*{hkl}* electrodes. Nafion structures adsorbed on Pt{111} and *ex-situ* XPS (X-ray photoelectron spectroscopy) was used to obtain surface composition and film thickness.

3.2 Cyclic Voltammetry

3.2.1 Single Crystal Measurements

All single crystal electrodes used in this study were manufactured in accordance with the methods reported by Clavilier[1] and Hazzazi[2]. Single crystal CV measurements were performed in a standard two compartment electrochemical cell (Fig 3.1). The cell comprised of a platinum mesh counter electrode together with a high surface area palladium hydride reference electrode. A CHi 600 electrochemical analyser (from CHi instruments) was used for potentiostatic control.

All glassware (the electrochemical cell and all components) must be kept contaminant free. The cell along with all glass components were immersed in "green acid solution" – a dilute solution of permanganic acid, formed from mixture comprising of sulphuric acid and a few grains of potassium permanganate – for at least one hour before use (often left overnight). This ensured that all internal surfaces were covered in green acid. Green acid was then decanted into the appropriate waste container and all equipment (the cell and all components)

was thoroughly rinsed with Milli-Q water (10 - 15 minutes) to ensure that all traces of green acid were removed. The cell and components were then steam cleaned with Milli-Q water. Once steamed, the cell was then thoroughly rinsed with Milli-Q water and filled to the bridge of the cell that separates the two compartments.

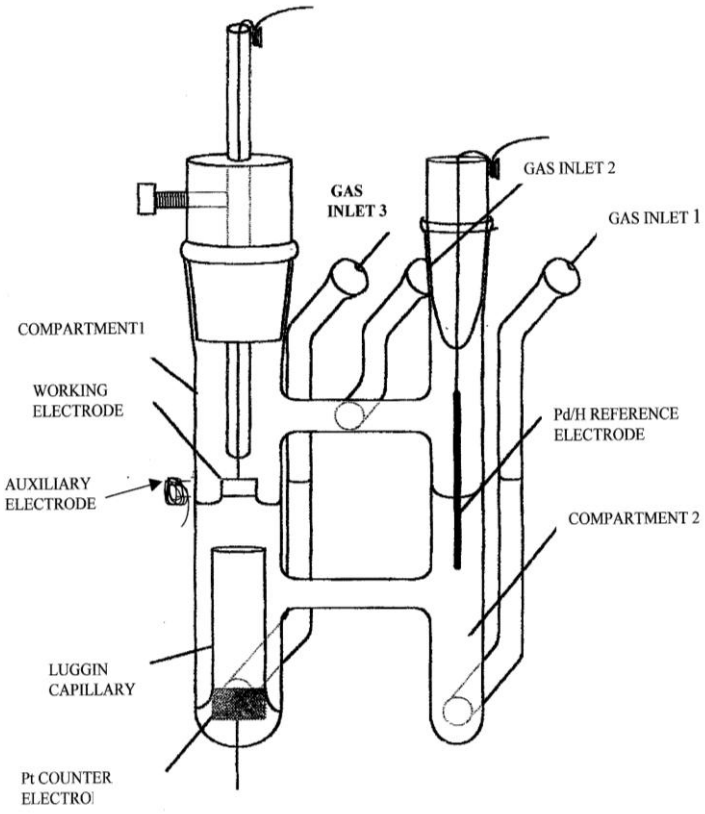

Figure 3.1 Electrochemical cell used for cyclic voltammetry, reprinted from[2]

The palladium reference consisted of 1 mm Pd wire spot-welded onto 1 mm Pt wire which was encased in a glass jacket. The palladium reference was first cleaned by gently heating the palladium wire in a Bunsen flame. The electrode was then placed into compartment 2 of the electrochemical cell and was bubbled with hydrogen gas for 30 minutes. The absorption of hydrogen resulted in the formation of a stable β - hydride phase of palladium and would maintain its potential for up to 10 hours in aqueous acidic electrolyte. On the Standard Hydrogen Electrode (SHE), the Pd-H reference electrode is at -50 mV.

As soon as the electrode had finished charging, the water in the cell was changed, The cell was thoroughly rinsed and was then filled with the desired electrolyte. Typical electrolytes used for single crystal measurements were 0.1 M $HClO_4$ and 0.1 M H_2SO_4. Dissolved oxygen in the electrolyte was removed by bubbling argon or nitrogen gas through inlet 3 for 20 - 30

minutes. An overpressure of the inert gas was maintained through inlet 2 of the electrochemical cell to maintain a positive overpressure. Once an overpressure was achieved in the cell (after 20-30 minutes of bubbling gas through inlet 2) voltammograms of the working electrode, were collected. The stem of the single crystal bead was wrapped around an electrical conducting wire and threaded through a glass capillary. The connecting wire running up the capillary tube and was secured by wrapping around the nub at the top of the capillary tube.

The capillary tube was located in the Teflon stopper. Hence the same working electrode could be either raised or lowered such that it could be manipulated to form a meniscus contact between the single crystal face and the electrolyte. Without the meniscus contact, the undefined surface sites on the outside of the single crystal bead would be accessible during the measurement and therefore contribute to the CV. Once secured in the glass tube and Teflon stopper, the single crystal was flame annealed in the hottest point of the blue flame of the Bunsen burner (the crystal would glow a bright yellow colour). It was then cooled in a bubbler containing Milli-Q water and a steady flow of hydrogen gas. Care must be taken here in order to avoid an explosion (ignition) of the hydrogen gas.

The crystal face was then dipped into the pure water of the hydrogen bubbler and was then removed from the bubbler and transferred to the electrochemical cell. A droplet of pure water was attached to the crystal face to prevent any contamination of the surface upon transfer from the hydrogen bubbler to the electrochemical cell. Once the crystal was placed in the electrochemical cell, connections were made to the potentiostat, the meniscus contact was formed between the crystal and electrolyte and the CV programme was initiated. The start potential for the sweep was set at 0.85 V (*vs* Pd/H) and swept to 0 V a scan rate of 0.05 Vs^{-1}. The start potential was selected as 0.85 V in order to observe the desorption of the thermal oxide that is formed whenever transferring a platinum surface from the hydrogen bubbler to the electrochemical cell[3].

3.2.2 Nafion Adsorption on Platinum Single Crystal Electrodes

All Nafion® solutions were prepared by diluting the as-received Nafion® stock solutions by a factor of 1000 using Milli-Q water. After the clean surface voltammograms were obtained, (confirming cleanliness and surface order), the electrode was rinsed with Milli-Q water and

dipped into a 10^{-3} M potassium bromide solution. Potassium bromide was used in order to form a monolayer of bromine atoms which protects the surface from organic contaminants present in the Nafion® and to preserve the integrity of the surface whilst being heated using the hair dryer (see below).

The electrode was rinsed again and a known amount of the diluted Nafion® solution was added to the front face of the electrode bead. This was then heated using a hair dryer for 2 - 3 minutes at a temperature between 100 - 145^{O}C to allow the excess liquid in the droplet to evaporate and allow the polymeric film to flow above its glass transition temperature. The temperature was measured by connecting the crystal electrode to a chromel-alumel thermocouple. The electrode was reintroduced to the electrochemical cell and underwent rapid potential cycling between hydrogen evolution potentials and the onset of surface oxide formation at a scan rate of 0.2 Vs^{-1}. This was the procedure used in order to both remove the bromide layer (still adsorbed) on the electrode surface and to re-adsorb and hydrate the Nafion® film. After approximately 200 - 300 scans at the fast scan rate, the voltammogram parameters were set to 'normal' parameters (potential range 0 - 0.85 V *vs* Pd/H at a scan rate 0.05 mVs^{-1}) and a stable voltammogram was recorded.

3.2.3 X-ray photoelectron spectroscopy (XPS) measurements of Nafion coated Pt{111}

XPS measurements were performed on a Kratos Axis Ultra-DLD photoelectron spectrometer using monochromatic Al radiation operating at 120 W. The base pressure during acquisition was $1x10^{-9}$ Torr. Spectra were collected in the Hybrid operating mode over an approximate area of 400 x 300 μm, at pass energies of 40 and 160 eV for high resolution and survey scans, respectively. The spectra were subsequently analyzed through CasaXPS v.2.3.15 using sensitivity factors supplied by the manufacturer.

3.2.4 Characterisation and Quantification of High Surface Area (HSA) 60% Platinum Electrocatalysts using Cyclic Voltammetry with Bismuth and Germanium Probes

The same procedure described in section 3.1.1 was followed in order to analyse HSA Pt 60% catalysts supplied by Johnson Matthey. Below, in Table 1, are listed the catalyst samples supplied by Johnson Matthey that were analysed.

Platinum Electrocatalyst Samples	
Number	**Name**
08/51	Baseline Pt on Carbon
08/62	Baseline Pt sintered in H_2
08/52	Baseline Pt Sintered in N_2
09/46	Baseline Pt Sintered in N_2 + Treatment 1
09/93	Baseline Pt Sintered in N_2 + Treatment 2
09/110	Baseline Pt Sintered in N_2 + Treatment 3
08/172	PtCr Alloy Annealed in H_2
08/279	PtCo Alloy Annealed in H_2

Table 1 60%Pt HSA Electrocatalyst Sample Provided by Johnson Matthey, where treatment 1 = exposure to hydrogen at 600^{O}C, treatment 2 = exposure to vacuum at 500^{O}C and treatment 3 = exposure to CO at 200^{O}C.

The electrolytes of choice when analysing the HSA electrocatalyst were 0.5 M $HClO_4$ or 0.5 M H_2SO_4. For analysis, the HSA electrocatalysts were loaded onto a platinum mesh support. The mesh was flame annealed before hand and characterised using CV in order to check the electrochemical cell for contaminants. Due to the high surface area of the electrocatalysts, only a small sample (typically 1-2 mg) was needed for the analysis. Once the electrocatalyst was loaded onto the mesh, it was characterised using CV. The parameters used were the same as when analysing single crystals except for a much slower scan rate being employed (< 0.01 Vs^{-1}). This was to minimise the Ohmic drop because of the high surface area exhibited by even a small mass of the electrocatalyst.

3.2.4.1 Quantification of High Surface Area (HSA) 60% platinum electrocatalysts with cyclic voltammetry using bismuth surface probes

Quantification of the amount of {111} and {100} surface sites present on the Pt electrocatalyst was carried out using bismuth and germanium as surface probes in accordance with the methods reported by Hazzazi[2],and Feliu[4]. To quantify {111} surface sites, a bismuth nitrate solution was prepared ($1x10^{-3}$ M). Once the as-received electrocatalyst was characterised using CV, 500 μL of bismuth nitrate was injected into the electrochemical cell (typical volume of electrolyte used was 47 - 50 cm^{-3}). A voltammogram was recorded and care was taken to not exceed a potential greater than 0.85 V (*vs* Pd/H). This was to ensure that the bismuth adlayer forming on the Pt electrocatalyst did not become oxidised and desorb from the surface. It was noticed that upon injecting the bismuth, the H_{UPD} coverage of the platinum decreased. Once the CV had stabilised, more bismuth was injected and the H_{UPD} signal was quenched even further. Once the {111} sites were blocked with bismuth, a unique bismuth redox peak would be observed at 0.5 - 0.6 V (*vs* Pd/H). The voltammogram was stopped when full blockage of all sites occurred. The ratio of the decrease of H_{UPD} charge of the clean Pt electrocatalyst to the charge increase of the bismuth surface redox peak allows for the precise quantification of the {111} surface sites present [5].

3.2.4.2 Quantification of High Surface Area (HSA) 60% platinum electrocatalysts with cyclic voltammetry using germanium surface probes

The same method was used as described in section 3.1.3.1 to determine the amount of {100} sites present, but instead of using bismuth, the surface probe used was germanium[4,5]. An aqueous $1x10^{-2}$ M germanium hydroxide in 0.5M NaOH solution was prepared. This solution was injected into the electrochemical cell (500 μL) after the as-received electrocatalyst had been characterised. To record the CV with germanium in the cell, the start potential was held at 0.2 V (*vs* Pd/H) and the maximum potential set to 0.6 V (*vs* Pd/H) in accordance with the procedure of Feliu and co-workers[4,5]. Whilst recording the voltammogram, it was observed that a germanium oxide redox peak between 0.4 - 0.5 V would form. This was ascribed to adsorption of germainum at {100} sites exclusively. Once all of the Pt H_{UPD} surface sites were blocked and the germanium oxide peak stopped growing the voltammogram was

stopped. The ratio of H_{UPD} charge to that of the surface adsorbed peak of germanium at 0.6 V allowed for the precise quantification of the {111} terrace sites[5].

3.3 Metal Deposition on Single Crystal Electrodes

$Pd^{2+}_{(aq)}$ and $Bi^{3+}_{(aq)}$ aqueous solutions were prepared using a palladium nitrate ($Pd(NO_3)_2$ from Sigma Aldrich) and bismuth nitrate pentahydrate ($Bi(NO_3)_2.5H_2O$ from Sigma Aldrich) solutions respectively in the concentration ranges between 10^{-5}-10^{-6} M using Milli-Q water. These electrolytes were used as the source of metal adatoms in subsequent measurements of Pt bimetallic surfaces.

The forced deposition method was used to produce ordered palladium adlayers onto single crystal electrodes (from sub-monolayer to multilayer coverage)[6]. The technique of depositing metals via forced deposition involved first obtaining a CV of the clean, well ordered single crystal electrode (to verify surface order and cleanliness). Once a good CV of the electrode was obtained, the electrode was rinsed with Milli-Q water and then dipped into the aqueous $Pd(NO_3)_2$ solution. The electrode with a droplet of palladium nitrate attached, was then transferred to the hydrogen bubbler, and held above the water level for 1-2 seconds to allow a stream of hydrogen to pass over the droplet of $Pd(NO_3)_2$. This resulted in palladium being reduced to form palladium metal on the surface of the electrode. The deposition of Pd at Pt single crystals therefore occurs as follows:

$$H_{2(g)} \rightarrow 2H^+_{(aq)} + 2e^- \qquad \text{(oxidation)}$$

$$Pd^{2+}_{(aq)} + 2e^- \rightarrow Pd_{ads} \qquad \text{(reduction)}$$

$$Pt + Pd^{2+}_{(aq)} + H_{2(g)} \rightarrow Pt - Pd_{ads\,metal} + 2H^+_{(aq)} \qquad \text{(overall reaction)}$$

The electrode was then removed from the hydrogen bubbler and rinsed with Milli-Q water, in order to remove the excess palladium nitrate. It was then re-introduced to the electrochemical cell via a meniscus contact. The electrode was subsequently characterised by CV. Further layers of palladium were deposited by repeating the steps described above. Flame annealing the electrode would remove the palladium film as a volatile palladium oxide and the subsequent cooling in hydrogen would recover the platinum single crystal features. Similarly, palladium could be adsorbed on to Nafion® coated Pt*{hkl)* by following the same forced deposition procedure. For producing PtPd alloy surfaces, a partial flame anneal of a palladium adlayer was carried out[6].

For bismuth, simply dipping the previously flame annealed platinum single crystal electrode into the bismuth nitrate solution and subsequent rinsing gave rise to an irreversibly adsorbed adlayer of bismuth adatoms. It has been shown previously that the immersion of single crystal electrodes into certain metal ion solutions at open circuit can result in the spontaneous deposition of the metal onto the single crystal electrodes[7]. The amount of metal that is deposited is dependent on the concentration of the metal solution and how long the electrode is held in the metal solution. For the deposition of bismuth, a Pt single crystal electrode (after it was flame annealed and characterised by CV), was immersed in a bismuth nitrate solution (10^{-5} M) for a net length of time needed to obtain the desired coverage. The electrode was then rinsed with Milli-Q water to remove excess nitrate ions and then re-introduced to the electrochemical cell for further characterisation. Repeated immersions in the bismuth nitrate solution followed by rinsing would increase the coverage of the bismuth adlayer. The bismuth adlayer could then be removed by flame annealing the electrode and cooling in hydrogen in order to recover the platinum voltammetric features.

3.4 Preparation of the Rotating Disc Electrode (RDE) for the Oxygen Reduction Reaction (ORR) on Nafion® Coated and Nafion Free Pt{*hkl*}

All RDE experiments were performed on a Rotating Disc Electrode RDE-2 purchased from BASi Analytical. ORR experiments were performed in aqueous 0.1 M $HClO_4$ electrolyte. A specially crafted electrochemical cell for RDE studies was manufactured at Cardiff for these studies (figure 3.2). The cell, along with the Luggin capillary and all Teflon parts were soaked in green acid and steam cleaned as described previously for the CV electrochemical cell. It was imperative that all components were thoroughly cleaned as traces of sulphate anions would show in perchloric acid solutions, due to sulphate anions being more strongly adsorbing than perchlorate anions.

Once all components were cleaned, the cell was configured as shown in fig 3.2 and filled with electrolyte. Oxygen gas was bubbled into the solution for 20 minutes via the gas inlet at a constant bubble rate (2-3 bubbles a second). An overpressure was maintained by altering the height of the gas inlet to be just above the electrolyte solution and then increasing the flow of oxygen. The flow rate was increased to a level sufficient to provide a positive pressure but ensuring the surface of the solution was not disturbed.

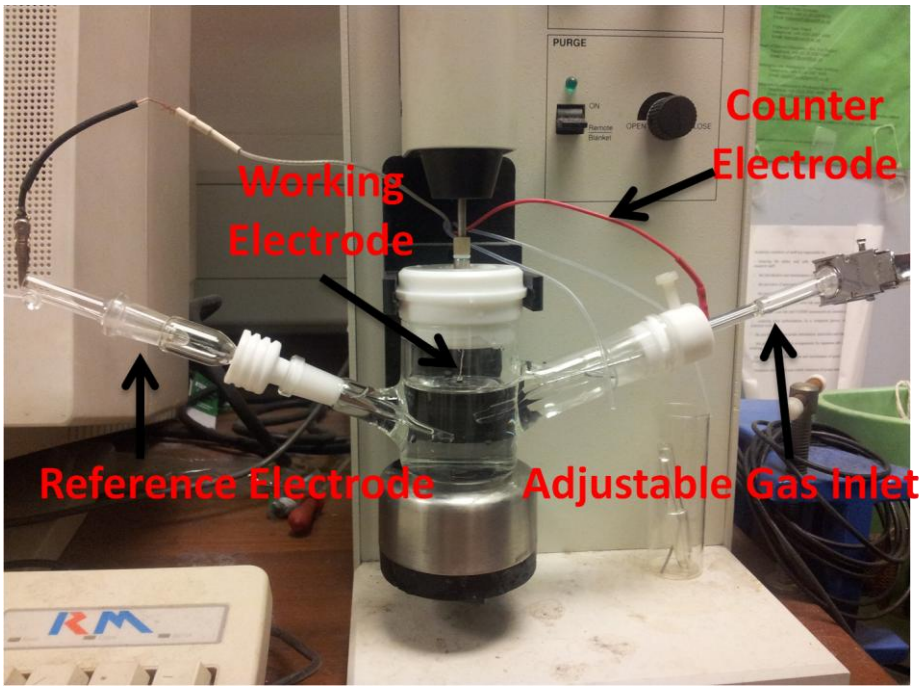

Fig 3.2 Picture of RDE electrochemical cell used for ORR measurements.

The palladium hydride reference was prepared as previously described in section 3.1.1. The reference electrode was not kept in direct contact with solution, it was in fact located in a separate Luggin capillary that was filled with 0.1 M $HClO_4$ and introduced to the cell as shown in figure 3.2. Care was taken in order to ensure that no air bubbles were present in the Luggin. The counter electrode was securely located in a round hole in the Teflon holder holding the adjustable glass gas inlet tube.

The orientation of the working electrode was adjusted such that the bead of the single crystal was centred with respect to the rotating shaft. The electrode was kept wet whilst the electrode was being orientated in order to keep it contaminant free. The electrode was then reintroduced to the cell via a meniscus contact with the electrolyte and electrical connections to the potentiostat were made. The initial start potential was set at -0.04 V (*vs* Pd/H) and the final potential was set to 1.0 V (*vs* Pd/H*).* It was found that the height of the meniscus greatly influenced the limiting current[8,9] whilst the crystal is rotating. Therefore, prior to actual measurements being recorded, for ORR experiments, at 1600 rpm the height of the meniscus was adjusted such the limiting current read between 5.6 $x10^{-3}$ - 6 $x10^{-3}$ A cm^{-2}, the expected current density[10] for O_2 saturated $HClO_4$ at 1600 rpm. Once the scan had been completed at 1600 rpm, the rotation speed was adjusted to 1250 rpm, 1000 rpm, 750 rpm, 500 rpm and 250

rpm. All data recorded was analysed using mathematical based software such as Microsoft Excel, Origin Lab and MatLab to produce Koutecky Levich and Tafel plots.

3.5 Water purification system

The Millipore Milli-Q Plus water system (Millipore, Watford, Hertfordshire) supplied research grade ultra-pure water at a rate of 1.5 litres per minute [[11]]. Laboratory mains water was initially passed through 5 μm filter (Water Filtration Ltd., Cardiff) before flowing into the Milli-RO 10 Plus purification system. This contained an activated charcoal pre-filtration unit to remove chloride and organic compounds. The water then passed through a semi-permeable reverse osmosis membrane before being stored in a sixty litre reservoir. This was an automated process that ran when the volume in the reservoir dropped below a certain level. Note that at all times the reservoir was kept in dark conditions to prevent growth of photosynthetic bacteria.

To obtain Milli-Q water, the Milli-Q system was set to 'operate' and switched on. Water from the reservoir was pumped into the Milli-Q system where it passed through a mixed bed of purification media and achieved a resistivity of 18.2 MΩ cm. The Milli-Q system is switched to 'production' where the water passed through a 0.22 μm final filter and out of the delivery nozzle.

3.6 Chemical reagents used in this study

Chemical Reagents			
Chemical	**Formula**	**Grade**	**Supplier**
Perchloric Acid	$HClO_4$	Aristar	VWR
Sulphuric Acid	H_2SO_4	Aristar	VWR
Sulphuric Acid	H_2SO_4	Reagent	Fischer Scientific
Potassium Permanganate	$KMnO_4$	Reagent	BDH, Poole
Nafion	$C_7HF_{13}O_5S$. C_2F_4	5% 1100EW	Johnson Matthey
Formic Acid	HCOOH	Aristar	VWR
Methanol	CH_3OH	HPLC	Fischer Scientific
Palladium Nitrate Hydrate	$Pd(NO_3)_2.H_2O$	41.54%	Johnson Matthey
Bismuth Nitrate Pentahydrate	$Bi(NO_3)_3).5H_2O$	98%	Sigma Aldrich
Platinum Wire (for single crystal manufacture)	Pt	99.999%	Goodfellows & Johnson Matthey
Platinum Wire (2 mm diameter)	Pt	99.995%	Goodfellows & Johnson Matthey
Palladium Wire (for reference electrode)	Pd	99.99%	Advent Research Materials Ltd, Eynsham, Oxon.UK
Nitrogen Gas	N_2	Pureshield	BOC

Hydrogen Gas	H_2	High Purity 99.995%	BOC
Oxygen Gas	O_2	High Purity N6.0	BOC
60% HSA Platinum Catalysts	Pt	60% Pt	Johnson Matthey

Table 2 List of Chemical Reagents Used for Experiments

3.6 References

(1) Clavilier, J.; Faure, R.; Guinet, G.; Durand, R. *Journal of Electroanalytical Chemistry* **1980**, *107*, 205.

(2) Hazzazi; Abdullah, O. Electrochemical Studies of Metal Deposition and Surface Chirality at Well-Defined Platinum Single Crystal Electrodes, 2002.

(3) Clavilier, J.; Durand, R.; Guinet, G.; Faure, R. *Journal of Electroanalytical Chemistry* **1981**, *127*, 281.

(4) Solla-Gullon, J.; Rodriguez, P.; Herrero, E.; Aldaz, A.; Feliu, J. M. *Physical Chemistry Chemical Physics* **2008**, *10*, 1359.

(5) Rodriguez, P.; Herrero, E.; Solla-Gullon, J.; Vidal-Iglesias, F. J.; Aldaz, A.; Feliu, J. M. *Electrochimica Acta* **2005**, *50*, 4308.

(6) Vidal-Iglesias, F. J.; Al-Akl, A.; Watson, D. J.; Attard, G. A. *Electrochemistry Communications* **2006**, *8*, 1147.

(7) Schmidt, T. J.; Stamenkovic, V.; Attard, G. A.; Markovic, N. M.; Ross, P. N. *Langmuir* **2001**, *17*, 7613.

(8) Villullas, H. M.; Teijelo, M. L. *Journal of Electroanalytical Chemistry* **1995**, *385*, 39.

(9) Villullas, H. M.; Teijelo, M. L. *Journal of Electroanalytical Chemistry* **1995**, *384*, 25.

(10) Kuzume, A.; Herrero, E.; Feliu, J. M. *Journal of Electroanalytical Chemistry* **2007**, *599*, 333.

(11) Millipore General Catalogue; Millipore U.K. Ltd: Watford, Hertfordshire.

Chapter 4

Unprecedented Structural Sensitivity toward Average Terrace Width and ORR activity:

Nafion Adsorption at Pt*{hkl}* Electrodes

4.1 Introduction

At the heart of the functioning membrane electrode assembly (MEA) of a fuel cell is a complex three-phase interface in which ionic and electronic charge transfer is taking place.[1,2] Together with transport of reactants and products into and out of this multi interfacial region, there are also electrocatalytic reactions occurring within the electrical double layer of the electrocatalyst. Facilitating optimal operation of these electrocatalytic and mass transport processes represents at once both a fundamental challenge to present experimental capabilities and also an economic obstacle to the development of superior fuel cell designs[1-8]. Combinations of spectroscopic[9-20] and theoretical approaches[18,21-25] have generated a variety of models to describe the structure of Nafion at the Nafion-electrode interface. In particular, Schmidt-Rohr and Chen[26] have used neutron scattering among other techniques to establish that self-assembly of Nafion leads to the formation of both hydrophobic and hydrophilic polymeric regions. The hydrophilic regions are reported to consist of hydrophilic channels (containing exclusively sulphonate substituents of the polymer) which vary from 2 - 10 nm in diameter and are thought to facilitate proton transfer perpendicular to the electrode surface from one electrode of the fuel cell to the other. The channel properties are strongly dependent on the overall water content of the Nafion polymeric film.

In two recent papers, Markovic and co-workers[27,28] presented, for the first time, single crystal electrode data pertaining to the adsorption of Nafion on platinum. In this work, these authors addressed directly questions concerning possible site blocking by Nafion and the nature of the bonding between sulphonate groups of the Nafion and the electrode surface as a function of potential. In addition, perturbations by Nafion of the electrosorption properties of Pt{hkl} in the H_{UPD} and oxide regions were investigated. Feliu et al. have also investigated the problem of the Nafion - electrode - electrolyte interface at a Pt{111} electrode using in situ FTIR and electrochemical approaches[29]. Here, the changes in environment induced by potential at sulphonate groups and water contained within the proton conducting membrane

as a function of potential was emphasized. In an extension to these pioneering studies on single crystal electrodes by Markovic *et al.* and Feliu *et al.*, for this study data is presented pertaining to the behaviour of Nafion at stepped platinum electrodes. The earlier findings for Nafion adsorbed on Pt{111}, Pt{110}, and Pt{100} in perchloric acid electrolytes[27] are confirmed and, furthermore, the potential at which the Nafion CV peak is observed on the negative going potential sweep to is ascribed to protonation/deprotonation processes close to the potential of zero total charge (PZTC) of the platinum/Nafion/electrolyte interphase. In addition, the unusual and unprecedented electrochemical activity of Nafion in the vicinity of monatomic high steps is highlighted. Finally, the oxygen reduction reaction (ORR) is reported using Pt{hkl} and Nafion/ Pt{hkl} electrodes in a rotating disc electrode (RDE) configuration.

4.2 Results

4.2.1 Voltammetric studies: Nafion - free Pt{hkl} Basal Plane Electrodes

CVs of Nafion-free and Nafion-covered basal plane Pt{hkl} single crystal electrodes in 0.1 M $HClO_4$ are shown in Figure 1. For all three surfaces, the CV profile recorded is in accordance with previous reports of well-ordered and clean Pt{hkl} electrodes in aqueous perchloric acid[30,31]. Broadly speaking, two potential regions may be delineated from the data ascribable either to adsorbed oxygen fragments derived from water dissociation (OH_{ad}) at positive potentials or hydrogen underpotential deposition (H_{UPD}) adsorption states associated with chemisorbed hydrogen at more negative potentials. It is interesting to note that only Pt{111} gives rise to a clear separation of both of these electrosorption processes as a function of potential[32-35] as epitomised here by the electrosorption features in the range 0 and 0.4 V (H_{UPD}) and between 0.6 and 0.8 V (OH_{ad}).

For Pt{100} and Pt{110}, evidence is growing that some overlap between the potential regions of OH_{ad} and H_{UPD} electrosorption may occur[36-38]. It is well-known that strongly adsorbed anions may displace OHad,[34,39,40] and so an interesting question to be addressed in the present study is whether or not sulphonate groups of Nafion (which should interact more strongly with platinum than either perchlorate anions or OH_{ad}) may be used to probe the regions of the CV ascribable to "adsorbed OH". The true nature of the OH_{ad} species in terms of whether or not it corresponds to a covalently bonded Pt-OH species or an electrostatically adsorbed OH^- anion remains unknown at the present time. Therefore, we adopt the generic

term "OH_{ad}" to describe such an entity. For specifically adsorbed anions such as bisulphate or sulphonate, the electrosorption peak seen with these electrolytes in the "H_{UPD}" region of the CV is speculated to arise from deprotonation of the anion leaving behind the specifically adsorbed sulphonate and sulphate anion, respectively[27,41].

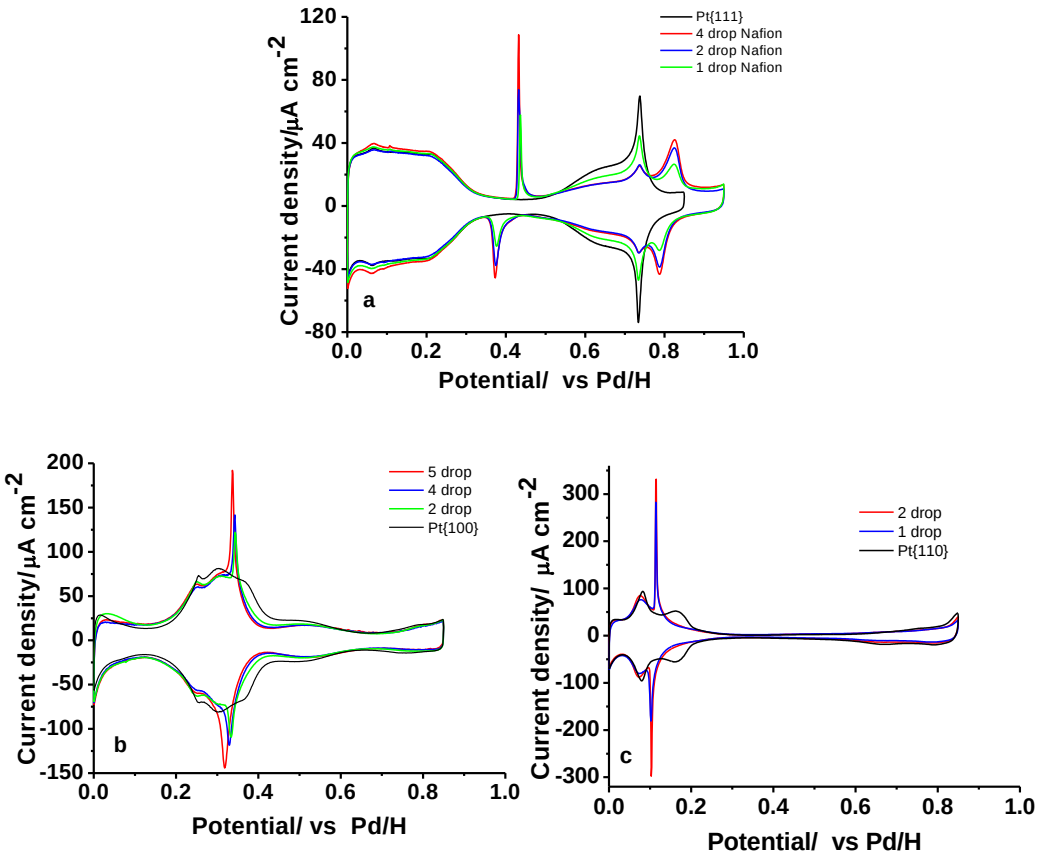

Fig 4.1 Nafion adsorption on a) Pt{111}, b) Pt{100} and c) Pt{110} in 0.1M $HClO_4$. Sweep rate = 50 mV/s.

4.2.2 Nafion-Covered Basal Plane Electrodes

Inspection of the CVs presented in Figure 4.1 of the Nafion-covered basal plane electrodes reveals several significant changes when compared to the Nafion-free surfaces, most probably associated with the displacement of adsorbed OH_{ad} by sulphonate groups of the Nafion. In Figure 4.1a, large "spike peaks'' are observed, reminiscent of when a phase transition is occurring in the double layer region[42-44]. However, we shall see later that the magnitude of these Nafion-induced features seems also to mimic the magnitude of the step

and terrace electrosorption peaks seen in aqueous sulphuric acid for Pt{hkl} electrodes[45-49], albeit with a much reduced peak width. That is, the peaks are consistent with the simultaneous adsorption and desorption of H_{UPD} components and anions with strong attractive lateral interactions generating a narrowing in CV peak width. In the case of Pt{111}, the Nafion-induced spike peak occurs at similar potentials to that observed for the analogous process of sulphate/bisulphate adsorption in aqueous sulphuric acid. Using CO charge transient measurements, Markovic and co-workers attributed the "spike peaks'' to the adsorption/desorption of the terminating sulphonate group of Nafion[27]. These workers postulated a so-called "spring model" to account for this behaviour with the sulphonate groups being attracted to both cations in the polymer film and negative charge on the platinum electrode, the greater of these interactions determining the overall position of the sulphonate. It should be noted, at least for the negative-going potential sweep, the proximity of the potential of zero total charge of Pt{111} with the potential of the Nafion-induced peak (see later)[36,50-52]. It can also be seen from Figure 4.1a that by increasing the amount of Nafion deposited onto the surface the size of the sharp sulphonate-induced peak at 0.43 V increases and shifts negatively. Closer inspection of Figure 4.1a also indicates that the H_{UPD} region of the Nafion-covered surface is largely unaffected when compared to the Nafion-free surface. This provides a strong indication that sulphonate anion adsorption is precluded in this range of potential (as expected since it is negative of the potential of zero total charge (PZTC))[36] and also the surface remains uncontaminated. That is, in spite of Nafion being adsorbed, no chemisorption sites for the electrosorption of hydrogen appear blocked. This means that if attachment of Nafion to the platinum electrode is via Van der Waals forces associated with the fluorinated polymer backbone, then these are weak relative to the binding of electrosorbed hydrogen. If H_{UPD} charge does decrease after Nafion adsorption, this behaviour is ascribed to the adsorption of more strongly adsorbed, blocking contaminants derived from organic molecules present in the as received Nafion solution.

The Pt-OH_{ad} region (0.5 - 0.78 V) of the clean Pt{111} electrode is gradually attenuated as Nafion loading is increased. It is replaced by the growth of an OH_{ad} peak at slightly more positive potentials (0.81 V). The growth of the Nafion "spike" peak at 0.43 V and the new, induced oxide peak is correlated, indicating that they are both dependent on the overall coverage of Nafion, in complete agreement with findings reported by Markovic et al[27]. In fact, there is a one-to-one correspondence between the diminution of clean surface Pt{111} OH_{ad} species and growth of the Nafion-induced peak at 0.81 V. A tentative interpretation of

this effect would be the sulphonate substituent successfully competing with OH_{ad} for Pt sites. Hence, a nominal coverage of Nafion may be determined in terms of the decrease in area of the clean surface OH_{ad} peak. If this is the case, it means that in spite of adding Nafion about 25% of the Pt{111} surface always remained unaffected by Nafion adsorption and that, furthermore, the existence of the clean surface peak at 0.67 V would suggest that such areas correspond to quite extended Pt{111} terraces being present at the interface. This may indicate either a limitation to the degree of wetting of platinum by the Nafion film or that regions of Pt{111} are covered exclusively by hydrophobic portions of the Nafion film, free of sulphonate groups.

A final question that arises is why there is still a significant hysteresis in the potential separation of the Nafion peaks, a phenomenon observed even at sweep rates of 1 mV/s (not shown). This behaviour corresponds to what has previously been referred to by Feldsberg and Rubinstein as "unusual quasi-reversible" (UQR) behaviour or apparent non-kinetic hysteresis[53] (see also still earlier work by Everett et al. in this context[54-56]). In their analysis, the underlying explanation of both UQR and the change in peak width observed on the forward and reverse potential sweeps may be paraphrased from ref[53] as follows:

i. For an N-shaped free energy curve describing the transition between two phases, the probability of hysteretic behaviour (separation between voltammetric peaks) may be ascribed to the size of the surface domains. A uniform dispersion of small domains will give rise to a small peak-to-peak separation whereas a uniform dispersion of large domains will give rise to a greater peak to peak separation (ΔVpp). The value of ΔVpp itself corresponds to the difference in free energy between the maximum and minimum of the N-shaped free energy curve.
ii. The width of the peaks reflects the uniformity in size of the surface domains. For a well defined, uniform, domain size, a sharp transition peak is expected whereas a wide distribution of domain sizes results in broadening of the peak.

Based on this analysis, the large hysteresis in Nafion peaks seen in the CV of Pt{111} reflects the existence of large surface domains and the asymmetry/peak broadening observed on the negative-going potential scan relative to the positive-going sweep reflects relaxation of the domains into a wider range of presumably smaller Nafion surface domains after sulphonate is adsorbed at the platinum electrode. In this case, the multiple potential cycles (see chapter 3

section 3.2.2) used to prepare the most intense Nafion peaks must also correspond to an electrochemical "annealing" of the Nafion film itself. It should be noted that the CV response reported in Figure 4.1 is metastable and that the Nafion peaks shift to more positive potentials, broaden, and decrease in magnitude when the electrode is left at open circuit for short periods (5-10 min), illustrating a tendency for the Nafion film to relax back to a more heterogeneous form. Thus, it is predicted that in situ STM measurements of thin Nafion films on Pt{111} may reveal potential-dependent changes in ordered surface domains as a function of potential.

For Nafion-covered Pt{100} (Figure 4.1b), it is seen that there is again a sharp spike generated in the H_{UPD} region, the magnitude of which depends on Nafion loading. The potential of this sharp peak is close to the PZTC of Pt{100}[36,51], with increasing Nafion coverage, it increases in size and shifts slightly negative in potential. From this it is again deduced that such behaviour must be indicative of sulphonate adsorption[27]. In addition, the hysteresis in the potential of the spike peaks on the forward and reverse sweeps is much reduced as compared with Nafion adsorbed on Pt{111}. The Nafion-coated Pt{100} CV shows that as Nafion coverage increases, the charge under the OH region (0.4 V onward) is suppressed and that some of this charge is displaced into the Nafion spike peak. The H_{UPD} charge negative of the spike peak remains unchanged as found for Pt{111}, suggesting that the spike demarcates H_{UPD} (features negative of this potential) from OH_{ad} (CV features positive of the spike). Support for this contention is also gleaned from ref[36] whereby a thermodynamic analysis of the Pt{hkl} CVs as a function of temperature combined with CO charge transient displacement measurements leads to the inescapable conclusion that OH_{ad} species do indeed occur in this range of potential. Displacement of OH_{ad} by more strongly adsorbing anions is normal behaviour observed with "specifically adsorbing anions", such as sulphate, and is presumably occurring here due to the stronger interaction of the terminating sulphonate group of Nafion with the surface compared to perchlorate anions and OH_{ad} formed in the H_{UPD} region. Since the magnitude of the electrosorption charge between 0 and 0.35 V hardly changed when Nafion was added, we conclude that the polymer backbone does not block these electrosorption sites; i.e., the polymer is weakly and non - covalently bonded to the electrode surface.

A similar story emerges for Nafion-covered Pt{110} (Figure 4.1c). The CVs show a sharp, highly reversible spike developing in the H_{UPD} region at 0.1 V due to sulphonate adsorption close to the PZTC of Pt{110}[36,51]. Again, one sees that the magnitude of the spike increases

with Nafion coverage, but this time it does not shift negatively with potential and unlike for Pt{111} displays hardly any potential hysteresis between forward and reverse sweeps. The sharp, narrow, almost reversible peaks would correspond to phase transitions occurring in a uniform distribution of rather small Nafion surface domains. Electrosorption states negative of 0.1 V remain unperturbed by the addition of Nafion and therefore may be ascribed to H_{UPD}. Clean surface charge between 0.1 and 0.4 V is seen to be shifted negatively to form the sharp peak in the presence of Nafion. Hence, for the clean surface, we ascribe the charge at 0.1 V and above to OH_{ad} species that are displaced by adsorbed sulphonate groups of the Nafion. In this context, comparison should be made between the CV of Pt{110} in perchloric and sulphuric acids whereby a more intense, less broad H_{UPD} feature is obtained in the presence of the specifically adsorbed sulphate anion at 0.15 V, just as found here for Nafion although the lateral interactions between H_{UPD} and anion that control peak width appear to be very different[36,48]. Later in section 4.2.7, charge versus potential plots for a number of the surfaces reported here with and without adsorbed Nafion are provided in order to confirm the discussion highlighted here of a demarcation by the Nafion peak of positive and negative components to the total charge, at least for Pt{hkl} electrodes other than Pt{111}. The reasons for this discrepancy will be considered in section 4.2.7.

4.2.2.1 XPS of Nafion Coated Pt{111}

Finally XPS data (fig 4.2) is used to estimate the thickness and composition of a Nafion film deposited on Pt{111} and transferred from the electrochemical cell for *ex situ* evaluation. Nafion film thicknesses were deduced from measurements of Pt XPS peaks of both the Nafion-covered electrode surface and the (subsequently) sputtered clean sample. For the CV/XPS data depicted in Figure 4.2a, a film thickness of 3.3 nm was evaluated (figure 3 tables 1 - 2). Detailed analysis of relative peak intensities indicates that in addition to C 1s peaks arising from Nafion, a small amount of contamination was detected corresponding to C 1s emission at ~284 eV binding energy picked up during transfer to UHV. Since Nafion should only contain CF_x, C-O, and C-SO_3H carbon environments, when C 1s contributions at ~284 eV are discounted and elemental analysis is performed on the remaining C, O, S, and F XPS peaks, a nominal stoichiometry for the polymer monomer of $C_{20}F_{38}O_5S$ is obtained in satisfactory agreement ((+/-10% error) with the theoretical stoichiometry of $C_{21}F_{41}O_5S$ based on an idealized Nafion monomer of equivalent weight 1100.[34]

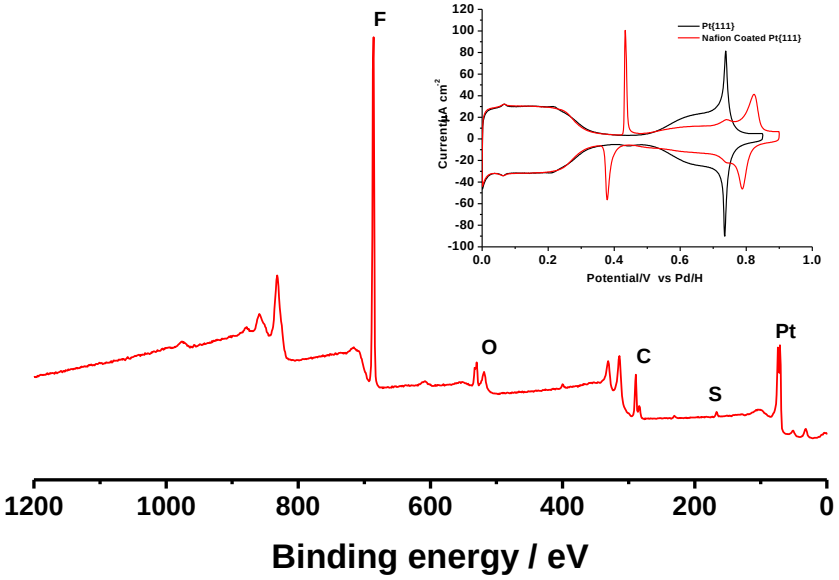

Fig 4.2a XPS and of Nafion film on Pt{111}.

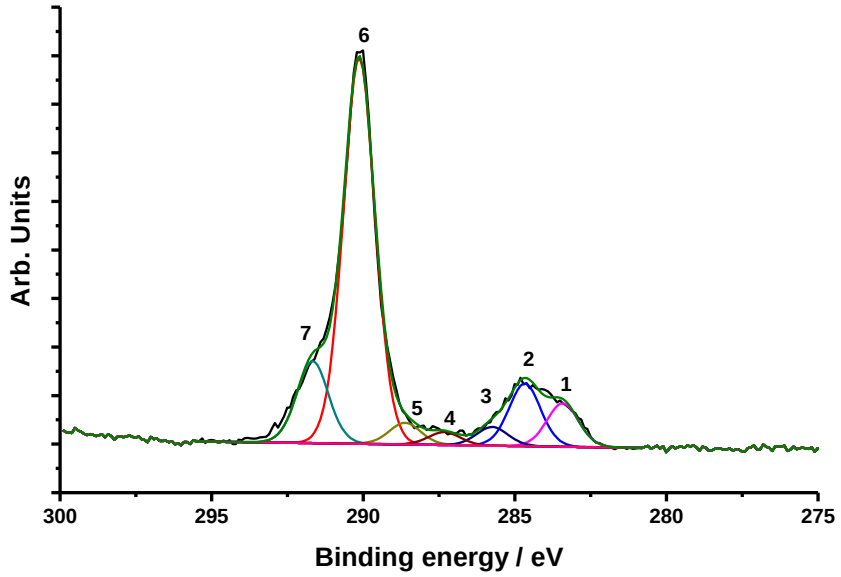

Figure 4.2b Peak fitting the carbon 1s region of the XPS signal of the Nafion film in figure 4.2a.

Peak number	Name	Position	% Concentration
1	C	283.4	6.93
2	C-C/C-H	284.8	9.98
3	C-S	285.7	3
4	(F)C-O-C(F)	287.3	2.06
5	CF	288.6	3.46
6	CF_2	290.1	61.48
7	CF_3	291.7	13.1

Table 1 curve fitting analysis for figure 4.2b.

Element	% Concentration with adventitious carbon	% Concentration without adventitious carbon
C	35.99	29.72
O	6.54	7.18
F	1.33	1.46
S	51.03	56.03
Pt	5.11	5.61

Table 2 XPS elemental analysis of Nafion film in figure 4.2a.

4.2.3 Nafion free platinum vicinal plane electrodes

The CVs in Figure 4.3a,b summarize the systematic changes in electrosorption behaviour upon travelling along the stereographic triangle from the {100} to the {111} pole. The different surface densities of step and terrace sites and their individual nature are readily observed by CV, and arrows are marked to indicate the trends. The turning point of the zone whereby step and terrace contributions are equally important (Pt{311}) is used in Figure 4.3a,b to delineate the changes on going from "{100}"-terraced surfaces to "{111}"-terraced surfaces. The nature of the step for all surfaces listed is that of a junction between a {111} and a {100} plane referred to henceforth as a {100}x{111} step (0.15-0.3 V). In Figure 4.3b, the OH_{ad} on {111} terrace contributions may be identified as corresponding to the peaks in the potential range 0.5 - 0.9 V and H_{UPD} on {111} terraces between 0 and 0.35 V. In Figure

4.3a, the boundary between H_{UPD} and OH_{ad} is less straightforward, but broadly, attenuation of peak intensity between 0.35 and 0.6 V corresponds to diminution in the average width of the {100} terrace sites. It is also seen that there is a corresponding decrease in the magnitude of the CV peak in Figure 4.3a between 0 and 0.15 V as terrace width increases, and so any intensity in this potential region may be ascribed to the "{111}" part of the "{100}x{111}" step. For a perfectly flat Pt{100} electrode, only CV features due to hydrogen evolution should be observed below 0.15 V[46]. One final note concerning the Pt{311} (= Pt 2{111}x{100}), Pt{211} (= Pt 3{111}x{100}), and Pt{511} (= Pt 3{100}x{111}) electrode surfaces is that the "step" electrosorption peak splits into two components: one component at 0.21 V and the other between 0.26 and 0.3 V. This behaviour is also reported for "{110}" steps[30,31] whereby a high surface density of "{110}" or {111}x{111} sites leads to step peak splitting in aqueous perchloric acid. Such surface sensitivity of H_{UPD} and OH_{ad} to terrace width becomes extremely important later in the context of Nafion adsorption, particularly in relation to the peak at 0.26 - 0.3 V.

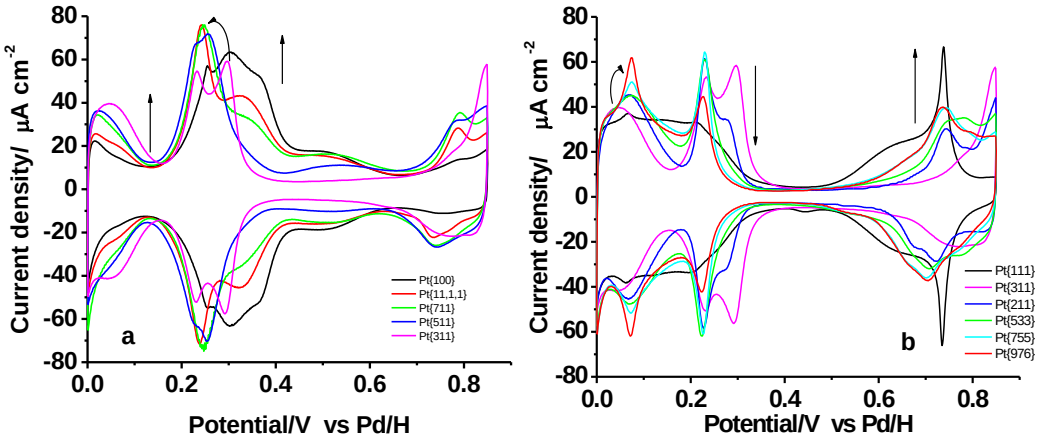

Fig 4.3 Nafion free vicinal platinum surfaces, where a) Pt n*{100}x{111}* and b) Pt n*{111}x{100}* surfaces in 0.1M $HClO_4$. Sweep rate = 50 mV/s.

4.2.4 Nafion coated platinum vicinal plane electrodes: Pt *n{100}x{111}* surfaces

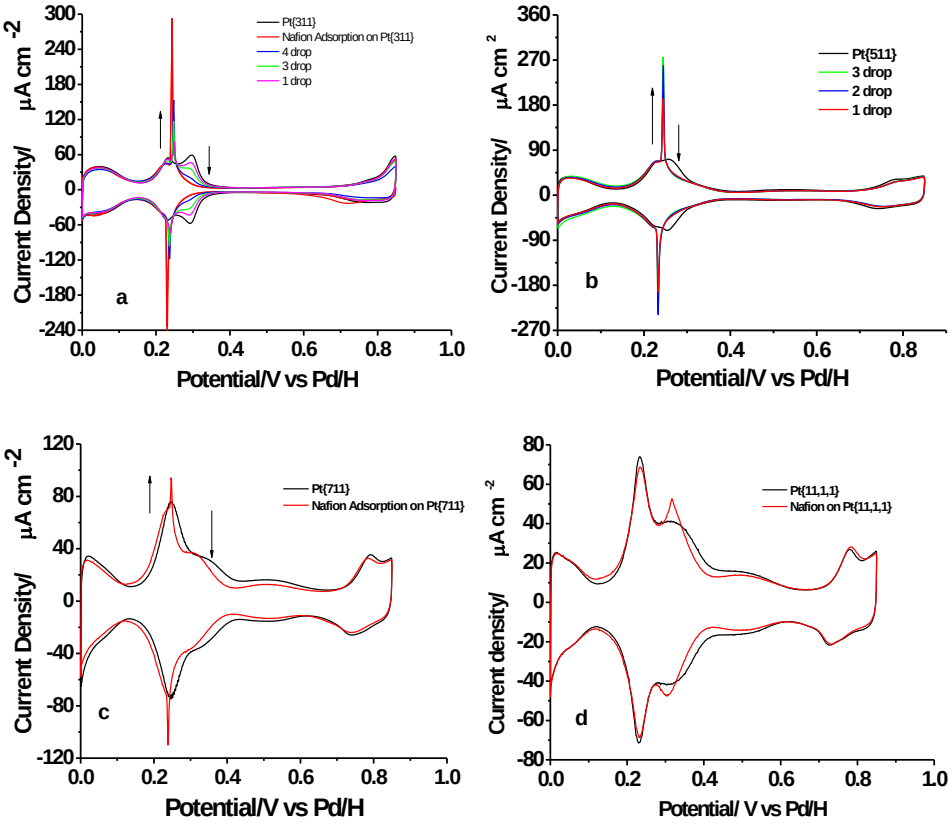

Fig 4.4 Nafion adsorption on Pt{100}x{111} surfaces, where a) Pt{311}, b) Pt{511}, c)Pt{711} and d) Pt{11,1,1} in 0.1M $HClO_4$. Sweep rate = 50 mV/s.

Figure 4.4 contains CVs of Nafion adsorbed onto Pt n{100}x{111} electrodes. Adsorption of Nafion on Pt{311} shows the formation of a large spike at 0.24 V which was attributed to sulphonate adsorption. The gradual diminution of the peak at 0.3 V (the more positive of the two step peaks) exclusively as a function of Nafion coverage and the correlated increase in the magnitude of the 0.24 V "spike" peak is reminiscent of the behaviour observed with the basal plane Pt surfaces. Hence, H_{UPD} charge at potentials negative of the Nafion peak remains unperturbed (including the step peak contribution negative of the 0.3 V peak). The 0.24 V Nafion peak reaches its maximum intensity as the last vestiges of the clean surface peak at 0.3 V are lost. Since this behaviour mimics precisely that of the basal plane electrode surfaces (even the potential of the spike peak being situated close to the PZTC of the surface),[30,51] it is concluded that the splitting of the clean surface step peak of Pt{311} in perchloric acid is due

to the adsorption of two components: H_{UPD} at the more negative potential which remains unperturbed by Nafion and OH_{ad} at 0.3 V.

Recent work confirms the unusual finding of stable oxygenated species at step sites at these negative potentials on platinum[38,57]. The sulphonate groups of the Nafion are capable of displacing these oxygenated species. This results in shifting of the charge associated with step OH_{ad} to the "spike" peak of Nafion corresponding to deprotonation of sulphonate groups and their subsequent specific adsorption close to the PZTC of the surface. If correct, the present model predicts that the clean surface step peaks (and basal planes also) that cannot generate splitting into both of these electrosorption components (H_{UPD} and OH_{ad}) will not generate sharp Nafion CV peaks; i.e., if no OH_{ad} is present to begin with, there will be no Nafion induced feature. This point will be emphasized in section 4.2.5 in relation to Pt{755} and Pt{976} (figure 4.5).

4.2.5 Nafion coated platinum vicinal plane electrodes: Pt n*{111}*x*{100}* surfaces

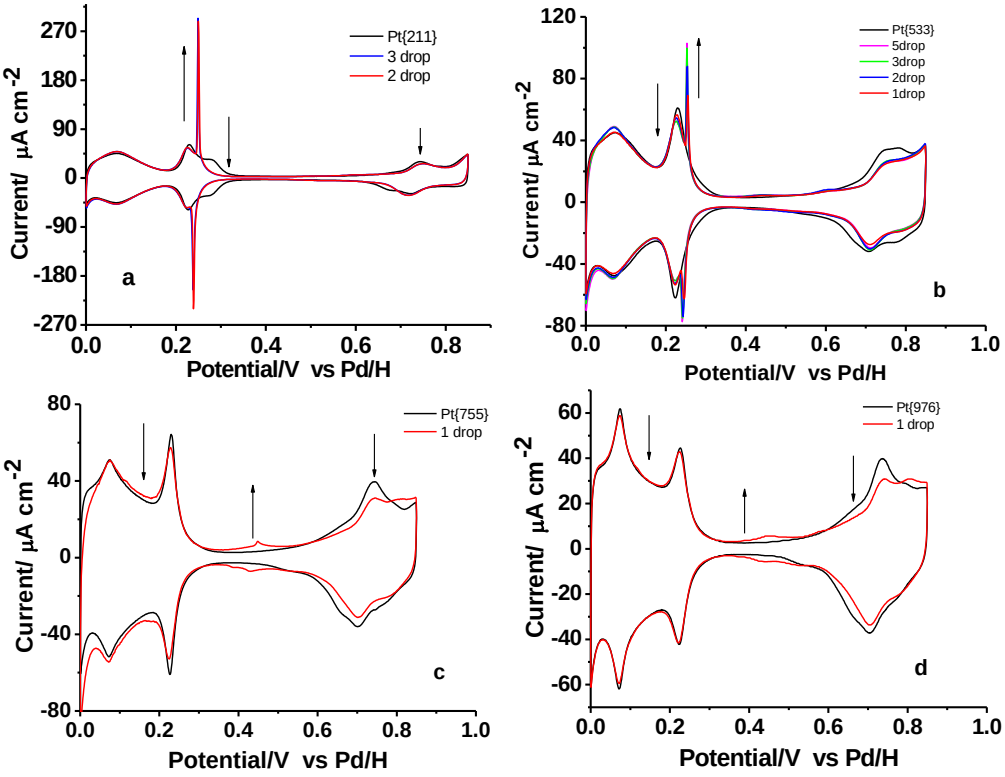

Fig 4.5 Nafion adsorption on Pt n*{111}*x*{100}* surfaces where a) Pt{211}, b) Pt{533}, c) Pt{755} and d) Pt{976} in 0.1M $HClO_4$. Sweep rate = 50 mV/s.

Figure 4.5 show CVs of Nafion adsorbed onto Pt n{111}x{100} surfaces. Inspection of the CVs depicted in Figure 4.5 support the conjecture postulated in section 4.2.4, i.e. if the clean surface step peaks and also the basal planes, cannot generate the splitting of water into electrosorption components H_{UPD} and OH_{ad}, no Nafion feature will be present in the CV. For example, Pt{211} (figure 4.5a) and Pt{511} (figure 4.4b) are each seen to support splitting of the CV step peak in 0.1M aqueous perchloric acid. If one now considers the CVs of the 4 atom wide terrace surfaces (Pt{711} (Figure 4.4c) and Pt{533} (Figure 4.5b)), it is evident that the Nafion free surface CVs only show minimal splitting of the step peak due to the low intensity of the component lying at more positive potentials. This would suggest that only a small Nafion-induced peak should be observed, and this indeed is found to be the case. For electrodes with an average terrace width of 5 atoms or more, no Nafion-induced step peaks are observed, nor any CV components at 0.29 - 0.30 V in the clean surfaces. Hence, for terrace widths >5 atoms, no OH_{ad} should be formed at the step, and so no Nafion spike peak will be observed. Why OH_{ad} should only form at steps which are spaced relatively close together is unknown but may be due to through-metal electronic perturbations (step wave function overlap) generating more oxyphilic sites in the process. For well-separated steps, such through-metal interactions would appear to be very weak. For Pt{976} (Figure 4.5d), a kinked Pt surface, no step Nafion peak is observed, as expected since the average step spacing is 6 atoms. Rather, a broad peak in the double-layer region at 0.45 V is seen when Nafion is adsorbed, corresponding to displacement of the OH_{ad} species by sulphonate groups on {111} terrace sites. The same feature is obtained using Pt{755} which also possesses an average step separation of 6 atoms.

Data for Pt{332} (not shown) which may be written in microfacet notation as Pt 6{111}x{111} or Pt 5{111}x{110} also gives rise to the same feature at 0.45 V when Nafion is deposited. However, in agreement with the present model, the step peak for the clean surface CV of Pt{332} in perchloric acid does not split into a H_{UPD} and OH_{ad} component[30,31] so a step Nafion peak is not expected to be observed. In fact, there is some discussion in the literature as to whether or not Nafion does perturb the H_{UPD} response of supported electrocatalysts compared to Nafion-free substrates in perchloric acid[58]. From the present study, it is predicted that only those Pt electrocatalysts that possess the appropriate morphological features (significant {111}, {100}, or {110} terrace order and linear steps of the appropriate spacing) will give rise to substantial voltammetric differences in perchloric acid with and without Nafion. For Pt{533} the {111} terrace feature is observable at 0.45 V

but is very weak (because the average terrace width is only 4 atoms wide). Hence, sulphonate groups adsorb at the steps of this surface at 0.24 V and then adsorb at the terraces at somewhat more positive potentials. It would be interesting to examine this phenomenon by in situ STM in order to investigate if different parts of the polymer interacting with the surface at different potentials change the overall morphology of the film as a function of potential. One final observation to be considered from Figure 4.5 is the limited suppression of electrosorbed oxide formed at 0.8 V when Nafion is adsorbed. This is consistent with specific anion adsorption inhibiting this process depending on anion adsorption strength[59].

To summarize, the adsorption of Nafion on stepped, Pt single crystal electrode surfaces displays unprecedented sensitivity to the average separation of step sites. It is proposed that this sensitivity is due to the ability of steps that are not well separated to generate oxyphilic sites capable of splitting water into protons and an "OH_{ad}" species. Irrespective of its true nature, sulphonate groups of Nafion are capable of competing successfully with water dissociation processes at, or positive of, the PZTC of the adsorption site necessary to generate sulphonate anion-Pt surface interactions. It is these interactions and the deprotonation of the sulphonate group that may be ascribed to the sharp, Nafion-induced peaks. The conclusion that one must draw therefore is that Nafion is an electrochemical probe of adsorbed OH_{ad} in that it acts just like a specifically adsorbed anion. If a Nafion-induced feature appears in the CV, it reflects the stronger interaction of the sulphonate with Pt compared to OH_{ad} in aqueous perchloric acid. This conclusion has important implications for electrocatalysis at Pt and other metals since measurements in aqueous perchloric acid may not map directly onto Nafion-coated "real" electrocatalysts. Intriguingly, direct extrapolation of electrocatalytic measurements in aqueous sulphuric acid to Nafion-coated surfaces may not be straightforward either since, from Figure 4.5, Pt{755} and Pt{976} H_{UPD} {100}x{111} step peaks at 0.2 V do not appear to show any perturbation from the CV collected in aqueous perchloric acid. Normally, for a more strongly adsorbed anion such as sulphate, a narrowing in the step peak and an increase in intensity would be expected. Hence, in this case, sulphonate anions from Nafion do not appear to be causing such an effect. It is deduced from this that in terms of Pt-anion interaction either sulphonate is a somewhat more weakly interacting anion than sulphate or the surface density of sulphonate groups is low relative to sulphate anions from aqueous sulphuric acid.

4.2.6 Charge vs Potential Curves for Nafion adsorption on Pt{111}, Pt{100}, Pt{110} and Pt{311}

For all Pt{hkl} electrodes, although a good correlation is found between Nafion peak potential and the PZTC of the clean surface (and indeed also with the potential of maximum entropy (PME)[30,60] which is very similar to the PZTC for all stepped and terrace surfaces) for Pt{111}, the Nafion-induced peak lies at a significantly more positive potential (figure 6).

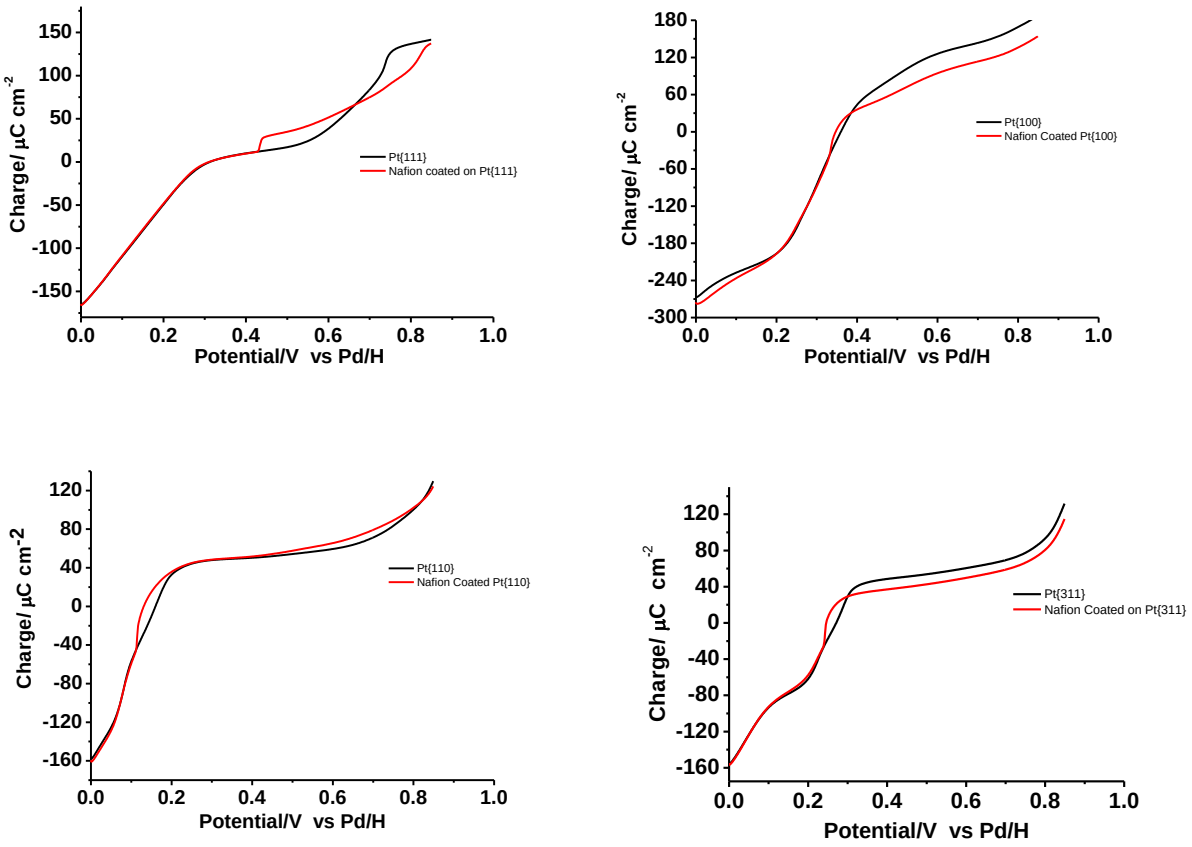

Figure 4.6 Charge *vs* potential curves for Nafion free (black) and Nafion covered low Miller index planes of platinum and Pt{311} in 0.1M $HClO_4$.. The PZTC values are taken from references[36,46,51,60].

A question therefore arises as to why Pt{111} is an exception to the general correlation found between the potential of the Nafion "spike" and the PZTC of the Nafion-free electrode surface in aqueous perchloric acid? The simple answer would be that the PZTC of a Nafion-coated Pt{111} electrode in aqueous perchloric acid exhibits a PZTC at more positive potentials than the unmodified surface. Some evidence for this hypothesis may be gained from reference[27] whereby CO charge transient measurements show a very small (but unfortunately not quite zero) transient at the potential of the Nafion spike on the negative

sweep. In fact, these measurements were used by these authors to deduce the anionic nature of the adsorbing species. This would suggest a shift in the PZTC to more positive values by about 70 mV. Of course, confirmation of this hypothesis awaits a full and more detailed series of CO transient experiments on well-defined Nafion/Pt{111}. One may only speculate upon the reasons as to the mechanism of the positive shift at the moment. For example, there is some precedent for adsorbed species on Pt{111} causing break-up the long-range order of the water layer immediately adjacent to the electrode surface which might induce such a change[60]. Inspection of charge density *vs* potential curves in Figure 4.6 for Pt{hkl}reveals also a small negative shift (10 to 20 mV) of the Nafion-induced spike relative to the PZTC of the Nafion-free surface. This would be consistent with a stronger interaction of sulphonate anions with the electrode surface compared with OH_{ad} (specific adsorption). It should also be noted that for platinum surfaces exhibiting narrow, six-atom-wide {111} terraces such as {332}, {755}, and {976} the broad, Nafion-induced peak at 0.45 V is quite reversible, this is consistent with a uniform array of small Nafion domains.

4.2.7 Oxygen Reduction Reaction (ORR) measurements on Nafion free and Nafion covered Pt{hkl} electrodes using RDE

Figure 4.7 contains the rotating disc electrode (RDE) polarisation curves for oxygen reduction on Pt{hkl} in 0.1 M perchloric acid saturated with di-oxygen at 1 atmosphere pressure. The adsorption of Nafion onto a Pt{111} single crystal electrode and the Nafion free surface is compared. Analysis of the Nafion free polarisation curves in the non-specifically adsorbing electrolyte 0.1 M $HClO_4$ at different rotation rates shows that the onset of oxygen reduction occurs at ~ 0.8 V. This is a rather large deactivation of the ORR considering that the equilibrium potential for ORR occurs at 1.23 V. The adsorption of Nafion is found to inhibit still further the ORR reaction. The polarisation curves for the Nafion coated surface at different rotation rates are shown to shift approximately 20 mV negative in potential compared to the clean surface. This is attributed to the specific adsorption of sulphonate ions blocking di-oxygen adsorption sites, previously shown by Markovic *et al*[28].

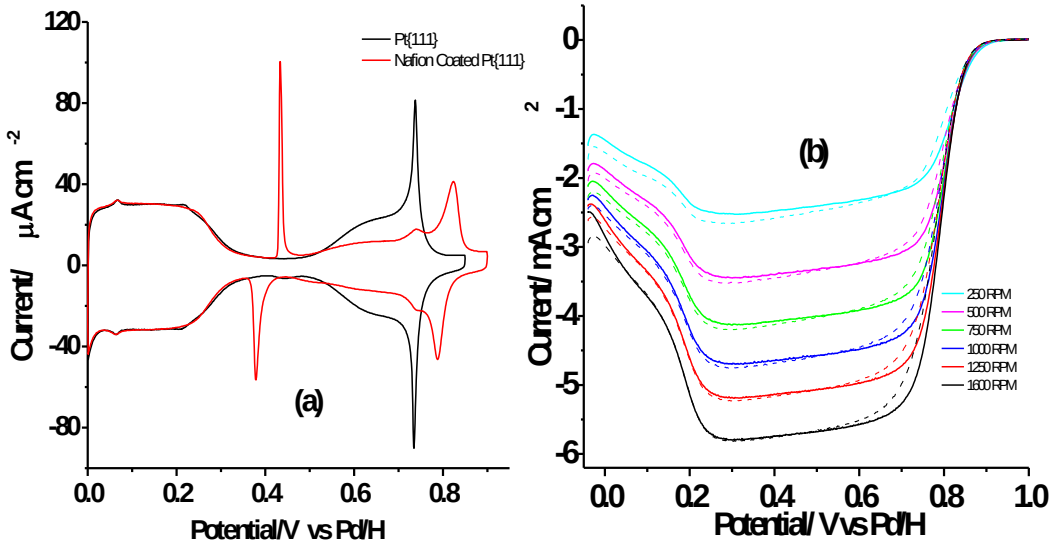

Figure 4.7 a) Nafion adsorption on Pt{111} in 0.1M $HClO_4$ and b) polarisation curves for Nafion free and Nafion coated Pt{111}. Sweep rate = 30 mV/s. The complete curves represent the Nafion free Pt{111} whilst the dashed curves represent the Nafion coated curves.

Levich and Tafel plots are shown in figures 4.8 and 4.9 corresponding to Nafion free and Nafion coated Pt{111}. The gradient of the line is equal to:

$$m = 0.62nFAD^{2/3}v^{-1/6}C_b\omega^{1/2} \qquad \text{(eq 4.1)}$$

All symbols have their usual meanings (see Chapter 2.3.2). The equation can therefore be rearranged to determine n (the number of electrons) involved in oxygen reduction overall. It was found that for the Nafion free surface and Nafion clean surfaces, the number of electrons transferred was approximately 4 (3.7 for Nafion free and 3.6 for the Nafion coated Pt{111} electrodes) corresponding to complete reduction of di-oxygen to water in the potential range investigated.

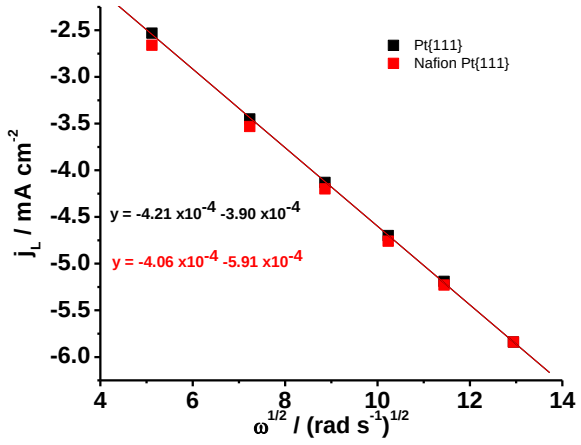

Fig 4.8 Levich plot for ORR measurements using Nafion free and Nafion coated Pt{111} electrodes in 0.1 M perchloric acid saturated with di-oxygen at 1 atmosphere pressure.

From the Tafel plots presented in figure 4.9, the number of electrons in the rate determining step and the exchange current density for the ORR reaction on Nafion free and Nafion coated Pt{111} can be obtained (see Chapter 2). However in order to study the kinetics of ORR, the kinetic current density in the absence of mass transport must be calculated[61]. A Tafel plot was therefore obtained by plotting ORR overpotential *vs* $\log_{10}(j_{trans})$, where j_{trans} is the current density in the absence of mass transport. Figure 4.9 shows the Tafel plots for the whole overpotential range studied. For ORR, Tafel plots should be obtained at "low" and "high" overpotential ranges where according to previous studies[62-65] the theoretical slope of the lines would equal 60 mV/dec for a 2 electron reduction in the "low" overpotential range (when electrosorbed oxide is also present) and 120 mV/dec (one electron transfer) in the "high" overpotential range (where electrosorbed oxide is absent).

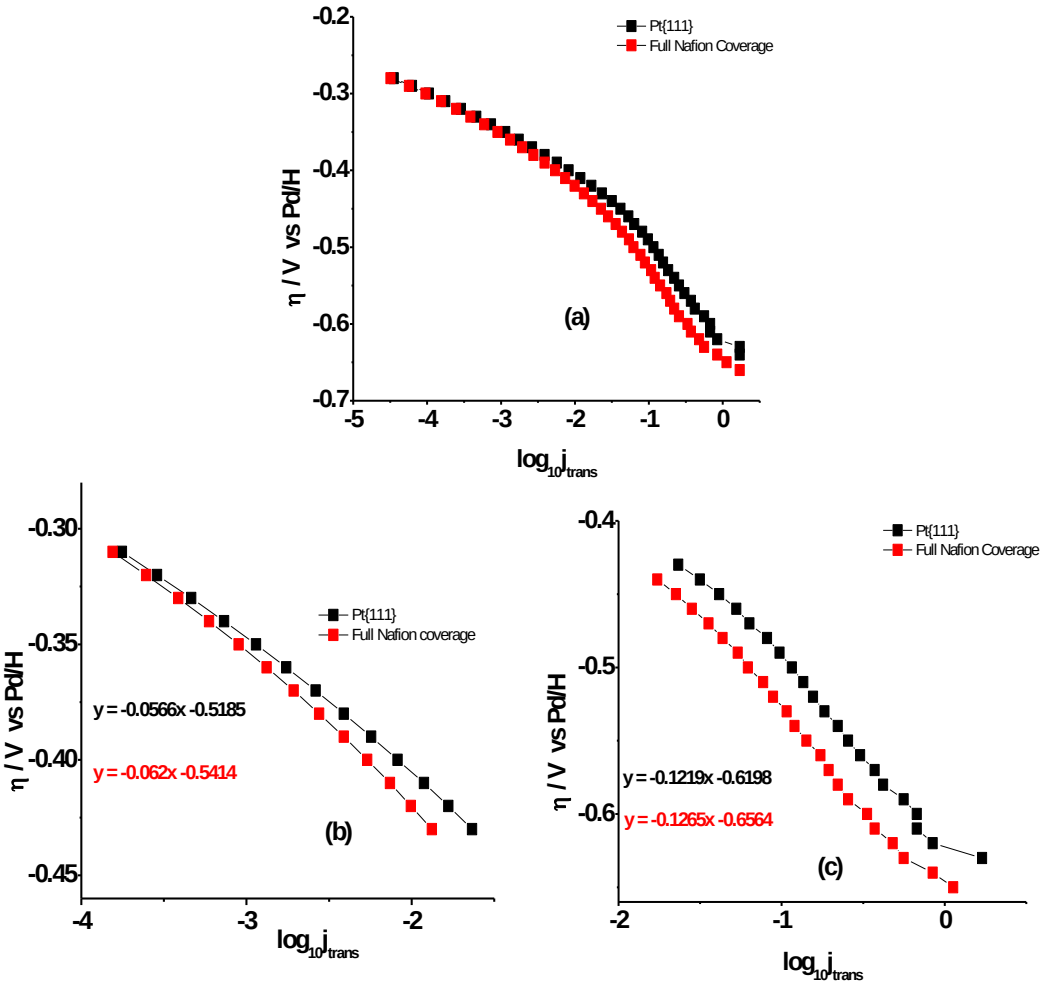

Fig 4.9 Tafel plots for ORR on Nafion free and Nafion coated Pt{111}, where a) full overpotential range, b) low overpotential range and c) high overpotential range.

At low overpotential, gradients of 56.6 mV/dec and 62 mV dec were obtained for the Nafion free and Nafion coated surfaces respectively. The number of electrons in the rate determining step (rds) and the exchange current density (j_0) were then determined from these gradients and the intercept respectively (see Chapter Two section 2.3.2 for background theory). At low overpotential, the number of electrons in the rate determining step for Nafion free Pt{111}and Nafion coated Pt{111} were 2.01 and 1.91 respectively. The corresponding values of j_0 for Nafion free and Nafion coated surfaces were found to be 6.85 $x10^{-10}$ A cm^{-2} and 6.58 $x10^{-10}$ A cm^{-2}. Therefore, little deviation from the clean surface behaviour was observed in this overpotential range when Nafion was adsorbed. For higher overpotential values, the gradients obtained were 121.9 mV/dec and 126.5 mV/dec for Nafion free and

Nafion coated surfaces respectively. Again, a small decrease in the activity of the Nafion covered Pt{111} surface compared to the clean surface is obtained but the essential rate limiting step mechanism (of a one electron transfer) appears not to change. Markovic and co-workers[66] have proposed a model where the adsorbed OH, in addition to site blocking, alters the adsorption energy of ORR intermediates, thus having a deleterious effect on ORR kinetics and this is why the Tafel slope (and ORR mechanism) changes dramatically at high overpotential values. Based on this assumption, this would explain why in H_2SO_4 solutions (in the absence of OH) only a *single* Tafel slope is observed[67]. Feliu and co-workers[68] found that the step density greatly affected the $E_{1/2}$ of the polarisation curve for ORR, in particular for the Pt n*{111}*x*{111}* series of surfaces. Hence, the ORR is a structure sensitive reaction on platinum electrodes. The best surfaces for ORR were found to be surfaces with an average terrace width of 3 atoms and ORR activity was found to decrease linearly as step density either increased or decreased past this point[77].

For ORR on Pt{111} at high overpotential, the number of electrons in the rds for both the Nafion free and Nafion coated electrodes was 0.97 and 0.93 respectively. Exchange current density values obtained for both surfaces were 8.23 $x10^{-6}$ A cm^{-2} (Nafion free Pt{111}) and 6.67 $x10^{-6}$ A cm^{-2} (Nafion coated Pt{111}). The value of j_0 obtained in this study for Pt{111} is of similar magnitude to the value reported by Adzic and co-workers[66]. The decrease in the exchange current density is indicative of the inhibition in the ORR of the Nafion coated Pt{111} compared to the Nafion free surface. This is proposed to be caused by the electrosorption of sulphonate group of Nafion blocking di-oxygen adsorption as speculated previously by Markovic et al[28].

ORR measurements were also performed on Pt{100}, Pt{976} and Pt{311}. Figure 4.10 contains the characteristic ORR RDE CV profiles of the three surfaces with and without Nafion coating. Figure 4.11 shows the corresponding Levich plots for the three surfaces coated in Nafion and free from Nafion. Analysis of the polarisation curves shows again, as with Pt{111} Nafion adsorption inhibits the ORR of Pt{hkl}. It can be seen from the Levich plots that for all three surfaces, a four electron transfer overall occurs.

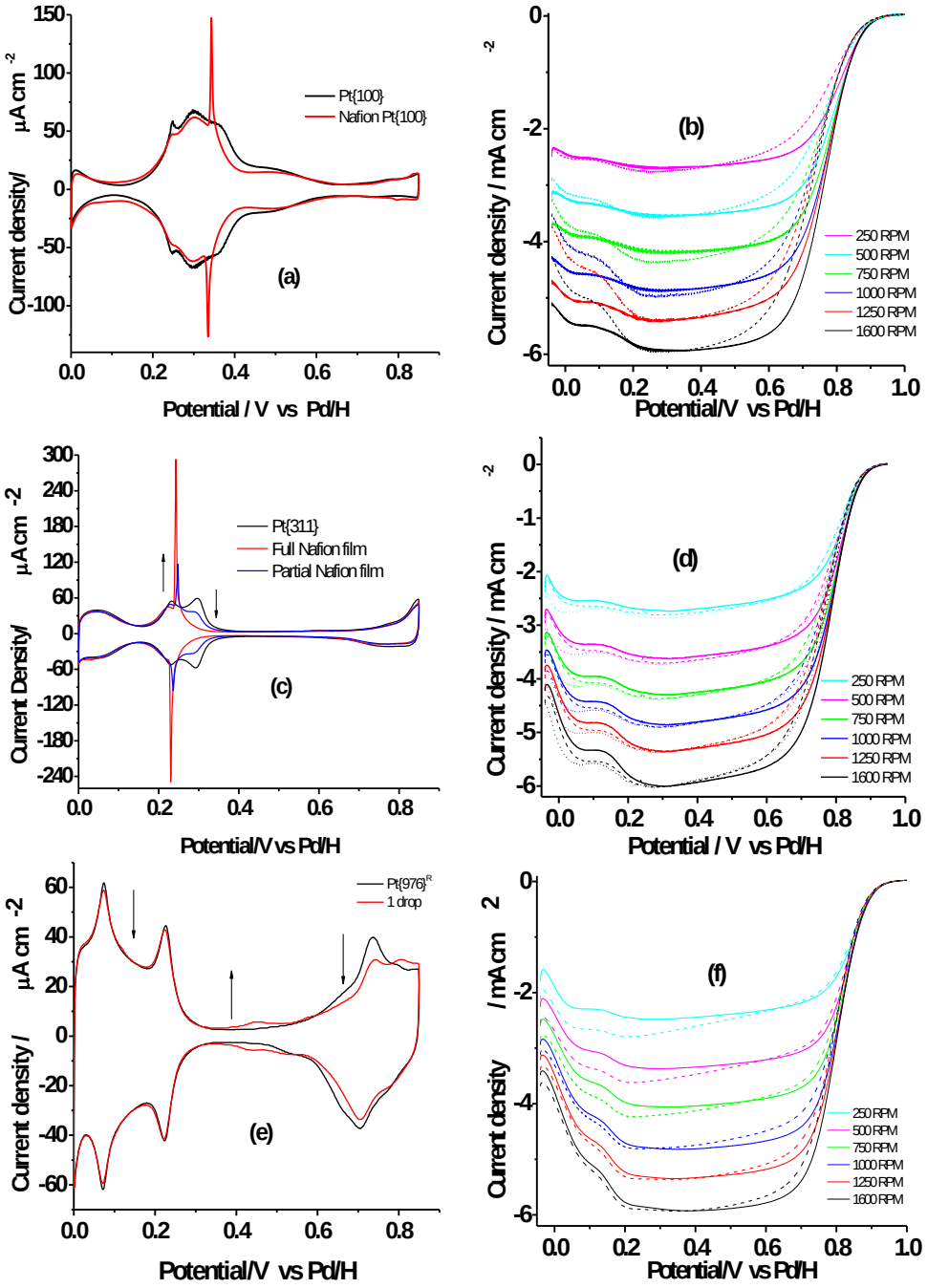

Fig 4.10 CVs and RDE polarisation curves for the ORR of various Nafion free and Nafion coated Pt{hkl} where a and b are for Pt{100}, c and d are for Pt{311} and e and f are for Pt{976} in 0.1M $HClO_4$. For the RDE polarisation curves, the continuous curves represent the Nafion free electrode surfaces whereas the dashed curves are for the Nafion coated electrode surfaces. Sweep rate = 30 mV/s.

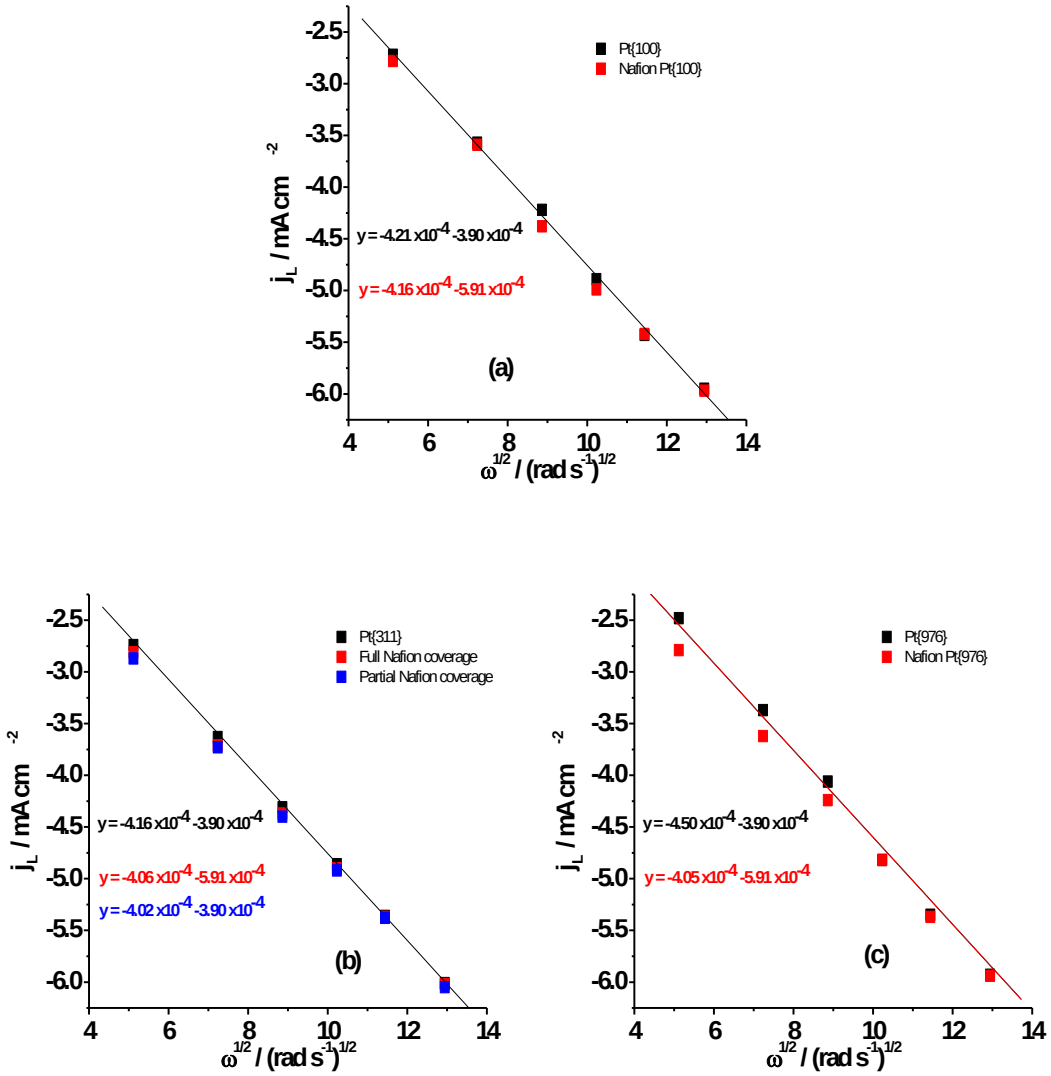

Figure 4.11 Levich plots for Nafion free and Nafion coated Pt single crystal electrodes where a) Pt{100}, b) Pt{311} and c) Pt{976} surfaces. All show that a four electron process occurs during ORR experiments.

Tafel plots were also obtained for all three surfaces (figures 4.12 - 4.14). In all cases it can be seen that two different gradients are obtained, one at "low" and one at "high" values of overpotential in accordance with previous investigations and data reported above. Below, in Tables 1 and 2, are listed the number of electrons involved in the rate determining step together with the exchange current density values at high and low overpotential values. It can be seen that Nafion adsorption causes the value of j_0 to decrease, again this is speculated to be due to sulphonate adsorption on the surface blocking access of dioxygen to active sites. At high overpotential values, it can be seen that the value of j_0 decreases as one changes the

surface from {111}to contain more{100} character. This is in agreement with Feliu and co-workers[68,77]. The same can also be said of the Tafel plots in the low overpotential range. The gradients obtained for all surfaces are of a similar magnitude and correspond to predicted values of the theoretical gradient (60 mV/dec) for a two electron transfer. However, j_0 and the number of electrons in the rate determining step decrease slightly as Nafion is adsorbed onto the surface. Nonetheless, the closeness of all values indicates no change in ORR mechanism when Nafion is adsorbed.

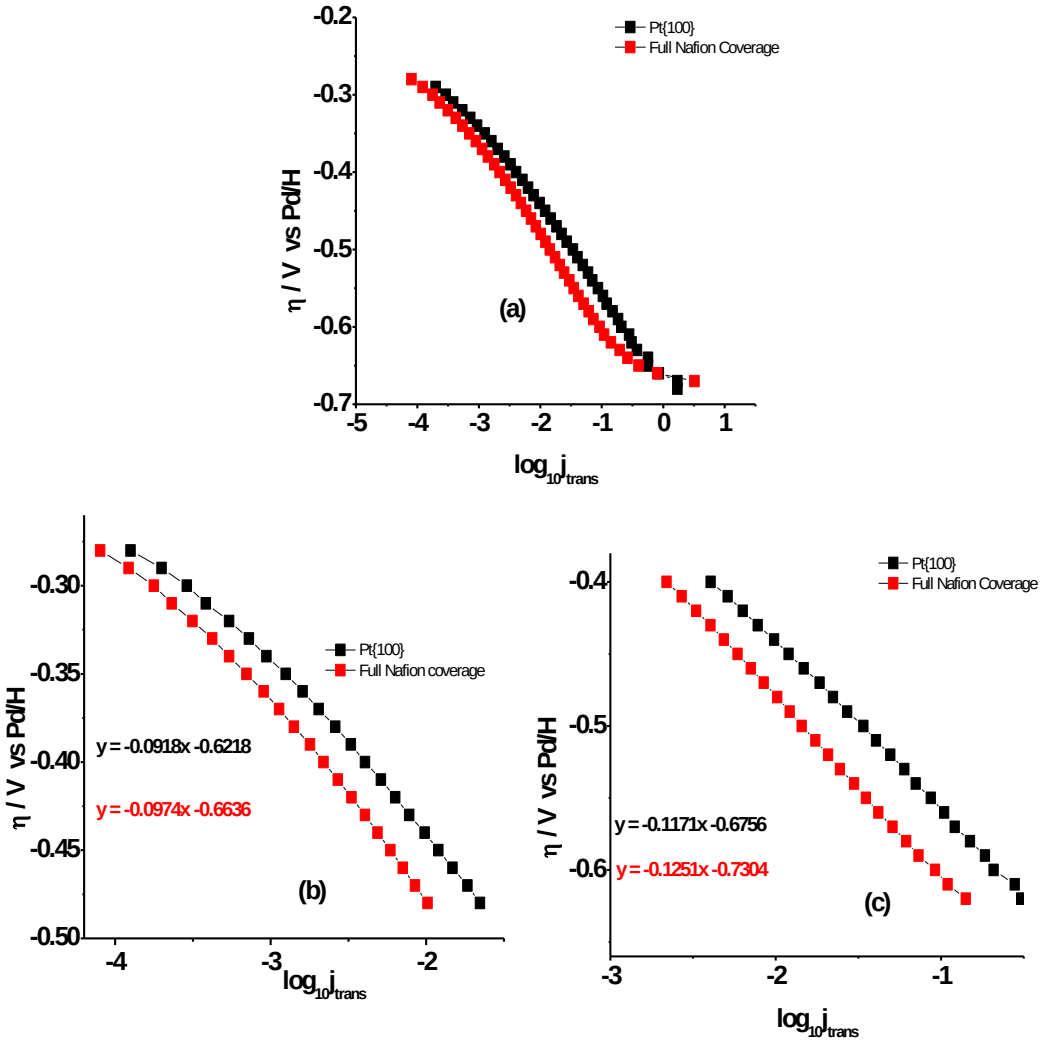

Fig 4.12 Tafel plot for Nafion free and Nafion coated Pt{100} where (a) is the full Tafel overpotential range, (b) is the low overpotential range and (c) is the high overpotential range.

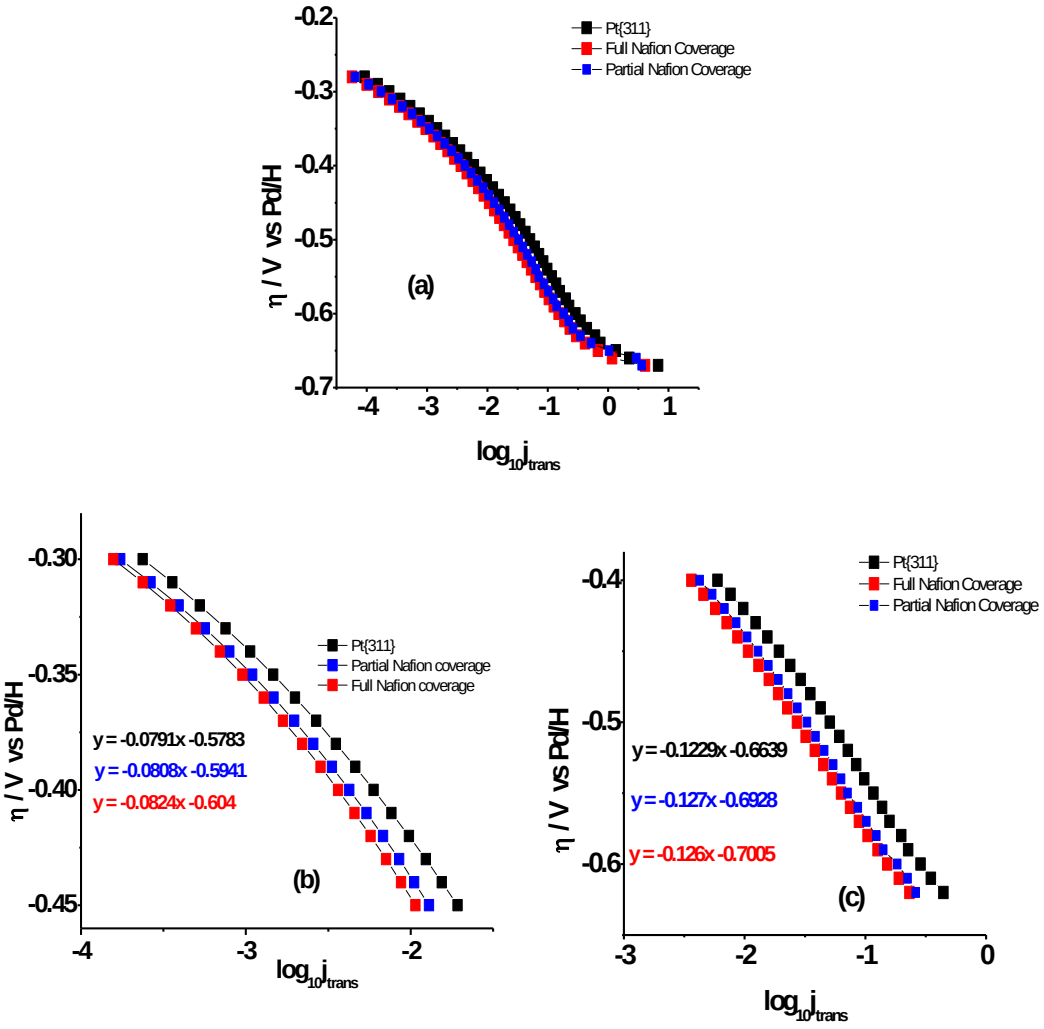

Fig 4.13 Tafel plots for Nafion free and Nafion coated Pt{311} where (a) is the full Tafel plot, (b) low overpotential range and (c) high overpotential range.

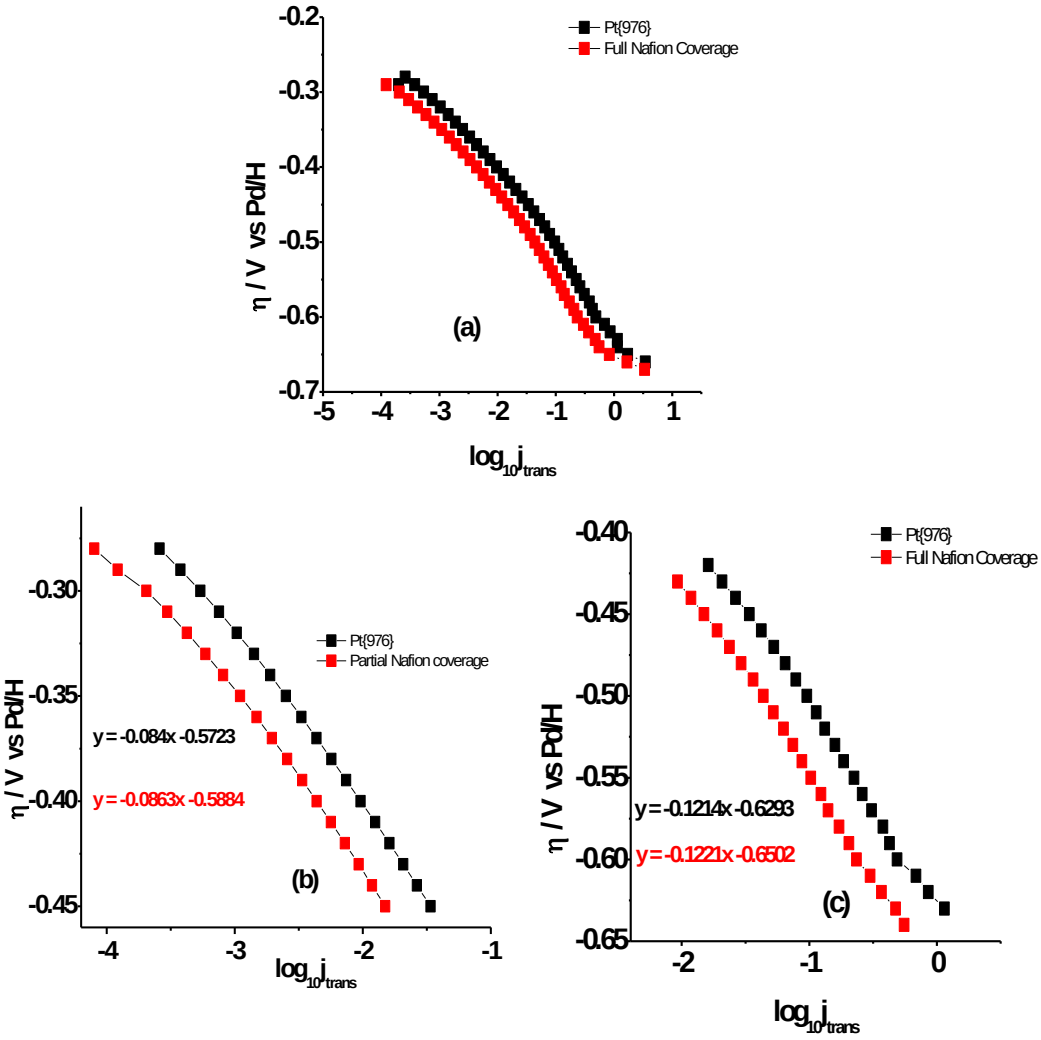

Fig 4.14 Tafel plots for Nafion free and Nafion coated Pt{976} where (a) is the full Tafel plot, (b) low overpotential range and (c) high overpotential range.

"High" Overpotential Range				
Surface	**J_0 / A cm^{-2} Nafion Free**	**J_0 / A cm^{-2} Nafion Coated**	**No of electrons in rds Nafion Free**	**No of electrons in rds Nafion coated**
Pt{111}	8.23 x10^{-06}	6.47 x10^{-06}	0.97	0.93
Pt{976}	6.55 x10^{-06}	4.73 x10^{-06}	0.97	0.97
Pt{311}	3.96 x10^{-06}	3.51 x10^{-06} for Partial Nafion Coverage 2.57 x10^{-06} full Nafion Coverage	0.96	0.94 for both coverage's
Pt{100}	1.70 x10^{-06}	1.45 x10^{-06}	1	0.95

Table 3 j_o and number of electrons in the rate determining step at high overpotential values for various Nafion free and Nafion coated Pt{hkl} electrodes.

"Low" Overpotential Range				
Surface	**J_0 / A cm^{-2} Nafion Free**	**J_0 / A cm^{-2} Nafion Coated**	**No of electrons in rds Nafion Free**	**No of electrons in rds Nafion coated**
Pt{111}	6.90 x10^{-10}	6.58 x10^{-10}	2	1.9
Pt{976}	1.54 x10^{-07}	1.52 x10^{-07}	1.5	1.4
Pt{311}	4.90 x10^{-08}	4.68 x10^{-08} for Partial Nafion Coverage 3.59 x10^{-08} full Nafion Coverage	1.49	1.49 for partial Nafion 1.43 for full Nafion coverage
Pt{100}	1.64 x10^{-07}	1.54 x10^{-07}	1.3	1.2

Table 4 j_o and number of electrons in the rate determining step at low overpotential values for various Nafion free and Nafion coated Pt{hkl} electrodes.

4.3 Conclusions

New protocols for the deposition of Nafion films onto Pt{hkl} electrodes without contamination have been described. For basal planes of platinum, the results recently reported by Markovic and co-workers[27,28] were reproduced, and models proposed in that work to describe the interaction of Nafion with Pt surfaces were supported in the present study. Moreover, the potential at which Nafion CV peaks occur has been assigned to local PZTC of

step or terrace sites based on an assessment of several stepped platinum electrode surfaces and correlations with previous measurements of local PZTC. Pt{111} is somewhat exceptional since Nafion peaks occur at slightly more positive potentials than the PZTC of the Nafion-free surface, suggesting a shift in the PZTC to more positive potentials in this case. No impact of Nafion on H_{UPD} sites is reported suggesting that for potentials negative of the PZTC binding of Nafion to platinum is dominated by van der Waals interactions of the polymer backbone with the electrode surface. Positive of the local PZTC, sulphonate-platinum interactions also will come into play. Most importantly however is the finding that Nafion displays unprecedented sensitivity to the average spacing of linear step sites in that intense Nafion redox peaks at step sites are quenched rapidly as average terrace width increases from 2 to 6 atoms. This behaviour is ascribed to competitive adsorption of Nafion with OH_{ad} species formed in the H_{UPD} region of highly stepped Pt{hkl} electrodes in acidic aqueous perchloric acid. This phenomenon also applies to basal Pt{111}, Pt{100}, and Pt{110} planes whereby displacement of OH_{ad} species by more strongly adsorbed sulphonate substituent's of Nafion also leads to quenching of CV peaks ascribable to OH_{ad}. As such, Nafion may be considered as a probe of adsorbed OH. Hence, clean electrochemistry is seen to offer unique opportunities for greater understanding of both complex “buried” interfaces such as Nafion/Pt and the production of new knowledge concerning electrosorption peaks originating from single crystal electrode surfaces. The effect of Nafion adsorption on various Pt{hkl} electrodes in relation to the ORR reaction was also studied. It was found that although the ORR was inhibited to a limited extent when Nafion was adsorbed (shift of ORR $E_{1/2}$ to slightly more negative potentials, decrease in exchange current density) the overall reduction mechanism remained unchanged relative to the clean surface. Hence, the rate limiting step at “low” overpotential (when electrosorbed oxide was present) involved a two electron transfer whereas at “high” overpotential (when the surface was free of electrosorbed oxide), a one electron transfer characterised the rds. Future work should concentrate on *in situ* STM studies of Nafion on Pt{hkl} under electrochemical control, allowing for highly precise and novel insights into redox and structural processes associated with important proton conducting membranes such as Nafion in fuel cells under reactive conditions.

4.4 References

(1) Mauritz, K. A.; Moore, R. B. *Chemical Reviews* **2004**, *104*, 4535.

(2) Hiesgen, R.; Wehl, I.; Aleksandrova, E.; Roduner, E.; Bauder, A.; Friedrich, K. A. *International Journal of Energy Research* **2010**, *34*, 1223.

(3) Hsu, W. Y.; Gierke, T. D. *Journal of Membrane Science* **1983**, *13*.

(4) Hsu, W. Y.; Gierke, T. D. *Journal of the Electrochemical Society* **1982**, *129*, C121.

(5) Eikerling, M.; Kornyshev, A. A.; Spohr, E. *Fuel Cells I* **2008**, *215*, 15.

(6) Kreuer, K. D. *Journal of Membrane Science* **2001**, *185*, 29.

(7) Paddison, S. J.; Reagor, D. W.; Zawodzinski, T. A. *Journal of Electroanalytical Chemistry* **1998**, *459*, 91.

(8) Yeager, H. L.; Kipling, B.; Steck, A. *Journal of the Electrochemical Society* **1980**, *127*, C404.

(9) Buzzoni, R.; Bordiga, S.; Ricchiardi, G.; Spoto, G.; Zecchina, A. *Journal of Physical Chemistry* **1995**, *99*, 11937.

(10) HeitnerWirguin, C. *Journal of Membrane Science* **1996**, *120*, 1.

(11) Ludvigsson, M.; Lindgren, J.; Tegenfeldt, J. *Electrochimica Acta* **2000**, *45*, 2267.

(12) Gruger, A.; Regis, A.; Schmatko, T.; Colomban, P. *Vibrational Spectroscopy* **2001**, *26*, 215.

(13) Liang, Z. X.; Chen, W. M.; Liu, J. G.; Wang, S. L.; Zhou, Z. H.; Li, W. Z.; Sun, G. Q.; Xin, Q. *Journal of Membrane Science* **2004**, *233*.

(14) Basnayake, R.; Peterson, G. R.; Casadonte, D. J., Jr.; Korzeniewski, C. *Journal of Physical Chemistry B* **2006**, *110*, 23938.

(15) Basnayake, R.; Wever, W.; Korzeniewski, C. *Electrochimica Acta* **2007**, *53*, 1259.

(16) Korzeniewski, C.; Adams, E.; Liu, D. *Applied Spectroscopy* **2008**, *62*, 634.

(17) Byun, C. K.; Sharif, I.; DesMarteau, D. D.; Creager, S. E.; Korzeniewski, C. *Journal of Physical Chemistry B* **2009**, *113*, 6299.

(18) Idupulapati, N.; Devanathan, R.; Dupuis, M. *Journal of Physical Chemistry A* **2010**, *114*, 6904.

(19) Webber, M.; Dimakis, N.; Kumari, D.; Fuccillo, M.; Smotkin, E. S. *Macromolecules* **2010**, *43*, 5500.

(20) Warren, D. S.; McQuillan, A. J. *Journal of Physical Chemistry B* **2008**, *112*, 10535.

(21) Malek, K.; Eikerling, M.; Wang, Q.; Liu, Z.; Otsuka, S.; Akizuki, K.; Abe, M. *Journal of Chemical Physics* **2008**, *129*.

(22) Malek, K.; Eikerling, M.; Wang, Q.; Navessin, T.; Liu, Z. *Journal of Physical Chemistry C* **2007**, *111*, 13627.

(23) Zhdanov, V. P. *Physical Review E* **2003**, *67*.

(24) Zhdanov, V. P.; Kasemo, B. *Electrochemistry Communications* **2006**, *8*, 561.

(25) Zhdanov, V. P.; Kasemo, B. *Surface Science* **2004**, *554*, 103.

(26) Schmidt-Rohr, K.; Chen, Q. *Nature Materials* **2008**, *7*, 75.

(27) Subbaraman, R.; Strmcnik, D.; Stamenkovic, V.; Markovic, N. M. *Journal of Physical Chemistry C* **2010**, *114*, 8414.

(28) Subbaraman, R.; Strmcnik, D.; Paulikas, A. P.; Stamenkovic, V. R.; Markovic, N. M. *Chemphyschem* **2010**, *11*, 2825.

(29) Ma Gomez-Marin, A.; Berna, A.; Feliu, J. M. *Journal of Physical Chemistry C* **2010**, *114*, 20130.

(30) Garcia-Araez, N.; Climent, V.; Feliu, J. M. *Electrochimica Acta* **2009**, *54*, 966.

(31) Hoshi, N.; Suzuki, T.; Hori, Y. *Electrochimica Acta* **1996**, *41*, 1647.

(32) Herrero, E.; Mostany, J.; Fejiu, J. M.; Lipkowski, J. *Journal of Electroanalytical Chemistry* **2002**, *534*, 79.

(33) Herrero, E.; Feliu, J. M.; Wieckowski, A.; Clavilier, J. *Surface Science* **1995**, *325*, 131.

(34) Aljaafgolze, K.; Kolb, D. M.; Scherson, D. *Journal of Electroanalytical Chemistry* **1986**, *200*, 353.

(35) Ahmadi, A.; Evans, R. W.; Attard, G. *Journal of Electroanalytical Chemistry* **1993**, *350*, 279.

(36) Gomez, R.; Orts, J. M.; Alvarez-Ruiz, B.; Feliu, J. M. *Journal of Physical Chemistry B* **2004**, *108*, 228.

(37) Gasteiger, H. A.; Markovic, N. M.; Ross, P. N. *Langmuir* **1996**, *12*, 1414.

(38) van der Niet, M. J. T. C.; den Dunnen, A.; Juurlink, L. B. F.; Koper, M. T. M. *Angewandte Chemie-International Edition* **2010**, *49*, 6572.

(39) Markovic, N.; Hanson, M.; McDougall, G.; Yeager, E. *Journal of Electroanalytical Chemistry* **1986**, *214*, 555.

(40) Orts, J. M.; Gomez, R.; Feliu, J. M.; Aldaz, A.; Clavilier, J. *Electrochimica Acta* **1994**, *39*, 1519.

(41) Su, Z.; Climent, V.; Leitch, J.; Zamlynny, V.; Feliu, J. M.; Lipkowski, J. *Physical Chemistry Chemical Physics* **2010**, *12*, 15231.

(42) Hermse, C. G. M.; van Bavel, A. P.; Koper, M. T. M.; Lukkien, J. J.; van Santen, R. A.; Jansen, A. P. J. *Physical Review B* **2006**, *73*.

(43) Blum, L.; Marzari, N.; Car, R. *Journal of Physical Chemistry B* **2004**, *108*, 19670.

(44) Mrozek, P.; Sung, Y. E.; Han, M.; Gamboaaldeco, M.; Wieckowski, A.; Chen, C. H.; Gewirth, A. A. *Electrochimica Acta* **1995**, *40*, 17.

(45) Clavilier, J.; Elachi, K.; Rodes, A. *Chemical Physics* **1990**, *141*, 1.

(46) Domke, K.; Herrero, E.; Rodes, A.; Feliu, J. M. *Journal of Electroanalytical Chemistry* **2003**, *552*, 115.

(47) Markovic, N. M.; Marinkovic, N. S.; Adzic, R. R. *Journal of Electroanalytical Chemistry* **1991**, *314*, 289.

(48) Furuya, N.; Koide, S. *Surface Science* **1989**, *220*, 18.

(49) Hoshi, N.; Suzuki, T.; Hori, Y. *Journal of Electroanalytical Chemistry* **1996**, *416*, 61.

(50) Attard, G. A.; Ahmadi, A. *Journal of Electroanalytical Chemistry* **1995**, *389*, 175.

(51) Climent, V.; Attard, G. A.; Feliu, J. M. *Journal of Electroanalytical Chemistry* **2002**, *532*, 67.

(52) Attard, G. A.; Hazzazi, O.; Wells, P. B.; Climent, V.; Herrero, E.; Feliu, J. M. *Journal of Electroanalytical Chemistry* **2004**, *568*, 329.

(53) Feldberg, S. W.; Rubinstein, I. *Journal of Electroanalytical Chemistry* **1988**, *240*, 1.

(54) Everett, D. H.; Whitton, W. I. *Transactions of the Faraday Society* **1952**, *48*.

(55) Everett, D. H.; Smith, F. W. *Transactions of the Faraday Society* **1954**, *50*.

(56) Everett, D. H. *Transactions of the Faraday Society* **1954**, *50*.

(57) Wakisaka, M.; Suzuki, H.; Mitsui, S.; Uchida, H.; Watanabe, M. *Langmuir* **2009**, *25*, 1897.

(58) McGovern, M. S.; Garnett, E. C.; Rice, C.; Masel, R. I.; Wieckowski, A. *Journal of Power Sources* **2003**, *115*, 35.

(59) Angersteinkozlowska, H.; Conway, B. E.; Barnett, B.; Mozota, J. *Journal of Electroanalytical Chemistry* **1979**, *100*, 417.

(60) Garcia-Araez, N.; Climent, V.; Feliu, J. M. *Journal of the American Chemical Society* **2008**, *130*, 3824.

(61) Macia, M. D.; Campina, J. M.; Herrero, E.; Feliu, J. M. *Journal of Electroanalytical Chemistry* **2004**, *564*.

(62) Parthasarathy, A.; Srinivasan, S.; Appleby, A. J.; Martin, C. R. *Journal of the Electrochemical Society* **1992**, *139*.

(63) Appleby, A. J.; Baker, B. S. *Journal of the Electrochemical Society* **1978**, *125*.

(64) Damjanov.A; Brusic, V. *Electrochimica Acta* **1967**, *12*.

(65) Damjanov.A; Genshaw, M. A. *Electrochimica Acta* **1970**, *15*.

(66) Wang, J. X.; Markovic, N. M.; Adzic, R. R. *Journal of Physical Chemistry B* **2004**, *108*, 4127.

(67) Markovic, N. M.; Marinkovic, N. S.; Adzic, R. R. *Journal of Electroanalytical Chemistry* **1988**, *241*, 309.

(68) Kuzume, A.; Herrero, E.; Feliu, J. M. *Journal of Electroanalytical Chemistry* **2007**, *599*, 333.

Chapter 5

Metal Deposition onto Nafion Coated and Nafion Free Well Defined Platinum Single Crystal Electrodes

5.1 Introduction

The use of well defined electrodes to understand the structural aspects of electrochemical reactivity has been intensively investigated since the discovery of the flame treatment by Clavilier[1,2] as a convenient method to obtain clean well ordered electrode surfaces. Since these pioneering studies by Clavilier, a wide number of studies have been performed which have revealed the structure sensitivity of a great number of electrochemical processes. The reactivity of different platinum basal planes and the effect of introducing step sites are well described in literature[3-7]. Indeed, the structure sensitive nature of many of these electrocatalytic processes make the use of well defined electrodes a prerequisite for gaining fundamental insight into structure-reactivity relationships[8-10]. Electrochemical reactivity of well defined Pt*{hkl}* electrodes can also be modified by the adsorption of foreign metal adatoms to alter the surface composition[11-13]. Two such metals, bismuth and palladium, have been shown (even at a sub - monolayer coverage) to significantly enhance the reactivity of the electrochemical oxidation of formic acid for example[14,15]. At a fundamental level, the use of adatom modified Pt*{hkl}* help understand better the processes that occur at fuel cell electrocatalyts[16-19].

Polymer electrolyte fuel cells (PEMFC) are seen as a promising alternative to fossil fuel combustion in providing power[20]. Moreover, the interface between the supported electrocatalyst and the electrolyte is of crucial concern since transport of reactant, products, water and charge across this region controls the ultimate performance of the fuel cell[21-24]. Nafion is a polymer electrolyte that is used in fuel cells to transport protons from the anode to cathode. Nafion gives rise to efficient proton conduction when water content/structure and film thickness are optimised[25]. Combinations of spectroscopic[26-30] and theoretical approaches[31-35] have generated a variety of models to describe the structure of Nafion at the Nafion-electrode interface, in particular the work by Schmidt-Rohr and Chen[36] has established the formation of both hydrophobic and hydrophilic polymeric regions with the hydrophillic region consisting purely of sulphonate groups that form a network from one electrode to the other. Recent single crystal electrode studies of ultra-thin Nafion films

presented in chapter 4 and published by Attard[37], Feliu[38] and Markovic[39], have established that Nafion, (once thought to be a non-adsorbing electrolyte), acts as a "specifically" adsorbing electrolyte. The sulphonate groups have been shown to adsorb onto the surface (via CO displacement experiments[39]). In addition, the sulphonate groups have been shown to displace OH_{AD} species (see Chapter 4).

In order to further understand the interface between Nafion and the electrocatalyst, voltammetry of adatom modified and Nafion coated Pt*{hkl}* will be presented. As mentioned earlier, the adsorption of bismuth and palladium on platinum electrode surfaces is already well characterised. Hence, the voltammetry of Pt*{hkl}* surfaces modified with bismuth and palladium with and without Nafion present will be compared. This is in order to make comparisons and understand better the processes occurring on the Nafion coated surfaces modified by adatoms.

5.2 Results

5.2.1 Palladium deposition onto Nafion free and Nafion coated low Miller index platinum single crystal electrodes

Figures 5.1a and 5.1b show cyclic voltammograms (CVs) collected as a function of Pd coverage on Pt{111} in sulphuric and perchloric acid.

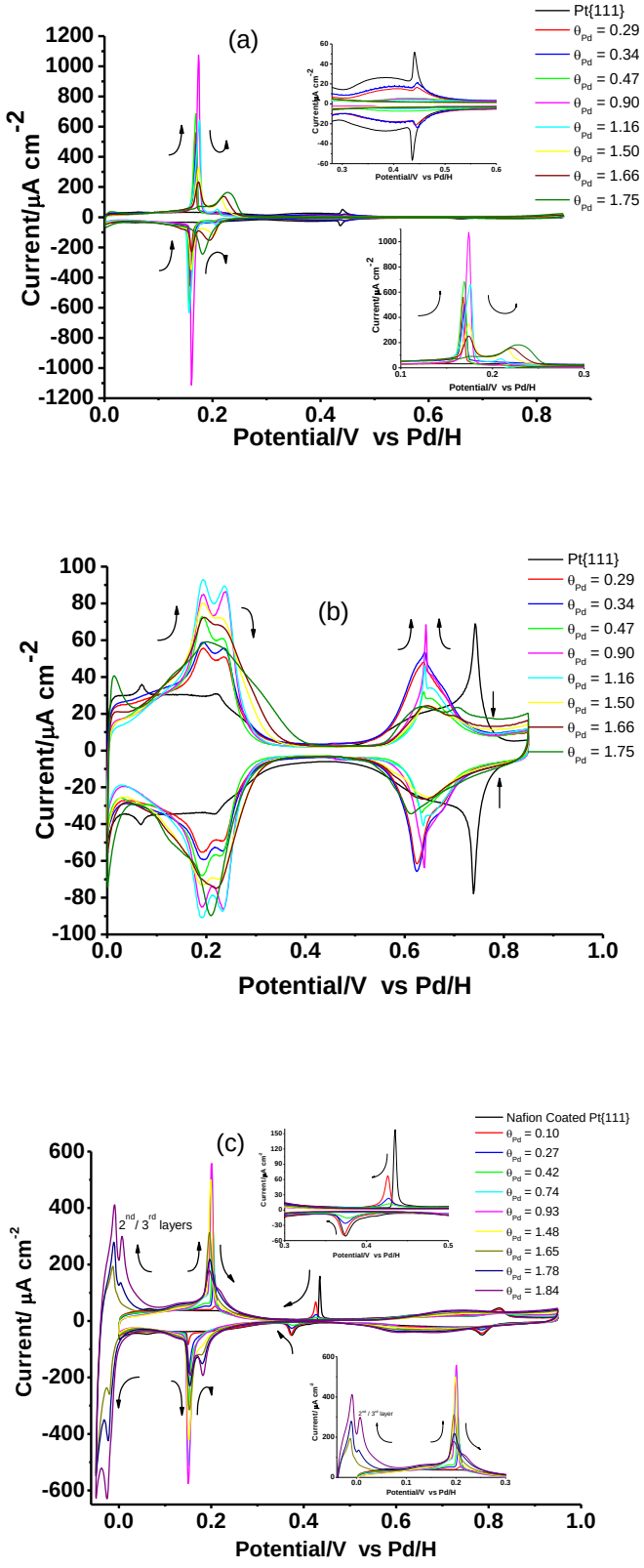

Fig. 5.1 Cyclic voltammograms of Pt{111} as a function of palladium coverage in monolayers. Sweep rate = 50 mV/s and (a) 0.1 M aqueous sulphuric acid, (b) 0.1 M aqueous perchloric acid and (c) nafion-coated electrode in 0.1 M aqueous perchloric acid electrolyte. In figure 1 (c), 2/3 refers to peak that emerges in hydrogen evolution

potential region when palladium coverage exceeds one monolayer and is therefore ascribed to second and third layer palladium.

Figure 5.1c corresponds to a Nafion-coated Pt{111} electrode in contact with perchloric acid. The thickness of the Nafion film in this case was estimated to be 3.5 nm[37]. In aqueous sulphuric acid (figure 5.1a), it is seen that the growth of the palladium adlayer is marked by the increase in intensity of a sharp electrosorption peak at 0.17 V corresponding to first layer palladium. Growth of first layer palladium also resulted in the attenuation of the bisulphate "butterfly" between 0.35 V - 0.45 V (top inset, figure 5.1a). Second and third layer palladium manifests itself as a single, broader voltammetric peak at more positive potentials (0.21 V) [13,40-46 41-48]. Palladium coverages were estimated using the charge calculated after integrating the area under each of the palladium peaks and assuming that a palladium adatom in the second layer would block adsorption in the first palladium monolayer[47].

In figure 5.2, the charge under the palladium peaks (first and second layer) for different palladium adlayers in sulphuric acid has been integrated and it was found that growth of palladium second layer occurs before the completion of a complete monolayer of palladium.

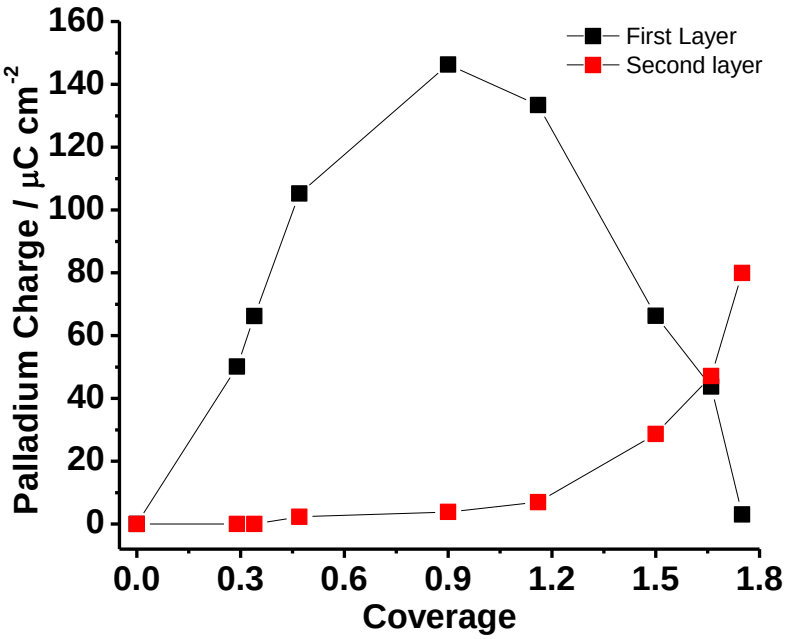

Figure 5.2 Integrated palladium charge *vs* coverage on Pt{111} showing growth of second layer occurs before completion of the first palladium monolayer in sulphuric acid.

Arrows on figures 5.1 a - c highlight the rise and fall in intensity of the first monolayer peak as the coverage reaches, then exceeds 1 monolayer. In a similar fashion, the changes in CV

response when palladium coverage, as measured in perchloric acid electrolyte are reported in figure 5.1b. The presence of palladium at the Pt{111} surface is now signified by two overlapping, broad electrosorption peaks at around 0.2 V. These peaks reach a maximum intensity at a palladium coverage of 1 monolayer and then decrease in intensity and broaden further with significant intensity appearing at potentials > 0.25 V. A marked perturbation of the so-called "butterfly peak" at 0.75 V corresponding to OH adsorption on Pt{111}[46] is also observed as palladium coverage increases. An analogous peak at more negative potentials (0.62 V) appears attributable to OH adsorption on palladium. It is noteworthy that at precisely one monolayer of palladium, this Pd-OH feature exhibits a sharp "spike" at 0.63 V[48] but this feature is attenuated upon increasing palladium coverage still further.

Both figure 5.1a and figure 5.1b illustrate the marked influences of anion adsorption on the voltammetry observed. In the case of the more strongly adsorbing sulphate anion, the Pt-OH peak at 0.75 V (and Pd-OH at 0.62 V) is completely absent because water splitting to produce OH is inhibited by the strongly adsorbed sulphate anion. In sulphuric acid Pt-OH formation is reported to take place on Pt{111} at much more positive potentials, 1.2 V vs Pd/H[2]. This shift or overpotential for adsorption of components of the double layer caused by anion adsorption is also observed in the hydrogen underpotential (H UPD) region between 0 and 0.3 V in that protons can be converted to adsorbed hydrogen on palladium more readily in perchloric acid (as signified by the onset of this process at 0.3 V for the monolayer of palladium in the first layer) than in sulphuric acid where adsorption begin at potentials < 0.2 V. Above 1 monolayer, the palladium H UPD peaks broaden and decrease in magnitude as does the Pd-OH peak at 0.62 V.

Nafion – coated Pt{111} in perchloric acid as a function of palladium coverage is recorded in figure 5.1c. An interesting juxtaposition of elements pertaining to palladium deposition behaviour in both aqueous sulphuric and perchloric acid behaviour is deduced. For Pd H UPD, the electrosorption peaks most resemble those in sulphuric acid with a marked narrowing and a shift to more negative potentials relative to perchloric acid. There is a degree of hysteresis in the palladium monolayer peak on the forward and reverse potential sweeps as also observed for Nafion induced peaks on clean Pt{111} (0.43 V "spike" on positive-going sweep and a broader asymmetric peak on the negative-going potential sweep at 0.38 V). The origin of this effect was discussed in detail in reference 49 but in summary is thought to reflect the degree of long range order in the Nafion/palladium adlayer[49]. A single peak ascribable to second and third layer palladium may also be discerned at potentials < 0 V

(peak 2/3) in figure 5.1c. Although the absolute intensity of the palladium H UPD electrosorption peaks (for palladium coverages < 1 monolayer) is less than in sulphuric acid, the onset of second/third layer palladium is signified by the growth in a second H UPD peak at more positive potentials as also found in aqueous sulphuric acid. Furthermore, the potential of zero total charge (PZTC) for Pd on Pt{111} in aqueous sulphuric acid is reported to be close to the Pd H UPD peak maximum[50]. It is speculated for Nafion covered Pd/Pt{111}, that this is also the case and therefore a model of how Nafion is interacting with the surface and generating such narrow H UPD peaks would involve a change in local surface charge at the peak potential causing Nafion sulphonate groups to adsorb/desorb from the surface with simultaneous desorption/adsorption of H UPD. Finally, CVs of approximately one monolayer of palldium adsorbed onto Pt{111} in 0.1M H_2SO_4, $HClO_4$ and Nafion coated Pt{111} in $HClO_4$ are presented in figure 5.3.

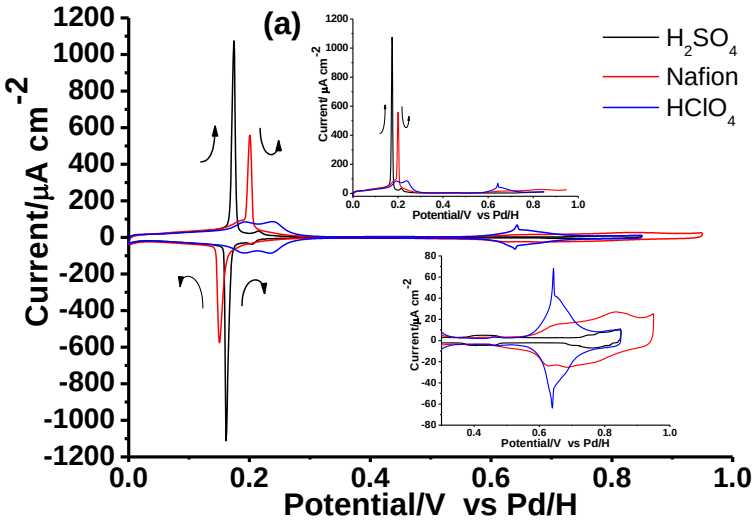

Figure 5.3 CVs of one monolayer coverage of palladium on Pt{111} in 0.1M H_2SO_4, $HClO_4$ and Nafion coated Pt{111} in 0.1M $HClO_4$, inset figures highlight effect of anions in H_{UPD} and oxide regions.

The action of even small amounts of adsorbed palladium (0.1 monolayers) is to cause a significant attenuation in the magnitude of the Pt{111} Nafion double layer feature (sharp peak at 0.42 V). This supports our original contention in reference 37 that the peak is a product of long range order in the Nafion film[37] and therefore, islands of palladium growing on the surface must lead to the break-up of the long range order in the Nafion/Pt{111} conjugate structure. To summarise the above, palladium appears to favour a strong interaction with sulphonate groups of the Nafion adlayer leading to significant changes in H_{UPD} behaviour relative to perchloric acid as would be expected for a "specifically" adsorbing

anion such as (bi-) sulphate[51]. So far as OH adsorption is concerned however, similarities with the action of specifically adsorbing anions ceases.

Unlike in figure 5.1a where strong specific adsorption of sulphate anions blocks completely the Pt-OH and Pd-OH features in the double layer observed in the potential range 0.6 – 0.8 V in perchloric acid (figure 5.2), in figure 5.1c such features, although modified slightly are always observed. From this, it appears that the strength of interaction of sulphonate groups with the electrode surface is insufficient for them to compete successfully for sites with adsorbed OH. Since adsorbed OH is often implicated in electroxidation activity of a material[51], it is interesting now to compare the activity towards formic acid and methanol electrooxidation of Pd/Pt{111}with and without Nafion adsorbed (see chapter 6).

Pd adsorption for Pt{100} in aqueous sulphuric acid, perchloric acid and Nafion coated Pt{100} in perchloric acid are shown in figs 5.4a - 5.4c. The adsorption of palladium in aqueous sulphuric acid (fig 5.4a) show the attenuation of the H_{UPD} area and as with the Pt{111} in sulphuric acid, is signified first by the formation of a first layer palladium redox peak at 0.1 V. The intensity of the peak is smaller than first layer palladium on Pt{111} (fig 5.1a) however as with Pt{111}, the magnitude of the peak increases with size as more palladium is added to the surface and reaches a maximum at one monolayer. Arrows in figure 5.4a indicate the rise of first layer palladium as coverage reaches and exceeds one monolayer. In a similar fashion to palladium adsorption on Pt{111}, second layer palladium formation occurs before the completion of a complete palladium monolayer. The peak is formed at 0.2 V, it should be noted the peak for palladium second layer is much more well defined compared to Pt{111} where the a broad feature at 0.21 V is formed representing second and multilayer palladium formation (see figure 5.1a). Eventually multilayer formation of palladium (not shown here) would have occurred if more palladium was added to the surface. The peak at 0.2 V would have decreased in intensity and broadened in shape. As the coverage of palladium on the surface increases, the amount of Pd-OH formed on the surface increases as well. However despite the ease with which palladium adsorbs oxygenated species, Feliu *et al*[52] have shown that palladium adlayers have a negative impact on the electrocatalytic activity for the electrooxidation of CO on the surface. Voltammetric results presented by Clavilier[53] and Feliu[52] show that palladium has a greater tendency than Pt{111} to form palladium second layer prior to the completion of palladium first layer. It was stated by Feliu *et al*[52] that the presence of the {100} terrace peak at 0.35 V, maintaining its characteristic shape as palladium is deposited on the surface, implies the presence of wide

Pt{100} domains on the palladium covered surface. Thus palladium must be undergoing island growth during deposition. Later *in situ* x-ray scattering data presented by Ross[54] and co-workers further supported island growth of palladium on Pt{100}. The charge under the palladium peaks are integrated and plotted in figure 5.5, again it is seen that palladium second layer formation occurs before the completion of a full palladium monolayer.

When the palladium adlayers are analysed in perchloric acid (figure 5.4b), unlike Pt{111} (figure 5.1b), a broad doublet redox peak in the voltammogram was not formed around 0.2 V. Instead like the voltammograms in sulphuric acid, singular Pd electrosorption redox peaks are seen for first layer palladium and second layer palladium. It was also found that the Pd-OH region was much bigger compared to sulphuric acid as well. Growth of first layer palladium is represented by an electrosorption peak at a slightly more positive potential (0.14 V) compared to sulphuric acid (0.11 V), whereas second layer palladium is at the same potential as the sulphuric acid counterpart (figure 5.4a). The electrosorption peaks are much more broad in shape and lower in intensity compared to the redox peaks in sulphuric acid. The decrease in intensity and loss in sharpness of the palladium redox peaks are due to the absence of sulphate anions. The growth of palladium in perchloric acid is the same as in sulphuric acid, the arrows in the CV indicate the growth and subsequent fall of first layer palladium as a complete monolayer is reached and exceeded. Island growth of palladium is again signified in the CVs, in perchloric acid growth of second layer palladium occurs before the completion of a monolayer. The peaks for second layer palladium are much broader compared to sulphuric acid.

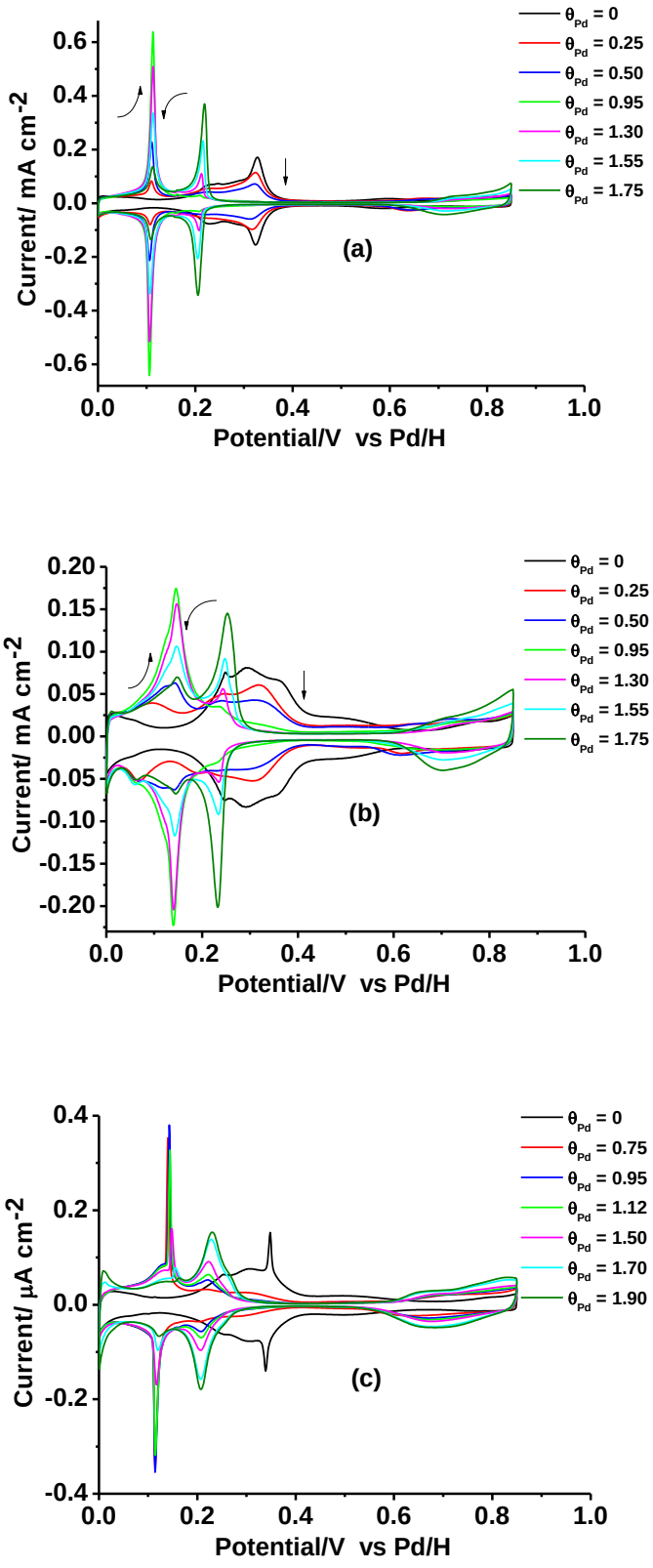

Fig 5.4 Cyclic voltammograms of Pt{100} as a function of palladium coverage in monolayers. Sweep rate = 50 mV/s and (a) 0.1 M aqueous sulphuric acid, (b) 0.1 M aqueous perchloric acid and (c) Nafion-coated electrode in 0.1 M aqueous perchloric acid electrolyte.

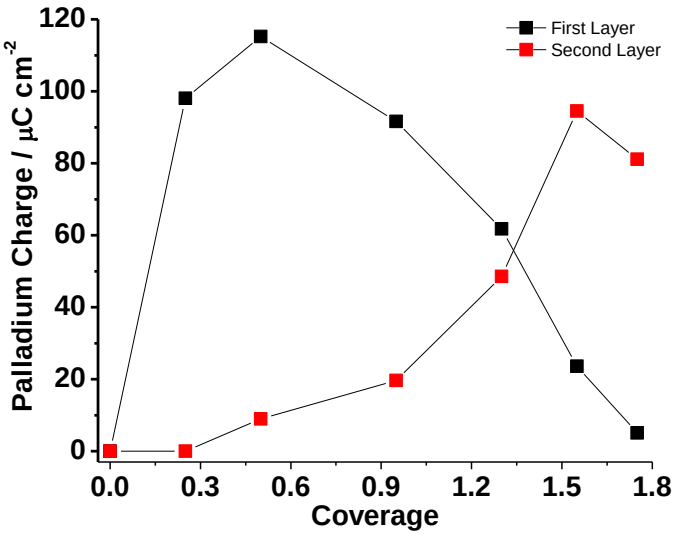

Fig 5.5 Charges under palladium peaks on Pt{100} showing palladium second layer formation occurs before completion of a palladium monolayer.

Palladium adsorption on Nafion coated Pt{100} in perchloric acid is recorded in fig 5.4c. As with palladium on Nafion coated Pt{111} (figure 5.1c), the CVs of palladium adsorbed on Nafion coated Pt{100} contain elements of both sulphuric and perchloric acid. The Pd H_{UPD} peaks for that of first layer palladium resembles the electrosorption peak in sulphuric acid with a marked narrowing and a shift to more negative potentials relative to perchloric acid. There is small a degree of hysteresis in the palladium monolayer peak on the forward and reverse potential sweeps as well. Second layer palladium however resembles that of perchloric acid, in that it is broad in shape and lower in intensity. Hence, interaction of sulphonate groups is much more marked for first layer palladium than subsequent layers. It should also be noted that a hydrogen oxidation/reduction peak at 0 V is also observed unlike in perchloric acid. Furthermore, the potential of zero total charge (PZTC) for palladium on Pt{100} in aqueous sulphuric acid is reported to be close to the Pd H_{UPD} peak maximum[52], as found with Pt{111} (see above). We speculate for Nafion covered Pd/Pt{100}, that this is also the case and therefore a model of how Nafion is interacting with the surface and generating such narrow H_{UPD} peaks would involve a change in local surface charge at the peak potential causing Nafion sulphonate groups to adsorb/desorb from the surface with simultaneous desorption/adsorption of H_{UPD}

Palladium adsorption on Pt{110} in different acid media is shown in figures 5.6a - 5.6c. Unlike the other basal planes, Pt{110} does not form sharp electrosorption peaks in the H_{UPD}

region. Instead for palladium adsorption on Pt{110} in sulphuric acid (figure 5.6c), charge under the H_{UPD} area is attenuated as the amount of palladium coverage increases. Eventually palladium will form a broad feature that has been attributed to palladium formation on Pt{110} between 0.12 V - 0.22 V. This is also coupled with the formation of a broad Pd-OH peak at 0.75 V. A similar story occurs for Pd adsorption in Pt{110} in perchloric acid (figure 5.6b), where a broad feature implying palladium formation between 0.1 V - 0.2 V is formed, coupled with the broad oxide formation. The Pd-OH feature is much broader in shape and not as well defined as Pd-OH in sulphuric acid.

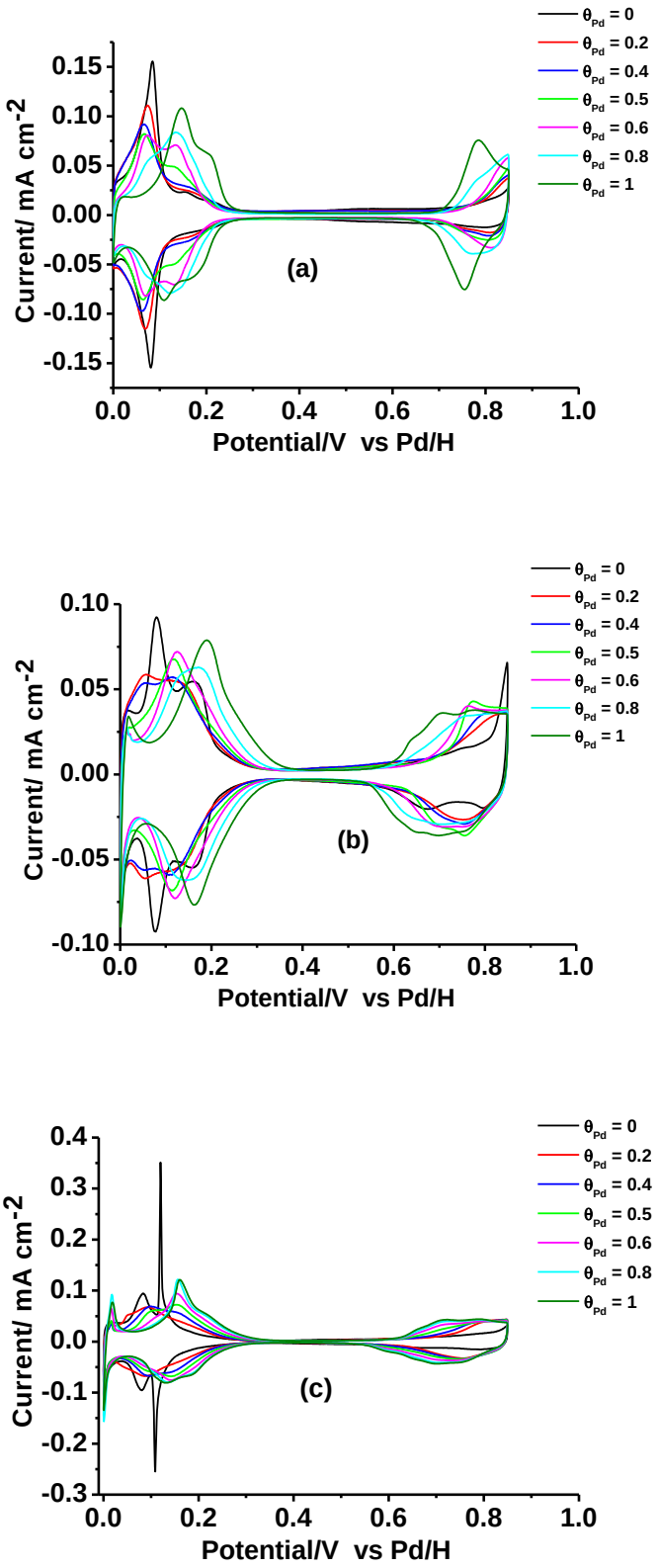

Fig. 5.6 Cyclic voltammograms of Pt{110} as a function of palladium coverage in monolayers. Sweep rate = 50 mV/s and (a) 0.1 M aqueous sulphuric acid, (b) 0.1 M aqueous perchloric acid and (c) nafion-coated electrode in 0.1 M aqueous perchloric acid electrolyte.

Finally, from figure 5.6c (palladium adsorption on Nafion coated Pt{110}) it is seen that the profile contains features of palladium adsorption on Pt{110} in both sulphuric acid and perchloric acid. Figure 5.6c shows that Pd adsorption on Nafion coated Pt{110} simply results in the attenuation of the H_{UPD} followed by the formation of a broad Pd peak at 0.1 V - 0.18 V, similar to behaviour found in sulphuric acid. The hydrogen oxidation/reduction peak at 0 V is also observed. The Pd-OH region resembles more the Pd-OH formed in perchloric acid than in sulphuric acid. Rapid attenuation of the Nafion/Pt{110} "spike" at 0.1 V as palladium is dosed onto the surface is also a notable feature of the electrochemical response.

5.2.2 Characterisation of Nafion covered and Nafion free platinum-palladium surface alloys

Platinum-palladium alloys were prepared on Pt{hkl} (see chapter 3 section 3.3) and CVs were recorded of the clean surfaces in 0.1M H_2SO_4 and 0.1M $HClO_4$ electrolyte solutions. CVs recorded in $HClO_4$ were poorly defined compared to those recorded in H_2SO_4, and it was the latter that was used to gauge palladium coverage initially. The perchlorate data was necessary for overlaying of the Nafion CVs of the alloys to ensure:

a) excessive contamination of the surface had not occurred,
b) that alloy composition was not changed by the Nafion deposition process and
c) to compare the alloy surface in the presence and absence of Nafion.

The surface alloys were constructed by following the procedures provided in chapter 3 section 3.3 and references 55 and 56. Briefly, palladium was deposited onto a flame annealed, CV characterised platinum single crystal via the forced deposition method and then heated gently, using a Bunsen flame[55,56]. Depending on the time in the flame, changes in the alloy composition were engendered (towards more Pt rich surfaces), eventually leading to the complete removal of all palladium from the electrode. On the Pt{111} electrode, the alloys, characterised in aqueous sulphuric acid, ranged from approximately 90% to 20% Pd composition (figure 5.17a). Coverage of palladium in the surface alloy can be calculated by integrating the charge under the palladium peak for the different alloys, taking as a baseline the charge under the H_{UPD} of pure Pt{111}[55,56]. The alloys produced match those in reference 55, high palladium compositions appear to favour H^+ adsorption from solution around 0.20 V, lower than on platinum (0.30 V). As palladium concentration decreases in the surface, the

Pd H_{UPD} feature decreases in intensity and shifts positive in potential towards that of platinum. It was also observed that the butterfly feature between 0.35 V - 0.45 V corresponding to bisulphate adsorption on P{111} terraces becomes more visible, with increasingly sharp spikes at 0.45 V. Oxide formation is suppressed for clean Pt{111} in H_2SO_4 by the adsorbed bisulphate layer. However, as surface coverage of palladium increases there is an increase in the amount of OH species adsorbed onto the surface. Only at high concentrations of palladium is a significant increase in the amount of adsorbed oxide was noticeable.

In figure 5.7b the same platinum-palladium surface alloys in sulphuric acid are now characterised in aqueous perchloric acid. The absence of the strongly adsorbing anion species in figure 5.7b is noticeable compared to figure 5.7a. In aqueous perchloric acid it is observed that the introduction of palladium in the surface results in the attenuation and shift to a lower onset potentials of the adsorbed OH butterfly at 0.75 V. The amount of adsorbed oxide on platinum - palladium alloys increases as the surfaces coverage of palladium turns to bulk palladium. In terms of fuel cell output, this increasing adsorption of oxide at lower potentials would have a negative outcome for fuel cell applications in relation to ORR, as it would lower the working potential of the cell. Due to the absence of bisulphate anions, it was found that the Pd H_{UPD} feature was much broader in shape and lower in intensity. However the onset potential of Pd H_{UPD} was found to be the same as in sulphuric acid.

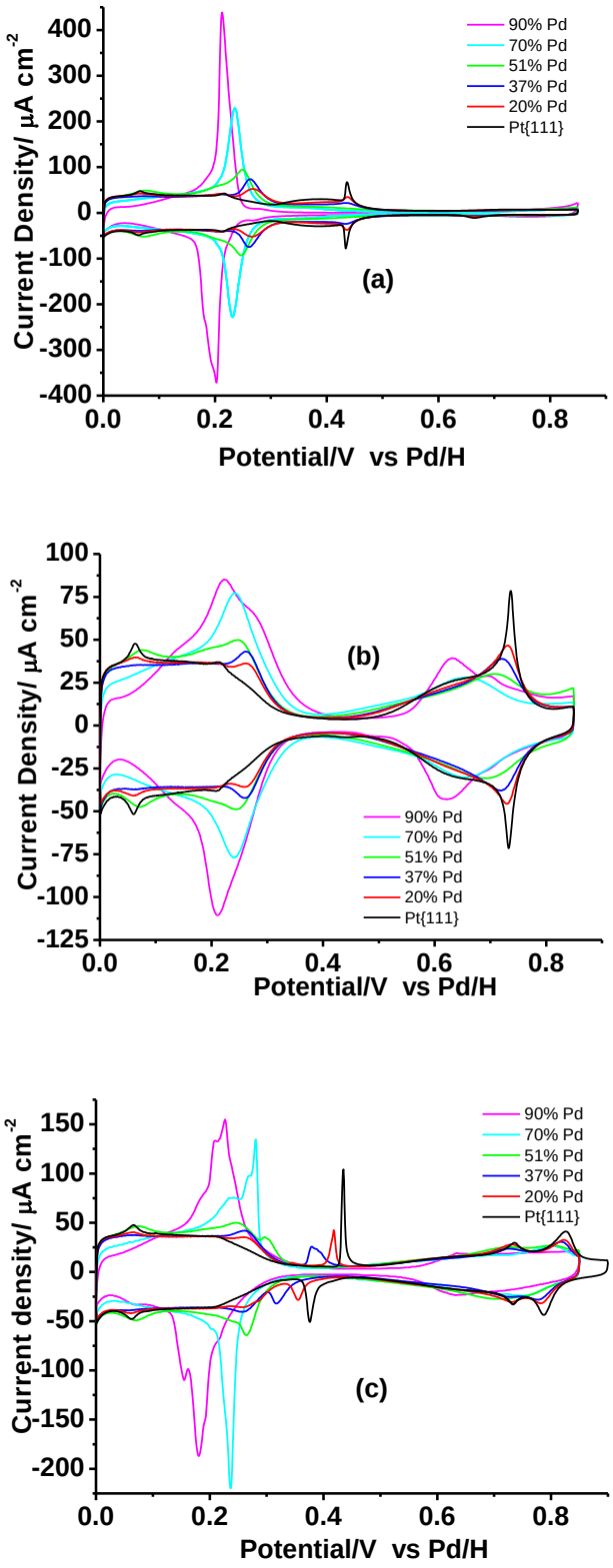

Fig. 5.7 Cyclic voltammograms of PtPd{111} surface alloys as a function of palladium coverage. Sweep rate = 50 mV/s and (a) 0.1 M aqueous sulphuric acid, (b) 0.1 M aqueous perchloric acid and (c) Nafion-coated electrode in 0.1 M aqueous perchloric acid electrolyte.

When Nafion was applied to the PtPd{111} alloys and characterised in aqueous perchloric acid (figure 5.7c), it was evident that CVs of the alloys contained components of both sulphuric and perchloric acid CVs. Compared to perchloric acid, the Pd H_{UPD} electrosorption peaks of the Nafion coated surfaces were found to be slightly narrower, more intense and mimicked that of the sulphuric acid CVs. As with sulphuric acid solution characterised alloys, the onset potential for Pd H_{UPD} formation was found to be 0.2 V for the high palladium composition alloys and shifted to positive potentials (0.3 V) as palladium composition decreased. It was also found that the adsorbed oxide region resembled that of the perchloric acid CVs, where for the high palladium compositions, the onset of adsorbed oxide formation occurred at a lower potential (0.6 V). Finally a clear trend was seen in the appearance of the irreversible pseudocapacitance spike, observed on clean Pt{111} from 0.40 to 0.44 V (figure 5.7c) which was attributed to sulphonate adsorption and desorption from the surface. This feature shifted to lower potential as the relative percentage of palladium in the alloy increased, appearing at around 0.28 to 0.35 V. The spike also appears to broaden and reduces in size and eventually disappears as bulk palladium is formed on the surface. The shift in the Nafion pseudocapacitance is speculated to be due to a change in the PZTC of Pt{111} as palladium is introduced to the surface.

PtPd{100} alloys were also prepared with compositions ranging from 31 to 90% surface Pd (figure 5.8). The alloys are similar to those in reference 55. The overlay of the CVs characterised in sulphuric acid (figure 5.8a) shows that as with PtPd{111} alloys characterised in sulphuric acid, the onset of Pd H_{UPD} for the highest palladium surface alloy was at 0.2 V. With decreasing palladium coverage the peak at 0.20 V, shifts positively in potential relative to the Pt{100} terrace at 0.35 V. Oxide adsorption is enhanced by high Pd concentrations, but the broad and symmetric pseudocapacitance peak between 0.50 and 0.70 V in the double layer appears to be suppressed.

When the surfaces where analysed in perchloric acid, figure 5.8b, the absence of bisulphate anions is clearly noticeable in the CVs. Analysis of the H_{UPD} region shows that the palladium CVs are much broader in shape and less well defined and lower in intensity compared to sulphuric acid. The oxide region was found to grow as more palladium was introduced to the surface.

When the Nafion films were applied to the PtPd{100} alloys (figure 5.8c), the general shape of the Nafion coated alloy CVs show components of both sulphuric acid and perchloric acid CVs. The sulphonate spike growth followed a similar trend to the PtPd{111} alloys, by

shifting to progressively lower potential with increasing palladium coverage. For palladium compositions 46% and 60% the CV profiles were more like perchloric acid profiles where the electrosorption peaks corresponding to sulphonate adsorption either too small to measure or were possibly inhibited by a surface contaminant. Oxide formation occurs at a lower potential (0.60 V) compared to the Nafion free alloy surface (0.69 V) and is noticeably greater in area, although this area effect is very small apart from at highest palladium coverage (90%).

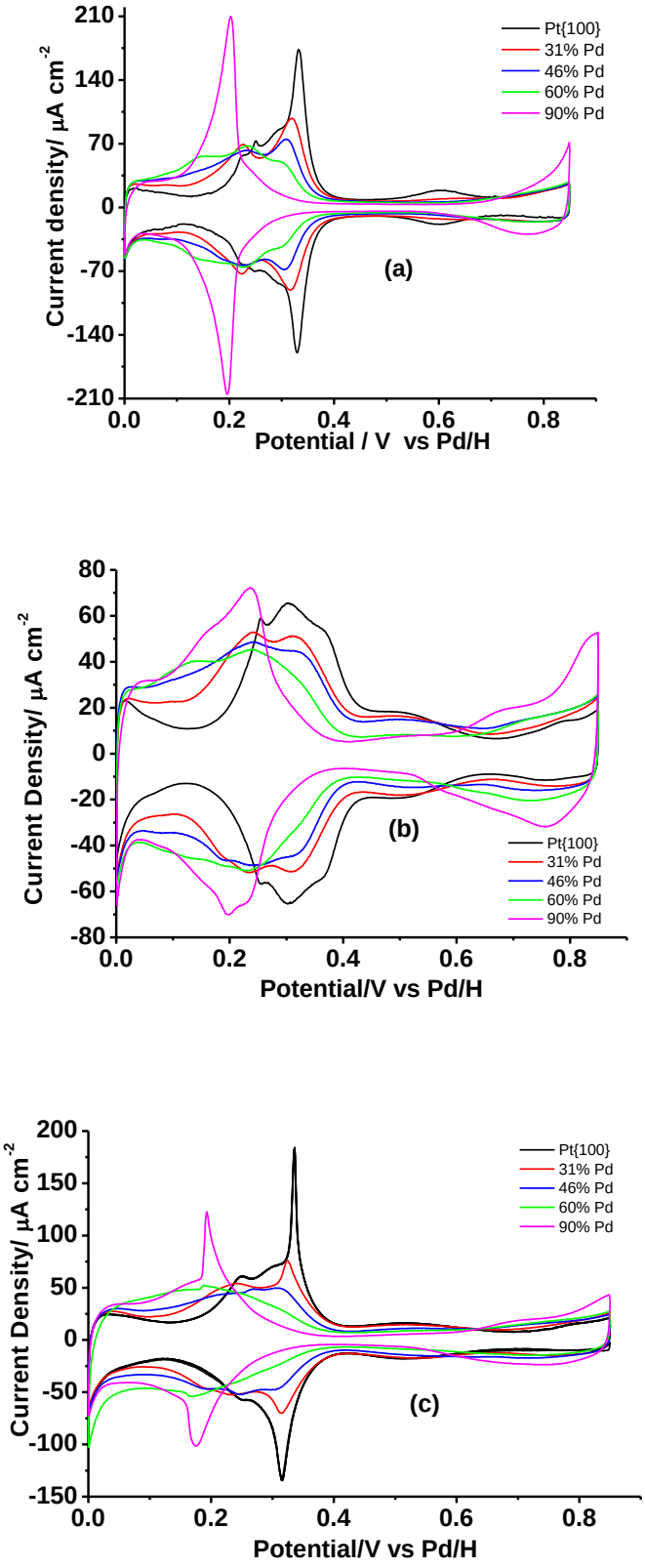

Fig. 5.8 Cyclic voltammograms of PtPd{100} surface alloys as a function of palladium coverage in monolayers. Sweep rate = 50 mV/s and (a) 0.1 M aqueous sulphuric acid, (b) 0.1 M aqueous perchloric acid and (c) nafion-coated electrode in 0.1 M aqueous perchloric acid electrolyte.

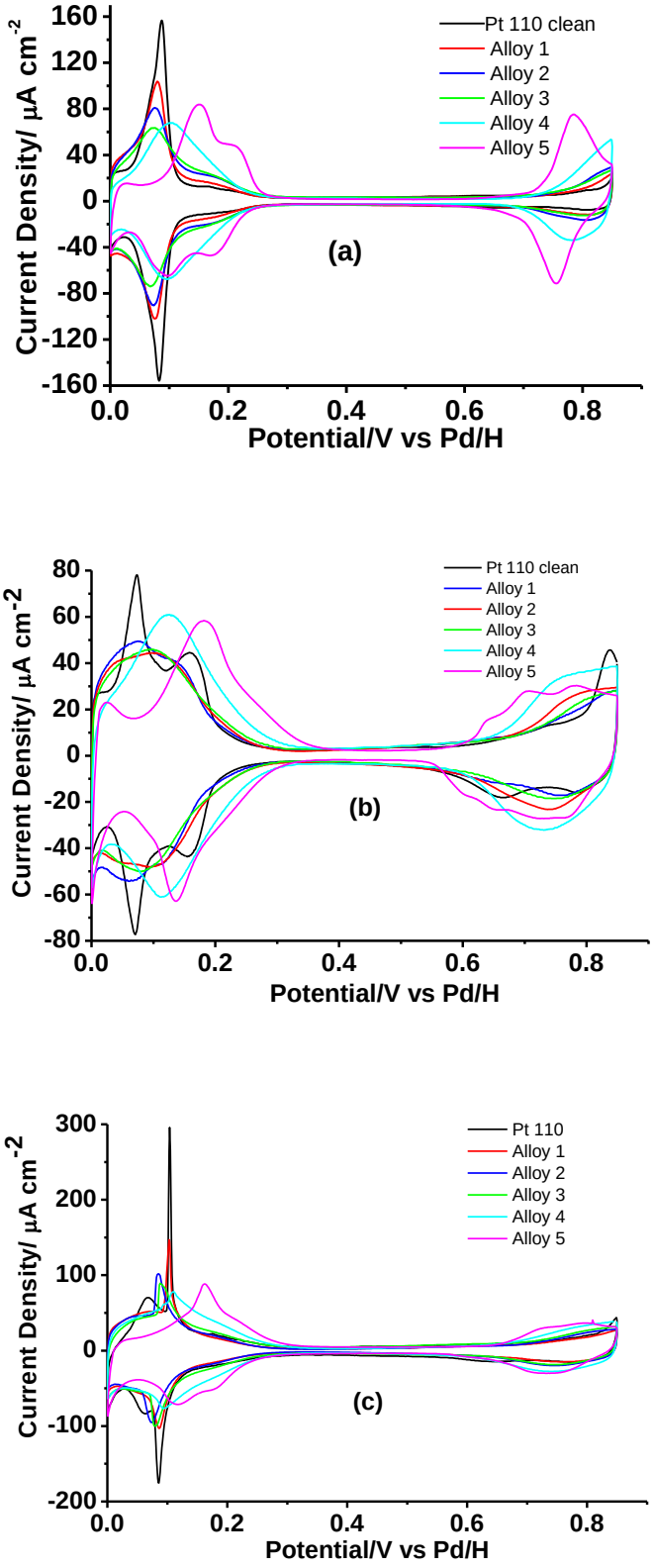

Fig. 5.9 Cyclic voltammograms of PtPd{110} surface alloys as a function of palladium coverage in monolayers. Sweep rate = 50 mV/s and (a) 0.1 M aqueous sulphuric acid, (b) 0.1 M aqueous perchloric acid and (c) nafion-coated electrode in 0.1 M aqueous perchloric acid electrolyte.

The final sequence of PdPt{110} alloys (figure 5.9) followed a similar pattern to the other basal planes. In aqueous sulphuric acid, figure 5.9a, as palladium coverage increased the Pt{110} peak in the H_{UPD} decreased and shifted positive in potential. Eventually a structure indicative of palladium adsorbed onto Pt{110} was formed[56]. The amount of adsorbed oxide was enhanced and brought to lower potential with increasing palladium coverage. The same effect was also observed in perchloric acid (figure 5.9b), however Pd H_{UPD} and Pd-OH features were not as well defined as in sulphuric acid.

The Nafion coated alloy surfaces resembled components of sulphuric and perchloric acid solutions and are presented in figure 5.9c. The same pattern was observed as before in sulphuric and perchloric acid solutions, where the sulphonate spike reduces in magnitude and disappears as bulk palladium is produced. Enhancement of the oxide region occurs as palladium coverage is increased as well. The Pd H_{UPD} feature in the Nafion coated CV resembles more closely the feature in the sulphuric acid CVs but the oxide feature resembles that of the percloric acid CVs.

5.2.3 Bismuth deposition on Nafion free and Nafion coated low Miller index platinum single crystal electrodes

Before studying the effects of bismuth deposition onto the Nafion coated electrodes, it was first necessary to understand the effects of bismuth adsorption onto Nafion free electrodes in 0.1M H_2SO_4 and $HClO_4$ electrolyte solutions. Adsorption of bismuth onto Nafion free Pt{111} in 0.1M H_2SO_4 and $HClO_4$ are shown in figures 5.21 and 5.23. Progressive deposition of bismuth onto Pt{111} leads to attenuation of all hydrogen adsorption states corresponding to terrace sites. The electrochemical characterisation of bismuth on Pt{111} is well-developed[57-62] and has been corroborated by UHV studies[63].

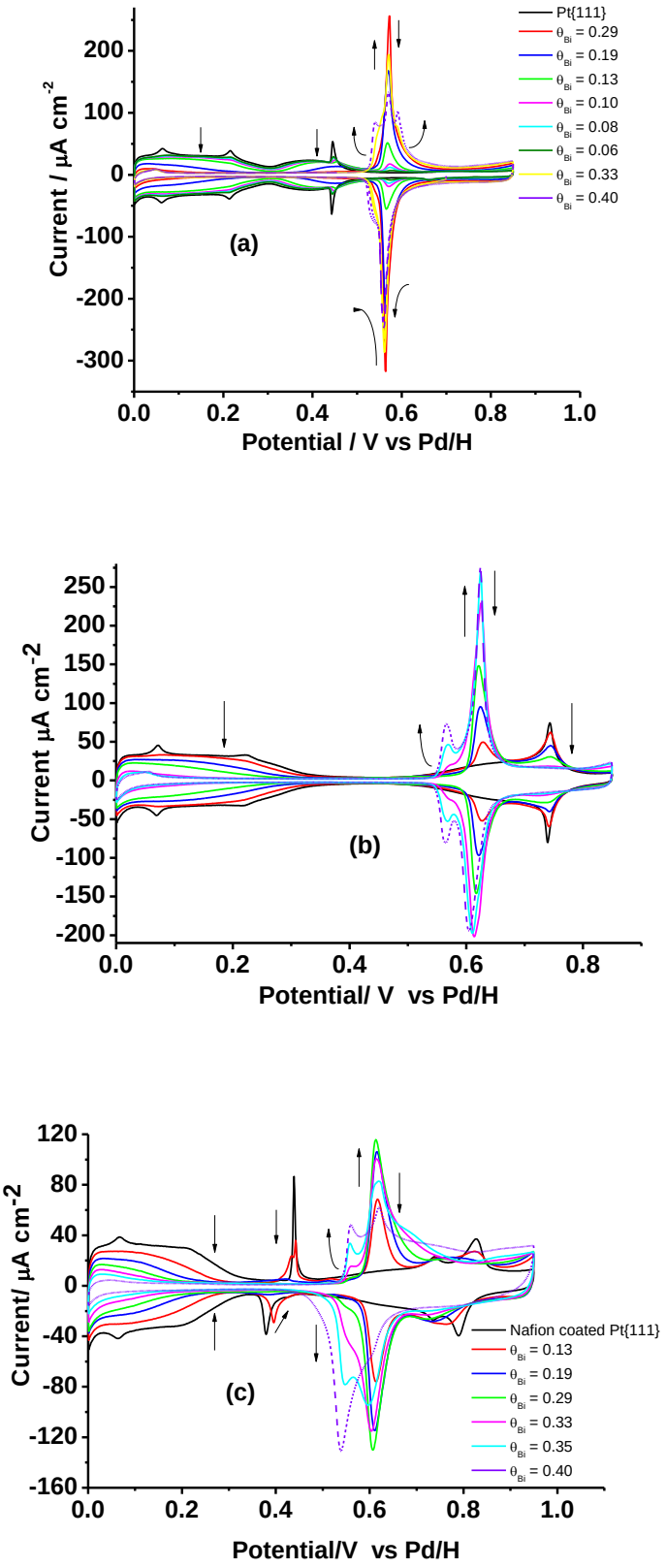

Fig 5.10 Cyclic voltammograms of Pt{111} as a function of bismuth coverage in monolayers. Sweep rate = 50 mV/s and (a) 0.1 M aqueous sulphuric acid, (b) 0.1 M aqueous perchloric acid and (c) nafion-coated electrode in 0.1 M aqueous perchloric acid electrolyte.

From figure 5.10a it is clearly seen that bismuth adsorption leads to the attenuation of the H_{UPD} region and sulphate spike at 0.44 V, culminating in the formation of a single bismuth redox peak at 0.56 V, characteristic of bismuth adsorbed on Pt{111} terraces. This peak grows in magnitude and broadens slightly until all of the H_{UPD} sites are blocked at a coverage of bismuth of 0.33 monolayers. A plot of residual charge in the H_{UPD} versus the charge under the bismuth oxide peak (figure 5.11) can be used to estimate the number of hydrogen sites blocked by bismuth and the overall number of electrons transferred[64]. The plot, (figure 5.11 shows residual hydrogen charge decreases as bismuth oxide charge increases), is in good agreement with Evans and Attard[64], where one bismuth adatom blocks three H_{UPD} sites[58,63-65 66-69], which is also in good agreement with *ex situ* LEED studies that report a $\sqrt{3}$ x $\sqrt{3}R30^{O}$ surface structure for a bismuth coverage of 0.33 monolayers[66].

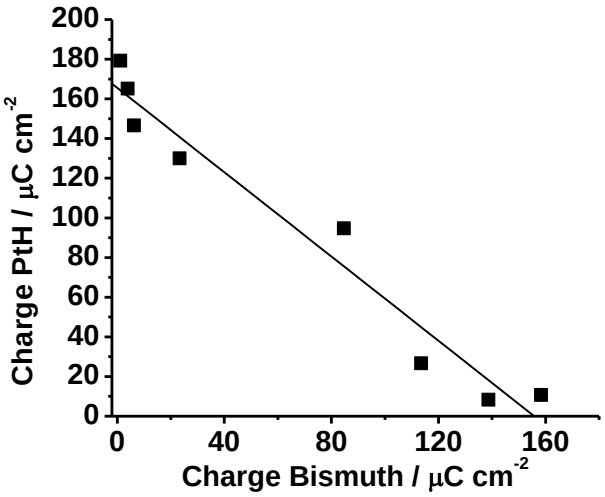

Figure 5.11 plot of residual hydrogen charge *vs* bismuth oxide redox charge for Pt{111}.

For all surfaces, bismuth coverage is defined via residual H_{UPD} charge, expression 5.1 can be used[67]:

$$\theta_{Bi} = \frac{(Q_0^H - Q^H)}{3Q_0^H} \qquad \text{(eq 5.1)}$$

where θ_0^H is the the maximum amount of charge associated with the clean surface and θ^H is the residual charge of the bismuth decorated surface. For $\theta_{Bi} > 0.33$ monolayers, the surface redox peak splits into components at more negative and more positive potentials. Also a small bump forms in the $H_{UPD,}$ this can be discerned in the purple curve of Fig 5.1a.

A similar story is observed in $HClO_4$ but there is a difference when bismuth coverage exceeds 0.33 monolayers (a second bismuth redox peak is seen (figure 5.10b)). Initial bismuth adsorption leads to attenuation of the Pt-OH peak at 0.75 V *vs* Pd/H and the formation of a bismuth redox peak at 0.62 V *vs* Pd/H, this peak reaches a maximum when all the H_{UPD} sites are blocked. Once this peak reaches a maximum a second Bi redox peak forms at 0.58 V, coupled with a small 'bump' forming in the H_{UPD} at 0.02 V *vs* Pd/H which indicates the formation of Bi in a compressed, close packed adlayer (coverage approximately 0.5 monolayers)[64]. Addition of bismuth to higher loadings results in multilayer peaks of bismuth islands between 0.1 and 0.6 V (not shown) which are readily stripped off the electrode surface with multiple potential cycles within the potential range shown in the figures.

Bismuth deposition on Nafion coated Pt{111} is reported in Figure 5.10c. Deposition of Nafion onto Pt{111} has been reported in chapter 3 section 3.2.2 and analysis was performed in chapter 4. The bismuth CVs were first characterised in 0.1M H_2SO_4 and after rinsing, was transferred to a 0.1M $HClO_4$ solution. The results in figure 5.10c are similar to the results in figs 5.10a and 5.10b. The H_{UPD} is initially quenched along with the Nafion sulphonate spike (0.44 V *vs* Pd/H), similar to sulphuric acid where all H_{UPD} and bisulphate butterfly sites are equally quenched during bismuth deposition. As before, the Bi redox peak forms at 0.62 V *vs* Pd/H and whilst H_{UPD} sites are blocked. Similarly to both sulphuric and perchloric acid electrolytes, a second Bi redox peak forms at 0.58 V when the first bismuth oxide electrosorption peak reaches a maximum, this is also coupled with the small bump that forms in the H_{UPD} region signifying the formation of compressed bismuth adlayers with a coverage of approximately 0.5 monolayers. When comparing to figure 5.10b, (Bi adsorption in 0.1M $HClO_4$), it can be seen that the bismuth redox peaks are much smaller in magnitude and are broader, the H_{UPD} region however is unaffected.

Figures 5.12a and 5.12b show the effect of Bi adsorption on Pt{100} in different acid media. For Pt{100}, the voltamograms in both sulphuric and perchloric acid show a stark similarity. For both electrolytes bismuth adsorption results in first the attenuation of the H_{UPD} followed by the formation of the bismuth redox peak between 0.88 - 0.9 V. The plot in figure 5.13 shows residual hydrogen charge decreases as bismuth oxide charge increases.

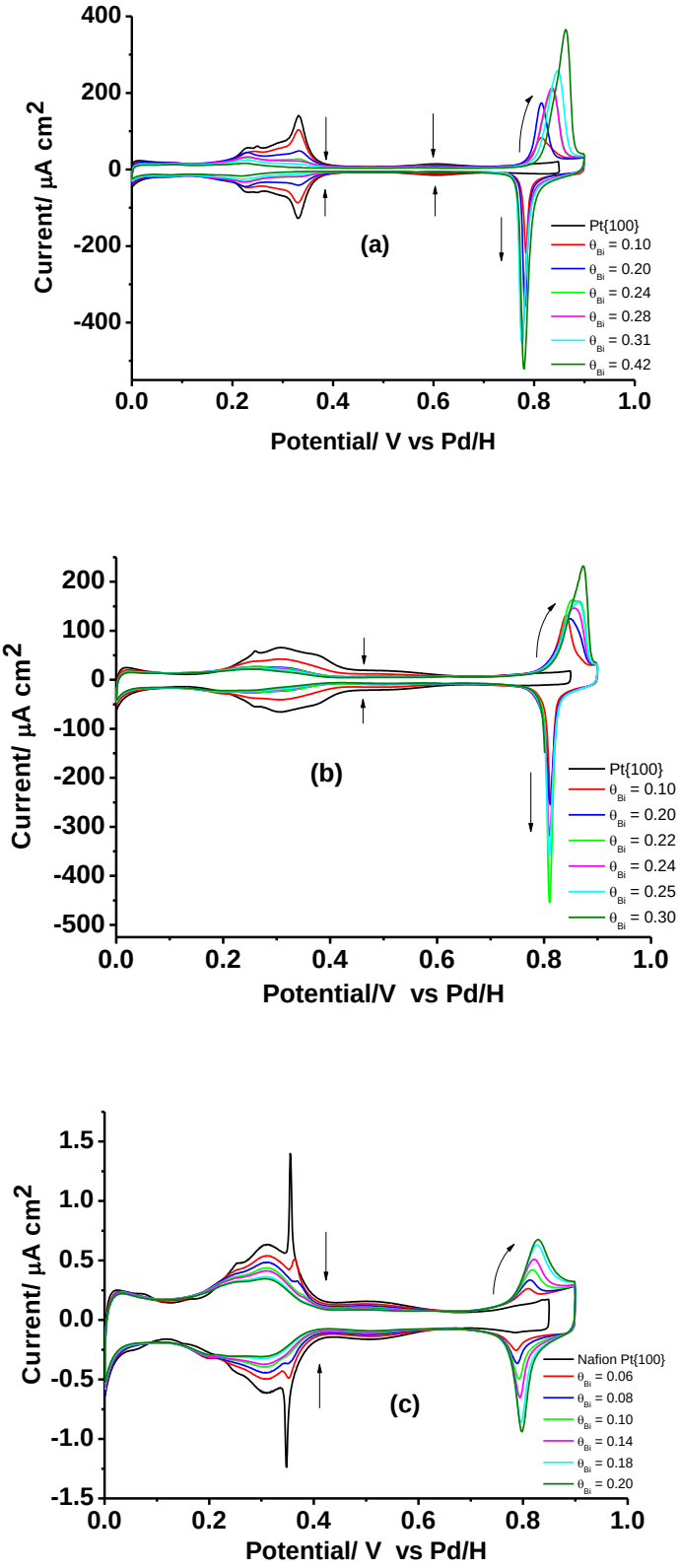

Fig 5.12 Cyclic voltammograms of Pt{111} as a function of bismuth coverage in monolayers. Sweep rate = 50 mV/s and (a) 0.1 M aqueous sulphuric acid, (b) 0.1 M aqueous perchloric acid and (c) nafion-coated electrode in 0.1 M aqueous perchloric acid electrolyte.

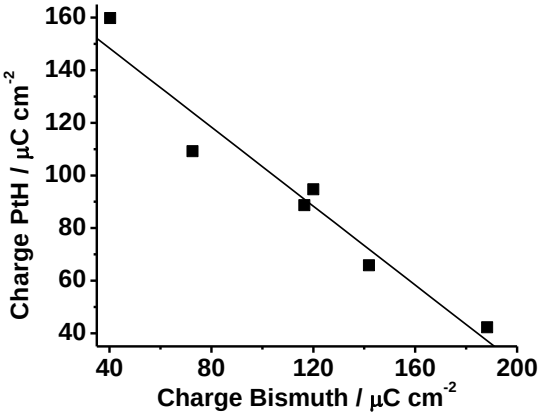

Figure 5.13 plot of residual hydrogen charge of Pt{100} *vs* growth in bismuth oxide charge.

For bismuth adsorption on Pt{100}, Stuve et al[68] have already shown by LEED that a c(2×2) adlayer is formed at 0.5 monolayers. The CV data suggests strongly that bismuth is growing as islands which eventually coalesce and block all H UPD processes at 0.5 monolayers. Island growth of bismuth is signified by the presence of the long range (1×1) Pt {100} terrace peak (extended two dimensional terraces) at 0.33 V is observed even at highest bismuth loading (0.5 monolayers[58]). If bismuth was spreading out across the surface, it would break up this long-range order, as it does in Pt{111}, see above. Hence although bismuth adatoms exhibit repulsive nearest-neighbour lateral interactions, densely packed c(2×2) islands must be forming. This is in accordance with previous UHV studies by Campbell et al. for bismuth on Pt{111}[63]. This behaviour contrasts with bismuth on Pt{111} since here, the long-range order associated with the "spike" at 0.42 V, together with its associated secondary structure, is modified strongly at all bismuth coverages, indicating wide dispersion of bismuth across the surface.

Bi adsorption on the Nafion coated surface in aqueous perchloric acid (fig 5.12c) shows a very similar trend to bismuth adsorption characterised in figures 5.12a - 5.12b. First the H_{UPD} is blocked followed by the bismuth redox peak forming at a higher potential. The presence of the Nafion induced sulphonate spike at 0.35 V implies that bismuth is forming densely packed islands on the surface just like the Nafion free surfaces. However, unlike the Nafion coated Pt{111} electrode, the bismuth redox peak of the Nafion coated Pt{100} is not sharper when compared to figure 5.12b of Pt{100} in 0.1M $HClO_4$. In fact it is much smaller and broader in size although, like for sulphuric acid, the peak potential on the negative – going sweep at 0.8 V *vs* Pd/H is slightly more negative than for perchloric (more like in sulphuric

acid at 0.78 V *vs* Pd/H). The low intensity of the bismuth redox peak is due to the low coverage of bismuth attained as signified by the significant H UPD peaks remaining.

For Pt{110}, in both electrolytes bismuth adsorption (fig 5.28 - 5.29) results in the attenuation of the H_{UPD} regions. In sulphuric acid (figure 5.28), the broad bismuth redox feature at 0.7 V is likely to be due to the dissolution of bismuth from the surface**.** Figure 5.29 of bismuth adsorption on Pt{110} is very similar to the figure 5.28. For Pt{110}, it is very difficult to discuss from the CV alone, the range of adsorption sites being blocked, although Hayden and co-workers have reported that Bi on Pt{110}-(1×2) in UHV decorates the "troughs" of the missing row reconstruction first of all and that interatomic repulsions between the adatoms cause the formation of a series of "compression" structures[69]. These structures correspond to the bismuth adatom spacing along the rows decreasing as coverage is increased. Figure 5.30 shows that Bi adsorption on Nafion coated Pt{110} simply results in the attenuation of the H_{UPD}. A key point here for discussion is the quenching of the Nafion spike being correlated with the attenuation of the H_{UPD} peak in perchloric acid at 0.15 V.

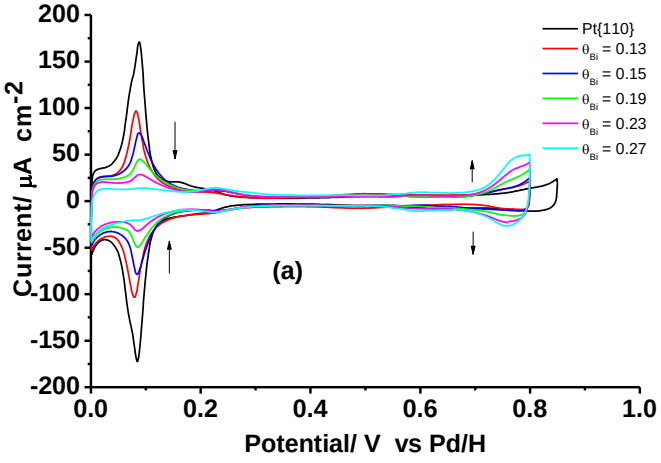

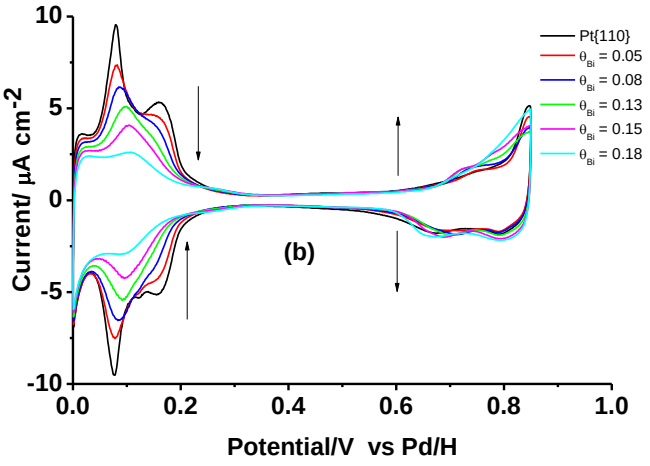

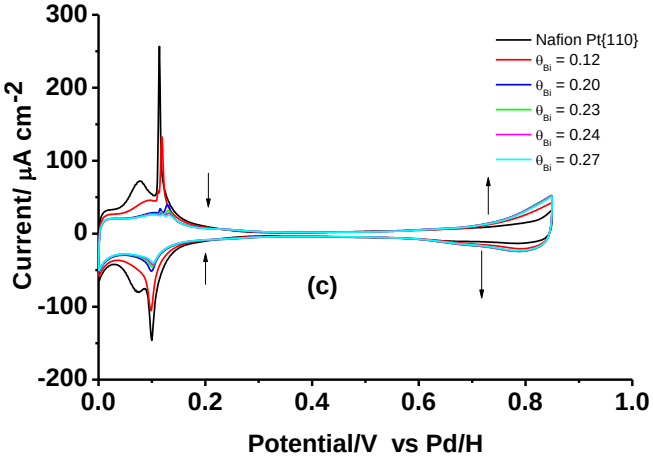

Fig 5.14 Cyclic voltammograms of Pt{111} as a function of bismuth coverage in monolayers. Sweep rate = 50 mV/s and (a) 0.1 M aqueous sulphuric acid, (b) 0.1 M aqueous perchloric acid and (c) nafion-coated electrode in 0.1 M aqueous perchloric acid electrolyte.

5.3 Conclusions

Palladium and bismuth adlayers have been deposited onto Nafion coated and Nafion free Pt*{hkl}* electrodes and were characterised using CV. PtPd*{hkl}* surface alloys were also created characterised and via CV (Nafion free and Nafion coated) as a function of alloy composition. Voltammetric results obtained in this study for Nafion free electrodes were in agreement with previous literature reports[41-43,52,53,55,56,58,60,63,64,68,69]. Voltammograms of palladium adlayers on Nafion free Pt{111} and {100} suggests the growth of palladium islands on the surface with palladium second layer growth occurring before the completion of a full monolayer of palladium. In 0.1M H_2SO_4, growth of first layer palladium is signified by the presence of a sharp electrosorption peak at 0.19 V. A second, broad peak appears at higher palladium loadings representing second and third layer palladium growth on the surface. Growth of second and third layer of palladium is more pronounced on Pt{100} in that it begins at even lower coverages than on Pt{111}. Presumably, the lower diffusion rate of palladium adatoms on the less close-packed surface is a key feature here. In 0.1M $HClO_4$, palladium peaks are much broader compared to H_2SO_4 since specific adsorption is absent. However, on Nafion coated Pt{111} and {100} in 0.1M $HClO_4$ it was found that the CV peak for palladium first layer was much more sharper and resembled more closely the voltammograms in H_2SO_4. This was due to the presence of sulphonate groups of Nafion being specifically adsorbed on the first monolayer of palladium. A similar story was found for platinum-palladium surface alloys. CVs in 0.1M $HClO_4$ showed that where the palladium surface composition was relatively high, Nafion adsorption would produce sharper, more well defined peaks compared to Nafion free alloy CVs. For Pt{111} and {100}, the CVs showed for Nafion coated alloy surfaces that the sulphonate peaks would shift negatively as palladium coverage was increased. This is speculated to be caused by a shift in the PZTC of the surface to more negative values as palladium composition increased, reflecting the lower work function of palladium compared to platinum[70]. CVs of bismuth deposition on clean Pt*{hkl}* resulted in the attenuation of all H_{UPD} peaks and the formation of Bi-OH peak between 0.75 V - 0.9 V depending on the exact nature of the surface structure. It was found that for the Nafion coated surfaces, bismuth deposition would again attenuate H_{UPD} features and produce Bi-OH features at 0.75 V - 0.9 V for the different surfaces. It was interesting to note that attenuation of H_{UPD} features was identical for Nafion free and Nafion coated surfaces but the Bi-OH features for the Nafion coated surfaces exhibited marked differences. For all Pt{110} surfaces, Nafion free or Nafion coated, bismuth or palladium modified or

platinum-palladium surface alloys, would simply result in the attenuation of H_{UPD} features and growth in the oxide region.

5.4 References

(1) Clavilier, J.; Faure, R.; Guinet, G.; Durand, R. *Journal of Electroanalytical Chemistry* **1980**, *107*, 205.

(2) Clavilier, J. *Journal of Electroanalytical Chemistry* **1980**, *107*.

(3) Motoo, S.; Furuya, N. *Berichte Der Bunsen-Gesellschaft-Physical Chemistry Chemical Physics* **1987**, *91*.

(4) Markovic, N. M.; Marinkovic, N. S.; Adzic, R. R. *Journal of Electroanalytical Chemistry* **1988**, *241*, 309.

(5) Clavilier, J.; Elachi, K.; Rodes, A. *Chemical Physics* **1990**, *141*, 1.

(6) Berenz, P.; Tillmann, S.; Massong, H.; Baltruschat, H. *Electrochimica Acta* **1998**, *43*.

(7) Abd El Meguid, E. A.; Berenz, P.; Baltruschat, H. *Journal of Electroanalytical Chemistry* **1999**, *467*.

(8) Clavilier, J.; Rodes, A.; Elachi, K.; Zamakhchari, M. A. *Journal De Chimie Physique Et De Physico-Chimie Biologique* **1991**, *88*.

(9) Gomez, R.; Orts, J. M.; Feliu, J. M.; Clavilier, J.; Klein, L. H. *Journal of Electroanalytical Chemistry* **1997**, *432*.

(10) Cuesta, A.; Kibler, L. A.; Kolb, D. M. *Journal of Electroanalytical Chemistry* **1999**, *466*.

(11) Ruban, A.; Hammer, B.; Stoltze, P.; Skriver, H. L.; Norskov, J. K. *Journal of Molecular Catalysis a-Chemical* **1997**, *115*.

(12) Hammer, B.; Norskov, J. K. *Surface Science* **1995**, *343*.

(13) Kibler, L. A.; El-Aziz, A. M.; Hoyer, R.; Kolb, D. M. *Angewandte Chemie-International Edition* **2005**, *44*.

(14) Schmidt, T. J.; Stamenkovic, V. R.; Lucas, C. A.; Markovic, N. M.; Ross, P. N. *Physical Chemistry Chemical Physics* **2001**, *3*, 3879.

(15) Vidal-Iglesias, F. J.; Solla-Gullon, J.; Herrero, E.; Aldaz, A.; Feliu, J. M. *Journal of Applied Electrochemistry* **2006**, *36*.

(16) Stamenkovic, V. R.; Fowler, B.; Mun, B. S.; Wang, G. F.; Ross, P. N.; Lucas, C. A.; Markovic, N. M. *Science* **2007**, *315*, 493.

(17) Lamy, C.; Leger, J. M.; Clavilier, J.; Parsons, R. *Journal of Electroanalytical Chemistry* **1983**, *150*.

(18) Grozovski, V.; Climent, V.; Herrero, E.; Feliu, J. M. *Physical Chemistry Chemical Physics* **2010**, *12*.

(19) Grozovski, V.; Climent, V.; Herrero, E.; Feliu, J. M. *Journal of Electroanalytical Chemistry* **2011**, *662*.

(20) Acres, G. J. K. *Journal of Power Sources* **2001**, *100*, 60.

(21) Neburchilov, V.; Martin, J.; Wang, H.; Zhang, J. *Journal of Power Sources* **2007**, *169*.

(22) Demirci, U. B. *Journal of Power Sources* **2007**, *169*, 239.

(23) Rhee, Y. W.; Ha, S. Y.; Masel, R. I. *Journal of Power Sources* **2003**, *117*.

(24) Wang, X.; Hu, J. M.; Hsing, I. M. *Journal of Electroanalytical Chemistry* **2004**, *562*.

(25) Mauritz, K. A.; Moore, R. B. *Chemical Reviews* **2004**, *104*, 4535.

(26) Gruger, A.; Regis, A.; Schmatko, T.; Colomban, P. *Vibrational Spectroscopy* **2001**, *26*, 215.

(27) Byun, C. K.; Sharif, I.; DesMarteau, D. D.; Creager, S. E.; Korzeniewski, C. *Journal of Physical Chemistry B* **2009**, *113*, 6299.

(28) Webber, M.; Dimakis, N.; Kumari, D.; Fuccillo, M.; Smotkin, E. S. *Macromolecules* **2010**, *43*, 5500.

(29) Korzeniewski, C.; Adams, E.; Liu, D. *Applied Spectroscopy* **2008**, *62*, 634.

(30) Basnayake, R.; Peterson, G. R.; Casadonte, D. J., Jr.; Korzeniewski, C. *Journal of Physical Chemistry B* **2006**, *110*, 23938.

(31) Malek, K.; Eikerling, M.; Wang, Q.; Liu, Z.; Otsuka, S.; Akizuki, K.; Abe, M. *Journal of Chemical Physics* **2008**, *129*.

(32) Malek, K.; Eikerling, M.; Wang, Q.; Navessin, T.; Liu, Z. *Journal of Physical Chemistry C* **2007**, *111*, 13627.

(33) Zhdanov, V. P. *Physical Review E* **2003**, *67*.

(34) Zhdanov, V. P.; Kasemo, B. *Electrochemistry Communications* **2006**, *8*, 561.

(35) Zhdanov, V. P.; Kasemo, B. *Surface Science* **2004**, *554*, 103.

(36) Schmidt-Rohr, K.; Chen, Q. *Nature Materials* **2008**, *7*, 75.

(37) Ahmed, M.; Morgan, D.; Attard, G. A.; Wright, E.; Thompsett, D.; Sharman, J. *Journal of Physical Chemistry C* **2011**, *115*, 17020.

(38) Ma Gomez-Marin, A.; Berna, A.; Feliu, J. M. *Journal of Physical Chemistry C* **2010**, *114*, 20130.

(39) Subbaraman, R.; Strmcnik, D.; Stamenkovic, V.; Markovic, N. M. *Journal of Physical Chemistry C* **2010**, *114*, 8414.

(40) Baldauf, M.; Kolb, D. M. *Journal of Physical Chemistry* **1996**, *100*.

(41) Alvarez, B.; Climent, V.; Rodes, A.; Feliu, J. M. *Journal of Electroanalytical Chemistry* **2001**, *497*.

(42) Arenz, M.; Stamenkovic, V.; Ross, P. N.; Markovic, N. M. *Surface Science* **2004**, *573*.

(43) Attard, G. A.; Price, R.; Alakl, A. *Electrochimica Acta* **1994**, *39*.

(44) Lebouin, C.; Soldo-Olivier, Y.; Sibert, E.; De Santis, M.; Maillard, F.; Faure, R. *Langmuir* **2009**, *25*.

(45) Hoyer, R.; Kibler, L. A.; Kolb, D. M. *Electrochimica Acta* **2003**, *49*.

(46) Ball, M. J.; Lucas, C. A.; Markovic, N. M.; Stamenkovic, V.; Ross, P. N. *Surface Science* **2002**, *518*.

(47) Attard, G. A.; Price, R.; Alakl, A. *Surface Science* **1995**, *335*.

(48) Alvarez, B.; Feliu, J. M.; Clavilier, J. *Electrochemistry Communications* **2002**, *4*.

(49) Feldberg, S. W.; Rubinstein, I. *Journal of Electroanalytical Chemistry* **1988**, *240*, 1.

(50) Alvarez, B.; Climent, V.; Rodes, A.; Feliu, J. M. *Physical Chemistry Chemical Physics* **2001**, *3*.

(51) Markovic, N. M.; Ross, P. N. *Surface Science Reports* **2002**, *45*.

(52) Alvarez, B.; Berna, A.; Rodes, A.; Feliu, J. M. *Surface Science* **2004**, *573*.

(53) Llorca, M. J.; Feliu, J. M.; Aldaz, A.; Clavilier, J. *Journal of Electroanalytical Chemistry* **1993**, *351*.

(54) Ball, M. J.; Lucas, C. A.; Markovic, N. M.; Stamenkovic, V.; Ross, P. N. *Surface Science* **2003**, *540*.

(55) Vidal-Iglesias, F. J.; Al-Akl, A.; Watson, D.; Attard, G. A. *Journal of Electroanalytical Chemistry* **2007**, *611*.

(56) Vidal-Iglesias, F. J.; Al-Akl, A.; Watson, D. J.; Attard, G. A. *Electrochemistry Communications* **2006**, *8*, 1147.

(57) Smith, S. P. E.; Ben-Dor, K. F.; Abruna, H. D. *Langmuir* **1999**, *15*.

(58) Clavilier, J.; Feliu, J. M.; Aldaz, A. *Journal of Electroanalytical Chemistry* **1988**, *243*.

(59) Blais, S.; Jerkiewicz, G.; Herrero, E.; Feliu, J. M. *Journal of Electroanalytical Chemistry* **2002**, *519*.

(60) Gomez, R.; Feliu, J. M.; Aldaz, A. *Electrochimica Acta* **1997**, *42*.

(61) Ball, M.; Lucas, C. A.; Markovic, N. M.; Murphy, B. M.; Steadman, P.; Schmidt, T. J.; Stamenkovic, V.; Ross, P. N. *Langmuir* **2001**, *17*.

(62) Schmidt, T. J.; Behm, R. J.; Grgur, B. N.; Markovic, N. M.; Ross, P. N. *Langmuir* **2000**, *16*.

(63) Paffett, M. T.; Campbell, C. T.; Taylor, T. N. *Journal of Chemical Physics* **1986**, *85*.

(64) Evans, R. W.; Attard, G. A. *Journal of Electroanalytical Chemistry* **1993**, *345*.

(65) Smith, S. P. E.; Abruna, H. D. *Journal of Physical Chemistry B* **1998**, *102*.

(66) Hamm, U. W.; Kramer, D.; Zhai, R. S.; Kolb, D. M. *Electrochimica Acta* **1998**, *43*.

(67) Hazzazi; Abdullah, O. Electrochemical Studies of Metal Deposition and Surface Chirality at Well-Defined Platinum Single Crystal Electrodes, 2002.

(68) Kizhakevariam, N.; Stuve, E. M. *Journal of Vacuum Science & Technology a-Vacuum Surfaces and Films* **1990**, *8*.

(69) Hayden, B. E.; Murray, A. J.; Parsons, R.; Pegg, D. J. *Journal of Electroanalytical Chemistry* **1996**, *409*.

(70) Attard, G. A.; Hazzazi, O.; Wells, P. B.; Climent, V.; Herrero, E.; Feliu, J. M. *Journal of Electroanalytical Chemistry* **2004**, *568*, 329.

Chapter Six

Methanol and Formic acid Electrooxidation on Nafion Modified Pd/Pt{111}: the Role of Anion Specific Adsorption in Electrocatalytic Activity

6.1 Introduction

A major aspect of electrochemical surface science remains the understanding, at a fundamental molecular level, of the mechanism of the electrooxidation of "small" organic molecules such as formic acid and methanol since results obtained in this approach can impact directly on the design of "real" fuel cell catalysts [1-3]. Moreover, the interface between the supported electrocatalyst and the electrolyte is of crucial concern since transport of reactant, products, water and charge across this region controls the ultimate performance of the fuel cell [4-7]. Single crystal studies in particular [8,9] have emphasised the role of anions in modifying electrocatalytic activity by virtue of their strong adsorption relative to the organic fuel[10]. Nafion is a polymer electrolyte that gives rise to efficient proton conduction when water content/structure and film thickness are optimised[11]. Polymer electrolyte membrane fuel cells (PEMFCs) are considered an attractive means of generating power, particularly in relation to portable power devices and automotive applications[12,13]. Two fuels have dominated the field, namely hydrogen and methanol[14,15]. The hydrogen PEMFC suffers from the need to store and transport hydrogen and also possesses a relatively low gas-phase energy density[16]. DMFCs based on methanol are far superior to hydrogen in terms of energy density per unit volume of fuel. However, methanol-based PEMFCs suffer significantly from the problem of "fuel crossover" through the polymer membrane (usually consisting of Nafion) during operation leading to poor fuel utilisation and this means that only low concentrations of methanol may be fed into the PEMFC thus limiting their effectiveness as energy transducers. In contrast to hydrogen and methanol, formic acid has recently been recognised as an alternative fuel to both of these since it exhibits much reduced fuel crossover problems compared to methanol, contains a significant energy density of its own (though not as high as methanol[16] and can be stored at room temperature as a liquid so does not require cryogenic conditions for storage like hydrogen. In favourable circumstances, the performance of PEMFCs based on formic acid can approach that of a hydrogen PEMFC[16]. In the case of Nafion as electrolyte, because the interface is "buried" within a bulk Nafion matrix, until

recently there was a relative paucity of information regarding the interactions occurring at the electrocatalyst/Nafion interface itself[17-19] although much work has been carried out on the bulk properties of Nafion films and their structure under a variety of experimental conditions[20-23].

Recently, work utilising single crystals has been published in which the influence of Nafion adsorbed on Pt{hkl} under well-defined conditions has been used to shed light on the elusive nature of Nafion adsorbed on platinum as a function of potential and electrolyte[24-26]. From the impact of Nafion on the singular voltammetric response of flat and stepped Pt{hkl} electrodes it was concluded that Nafion physisorbs on platinum but as the charge on the surface of the platinum changes from positive to negative, sulphonate groups of Nafion adsorb causing a significant perturbation upon subsequent surface OH adsorption[24,25]. The electrosorption strength of Nafion sulphonate groups was reported to be intermediate between that of (bi-) sulphate and OH[24,25]. Therefore, the question arises, do sulphonate anions originating from the Nafion polymer cause a similar inhibition in the activity of electrocatalysts towards formic acid and methanol electrooxidation as do electrosorbed anions such as bi-sulphate? In this chapter, this question is directly addessed. Furthermore, the role of palladium coverage in influencing the electrocatalytic activity of Pt{111}[27-29] will be investigated. Palladium on Pt{hkl} is a well-studied system[27-35] and its behaviour in the absence of Nafion depends on the nature of the anion present in the aqueous electrolyte[30]. Palladium exhibits a much stronger interaction with anions than platinum[30] and this is reflected in many of its electrocatalytic properties[31]. There is only one other report of Nafion adsorbed on a bimetallic single crystal surface (PtNi{111}[36]). The present study is the first to report the influence of Nafion on a bimetallic PtPd electrode.

6.2 Results and discussion

6.2.1 Formic acid electrooxidation on Pd/Pt{111}with and without Nafion adsorbed.

Figure 6.1 shows cyclic voltammograms (CVs) collected as a function of Pd coverage on Pt{111} in sulphuric and perchloric acid. Analysis of figure 6.1 was performed in chapter 5 section 5.2.1.

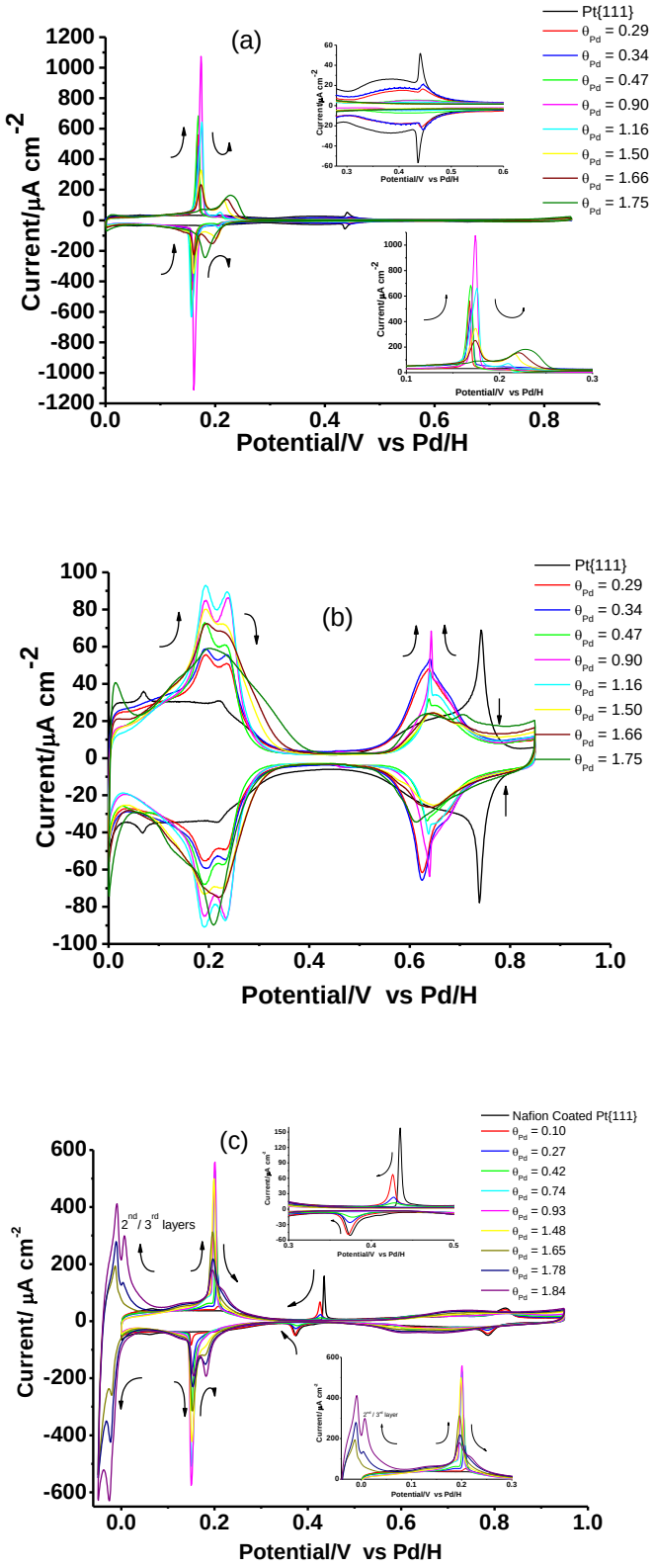

Fig. 6.1 Cyclic voltammograms of Pt{111} as a function of palladium coverage in monolayers. Sweep rate = 50 mV/s and (a) 0.1 M aqueous sulphuric acid, (b) 0.1 M aqueous perchloric acid and (c) Nafion-coated electrode in 0.1 M aqueous perchloric acid electrolyte. In figure 1 (c), 2/3 refers to peak that emerges in hydrogen

evolution potential region when palladium coverage exceeds one monolayer and is therefore ascribed to second and third layer palladium.

Figure 6.2 shows the positive-going potential sweep for a series of Pd/Pt{111}bimetallic electrode surfaces undergoing formic acid electrooxidation (0.1 M HCOOH).

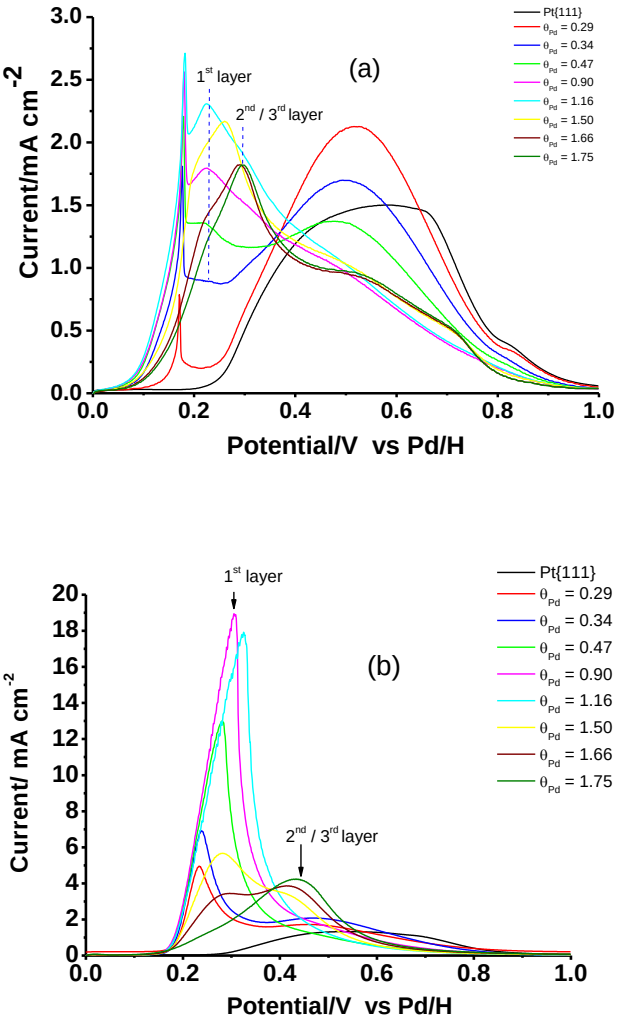

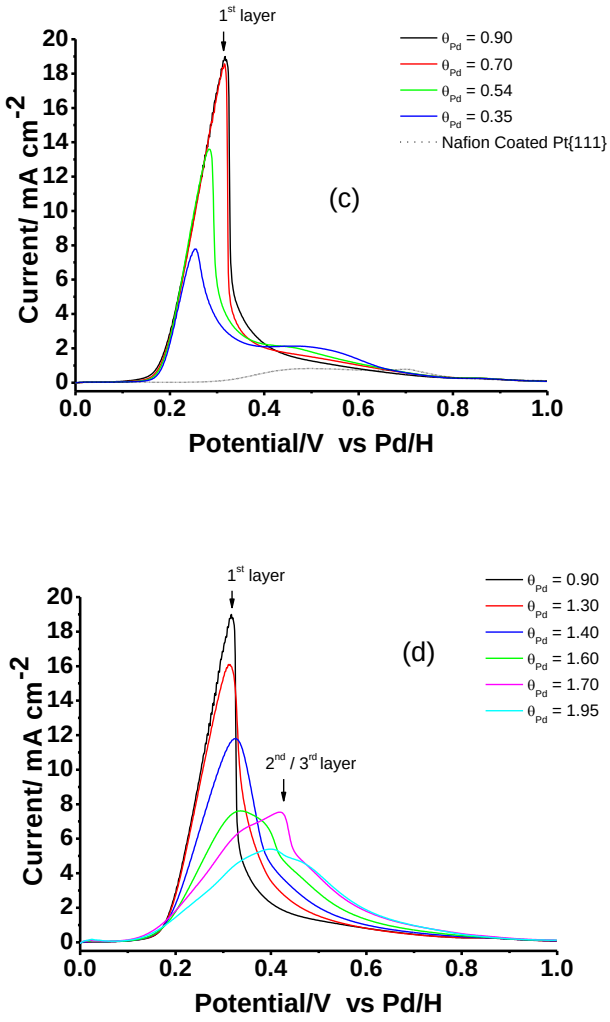

Fig. 6.2. 0.1 M HCOOH electrooxidation voltammetry as a function of palladium coverage in monolayers. Sweep rate = 50 mV/s and (a) 0.1 M aqueous sulphuric acid, (b) 0.1 M aqueous perchloric acid, (c) Nafion-coated Pt{111} in 0.1 M aqueous perchloric acid electrolyte for $\theta_{Pd} < 1$ monolayer and (d) same as (c) but for $\theta_{Pd} > 1$ monolayer.

As discussed in chapter 5 section 5.2.1, each electrolyte will therefore exhibit a different extent of anion interaction in the presence of a constant concentration of formic acid. In figure 6.2 (a) it is seen that the onset of electrooxidation occurs just positive of 0.2 V when the last vestiges of adsorbed hydrogen are desorbing from the Pt{111} surface. As palladium coverage increases, the onset of HCOOH electrooxidation is seen to shift to more negative potentials, the magnitude of the shift being commensurate with the difference in pztc values between clean Pt{111} and Pd/Pt{111} in sulphuric acid[37,38]. On Pt{111} a broad maximum in HCOOH electrooxidation current is observed between 0.5 and 0.7 V as reported

previously[39,40]. Low coverages of palladium (< 0.3 monolayers) lead to an increase in formic acid electrooxidation current in this potential range but subsequent palladium additions quench surface activity. We ascribe electrooxidation in this potential range to free platinum sites. The small apparent increase in activity observed for small palladium dosages is probably due to the convolution of two processes:

i) HCOOH electrooxidation on free platinum sites,
ii) HCOOH electrooxidation on palladium islands (peak at 0.22 V indicated on figure as 1st layer Pd) which give rise to currents that overlap with the free platinum sites region (0.4 - 0.8 V).

The sharp H UPD peak associated with first layer palladium at 0.18 V (figure 6.1 (a)) is hardly perturbed by reaction with HCOOH (figure 6.2 (a)) indicative of a rather small surface coverage of adsorbed HCOOH species. The appearance of a second HCOOH peak maximum at 0.28 V is correlated with palladium in the second/third monolayer. When the data in figures 6.2 (a) and (b) are compared, it is seen that the HCOOH electrooxidation currents on palladium in perchloric acid are almost an order of magnitude larger. This exemplifies the influence of a strongly adsorbing anion ((bi-) sulphate) competing successfully for HCOOH adsorption sites and its impact on electrocatalytic activity. In the absence of such a strong specific adsorption (perchloric acid), electrooxidation current is enhanced. This finding is in complete agreement with previous studies[41,42] indicating that palladium adlayers on Pt{111} can significantly enhance electrocatalytic activity for HCOOH electrooxidation in perchloric acid. Again, figure 6.2 (b) highlights the sensitivity of HCOOH electrooxidation to the overall morphology of the palladium film with discrete peaks being observed for regions of clean Pt{111}, first and second/third layer palladium (centred at 0.5 – 0.6, 0.2 - 0.3 and 0.43 V respectively). What is also evident from figure 6.2 (b) is the greater activity exhibited by the first palladium monolayer relative to atoms in the second monolayer as signified by the drop in absolute current when the coverage of palladium exceeds one monolayer.

The changes induced upon the behaviour depicted in figure 6.2 (b) by forming a Nafion adlayer are shown in figures 6.2 (c) and (d). It is seen that despite the HCOOH electrooxidation peak from Nafion on first layer palladium on Pt{111} exhibiting a slightly narrower peak width at half maximum than observed in perchloric acid alone, all the features of figure 6.2 (b) are reproduced with singular reaction potential ranges for clean Pt{111}, first, second/third palladium adlayers almost identical to behaviour recorded using Nafion-

free surfaces. The narrowing of the HCOOH electrooxidation peak for first layer palladium may be related to the stronger interaction of sulphonate with the palladium compared to perchlorate anions but evidently, this interaction is of insufficient intensity to block HCOOH adsorption.

Figure 6.3 summarises this set of results for HCOOH electrooxidation as a function of palladium coverage.

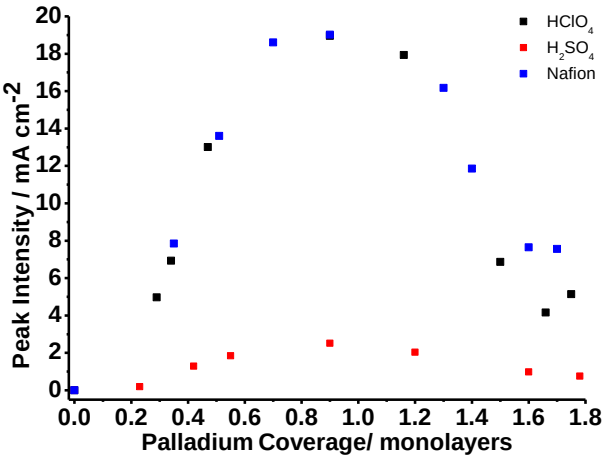

Fig. 6.3 HCOOH peak current for HCOOH electrooxidation as a function of palladium coverage.

It is evident that the high activity of a palladium monolayer on Pt{111} is reflected irrespective of the adsorbing anion. However, activity in sulphuric acid is significantly reduced as compared with the non-specifically adsorbing medium perchloric acid. Astonishingly, specific adsorption of sulphonate anions from Nafion upon the palladium adlayer hardly changes activity in perchloric acid. This indicates that the order of adsorption strength for the various double layer anions and HCOOH on palladium monolayer islands is:

perchlorate < Nafion sulphonate < HCOOH < (bi-) sulphate

6.2.2 Methanol electrooxidation on Pd/Pt{111} with and without Nafion adsorbed

Figure 6.4 shows methanol electrooxidation behaviour (0.1 M MeOH) as a function of palladium coverage on Pt{111} for aqueous acidic (bi-) sulphate, perchlorate and Nafion electrolytes.

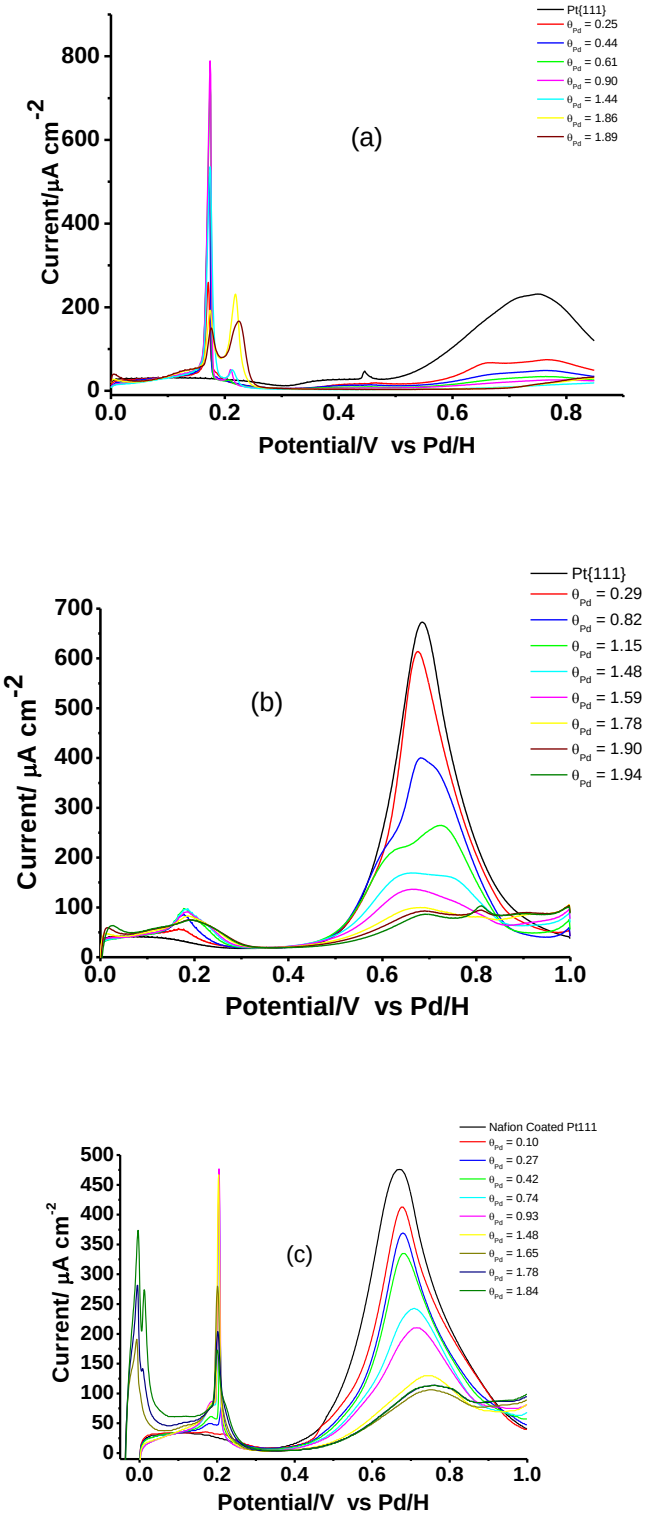

Fig. 6.4 0.1 M CH_3OH electrooxidation voltammetry as a function of palladium coverage in monolayers. Sweep rate = 50 mV/s and (a) 0.1 M aqueous sulphuric acid, (b) 0.1 M aqueous perchloric acid, (c) Nafion-coated Pt{111} in 0.1 M aqueous perchloric acid electrolyte.

In contrast to figure 6.2, the trends in methanol electrooxidation peak intensity as palladium coverage increases suggests rapid de-activation of the electrode surface towards methanol electrooxidation irrespective of the nature of the anion involved. This highlights the differences between the mechanisms of methanol and formic acid electrooxidation on platinum and palladium and has been noted elsewhere[43-45]. Although in both cases a so-called "dual pathway" mechanism has been postulated involving various types of "reactive" and "poisoning" (usually adsorbed CO) reaction intermediate, clearly the nature of the adsorbed reactive intermediate is different in both cases[43-45]. A key aspect of the methanol activation mechanism is the need to facilitate C-H bond dissociation at the methyl substituent[43-45]. Platinum, especially under aqueous acidic conditions may undertake this transformation more readily than palladium[46]. The relatively small perturbation of Pd H UPD peaks by methanol adsorption (potentials < 0.3 V) is also a common feature of all electrolytes used confirming the poor reactivity of the palladium adlayer towards methanol activation. Furthermore, it is evident from the data that specific adsorption of anions may also be playing a part in controlling electrocatalytic activity. In figure 6.5, the methanol electrooxidation peak current density is plotted as a function of palladium coverage for the three different electrolytes.

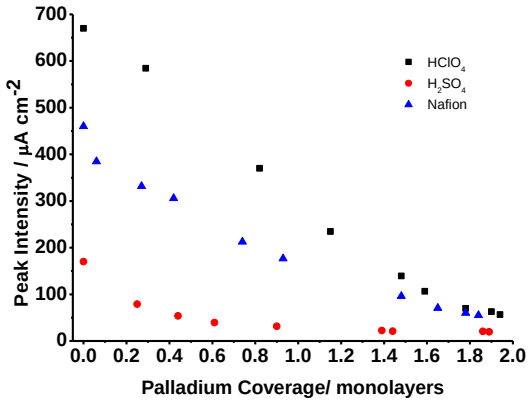

Fig. 6.5 CH_3OH peak current for CH_3OH electrooxidation as a function of palladium coverage**.**

As in figure 6.3, maximum electrooxidation rates are observed in perchloric acid and minimum electrooxidation rates in aqueous sulphuric acid. However, in contrast to figure 6.3, the data for methanol electrooxidation in perchloric acid but with a Nafion layer attached to the electrode show a substantial lowering in methanol peak intensity relative to Nafion-free surfaces in perchloric acid. This indicates that methanol cannot compete as easily for Pt sites when Nafion is present and contrasts with HCOOH in this regard. Hence, the following order of activity under aqueous acidic conditions for species at 0.1 M concentration is suggested:

Perchlorate < methanol < Nafion sulphonate < HCOOH < (bi-) sulphate

This requires a revision of the potential utility of Nafion as a polymeric proton conductor in direct methanol fuel cells. Irrespective of problems of "crossover", the specific interaction of Nafion sulphonate groups with the electrode surface would disfavour methanol adsorption and Nafion would therefore be deleterious to effective methanol electrooxidation in a fuel cell. In contrast, Nafion appears to be an ideal candidate as a proton exchange membrane for fuel cells based of formic acid since the reaction intermediate in this case competes successfully for metal sites on the anode against specific adsorption of sulphonate.

6.3 Conclusions

The changes in the electrocatalytic activity of palladium adlayers on Pt{111} towards methanol and formic acid electrooxidation as a consequence of nafion adsorption are reported. For formic acid, Nafion adsorption results in negligible attenuation in electrooxidation currents compared to those found using acidic aqueous perchloric acid electrolyte. This suggests that specific adsorption of the sulphonate anions of the polymer does not interfere with the adsorption and subsequent surface decomposition of formic acid at Pd/Pt{111} electrodes. In contrast, methanol electrooxidation in perchloric acid is significantly inhibited when nafion is also adsorbed indicating that competition for surface sites between specifically adsorbed sulphonate anions and methanol is important in determining electrode activity. Both of these factors highlight the potential utility of nafion in fuel cells based on formic acid and methanol in that little adverse influence should be expected in the former whereas the intrinsic activity of the methanol fuel cell could be compromised.

6.4 References

(1) Lamy, C.; Leger, J. M.; Clavilier, J.; Parsons, R. *Journal of Electroanalytical Chemistry* **1983**, *150*.

(2) Grozovski, V.; Climent, V.; Herrero, E.; Feliu, J. M. *Journal of Electroanalytical Chemistry* **2011**, *662*.

(3) Grozovski, V.; Climent, V.; Herrero, E.; Feliu, J. M. *Physical Chemistry Chemical Physics* **2010**, *12*.

(4) Neburchilov, V.; Martin, J.; Wang, H.; Zhang, J. *Journal of Power Sources* **2007**, *169*.

(5) Demirci, U. B. *Journal of Power Sources* **2007**, *169*, 239.

(6) Rhee, Y. W.; Ha, S. Y.; Masel, R. I. *Journal of Power Sources* **2003**, *117*.

(7) Wang, X.; Hu, J. M.; Hsing, I. M. *Journal of Electroanalytical Chemistry* **2004**, *562*.

(8) Markovic, N. M.; Ross, P. N. *Surface Science Reports* **2002**, *45*.

(9) Magnussen, O. M. *Chemical Reviews* **2002**, *102*.

(10) Tripkovic, D. V.; Strmcnik, D.; van der Vliet, D.; Stamenkovic, V.; Markovic, N. M. *Faraday Discussions* **2008**, *140*.

(11) Schmidt-Rohr, K.; Chen, Q. *Nature Materials* **2008**, *7*, 75.

(12) Carrette, L.; Friedrich, K. A.; Stimming, U. *Chemphyschem* **2000**, *1*, 162.

(13) Acres, G. J. K. *Journal of Power Sources* **2001**, *100*, 60.

(14) Arico, A. S.; Srinivasan, S.; Antonucci, V. *Fuel Cells* **2001**, *1*, 133.

(15) Song, C. S. *Catalysis Today* **2002**, *77*.

(16) Yu, X.; Pickup, P. G. *Journal of Power Sources* **2008**, *182*.

(17) Zhdanov, V. P. *Physical Review E* **2003**, *67*.

(18) Zhdanov, V. P.; Kasemo, B. *Electrochemistry Communications* **2006**, *8*, 561.

(19) Zhdanov, V. P.; Kasemo, B. *Surface Science* **2004**, *554*, 103.

(20) Wescott, J. T.; Qi, Y.; Subramanian, L.; Capehart, T. W. *Journal of Chemical Physics* **2006**, *124*.

(21) Gruger, A.; Regis, A.; Schmatko, T.; Colomban, P. *Vibrational Spectroscopy* **2001**, *26*, 215.

(22) Webber, M.; Dimakis, N.; Kumari, D.; Fuccillo, M.; Smotkin, E. S. *Macromolecules* **2010**, *43*, 5500.

(23) Kanamura, K.; Morikawa, H.; Umegaki, T. *Journal of the Electrochemical Society* **2003**, *150*.

(24) Ahmed, M.; Morgan, D.; Attard, G. A.; Wright, E.; Thompsett, D.; Sharman, J. *Journal of Physical Chemistry C* **2011**, *115*, 17020.

(25) Subbaraman, R.; Strmcnik, D.; Stamenkovic, V.; Markovic, N. M. *Journal of Physical Chemistry C* **2010**, *114*, 8414.

(26) Ma Gomez-Marin, A.; Berna, A.; Feliu, J. M. *Journal of Physical Chemistry C* **2010**, *114*, 20130.

(27) Baldauf, M.; Kolb, D. M. *Journal of Physical Chemistry* **1996**, *100*.

(28) Kibler, L. A.; El-Aziz, A. M.; Hoyer, R.; Kolb, D. M. *Angewandte Chemie-International Edition* **2005**, *44*.

(29) Attard, G. A.; Bannister, A. *Journal of Electroanalytical Chemistry* **1991**, *300*.

(30) Alvarez, B.; Climent, V.; Rodes, A.; Feliu, J. M. *Journal of Electroanalytical Chemistry* **2001**, *497*.

(31) Arenz, M.; Stamenkovic, V.; Ross, P. N.; Markovic, N. M. *Surface Science* **2004**, *573*.

(32) Attard, G. A.; Price, R.; Alakl, A. *Electrochimica Acta* **1994**, *39*.

(33) Lebouin, C.; Soldo-Olivier, Y.; Sibert, E.; De Santis, M.; Maillard, F.; Faure, R. *Langmuir* **2009**, *25*.

(34) Hoyer, R.; Kibler, L. A.; Kolb, D. M. *Electrochimica Acta* **2003**, *49*.

(35) Ball, M. J.; Lucas, C. A.; Markovic, N. M.; Stamenkovic, V.; Ross, P. N. *Surface Science* **2002**, *518*.

(36) Subbaraman, R.; Strmcnik, D.; Paulikas, A. P.; Stamenkovic, V. R.; Markovic, N. M. *Chemphyschem* **2010**, *11*, 2825.

(37) Alvarez, B.; Feliu, J. M.; Clavilier, J. *Electrochemistry Communications* **2002**, *4*.

(38) Alvarez, B.; Climent, V.; Rodes, A.; Feliu, J. M. *Physical Chemistry Chemical Physics* **2001**, *3*.

(39) Vidal-Iglesias, F. J.; Solla-Gullon, J.; Herrero, E.; Aldaz, A.; Feliu, J. M. *Journal of Applied Electrochemistry* **2006**, *36*.

(40) Llorca, M. J.; Feliu, J. M.; Aldaz, A.; Clavilier, J. *Journal of Electroanalytical Chemistry* **1994**, *376*.

(41) Arenz, M.; Stamenkovic, V.; Schmidt, T. J.; Wandelt, K.; Ross, P. N.; Markovic, N. M. *Physical Chemistry Chemical Physics* **2003**, *5*, 4242.

(42) Lu, G. Q.; Crown, A.; Wieckowski, A. *Journal of Physical Chemistry B* **1999**, *103*.

(43) Cohen, J. L.; Volpe, D. J.; Abruna, H. D. *Physical Chemistry Chemical Physics* **2007**, *9*.

(44) Sriramulu, S.; Jarvi, T. D.; Stuve, E. M. *Journal of Electroanalytical Chemistry* **1999**, *467*.

(45) Herrero, E.; Chrzanowski, W.; Wieckowski, A. *Journal of Physical Chemistry* **1995**, *99*.

(46) Ferrin, P.; Mavrikakis, M. *Journal of the American Chemical Society* **2009**, *131*, 14381.

Chapter Seven

Surface Structural Characterisation of Platinum High Surface Area (HSA) Electrocatalysts

7.1 Introduction

Electrocatalytic reactions are often structure sensitive i.e. the distribution of different surface adsorption sites has a profound influence on the rate and selectivity of the electrocatalytic reaction being studied[1,2]. Well-known examples are the oxidation of formic acid and methanol on Pt{*hkl*}electrodes, in which appreciable current density values are measured on Pt{111} electrodes in comparison to Pt{100} or Pt{110} samples under the same experimental conditions[3,4]. As a consequence, the use of surfaces with the appropriate structure would lead to a better use of the electrocatalyst, which usually is based on expensive, rare, transition metal nanoparticles. The first step to improve the properties of the surface of such electrocatalysts is to have tools that could be used to monitor the presence of the different types of sites on their surface. To be effective, the surface control should be made, if possible, under conditions as similar as possible to those in the reaction and provide general information of the whole surface, different to that which could be garnered from local probes, usually limited to the examination of a limited number of nanoparticles such as transmission electron microscopy or scanning electron microscopy. In these cases, it is necessary to perform long routine sample analysis in order to obtain statistically significant information from the whole sample. Electrochemical surface reactions are potential tools to determine the characteristics of the surface. For a probe reaction properly selected, all surface sites in contact with the solution should contribute to the overall response. In the case of platinum, hydrogen and anion adsorption may be used as probe reactions to define the properties of the surface. As we have seen, using cyclic voltammetry of platinum:

i. the overall adsorption charge is directly proportional to the amount surface atoms and thus can be used to calculate the real surface area, and
ii. the distribution of the charge among the different voltammetric peaks gives a first estimation of the presence of the different surface sites on the whole surface[5,6].

It was demonstrated that irreversibly adsorbed bismuth on Pt{111} shows a well-defined surface redox process at 0.62 V[7]. Contributions from the other basal planes are negligible in this potential range. In the same way, irreversibly adsorbed germanium on Pt{100} surfaces also gives rise to a similar well-defined surface redox process around 0.55 V[8]. In this latter case, some interference from other orientations should be controlled[9]. In both cases, the adsorbed adatoms remain on the surface of the corresponding platinum electrodes provided that the upper potential limit is controlled. Hence, bismuth adsorbed on Pt{111} and germanium adsorbed on Pt{100} could be good probes to test the presence of platinum sites with {111} and {100} symmetry respectively since the overall charge associated with each surface redox peak is directly proportional to its amount in the surface. This procedure has been used previously by Feliu *et al.*[10] to characterise a variety of shaped platinum nanoparticles. Here, it will be used to establish trends in terrace site dependency of supported Pt electrocatalysts after thermal treatments in different ambient environments.

7.2 Results

7.2.1 Characterisation and Quantification of HSA platinum electrocatalysts

7.2.1.1 Quantification of {111} and {100} surface sites using bismuth and germanium as surface probes

Figure 7.1 shows CVs of various platinum HSA electrocatalysts sintered in different environments and characterised in 0.5 M H_2SO_4. The standard electrocatalysts were supplied by Johnson Matthey and consist of 60 wt% Pt supported on a high surface area carbon. The graphite support had an estimated surface area of 850 m^2g^{-1}. In table 1, listed are the electrocatalysts provided by Johnson Matthey, along with metal area and particle size (all analytical data was supplied by Johnson Matthey).

Catalyst Code	Catalyst Description	[1]Catalyst Metal Area (m^2/g)	XRD Particle Size (nm)	TEM Particle Size (nm)
08/51	Standard 60% Pt Electrocatalyst	84.9	2	
08/62	Standard 60% Pt Electrocatalyst sintered in H_2	24.9	Range of particle sizes, so not possible to get number	
08/52	Standard 60% Pt Electrocatalyst sintered in N_2	25.3	5.4	6.26
09/46	Standard 60% Pt Electrocatalyst sintered in N_2 + treatment 1	24.5	6.13	
09/93	Standard 60% Pt Electrocatalyst sintered in N_2 + treatment 2	25.8	N/A	6.96
09/110	Standard 60% Pt Electrocatalyst sintered in N_2 treatment 3	23.5	5.7	
08/172	PtCr alloy annealed in H_2	31	4.9	
08/279	PtCo alloy annealed in H_2	31.4	Major amount of crystalline phase	

Table 1 Electrocatalysts provided by Johnson Matthey, where [1]measured at Johnson Matthey CO adsorption , treatment 1 = exposure to hydrogen at $600^{O}C$, treatment 2 = exposure to vacuum at $500^{O}C$ and treatment 3 = exposure to CO at $200^{O}C$.

Also shown are the CVs following irreversible adsorption of bismuth and germanium adatoms on the surface to quantify the amount of {111} and {100} terrace sites present. The procedure of germanium and bismuth deposition to the electrocatalysts is reported in chapter 3 section 3.2.4. Analysis of the bismuth- free standard HSA platinum electrocatalyst CV in fig 7.1a shows the presence of various surface sites such as {110}, {100} step and terrace sites and {111} terrace sites. Closer inspection of the CV shows the presence of small "bump" at 0.1 V on the forward scan which has been termed the "third peak"[11]. The third peak is present because CV has caused the surface to undergo surface reconstruction at potentials negative 0.1 V thus exposing new sites. On the negative sweep, the "third peak" is absent due to the adsorption of anions from solution, thus making the {110} peak look sharper.

For all electrocatalyst CVs in figure 7.1, addition of bismuth to the surface results in the attenuation of the H_{UPD} region. In particular, it is seen that bismuth will first block the step sites and upon blocking the terrace sites, a bismuth redox peak will form at 0.55 V. As more bismuth is added, platinum H_{UPD} features were gradually extinguished and the bismuth redox peak would grow in magnitude and in some cases, shift negative in potential. The maximum potential limit is restricted to 0.75 V in order to prevent bismuth being stripped off the surface. Similarly, addition of germanium to the electrocatalyst first attenuates the H_{UPD} region, but a broad germanium redox peak is formed between 0.50 V only when the {100} terrace sites are blocked with germanium. The maximum potential limit is restricted here to 0.55 V in order to prevent germanium being oxidised off the surface. The amount of {111} and {100} terraces present can be determined by following the methods of Feliu *et al*[10]. For the standard HSA platinum electrocatalyst, adsorption of bismuth onto the electrocatalyst has shown that 5.6 % of the surface is comprised of {111} terraces whereas the amount of {100} terrace sites present are 10.8 %.

The CVs of the standard HSA platinum electrocatalyst fired in N_2 are reported in figs 7.1c and 7.1d. The CVs of the adatom free electrocatalyst show that the platinum features are better defined than the standard catalyst, however the step sites are blocked by some fortuitous contaminant since ordinarily the peaks are more intense for sintered catalysts. The percentage of {111} terraces increased to 16% and it seems that the {100} terraces are not present since no Ge redox peak formed during experiment. This may indicate that the {100} terraces are thermodynamically unstable relative to the {111} terraces or that the {100} terraces are blocked due to sintering in a nitrogen atmosphere. Finally, the standard HSA platinum electrocatalyst was fired in hydrogen and results reported in figures 7.1e and 7.1f.

Closer inspection of the clean electrocatalyst CVs in figs 7.1e and 7.1f (the black curves) show that platinum features are more well defined compared to the standard electrocatalyst and standard electrocatalyst fired in N_2. The step sites are much sharper and the {111} terrace sites are the largest of the three electrocatalysts analysed so far. This response is typical for electrocatalysts with flat terraces and linear steps and such behaviour has been reported previously [12,13]. The presence of flatter terraces in the electrocatalyst is further supported by the fact that the bismuth redox peak at 0.55 V (fig 7.1e), shifts negative in potential as bismuth coverage increases[14]. It can be seen from the results of bismuth and germanium adsorption that as the standard electrocatalyst is sintered in hydrogen, the amount of {111} terrace sites increases (from 5.6 % to 19.4 %), however the proportion of {100} terrace sites decreases (from 10.8 % to 7.5 %), further indicating that the {100} terrace sites are thermodynamically unstable relative to {111}. Finally, table 1 summarises the amount of {111} and {100} terraces present in the three catalysts.

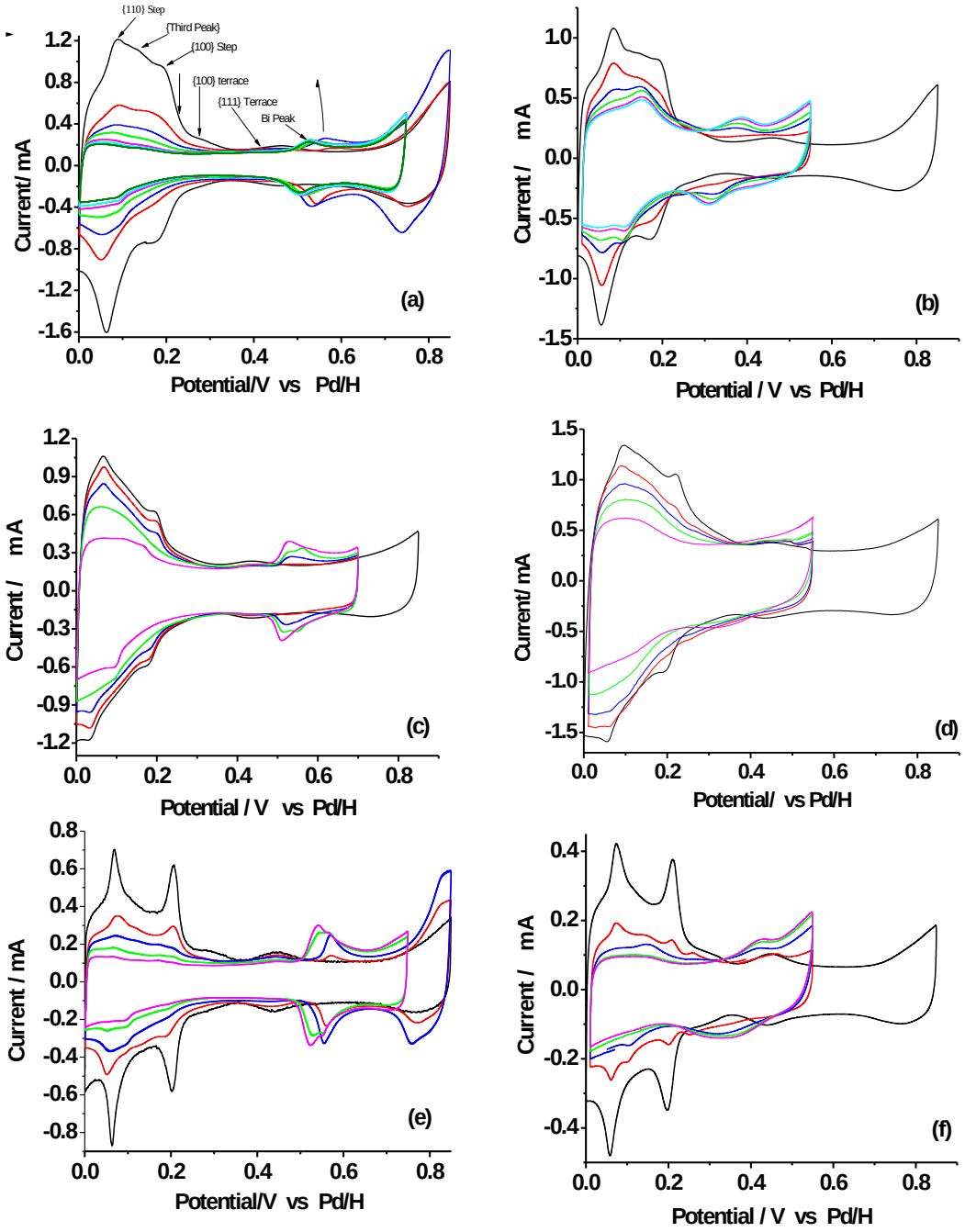

Fig 7.1 CVs of standard HSA 60% platinum electrocatalysts in 0.5M H_2SO_4 with increasing amounts of Bi and Ge irreversibly adsorbed, sweep rate = 10 mVs^{-1} where a) standard HSA platinum electrocatalyst with Bi adsorption, b) standard platinum electrocatalyst with Ge adsorption, c) standard electrocatalyst sintered in N_2 with Bi adsorption, d) standard electrocatalyst sintered in N_2 with Ge adsorption, e) standard electrocatalyst sintered in H_2 with Bi adsorption and f) standard electrocatalyst sintered in H_2 with Ge adsorption.

Catalyst	%{111} Terrace	%{100} Terrace
Standard HSA Pt electrocatalyst	5.6	10.8
Standard HSA Pt electrocatalyst sintered in nitrogen	16	-
Standard HSA Pt electrocatalyst sintered in hydrogen	19.4	7.5

Table 1 % {111} and {100} terraces present in the electrocatalysts in figure 1.

7.2.2 Characterisation of further treated N_2 sintered HSA Pt electrocatalyst in order to liberate step sites

7.2.2.1 Quantification of {111} and {100} surface sites using bismuth and germanium as surface probes

At Johnson Matthey, the standard HSA platinum electrocatalyst fired in N_2 underwent further treatment to liberate the step and terrace sites from whatever spiecies that was inhibiting them. These samples were provided to Cardiff and analysed using CV with bismuth and germanium surface probes to quantify the amount of {111} and {100} terrace sites present. These results are presented in figure 7.2. When the electrocatalyst sintered in N_2 underwent Treatment 1 (figs 7.2a and 7.2b), the clean CVs in Figs 7.2a and 7.2b (the black curves) showed the formation of linear step sites and an increase in the intensity of the {111} and {100} terrace sites in comparison to the electrocatalyst fired in N_2. The increase in the intensity of the {111} and {100} terrace sites is reflected in the adsorption of surface probes Bi and Ge. Bismuth adsorption in fig 7.2a show the %{111} terrace present was 20.20 %, an increase from 16 % for the electrocatalyst sintered in N_2. Germanium adsorption showed that the %{100} terraces present in was 3.6 %, treatment 1 has increased the amount of {100} terraces compared to standard HSA electrocatalyst sintered in N_2 but is considerably less than the amount present in the standard electrocatalyst sintered in H_2 (from 7.5 % to 3.6%). Treatments 2 and 3 to the standard HSA platinum electrocatalyst (figs 7.2c - 7.2f) followed the same pattern as treatment 1. Both treatments produce linear {110} and {100} step sites,

and there is an increase in the intensity of the {100} and {111} terrace sites. The intensity of the {110} and {100} step sites are not as intense as the treatment 1, as is the intensity of the {111} terrace sites. This is reflected during bismuth surface probe experiment for {111} terraces (figs 7.2c and 7.2e) where the %{111} terrace was calculated to be 19 % for treatment 2 and treatment 3. It is interesting to note that for electrocatalyst under treatment 2, bismuth deposition resulted in a second bismuth redox peak to form at 0.45 V. Germanium surface probe experiments to quantify the {100} terraces present found that the %{100} terraces in the electrocatalysts under treatment 2 and 3 were 3.6 % and 2.4 % respectively. Finally in table 2, the amount of {111} and {100} terrace sites present in the electrocatalysts is reported.

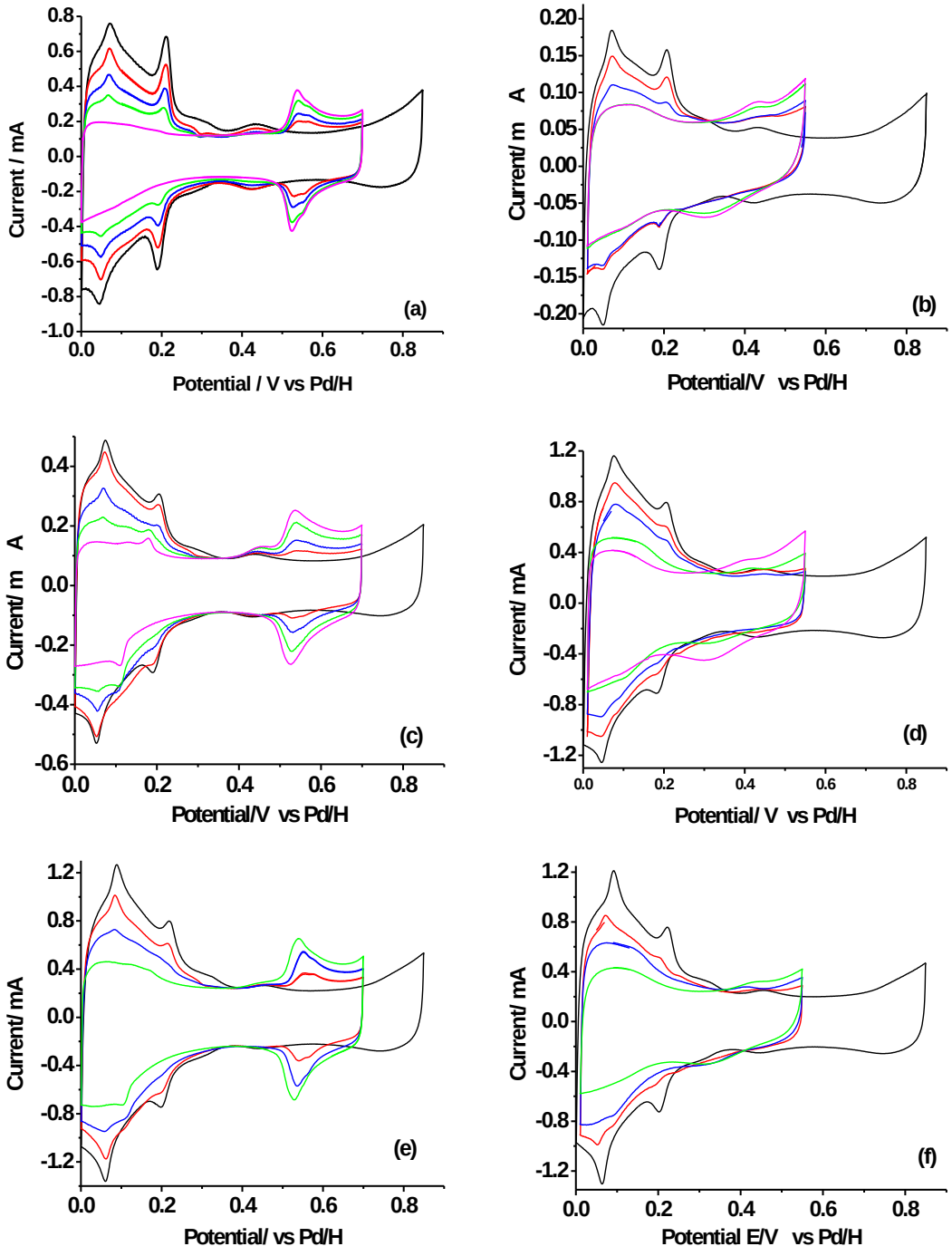

Fig 7.2 CVs of standard HSA 60% platinum electrocatalysts fired in nitrogen, treated further in different environments to liberate the surface site, in 0.5M H_2SO_4 with increasing amounts of irreversibly adsorbed Bi and Ge, sweep rate = 10 mVs^{-1} where a) standard HSA platinum electrocatalyst sintered in N_2, treatment 1 with Bi adsorption, b) standard platinum electrocatalyst sintered in N_2, treatment 1 with Ge adsorption, c) standard electrocatalyst sintered in N_2,treatment 2 with Bi adsorption, d) standard electrocatalyst sintered in N_2, treatment 2 with Ge adsorption, e) standard electrocatalyst sintered in N_2, treatment 3 with Bi adsorption and f) standard electrocatalyst sintered in N_2, treatment 3 with Ge adsorption.

Catalyst	%{111} Terraces	%{100} Terraces
Standard Pt Catalyst fired in N_2, Treatment 1	20.2	3.6
Standard Pt Catalyst fired in N_2, Treatment 2	18	3.6
Standard Pt Catalyst fired in N_2, Treatment 3	18	2.41

Table 2. % {111} and {100} terraces in each catalyst.

7.2.3 Characterisation of Nafion free and Nafion coated platinum HSA electrocatalysts

With the new insight gained from Chapter 4 on how Nafion interacts with well defined platinum electrodes and from chapter 5, where palladium and bismuth adlayers on well defined Pt{hkl} interact with Nafion coated surfaces, it was interesting to find what would occur when Nafion was deposited on HSA platinum electrocatalysts supplied by Johnson Matthey.

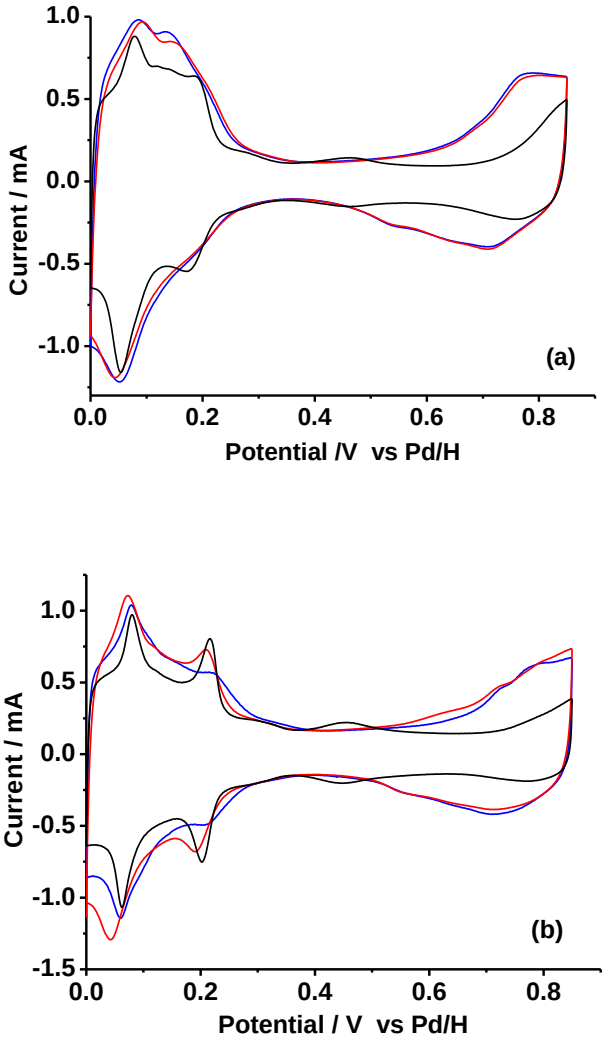

Fig 7.3 CVs of standard HSA Pt electrocatalysts, sweep rate = 10mVs^{-1}, where a) standard unsintered catalyst and b) standard HSA electrocatalyst sintered in hydrogen where the black curve was characterised in 0.5 M sulphuric acid, blue curve was characterised in 0.5M perchloric acid and the red curve electrocatalyst coated in Nafion and characterised in 0.5 M percloric acid.

In figure 7.3 are the voltammograms when Nafion was coated onto the standard HSA platinum electrocatalyst and standard HSA platinum electrocatalyst sintered in hydrogen, in comparison to the Nafion free electrocatalyst CVs in perchloric and sulphuric acid. For the standard HSA platinum electrocatalyst in perchloric acid, (the blue curve in figure 7.3a) a broad Pt H_{UPD} feature between 0 V - 0.2 V and a very broad Pt oxide feature between 0.6 V - 0.85 V formed. The only effect the coating of the electrocatalyst with Nafion seems to have had on the voltammogram (the red curve in 7.3a) is to inhibit to a very small degree the broad Pt H_{HUPD} and Pt oxide. Characterisation of the standard HSA electrocatalyst in sulphuric acid shows significant changes compared to Nafion coated and Nafion free

electrocatalyst CVs in perchloric acid. The H_{UPD} features are better defined, that is the {110} step peak at 0.1 V and in particular the {100} step peak at 0.2 V are much sharper. Between 0.35 V - 0.55 V the broad bump representing {111} terraces is present and the electrosorbed platinum oxide between 0.6 V - 0.85 V is inhibited. All of these features are related to sulphate adsorption on the surface.

As mention in section 7.2.1.1, sintering the standard electrocatalyst in hydrogen produces sharp platinum electrosorption peaks in the voltammograms. This is indicative of the catalyst having more well ordered surface sites. This effect is seen in the voltammograms in figure 7.3b where the black curve is the Nafion free electrocatalyst in sulphuric acid. This voltammogram has the sharpest electrosorption peaks due to the interaction with sulphate anions. For the Nafion free electrocatalyst characterised in perchloric acid (the blue curve in figure 7.3b) , the voltammogram again shows the presence of sharp H_{UPD} electrosorption peaks, though not as sharp as in sulphuric acid and the absence of the broad {111} terrace electrosorption peak between 0.35 V - 0.5 V. As with the standard HSA platinum electrocatalyst, the voltammogram contains a broad oxide peak between 0.6 V - 0.8 V. Coating the electrocatalyst in Nafion (the red curve in figure 7.3b) causes noticeable changes in the Pt H_{HUPD} features, both electrosorption peaks for the {110} and in particular {100} step sites are much sharper compared to the Nafion free electrocatalyst (the blue curve in figure 7.3b). This would be consistent with a stronger interaction of sulphonate groups of the Nafion with Pt compared to perchlorate or "OH_{Ad}" species. However, no sign of Nafion "spikes", as discussed in Chapter 4, was ever observed with any of the standard Johnson Matthey catalysts. This is a remarkable result. From Chapter 4, a necessary and sufficient condition to observe spikes was to have linear steps separated by rather narrow ($n < 6$) average atom separations. In addition, terraces exhibiting sufficiently large terrace widths (> 6 atoms) should also give rise to Nafion spikes. Since, these are absent, it is concluded that the supported catalysts consist of non-linear steps, perhaps separated by > 6 atoms on average. This would correspond to terraces > 1.8 nm in diameter which nonetheless, should still give rise to a small nafion terrace spike. However, if the terraces were also covered with isolated adatoms (i.e. they were not completely flat) this would certainly lead to a break-up of the long range order of the surface and a diminution of terrace spike peak intensity. Hence, in order to rationalise the present results with those of the single crystals, the long range one dimensional (steps) and two dimensional (terraces) order of the supported electrocatalysts is probably insufficient to support Nafion spike behaviour. It would be interesting to test larger

Pt nanoparticles, sintered in hydrogen to examine if Nafion spikes do start to appear eventually.

7.2.4 Quantification of {111} terraces with bismuth as a surface probe of platinum HSA electrocatalysts coated in Nafion

Bismuth adlayers grown on Nafion coated and Nafion free Pt{hkl} was reported in chapter 5. In particular for Pt{111}, it was found that attenuation of the H_{UPD} features during growth of bismuth adlayers on Nafion free and Nafion coated Pt{111} followed the same pattern. The bismuth oxide electrosorption peaks for Nafion coated Pt{111} however were lower in intensity and much broader in shape. It would therefore be interesting to see if the {111} terraces of both the standard HSA platinum catalyst and then the same catalyst fired in hydrogen could be quantified using the methods mentioned previously. Characterisation of the Nafion coated and Nafion free HSA platinum electrocatalysts is reported in section 7.2.2. Surface probe measurements of the {111} terrace of Nafion free and Nafion coated platinum HSA electrocatalysts in perchloric acid are reported in figure 7.4. The measurements are similar to those in sulphuric acid, (figure 7.1), H_{UPD} features are attenuated and a bismuth redox peak grows as the {111} terraces are blocked at 0.55 V. In the case of the electrocatalyst sintered in hydrogen, the bismuth redox peak is formed at 0.6 V. For the Nafion coated and Nafion free standard HSA platinum electrocatalyst, the bismuth decorated voltammograms are almost identical, the bismuth oxide peak is of the same magnitude as in sulphuric acid (figure 7.1a). The amount of {111} terraces quantified were approximately 5.6% for both Nafion free and Nafion coated electrocatalyst. For the Nafion coated sintered HSA electrocatalyst characterised in perchloric acid (fig 7.4d), the magnitude of the bismuth redox peak is of the same magnitude as the Nafion free electrocatalyst in sulphuric acid (fig 7.1e), the {111} terraces were quantified to be at 19.4%. However for the Nafion free electrocatalyst sintered in hydrogen and characterised in perchloric acid (fig 7.4b), the magnitude of the "maximum" bismuth redox peak is not as intense as that of the maximum bismuth coverage for the Nafion coated electrocatalyst. Closer inspection of the voltammograms of the Nafion free hydrogen sintered electrocatalyst reveals that the Pt H_{UPD} features are not fully blocked with bismuth, hence the bismuth redox peak is not as intense. Therefore, it is concluded that bismuth may also be used to quantify the extent of Pt{111} terraces for a Nafion coated sample. This finding may prove useful for *in situ* characterisation

of fuel cell catalysts under operating conditions. Certainly, no structural changes appear to occur when Nafion is adsorbed on platinum in accordance with the single crystal CV data.

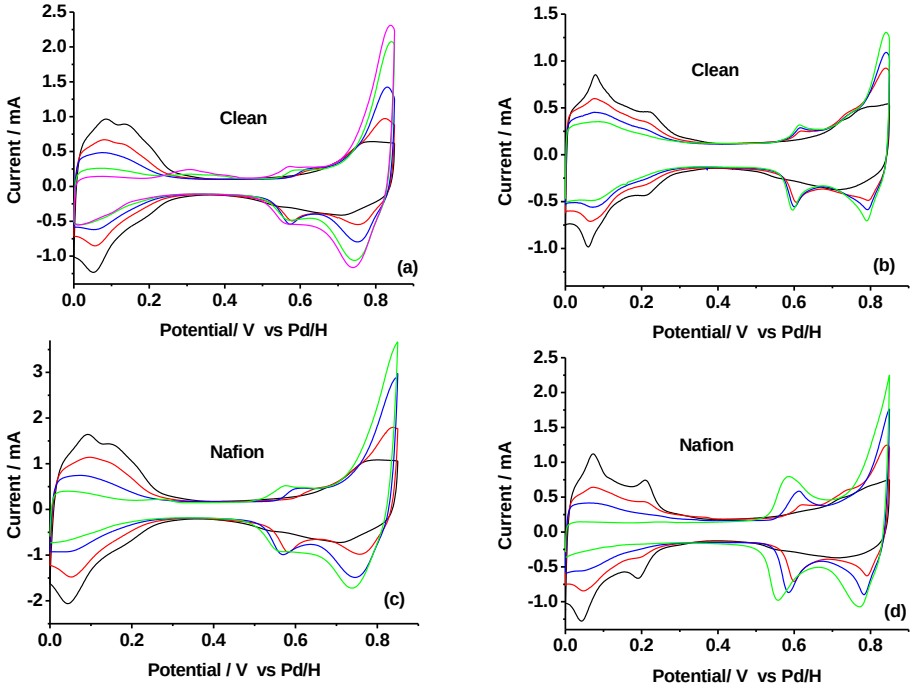

Fig 7.4 Quantification of {111} terraces, using bismuth as a surface probe in 0.5 M $HClO_4$, of Nafion coated and Nafion free HSA Pt electrocatalysts where a) and c) are Nafion free and Nafion coated standard HSA Pt electrocatalyst and b) and d) are Nafion free and Nafion coated standard HSA Pt electrocatalyst sintered in hydrogen. Sweep rate = 10 mV/s.

7.2.5 Characterisation of platinum alloy (PtX) electrocatalysts where X is a transition metal other than platinum

It has been well known that alloying platinum with other transition metals has been proven to enhance the oxygen reduction reaction (ORR) for fuel cell reactions compared to pure platinum [15,16]. In recent years, studies on well defined platinum bimetallic electrodes combined with modelling approaches have been performed to understand why platinum bimetallic surfaces show an activity enhancement compared to pure platinum and to predict new surfaces that show a greater enhancement for oxygen reduction. Adzic[17] reported enhancement in ORR from a Pt coated Pd{111} electrode whilst Markovic[18] reported an

enhancement in ORR on a Pt_3Ni alloy surface electrode. Based on studies of well defined electrodes, various platinum alloy core-shell nanoparticles and catalysts have been prepared for fuel cell use. Provided by Johnson Matthey for characterisation were two PtX alloy electrocatalysts where X = Cr and Co. The characterisation of the electrocatalysts, along with the quantification of {111} and {100} terrace sites with bismuth and germanium surface probes are shown in figure 7.5.

The double layer regions of both the PtCr and PtCo alloy electrocatalysts were rather large, consistent with deposition onto a high surface area carbon[12,13]. As the {111} terraces of both alloy catalysts become blocked with bismuth (figs 7.5a and 7.5c), the Ohmic drop seen in the clean surface samples correcting itself and TWO Bi electrosorption peaks formed at 0.45 V formed along with the majority (and typical of pure Pt) bismuth redox peak at 0.55 V. For the PtCo alloy, the second bismuth electrosorption peak was greater in intensity compared to the PtCr alloy. In fact, after quantification of bismuth redox charge, it was found that the %{111} terraces present in the PtCr alloy was greatest (42.26%) compared to PtCo alloy electrocatalyst (16.33%). The value for the PtCr alloy is even greater than that seen with the pure Pt supported electrocatalysts suggesting a strong propensity to form (111) terraces. Adsorption of germanium as a surface probe (to determine the amount of {100} terraces present in both electrocatalysts) followed the trends set earlier by the Pt electrocatalysts. That is, a broad germanium electrosorption peak formed between 0.35 V - 0.45 V. According to the evaluation of surface charge under the Ge redox peak, the amount of {100} terraces present in the electrocatalysts was low, the PtCr electrocatalyst having 1.90% compared to 1.16% for PtCo electrocatalyst. Hence, both alloys are virtually free of {100} terraces.

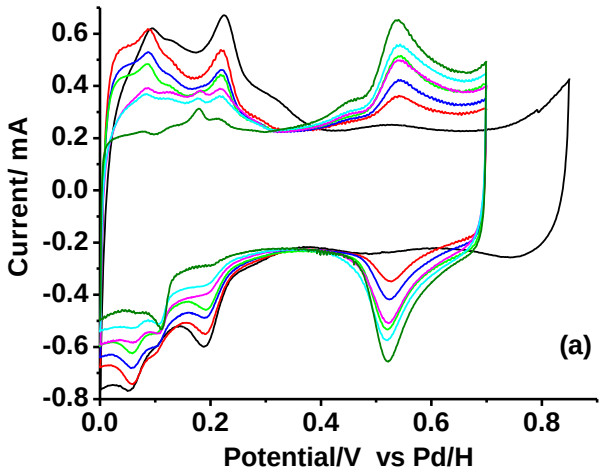
Current/ mA
0.6
0.4
0.2
0.0
-0.2
-0.4
-0.6
-0.8
0.0
0.2
0.4
0.6
0.8
Potential/V vs Pd/H
(a)

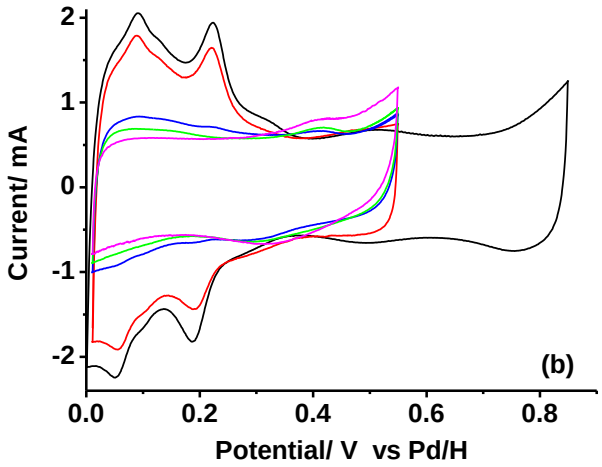
Current/ mA
2
1
0
-1
-2
0.0
0.2
0.4
0.6
0.8
Potential/ V vs Pd/H
(b)

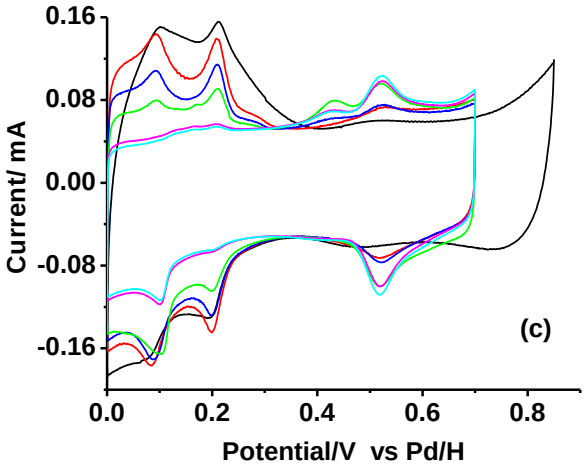
Current/ mA
0.16
0.08
0.00
-0.08
-0.16
0.0
0.2
0.4
0.6
0.8
Potential/V vs Pd/H
(c)

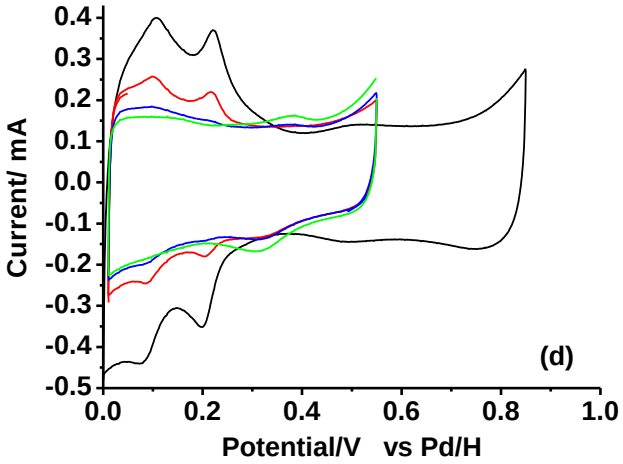

Fig 7.5 CVs of PtX alloy electrocatalysts, where X = Cr and Co in 0.5 M H_2SO_4 sweep rate = 10mVs^{-1}, where a) is PtCr alloy with Bi as surface probe, b) PtCr alloy with Ge as surface probe, c) PtCo alloy with Bi as surface probe and d) PtCo alloy with Ge as surface probe.

Unfortunately, in acidic electrolytes, dissolution of the transition metal alloyed in the PtX electrocatalyst is a major drawback for proton exchange membrane fuel cells (PEMFC)[15]. This is evident in figure 7.6a and 7.6b where the electrocatalysts were characterised in sodium hydroxide, prior to and following CV analysis in aqueous sulphuric acid. It is seen from figure 7.6a that the CV of the PtCo electrocatalyst characterised in NaOH before treatment in sulphuric acid (the black curve) that the platinum H_{UPD} features seem to be inhibited, possibly with excess surface cobalt blocking sites. It is also seen that a quasi-reversible oxide electrosorption peak is formed at 0.6 V on the forward sweep and at 0.4 V on the reverse sweep. The red curve in figure 7.6a represents the CV of the PtCo electrocatalyst in sodium hydroxide after characterisation in sulphuric acid. From this CV, it is seen that the platinum H_{UPD} features are now no longer inhibited and that the oxide peak at 0.6 V is not present. Hence, dissolution of excess cobalt from the surface occurs in acid together with loss of the quasi-reversible oxide peak which is ascribed to cobalt-oxide bond formation.

For the PtCr CV in aqueous sodium hydroxide before sulphuric acid characterisation (the black curve in figure 7.6b), it is seen that the platinum H_{UPD} features are inhibited only slightly by excess chromium. The red curve in figure 7.6b, where the PtCr electrocatalyst is collected in sodium hydroxide after sulphuric acid treatment, shows that the platinum H_{UPD} and oxide features have marginally increased in intensity. Assuming that excess chromium is not dissolving in aqueous sodium hydroxide, both of the CVs in figure 7.6b suggest that platinum is present in the surface of the catalyst to a greater extent after contact with

sulphuric acid, compared to cobalt i.e. that once again excess chromium has leeched out of the electrocatalyst although not so much of Cr is present in the surface compared to cobalt. Finally, the Pt quasi-reversible redox oxide peak present at 0.6 V in the PtCo electrocatalyst, is absent in the PtCr CV in fig 7.6b. Hence, it appears that this oxide peak only appears at high cobalt surface coverages. Tin also gives rise to such behaviour [19,20].

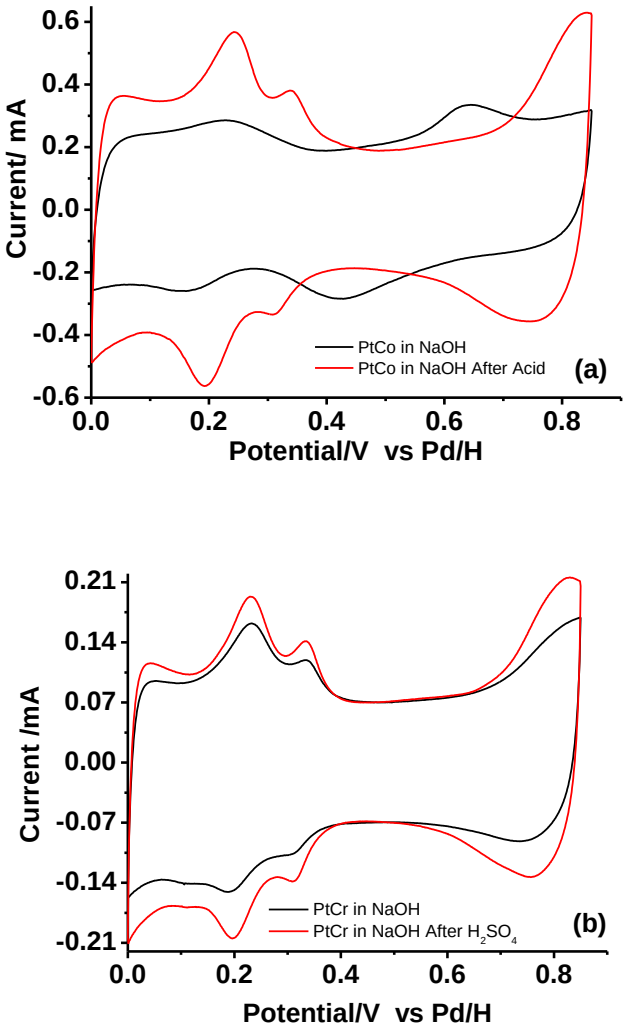

Fig 7.6 CVs of PtX alloy electrocatalysts where a) PtCo electrocatalyst characterised in 0.5M NaOH before (black curve) and after 0.5M H_2SO_4 characterisation (red curve) and b) PtCr electrocatalyst in 0.5M NaOH before (black curve) and after 0.1M H_2SO_4 characterisation (red curve), sweep rate for both = 10 mVs^{-1}.

7.3 Conclusions

Several high surface area (HSA) Pt fuel cell electrocatalysts provided by Johnson Matthey have been characterised using cyclic voltammetry (CV). Using bismuth and germanium as

surface probes, the amounts of {111} and {100} terraces present in the electrocatalysts were quantified using CV. Decorating the Pt electrocatalyst with bismuth produces a unique bismuth redox peak at 0.55 V in the CV, the charge being proportional to the {111} terraces present. Similarly, irreversibly adsorbed germanium produces a redox peak at 0.45 V where the charge is proportional to the {100} terrace sites present. The standard HSA Pt electrocatalyst contained 5.6% {111} terraces and 10.8% {100} terraces. Sintering the electrocatalysts in nitrogen and hydrogen was found to produce sharp linear step peaks in the voltammograms (in the case of hydrogen) but gave rise to a voltammogram with blocked step peaks in the case of sintering in nitrogen. The %{111} terraces was found to have increased (16% and 19.4% respectively for nitrogen and hydrogen treatments), but the {100} terraces were found to be unstable and decreased in amount (7.8% for sintering in hydrogen and 0% for sintering in nitrogen). The HSA Pt electrocatalyst sintered in nitrogen underwent further treatment to liberate the blocked step sites, this in turn had a positive effect during the surface probe experiments whereby all of the newly treated electrocatalysts a greater % of {111} and {100} terraces. This was consistent with cleaning of an impurity from the surface of the nitrogen sintered catalyst after treatment.

Analysis of Nafion coated HSA Pt electrocatalyst sintered in hydrogen undergoing CV in 0.5 M $HClO_4$ was found to produce sharper {100} step peaks compared to the Nafion free electrocatalyst. Comparisons between Nafion coated and Nafion free unsintered standard HSA electrocatalyst in perchloric acid was found to have produced no change in the CVs. This suggests, based on the chapter 4 results that the surface order necessary to observe nafion "spike" peaks is absent in all supported catalysts studied. Using bismuth as a surface probe to quantify the amount of {111} terraces of the Nafion coated and Nafion free electrocatalysts in perchloric acid was found to follow trends previously observed using both single crystals and aqueous sulphuric acid electrolyte. That is, decorating the catalyst with bismuth would attenuate all Pt H_{UPD} features and produce a bismuth redox peak at 0.55 V when the {111} terraces were blocked. The structure of the electrocatalysts before and after Nafion dosing remained unchanged and identical surface percentages of {111} and {100} terraces were estimated. Finally, characterisation of PtX alloy electrocatalysts where X = Cr and Co using CV was performed in acid and alkaline media. Voltammograms, before and after CV analysis in sulphuric acid (using sodium hydroxide as the electrolyte) suggests that the acid treatment causes the cobalt and chromium to leech out of the alloy. The PtCo electrocatalyst appears to have a significant quantity of "excess" cobalt on the surface of the

alloy that is removed easily by acid etching. In contrast, the majority of sites in the PtCr alloy appear to be Pt assuming that Cr cannot be etched in aqueous sodium hydroxide. Surface probe measurements suggest that a large amount of {111} terraces are present in both catalysts (particularly PtCr), but a very low extent of {100} terrace sites.

7.4 References

(1) Clavilier, J.; Faure, R.; Guinet, G.; Durand, R. *Journal of Electroanalytical Chemistry* **1980**, *107*, 205.

(2) Clavilier, J.; Durand, R.; Guinet, G.; Faure, R. *Journal of Electroanalytical Chemistry* **1981**, *127*, 281.

(3) Sun, S. G.; Yang, Y. Y. *Journal of Electroanalytical Chemistry* **1999**, *467*.

(4) Jarvi, T. D.; Sriramulu, S.; Stuve, E. M. *Colloids and Surfaces a-Physicochemical and Engineering Aspects* **1998**, *134*.

(5) Clavilier, J.; Elachi, K.; Rodes, A. *Chemical Physics* **1990**, *141*, 1.

(6) Rodes, A.; Elachi, K.; Zamakhchari, M. A.; Clavilier, J. *Journal of Electroanalytical Chemistry* **1990**, *284*.

(7) Clavilier, J.; Feliu, J. M.; Aldaz, A. *Journal of Electroanalytical Chemistry* **1988**, *243*.

(8) Gomez, R.; Llorca, M. J.; Feliu, J. M.; Aldaz, A. *Journal of Electroanalytical Chemistry* **1992**, *340*.

(9) Rodriguez, P.; Herrero, E.; Solla-Gullon, J.; Vidal-Iglesias, E. J.; Aldaz, A.; Feliu, J. M. *Electrochimica Acta* **2005**, *50*.

(10) Rodriguez, P.; Herrero, E.; Solla-Gullon, J.; Vidal-Iglesias, F. J.; Aldaz, A.; Feliu, J. M. *Electrochimica Acta* **2005**, *50*, 4308.

(11) Gomez, R.; Clavilier, J. *Journal of Electroanalytical Chemistry* **1993**, *354*.

(12) Price, M. M Phil Thesis, Cardiff University, **2000**.

(13) D.J., J. PhD Thesis, Cardiff University, **2003**.

(14) Hazzazi; Abdullah, O. PhD Thesis, Cardiff University, **2002**.

(15) Stassi, A.; D'Urso, C.; Baglio, V.; Di Blasi, A.; Antonucci, V.; Arico, A. S.; Castro Luna, A. M.; Bonesi, A.; Triaca, W. E. *Journal of Applied Electrochemistry* **2006**, *36*.

(16) Zhang, J. L.; Vukmirovic, M. B.; Sasaki, K.; Nilekar, A. U.; Mavrikakis, M.; Adzic, R. R. *Journal of the American Chemical Society* **2005**, *127*.

(17) Zhang, J. L.; Vukmirovic, M. B.; Xu, Y.; Mavrikakis, M.; Adzic, R. R. *Angewandte Chemie-International Edition* **2005**, *44*.

(18) Stamenkovic, V. R.; Fowler, B.; Mun, B. S.; Wang, G. F.; Ross, P. N.; Lucas, C. A.; Markovic, N. M. *Science* **2007**, *315*, 493.

(19) Herranz, T.; Garcia, S.; Martinez-Huerta, M. V.; Pena, M. A.; Fierro, J. L. G.; Somodi, F.; Borbath, I.; Majrik, K.; Tompos, A.; Rojas, S. *International Journal of Hydrogen Energy* **2012**, *37*, 7109.

(20) El-Shafei, A. A.; Eiswirth, M. *Surface Science* **2010**, *604*.

Chapter Eight

Conclusions and Final Remarks

8.1 Introduction

The present study was undertaken in order to further understand the structure of the interface between the ionomer Nafion and the electrode surface. The interface is at the heart of a functioning membrane electrode assembly (MEA) which is crucial to fuel cell operation. Knowledge of the actual nature of the "three phase" interface is vague and understanding this better will in turn help optimise the design of fuel cells. Indeed it can be said that new knowledge has been obtained in this study with regards to the interactions of Nafion and the electrode surface. This chapter will be used to give an overview of the conclusions outlined in the previous chapters in relation to the aims of the project. Later, a brief discussion outlining the outcome of this study in relation to future work will be given.

8.2 Conclusions

The adsorption of Nafion onto basal plane Pt{hkl} single crystal electrodes has reproduced the results of Markovic *et al*[1]. The Nafion induced sulphonate peaks produced in the voltammograms have been assigned to the local potential of zero charge (PZTC) of the surface, except for the {111} surface where the "spike" is slightly positive of the PZTC. It is speculated that the singular nature of the Pt{111} electrode may be related to (an unusual) positive shift in the PZTC in the presence of Nafion. Unusual since anions normally cause a decrease in the PZTC. Future studies using CO charge displacement should be carried out to verify this speculation. For all other surfaces, the potential at which the Nafion spike occurs is consistent with an adsorption/desorption of sulphonate groups reflecting the charged state of the electrode surface.

When Nafion was adsorbed on stepped Pt{hkl} electrodes, an important finding was obtained. Nafion displays unprecedented sensitivity to the average spacing of linear step sites in that intense Nafion redox peaks at step sites are quenched rapidly as average terrace width increases from 2 to 6 atoms. This behaviour is ascribed to competitive adsorption of Nafion with OH_{ad} species formed in the H_{UPD} region of highly stepped Pt{hkl} electrodes in acidic

aqueous perchloric acid. This phenomenon also applies to basal Pt{111}, Pt{100}, and Pt{110} planes whereby displacement of OH_{ad} species by more strongly adsorbed sulphonate substituents of Nafion also leads to quenching of CV peaks ascribable to OH_{ad}. Therefore fundamental single crystal electrode studies have shown that Nafion is a probe for OH_{AD} and sulphonate adsorption on the Pt surface is potential dependent.

XPS was used to determine the thickness and elemental composition of the Nafion film on a Pt{111} electrode. The film thickness was found to be 3.3 nm and a nominal stoichiometry for the polymer monomer of $C_{20}F_{38}O_5S$ is obtained in satisfactory agreement ((+/-10% error) with the theoretical stoichiometry of $C_{21}F_{41}O_5S$ based on an idealized Nafion monomer of equivalent weight 1100[2].

The effect of Nafion adsorption on various Pt{hkl} electrodes in relation to the ORR reaction was also studied. It was found that although the ORR was inhibited to a limited extent when the sulphonate groups of Nafion were adsorbed[3] (shift of ORR $E_{1/2}$ to slightly more negative potentials, decrease in exchange current density) the overall reduction mechanism remained unchanged relative to the clean surface. Hence, the rate limiting step at "low" overpotential (when electrosorbed oxide was present) involved a two electron transfer whereas at "high" overpotential (when the surface was free of electrosorbed oxide), a one electron transfer characterised the rate determining step.

Palladium and bismuth adlayers have been deposited onto Nafion coated and Nafion free Pt*{hkl}* electrodes and were characterised using CV. PtPd*{hkl}* surface alloys were also created and characterised via CV (Nafion free and Nafion coated) as a function of alloy composition. Voltammetric profiles of the Nafion free adatom modified electrodes were in agreement with those of the literature.[4-13]

CVs of palladium modified, Nafion coated Pt{111} and {100} in 0.1M $HClO_4$ showed the first layer palladium electrosorption peak was much more sharper and resembled more closely the voltammograms in H_2SO_4. This was due to the presence of sulphonate groups of Nafion being specifically adsorbed on the first monolayer of palladium.

CVs in 0.1M $HClO_4$ of the PtPd surface alloys showed where the palladium surface composition was relatively high, Nafion adsorption would produce sharper, more well defined peaks compared to Nafion free CVs. The PtPd{111} and {100} alloy surfaces CVs showed that the sulphonate peaks would shift negatively as palladium coverage was increased. This is speculated to be caused by a shift in the PZTC of the surface to more

negative values as palladium composition increased, reflecting the lower work function of palladium compared to platinum[14]. For bismuth adlayers adsorbed on Nafion coated Pt{hkl}, bismuth deposition would again attenuate H_{UPD} features and produce Bi-OH features at 0.75 V - 0.9 V for the different surfaces. It was interesting to note that attenuation of H_{UPD} features was identical for Nafion free and Nafion coated surfaces but the Bi-OH features for the Nafion coated surfaces exhibited marked differences. For all Pt{110} surfaces, Nafion free or Nafion coated, bismuth or palladium modified or platinum-palladium surface alloys, would simply result in the attenuation of H_{UPD} features and growth in the oxide region.

The changes in the electrocatalytic activity of palladium adlayers on Pt{111} towards methanol and formic acid electrooxidation as a consequence of Nafion adsorption were reported. For formic acid, Nafion adsorption results in negligible attenuation in electrooxidation currents compared to those found using acidic aqueous perchloric acid electrolyte. This suggests that specific adsorption of the sulphonate anions of the polymer does not interfere with the adsorption and subsequent surface decomposition of formic acid at Pd/Pt{111} electrodes. In contrast, methanol electrooxidation in perchloric acid is significantly inhibited when Nafion is also adsorbed indicating that competition for surface sites between specifically adsorbed sulphonate anions and methanol is important in determining electrode activity. Both of these factors highlight the potential utility of Nafion in fuel cells based on formic acid and methanol in that little adverse influence should be expected in the former whereas the intrinsic activity of the methanol fuel cell could be compromised.

Finally, real fuel cell Pt electrocatalysts from Johnson Matthey were characterised, as received using CV. The {111} and {100} surface sites were quantified using bismuth and germanium as surface probes[15]. Nafion was adsorbed onto selected electrocatalysts. The electrocatalyst sintered in hydrogen contained a sharper {100} step peak, compared to the Nafion free electrocatalyst in aqueous 0.5M $HClO_4$. No change however was observed for the unsintered electrocatalyst either Nafion free or Nafion coated. Using bismuth to probe the electrocatalyst for {111} sites, bismuth adsorption on the Nafion coated electrocatalysts followed the trends using single crystal electrodes and aqueous sulphuric acid. That is, upon bismuth adsorption, all H_{UPD} sites are quenched and a bismuth redox peak is formed at 0.55 V when {111} sites are blocked. Germanium was also used to probe the {100} surface sites of the Nafion coated surfaces. The structure of the electrocatalysts before and after Nafion

dosing remained unchanged and identical surface percentages of {111} and {100} terraces were estimated.

8.3 Future directions

Prior to this study, as shown in the literature review, various microscopic and spectroscopic methods have been used to study the Nafion / platinum interface. Spectroscopic measurements by Ayato *et al*[16], Gruger *et al*[17] and Kanamura *et al*[18] have shown using IR and Raman spectroscopy the dynamic behaviour of Nafion with a Pt electrode. The measurements by Ayato *et al*[16] and Kanamura *et al*[18] were performed on poly orientated Pt electrodes whilst Gruger *et al*[17] performed measurements on a bulk film.

At Cardiff, the Au@SiO_2 nanoparticles synthesised by Tian *et al*[19] are being fine tuned. These nanoparticles, for use in the spectroscopic technique SHINERS (shell isolated nanoparticle enhanced Raman spectroscopy) and consist of a gold core approximately 55 nm in diameter, coated in a thin 2 nm silica shell. SHINERS nanoparticles can deposited onto Pt single crystal electrodes and SERS (surface enhanced Raman spectroscopy) measurements can be obtained of the single crystal electrodes without the need for roughening. The gold component of the nanoparticles provides the SERS enhancement whilst the silica shell "insulates" the gold electrochemical signal so only platinum's electrochemistry is observed. Any changes in vibrational modes of Nafion due to surface structure can be observed using SHINERS nanoparticles. Hence, future studies could utilise SHINERS to study Nafion adsorbed on Pt{hkl} to study changes in vibrational bands ascribable to water and Nafion as a function of potential and in particular either side of the Nafion spike. This may shed more light on the nature of the Pt-sulphonate bond.

Microscopic measurements have the advantage of providing a direct visualisation of the size, shape and geometrical distribution of the ionic clusters, crystallites and the continuous perfluoronated matrix. Recently, Koestner *et al*[20] used *in situ* AFM to image Nafion being adsorbed onto a HOPG surface. At low concentrations it was found that preferential adsorption occurs along the step edge at a low polymer coverage[20]. Hiesgen *et al*[21] used *in situ* EC-STM to image Nafion adsorbed onto a catalyst powder. Hiesgen *et al*[21] observed the hydrophillic regions of Nafion. Zooming into the hydrophillic regions, an image consisting of circular globules was produced.

At Cardiff, preliminary EC-STM measurements have been performed on the Nafion film adsorbed onto Pt{111}. These measurements have been performed in the "dry" state and under an electrochemical environment. Preliminary images have shown globular structures on the surface in the dry state and in the electrochemical cell. Further, the electrochemical measurements have shown that these globular structures are aligned with respect to the step edge and are approximately 3-5 nm in diameter. The measurements need to be fine tuned to eliminate any hint of surface contamination so that images can be obtained at different potentials, and of different single crystal electrodes.

Other measurements to be performed are the ORR of different Pt{hkl} single crystal electrodes, in order to build a library and obtain activity *vs* structure relationships. Furthermore, ORR measurements of Nafion coated PtX{hkl} alloy surfaces need to be made in order to further understand at a fundamental level ORR, thus helping to optimise fuel cell electrode design. Similarly electrooxidation of methanol and formic acid on Nafion coated PtX{hkl} alloy single electrodes need to be made to discover if so-called "volcano plots"[22-25], for all reactions, are also valid when the aqueous electrolyte is replaced by Nafion.

8.4 References

(1) Subbaraman, R.; Strmcnik, D.; Stamenkovic, V.; Markovic, N. M. *Journal of Physical Chemistry C* **2010**, *114*, 8414.

(2) Ma Gomez-Marin, A.; Berna, A.; Feliu, J. M. *Journal of Physical Chemistry C* **2010**, *114*, 20130.

(3) Subbaraman, R.; Strmcnik, D.; Paulikas, A. P.; Stamenkovic, V. R.; Markovic, N. M. *Chemphyschem* **2010**, *11*, 2825.

(4) Attard, G. A.; Bannister, A. *Journal of Electroanalytical Chemistry* **1991**, *300*.

(5) Attard, G. A.; Price, R. *Surface Science* **1995**, *335*.

(6) Llorca, M. J.; Feliu, J. M.; Aldaz, A.; Clavilier, J. *Journal of Electroanalytical Chemistry* **1993**, *351*.

(7) Ball, M. J.; Lucas, C. A.; Markovic, N. M.; Stamenkovic, V.; Ross, P. N. *Surface Science* **2002**, *518*.

(8) Vidal-Iglesias, F. J.; Al-Akl, A.; Watson, D. J.; Attard, G. A. *Electrochemistry Communications* **2006**, *8*, 1147.

(9) Vidal-Iglesias, F. J.; Al-Akl, A.; Watson, D.; Attard, G. A. *Journal of Electroanalytical Chemistry* **2007**, *611*.

(10) Clavilier, J.; Feliu, J. M.; Aldaz, A. *Journal of Electroanalytical Chemistry* **1988**, *243*.

(11) Evans, R. W.; Attard, G. A. *Journal of Electroanalytical Chemistry* **1993**, *345*.

(12) Hayden, B. E.; Murray, A. J.; Parsons, R.; Pegg, D. J. *Journal of Electroanalytical Chemistry* **1996**, *409*.

(13) Kizhakevariam, N.; Stuve, E. M. *Journal of Vacuum Science & Technology a-Vacuum Surfaces and Films* **1990**, *8*.

(14) Attard, G. A.; Hazzazi, O.; Wells, P. B.; Climent, V.; Herrero, E.; Feliu, J. M. *Journal of Electroanalytical Chemistry* **2004**, *568*, 329.

(15) Rodriguez, P.; Herrero, E.; Solla-Gullon, J.; Vidal-Iglesias, F. J.; Aldaz, A.; Feliu, J. M. *Electrochimica Acta* **2005**, *50*, 4308.

(16) Ayato, Y.; Kunimatsu, K.; Osawa, M.; Okada, T. *Journal of the Electrochemical Society* **2006**, *153*.

(17) Gruger, A.; Regis, A.; Schmatko, T.; Colomban, P. *Vibrational Spectroscopy* **2001**, *26*, 215.

(18) Kanamura, K.; Morikawa, H.; Umegaki, T. *Journal of the Electrochemical Society* **2003**, *150*.

(19) Li, J. F.; Huang, Y. F.; Ding, Y.; Yang, Z. L.; Li, S. B.; Zhou, X. S.; Fan, F. R.; Zhang, W.; Zhou, Z. Y.; Wu, D. Y.; Ren, B.; Wang, Z. L.; Tian, Z. Q. *Nature* **2010**, *464*.

(20) Koestner, R.; Roiter, Y.; Kozhinova, I.; Minko, S. *Langmuir* **2011**, *27*.

(21) Hiesgen, R.; Eberhardt, D.; Aleksandrova, E.; Friedrich, K. A. *Fuel Cells* **2006**, *6*.

(22) Hammer, B.; Norskov, J. K. *Surface Science* **1995**, *343*.

(23) Norskov, J. K.; Rossmeisl, J.; Logadottir, A.; Lindqvist, L.; Kitchin, J. R.; Bligaard, T.; Jonsson, H. *Journal of Physical Chemistry B* **2004**, *108*.

(24) Ruban, A.; Hammer, B.; Stoltze, P.; Skriver, H. L.; Norskov, J. K. *Journal of Molecular Catalysis a-Chemical* **1997**, *115*.

(25) Stamenkovic, V. R.; Mun, B. S.; Arenz, M.; Mayrhofer, K. J. J.; Lucas, C. A.; Wang, G.; Ross, P. N.; Markovic, N. M. *Nature Materials* **2007**, *6*.